Ice dynamics of the Darwin-Hatherton glacial system, Transantarctic Mountains, Antarctica

A thesis
submitted in partial fulfilment of
the requirements for the degree of
Doctor of Philosophy in Geography

By
Mette Riger-Kusk

University of Canterbury
2011

Abstract

The Darwin-Hatherton glacial system (DHGS) drains from the East Antarctic Ice Sheet (EAIS) and through the Transantarctic Mountains (TAM) before entering the Ross Embayment. Large ice-free areas covered in glacial sediments surround the DHGS, and at least five glacial drift sheets mark the limits of previous ice extent. The glacier belongs to a group of slow-moving EAIS outlet glaciers which are poorly understood. Despite this, an extrapolation of a glacial drift sheet boundary has been used to determine the thickness of the EAIS and the advanced West Antarctic Ice Sheet (WAIS) during the Last Glacial Maximum (LGM). In order to accurately determine the past and present contributions of the Antarctic ice sheets to sea level changes, these uncertainties should be reduced. This study aims to examine the present and LGM ice dynamics of the DHGS by combining newly acquired field measurements with a 3-D numerical ice sheet-shelf model. The fieldwork included a ground penetrating radar survey of ice thickness and surface velocity measurements by GPS. In addition, an extensive dataset of airborne radar measurements and meteorological recordings from automatic weather stations were made available. The model setup involved nesting a high-resolution (1 km) model of the DHGS within a lower resolution (20 km) all-Antarctic simulation. The nested 3-D modelling procedure enables an examination of the impact of changes of the EAIS and WAIS on the DHGS behaviour, and accounts for a complex glacier morphology and surface mass balance within the glacial system.

The findings of this study illustrate the difference in ice dynamics between the Darwin and Hatherton Glaciers. The Darwin Glacier is up to 1500 m thick, partially warm-based, has high driving stresses (~150 kPa), and measured ice velocities increase from 20-30 m yr^{-1} in the upper parts to ~180 m yr^{-1} in the lowermost steepest regions, where modelled flow velocities peak at 330 m yr^{-1}. In comparison, the Hatherton Glacier is relatively thin (<900 m), completely cold-based, has low driving stresses (~85 kPa), and is likely to flow with velocities <10 m yr^{-1} in most regions. It is inferred that the slow velocities with which the DHGS flows are a result of high subglacial mountains restricting ice flow from the EAIS, large regions of frozen basal conditions, low SMB and undulating bedrock topography. The model simulation of LGM ice conditions within the DHGS implies that the ice thickness of the WAIS has been significantly overestimated in previous reconstructions. Results show that the surface of the WAIS and EAIS away from the TAM would have been elevated 600-750 and 0-80 m above present-day levels, respectively, for the DHGS to reach what was inferred to represent the LGM drift sheet limit. Ultimately, this research contributes towards a better understanding of the dynamic behaviour of slow moving TAM outlet glaciers, and provides new insight into past changes of the EAIS and WAIS. This will facilitate more accurate quantifications of contributions of the WAIS and EAIS to changes in global sea level.

Acknowledgements

This has been a long journey, which has taken me to one of the most remarkable places on the planet, and I would like to thank all of the people that have helped me on my way. First of all, a big thank you to my three supervisors Wendy Lawson, Wolfgang Rack and Brian Anderson. You have all helped me move forward when I most needed it, and I especially enjoyed the discussion and stories shared during dinner in a small yellow tent.

During my studies I have had had the privilege of working alongside helpful and enthusiastic people in the Department of Geography and Gateway Antarctica, some of whom I will mention here. Bryan Storey introduced me to the Antarctic environment for which I will always be grateful. Peyman Zawar-Reza inspired me about meteorological datasets and Ian Owens, with his wealth of knowledge, offered timely and important advice. I would also like to thank Irfon Jones who taught me about cartography with patience and humour, Justin Harrison and Nick Key who helped organise and plan my fieldwork, Marney Brosnan who twice 'volunteered' for the ungrateful task of designing my posters while I was away, and Graham Furniss and Steven Sykes who made the modelling part of this work possible with their knowledge of computers and programming.

I would also like to acknowledge the expertise and help offered by people from outside the department. In particularly, I would like to thank David Pollard for allowing me to use his model in my work and for providing invaluable advice along the way, and Donald D. Blankenship and his team for adjusting their ICECAP field campaign to include airborne radar measurements over the DHGS and letting me use these in my work. I am also grateful for the advice on GPR processing and interpretation offered by Mike Finnemore, Matt Nolan and David Nobes, which significantly improved this part of my work. Thank you also to Dean Arthur for his great company and ability to keep us safe during the fieldwork. Also of importance to this work is the SPIRIT DEM which was made available through the project IPY ASAID (Co-PI: W. Rack). Without the financial and logistical support of Antarctic New Zealand, none of this could have been possible, and I thank the staff in Christchurch and at Scott Base for an enjoyable working relationship. Education New Zealand has supported me throughout this research with a New Zealand International Doctoral Research Scholarship, and my participation in a course in Italy was financed by the Department of Geography and Gateway Antarctica.

Finally, I would like to thank my family and friends at home and in New Zealand, who have supported me with humour and love in whatever adventure I have embarked upon. I especially thank Mark, who despite these last crazy months, still plans to marry me this autumn.

Contents

Abstract ii

Acknowledgements iii

List of tables viii

List of figures ix

List of abbreviations xii

1 Introduction 1

1.1 Aims and objectives 2

1.2 General characteristics of the WAIS and EAIS 5

1.3 Current mass balance of the WAIS and EAIS 6

1.4 Changes in the WAIS and EAIS since the LGM 7

1.4.1 Changes in the WAIS during and since the LGM 8

1.4.2 Changes in the EAIS during and since the LGM 10

1.5 Glaciers in the Transantarctic Mountains 10

1.5.1 Mass balance 11

1.5.2 Characteristics of fast moving outlet glaciers 13

1.5.3 Characteristics of slow moving outlet glaciers 16

1.6 Change of glaciers in the Transantarctic Mountains since the LGM 18

1.7 Thesis outline 19

1.8 Summary 21

2 Introduction to the Darwin-Hatherton glacial system 22

2.1 Regional setting 24

2.2 Surface topography 25

2.3 Climate and surface mass balance 26

2.4 Ice surface features 27

2.5 Ice thickness 29

2.6 Ice velocity 30

2.7 Grounding line position 31

2.8 Basal properties 31
2.9 Geomorphology and glacial history 32
2.9.1 Glacial drift sheets 33
2.9.2 Glacial history of the DHGS 34
2.9.3 Evidence from the DHGS on past changes of the Antarctic Ice Sheet 36
2.10 Summary 37

3 Characteristics of the Darwin-Hatherton glacial system as determined from ground and airborne geophysical surveys 39
3.1 The application of radar systems in glaciological research 39
3.1.1 Propagation of electromagnetic waves in glacial environments 40
3.1.2 Evidence of SMB and glacier dynamics from internal reflections 42
3.1.3 Grounding zone characteristics 43
3.2 Data collection 44
3.2.1 Ground penetrating radar measurements 45
3.2.2 Airborne radar sounding 47
3.2.3 GPS measurements of ice velocity 48
3.3 Processing and accuracy of the GPR data 49
3.3.1 GPR processing 50
3.3.2 Accuracy of radar measurements 53
3.4 Vertical variations in radar wave velocity 55
3.4.1 Analysis of radar wave velocity 55
3.4.2 Radar firn correction 57
3.5 Ice thickness and bedrock topography 61
3.5.1 Cross sectional shape of the DHGS 61
3.5.2 Longitudinal ice thickness of the Darwin Glacier 65
3.5.3 3-D ice thickness and bedrock maps 67
3.6 Evidence of flow dynamics from internal reflectors 70
3.7 Evidence for variations in surface mass balance 72
3.8 Grounding zone description 76
3.8.1 Subsurface ponds 77
3.8.2 Downwarping of shallow internal layers 78
3.8.3 Character of the ice base interface 79
3.8.4 Calculations of hydrostatic equilibrium 80
3.8.5 Stability of the Darwin Glacier grounding line 83
3.9 Ice discharge through Darwin Glacier cross profiles 84

3.10 Oceanic melt rates near the Darwin Glacier grounding line 85
3.11 Conclusion 86

4 Integration of new geophysical data sets as input for the nested ice sheet-shelf model 89
4.1 Surface elevation 90
4.2 Ice thickness 93
4.3 Water column thickness 94
4.4 Bedrock topography 96
4.5 Surface mass balance 97
4.5.1 Automatic weather stations 98
4.5.2 Surface climatology at the Upper Darwin and Hatherton AWSs 100
4.5.3 Annual SMB at the Hatherton AWS 103
4.5.4 SMB variations with elevation in DHGS ablation areas 105
4.5.5 Surface mass balance maps 108
4.5.6 Validating the SMB scenarios 109
4.6 Surface and air temperature 113
4.6.1 Deriving the MAAT from summer measurements 113
4.6.2 Surface temperature interpolation 119
4.7 Conclusion 121

5 Model simulations of ice dynamics in the Darwin-Hatherton Glacial system 123
5.1 Introduction 123
5.2 Ice sheet-shelf model description 123
5.2.1 Model applications of the shallow ice and shallow shelf approximations 124
5.2.2 Model treatment of basal sliding 126
5.2.3 Temperature and surface mass balance equations 127
5.2.4 Basal melting underneath grounded and floating ice 128
5.2.5 Modelled bedrock elevation 129
5.2.6 Original and adjusted nesting approach 129
5.2.7 Applicability of the ice sheet-shelf model in the Darwin-Hatherton area 130
5.3 Modelling approach and experimental design 131
5.4 All-Antarctic model setup and results 132
5.4.1 All-Antarctic model setup 132

5.4.2 Comparison of the all-Antarctic model output to present-day ice conditions 134
5.4.3 Late Quaternary changes as simulated by the all-Antarctic model 137
5.5 Tuning the nested model to the DHGS 141
5.5.1 Modifications of the all-Antarctic boundary ice flux 142
5.5.2 Enhancement factors 143
5.5.3 Basal sliding coefficient 143
5.5.4 Oceanic melt rate 144
5.5.5 Surface mass balance 144
5.5.6 Final nested model setup 145
5.6 Modelled present-day DHGS characteristics 146
5.6.1 Accuracy of the present-day simulation 147
5.6.2 Modelled flow dynamics of the DHGS 150
5.6.3 DHGS characteristics in relation to outlet glaciers in the Transantarctic Mountains and other glacier types 155
5.7 LGM characteristics of the DHGS 156
5.8 Present-day mass balance of the DHGS 163
5.9 Conclusion 163

6 Conclusion 167
6.1 Summary 167
6.2 Future work 171

References 173

A Appendix 188
A.1 Airborne radar data 188
A.2 Interpolation routine for the ice thickness map 190

List of tables

Table 1.1. Measured surface ice velocities and ice discharges for fast moving TAM outlet glaciers 14
Table 1.2. Measured surface ice velocities and ice discharges for slow moving TAM outlet glaciers 17
Table 2.1. Ages of glacial drift sheets 35
Table 3.1. Relative permittivity, electrical conductivity, velocity and attenuation of materials found in the glacial environment 41
Table 3.2. GPR system configuration 47
Table 3.3. Calculated cross section areas 65
Table 3.4. Calculated ice flux 85
Table 4.1. Overview of weather stations in the proximity of the DH region 99
Table 4.2. Average daily changes in relative surface height during the two AWS measurement periods 103
Table 4.3. Catchment-wide annual SMB within the DHGS 110
Table 4.4. The correlation coefficients between datasets of daily mean air temperature for 2007–2008 and 2008–2009 114
Table 4.5. Summary of the comparison of daily mean air temperatures measured during 2007 by the Mulock and Brown Hills AWSs and the optimal temperature correction of the Mulock dataset to fit the Brown Hills dataset. 115
Table 4.6. Comparison of daily mean air temperatures observed by summer weather stations with temperatures recorded by Mulock AWS 116
Table 4.7. Measured yearly average air temperature from the Brown Hills AWS ... 118
Table 4.8. Calculated and measured MAAT compared to values of MAST 120
Table 5.1. Parameters, physical constants and time series which are consistent between the all-Antarctic and nested model runs 133
Table 5.2. Parameters and input datasets specific to the all-Antarctic model 133
Table 5.3. Parameters and input datasets for the nested model 146

List of figures

Figure 1.1. Regional setting of the DHGS 2
Figure 1.2. Map of Antarctica showing balance velocities 5
Figure 1.3. LGM ice sheet reconstruction 8
Figure 1.4. Swinging gate retreat of the WAIS grounding line 9
Figure 1.5. Map of outlet glacier in the Transantarctic Mountains 12
Figure 2.1. Satellite image of the study area with place-names 22
Figure 2.2. Location and nature of previous work in the region 23
Figure 2.3. Previously determined SMB scenario for the DHGS 27
Figure 2.4. Previously determined surface profiles and bedrock topography 30
Figure 2.5. Previously modelled and measured ice flow velocities 31
Figure 2.6. Examples of stoss-and-lee shaped boulders with clear striations 32
Figure 2.7. Moraine and perched boulder close to the present-day glacier margin 33
Figure 2.8. Elevation of present-day glacier surface and drift sheet boundaries 34
Figure 3.1. Grounding zone characteristics 43
Figure 3.2. GPR and airborne radar survey tracks 45
Figure 3.3. GPR data collection setup 46
Figure 3.4. GPS measurement setup 48
Figure 3.5. Position and magnitude of surface ice velocity measurements 49
Figure 3.6. Examples of basic and more advanced processing flow 50
Figure 3.7. Positioning traces along a straight line. 51
Figure 3.8. Example of a GPR profile at different stages of processing 52
Figure 3.9. Radar profile crossovers 54
Figure 3.10. Average velocities of the firn/ice 56
Figure 3.11. Subset of 25 average velocities and the moving average 58
Figure 3.12. Calculated radar firn correction for the uppermost 150 m. 59
Figure 3.13. Interpolated map of radar firn correction for the DHGS. 60
Figure 3.14. Map of GPR profiles where a basal reflection was detected and location of cross profiles 62
Figure 3.15. Radargram collected on the Touchdown Glacier 63
Figure 3.16. Variations in cross sectional shape along the Darwin and Hatherton Glaciers 64

Figure 3.17. Longitudinal variations in ice thickness and bedrock topography of the Darwin Glacier 66
Figure 3.18. Ice thickness and ice base elevation at the DHGS 68
Figure 3.19. GPR profile along the centre flowline of the upper Darwin Glacier 71
Figure 3.20. The top 1500 ns of Figure 3.19 73
Figure 3.21. Relative accumulation rates and surface elevation along Figure 3.19 75
Figure 3.22. GPR profile across the Darwin Glacier grounding line 77
Figure 3.23. Enlarged image of variations in internal layers across the grounding zone 78
Figure 3.24. Detailed view of the interface between ice and sea water below the grounding line 80
Figure 3.25. Surface elevation, measured ice base elevation, and calculated ice base elevation along the airborne transect crossing the Darwin Glacier grounding line 82
Figure 3.26. Comparison of grounding line positions 83
Figure 4.1. Location and outline of the nested model domain 90
Figure 4.2. Overview of the coverage of the three DEMs utilised to produce the final model of surface elevations 91
Figure 4.3. DEM for the nested grid 92
Figure 4.4. Final 1 km ice thickness interpolation map for the nested model domain 94
Figure 4.5. Surface elevation, ice base and bedrock elevation before and after correction 95
Figure 4.6. Adjusted water column thickness map 96
Figure 4.7. Bedrock topography within the nested model domain 97
Figure 4.8. Locations of various AWSs in the Darwin-Hatherton region 98
Figure 4.9. Hourly mean values of air temperature, wind speed, wind direction, relative air humidity and cumulative change in surface height 101
Figure 4.10. Outline of the MB-1 ablation areas and the largest DHGS BIAs 106
Figure 4.11. Variation in SMB for ablation areas between 50 and 2090 m a.s.l. 107
Figure 4.12. MB-1 with Arthern et al. (2006) accumulation rates 109
Figure 4.13. MB-3A with Arthern et al. (2006) accumulation rates 112
Figure 4.14. Variations in daily average air temperature during 2007 114
Figure 4.15. Daily mean air temperature comparison 117
Figure 4.16. Calculated and measured MAAT within the DHGS 119

Figure 4.17. Average surface temperature within the nested model domain 120
Figure 5.1. Outline of the modelling approach, experimental design and expected outcome. 131
Figure 5.2. Comparison between modelled and measured present-day Antarctic ice configuration 135
Figure 5.3. Modelled and measured ice thickness difference along the nested grid boundary 136
Figure 5.4. Modelled and measured average velocity difference 137
Figure 5.5. Temperature and sea level variations during the past 40,000 years 138
Figure 5.6. All-Antarctic model output of glacier geometry during the advance and retreat of the WAIS grounding line to and from its maximum extent at 14,000 year BP 139
Figure 5.7. Surface elevation, ice thickness and average ice column velocity variations from two all-Antarctic model grid cells 140
Figure 5.8. Map showing the location of the Darwin, Hatherton, Wellman and Dubris transects utilised to display model output 147
Figure 5.9. Measured and modelled glacier configuration, the difference between the two, and ice velocity along the Darwin transect 148
Figure 5.10. Measured and modelled glacier configuration, the difference between the two, and ice velocity along the Hatherton transect. 149
Figure 5.11. Present-day ice thickness, surface elevation, driving stress, basal temperature, surface ice velocity, and basal velocity within the nested model domain. 151
Figure 5.12. Summary of glacier characteristics along the Darwin transect 153
Figure 5.13. Summary of glacier characteristics along the Hatherton transect 154
Figure 5.14. Flow index in relation to ice thickness for a range of glacier types 158
Figure 5.16. 1000 yr glacier surfaces and LGM equilibrium surface along the Wellman and Dubris transects 160
Figure 5.17. LGM ice thickness, surface elevation, driving stress, basal temperature, surface ice velocity, and basal velocity of the DHGS. 162

List of abbreviations

ADD	Antarctic Digital Database
AGC	Automatic gain control
ALBMAP	Antarctic dataset for high resolution numerical ice sheet models
ALOS	Advanced Land Observing Satellite
APPS	Automatic Precise Positioning Service
ASAID	Antarctic Surface Accumulation and Ice Discharge,
AWS	Automatic weather station
BEDMAP	Bed topography of the Antarctic
BIA	Blue ice area
CMP	Common mid-point
DEM	Digital elevation model
DHGS	Darwin-Hatherton glacial system
EAIS	East Antarctic Ice Sheet
EM	Electromagnetic
GPR	Ground penetrating radar
GPS	Global positioning system
HDOP	Horizontal dilution of precision
ICECAP	International Climate and Environmental Change Assessment Project
IPCC	Intergovernmental Panel on Climate Change
IPY	International Polar Year
LGM	Last Glacial Maximum
LGP	Latitudinal Gradient Project
LIMA	Landsat Image Mosaic of Antarctica
LINZ	Land Information New Zealand
MAAT	Mean annual air temperature
MAST	Mean annual surface temperature
MOA	Mosaic of Antarctica
MODIS	Moderate-resolution Imaging Spectroradiometer
NIWA	National Institute of Water and Atmosphere
NSF	National Science Foundation
PDD	Positive degree day
RAMP	Radarsat Antarctic Mapping Project
RES	Radio echo sounding
SEC	Spreading and exponential compensation
SeaRISE	Sea-level Response to Ice Sheet Evolution
SIA	Shallow ice approximation
SMB	Surface mass balance
SPIRIT	SPOT 5 stereoscopic survey of Polar Ice: Reference Images and Topographies
SPRI	Scott Polar Research Institute
SSA	Shallow shelf approximation
TAM	Transantarctic Mountains
TUD	Technical University of Denmark
TWT	Two-way traveltime
USGS	U.S. Geological Survey
WAIS	West Antarctic Ice Sheet

1 Introduction

The Transantarctic Mountains (TAM) separate the East Antarctic Ice Sheet (EAIS) from the marine West Antarctic Ice Sheet (WAIS) and ice configurations of many TAM outlet glaciers are influenced by both ice sheets or have been so in the past. As the dynamics of the EAIS and WAIS differ significantly, their responses to climatic changes have varied considerably in the past (Bindschadler 2007; Waddington et al. 2007a). Studies of change of TAM outlet glaciers therefore offer an exceptional opportunity to examine past variations in both ice sheets, as well as the potential for future change.

Exposed glacial sediments deposited adjacent to TAM outlet glaciers constitute the best preserved terrestrial record of past changes in ice volume and extent of the two Antarctic ice sheets. In particular sediments from the most recent glaciation and subsequent deglaciation are well described and dated (Bockheim et al. 1989; Denton et al. 1989a; Mercer 1968). The distribution of glacial deposits illustrates that since the Last Glacial Maximum (LGM), ice thickness and extent of outlet glaciers have, in general, decreased significantly close to the Ross Embayment, while little change has occurred in the uppermost regions near the EAIS (Bockheim et al. 1989; Denton et al. 1989a; Mercer 1968). Current reconstructions of LGM ice extent in the Ross Embayment and the surrounding regions rely primarily on extrapolations and dating of geomorphological evidence (Bockheim et al. 1989; Bromley et al. 2010; Conway et al. 1999; Denton et al. 1989b; Denton and Hughes 2000, 2002). Reconstructions show that the WAIS grounding line advanced more than 1000 km into the Ross Embayment during the last glaciation, while the EAIS remained close to its present-day elevation inland of the TAM. The presence of a grounded Ross Ice Sheet in the Ross Embayment would have effectively dammed ice flow from the TAM outlet glaciers, and explains the asymmetric distribution of glacial sediment deposits (Bockheim et al. 1989; Denton et al. 1989a; Mercer 1968). However, to date, few attempts have been made to properly test the effect of a grounded Ross Ice Sheet on the dynamics of the TAM outlet glaciers (Anderson et al. 2004; Kavanaugh et al. 2009b).

This study aims to examine present and past behaviour of a slow moving TAM outlet glacial system through geophysical fieldwork and the application of a numerical ice-flow model. An improved understanding of the dynamic response of the glacial system to changes in the WAIS

and EAIS will ultimately contribute to better constraints on the ice thickness and extent of the two Antarctic ice sheets during the LGM. An accurate LGM reconstruction is critical to the understanding of past contributions of the Antarctic Ice Sheet to global sea level variations, as well as observed present-day changes.

1.1 Aims and objectives

This research aims to investigate the dynamic behaviour of the Darwin-Hatherton glacial system (DHGS) which drains from the EAIS through the TAM and into the Ross Ice Shelf in the Ross Embayment (Figure 1.1). Large ice free areas with well-preserved glacial drift sheets and moraines surround the glacial system, which has a catchment area of 9150 km^2 and drains a minor part of the EAIS.

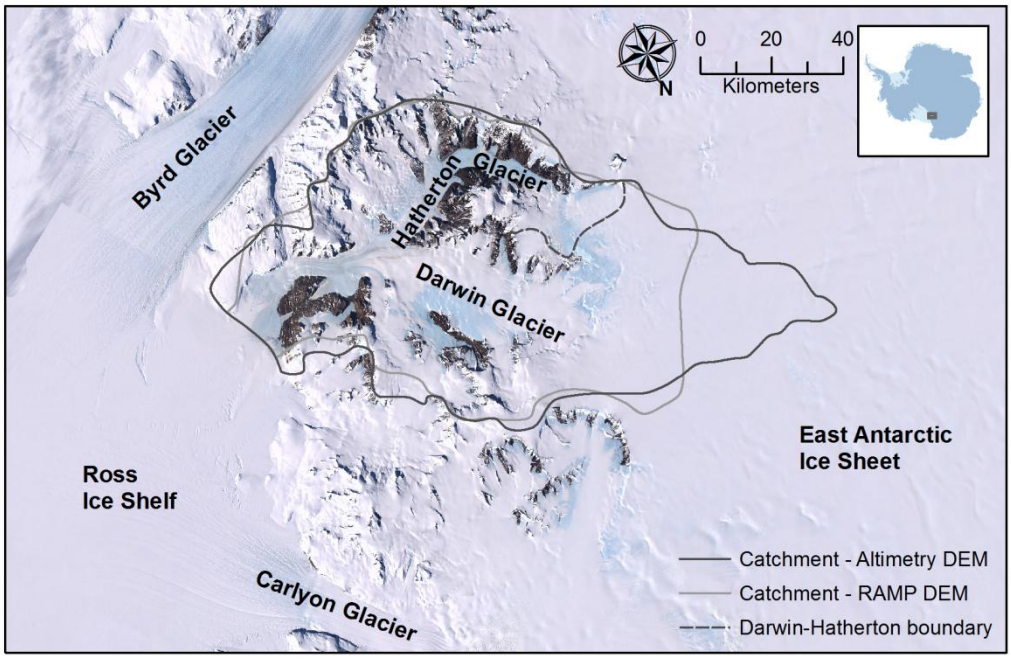

Figure 1.1. Regional setting of the DHGS and the adjacent ice free areas. DHGS catchment areas of 9150 km^2 and 7950 km^2 have been calculated from the Altimeter DEM produced by Bamber et al. (2009a) and the RAMP DEM produced by Liu et al. (2001) respectively (section 2.2). The boundary between the Hatherton and Darwin Glacier catchments was determined from the Altimeter DEM (see section 4.1). Map based on the Landsat Image Mosaic of Antarctic (LIMA, http://lima.usgs.gov).

The glacial system belongs to a group of slow moving TAM outlet glaciers of which very little is currently known. However, as mentioned above, although the dynamic response of this glacier type is poorly understood, extrapolations of glacial drift sheet boundaries have been readily

applied in the reconstruction of a grounded Ross Ice Sheet in the Ross Embayment during and following the LGM (Bockheim et al. 1989; Conway et al. 1999; Denton and Hughes 2000). The uncertainties of this approach were illustrated by a later modelling study, which found a noticeable difference between drift sheet extrapolations and model estimates of DHGS LGM ice thickness and timing of subsequent changes in the Ross Embayment (Anderson et al. 2004). However, the model was poorly constrained due to a lack of direct measurements of ice thickness, ice velocity and surface mass balance (SMB), and ignored the interaction between the DHGS and the buttressing Ross Ice Shelf. In addition, a recent study of glacial deposits in valleys adjacent to the Hatherton Glacier has introduced renewed uncertainties about the drift sheet ages used by previous studies to determine the magnitude and rate of change in the glacial system (Storey et al. 2010).

The research presented in this thesis builds upon this previous research by investigating the current and past behaviour of the DHGS in order to increase our understanding of slow moving TAM outlet glaciers as well as further constrain the magnitude of Holocene change in the region. This is achieved by combining newly acquired glaciological, glaciomorphological and meteorological field data with a modern 3-D numerical ice-flow model. Data from a ground penetrating radar (GPR) survey are used to measure ice thickness and bed morphology within the glacial system. From this dataset, variations in the bed shape and the effect of bedrock variations on ice flow dynamics will be investigated in detail. Variations in shallow internal layers are analysed to examine controls on SMB, and radar data collected across the Darwin Glacier grounding line allows a detailed description of grounding zone characteristics. Measurements by GPS of surface velocity provide evidence of current glacier dynamics, and in combination with the ice thickness measurements, facilitate the first accurate calculations of ice discharge and oceanic melt rates near the Darwin Glacier grounding line. Automatic weather stations (AWS) installed on the glacier surface aid in the construction of a new and more accurate SMB map which takes into account the large variability which exists in the region.

The new measurements along with results from previous studies in the Darwin-Hatherton area will be utilised to constrain and drive a high-resolution nested 3-D ice-flow model. The model, which is adapted from Pollard and DeConto (2009a; 2009b), allows for a freely migrating grounding line and has been shown to accurately simulate the transition in flow dynamics across the glacier grounding zone. The high-resolution model is nested within a lower resolution all-Antarctic simulation to account for influences from the EAIS and WAIS. The model is first applied to further examine present-day ice flow behaviour such as spatial variations in the velocity, force balance and basal temperature. Subsequently, simulations of ice configuration during the LGM are conducted to establish changes in ice thickness and extent within the DHGS. The results will be compared to previous estimates of Holocene

changes and are likely to clarify existing discrepancies on the LGM thickness of the Ross Ice Sheet (Anderson et al. 2004; Bockheim et al. 1989; Conway et al. 1999). In addition, as the flow dynamics of the DHGS is influenced by both the EAIS and the WAIS, the modelling results will provide evidence of past ice thickness fluctuations of both ice sheets.

In summary, the goal of this thesis is to investigate the flow behaviour of the DHGS through the following aims and objectives:

A. To identify the main processes which currently control the behaviour of the DHGS, more specifically:
    1. To use radar measurements to examine ice thickness and bedrock topography, and investigate how variations in these affect ice flow.
    2. To investigate the variations which occur in ice thickness and internal and basal characteristics across the Darwin Glacier grounding zone by using detailed GPR and airborne radar measurements.
    3. To examine variations in SMB and determine controls on these changes through analysis of internal layers in GPR data and meteorological field data.
    4. To apply an ice-flow model to examine the force balance and basal temperature, and determine how variations in these parameters affect ice-flow dynamics.

B. To determine the amount of change of the DHGS since the LGM, more specifically:
    1. To use an ice-flow model to determine the LGM ice thickness and extent in order to evaluate the significance of the moraine systems in the DHGS.
    2. To examine whether the DHGS has reached a state of equilibrium after the termination of the LGM from evidence of SMB, ice discharge and modelling results

The combination of new direct measurements of key parameters and a modern modelling approach represents a significant improvement to previous studies conducted on the DHGS. By investigating the present and past behaviour of the DHGS, this research aims to improve the understanding of the processes which control ice discharge of slower moving TAM outlet glaciers as well as add to the current discussion on magnitude of Holocene changes in the Ross Embayment. Ultimately this research contributes towards a better understanding of past behaviour of both the Antarctic ice sheets, which is of importance when estimating the influence of the Antarctic ice sheet on global sea level changes.

1.2 General characteristics of the WAIS and EAIS

The behaviour of the DHGS is influence by changes in both the WAIS and EAIS, and in order to investigate past changes of the glacial system it is important to understand the way in which the two Antarctic ice sheets have varied in the past. The behaviour of the highly dynamic marine-based WAIS differs significantly from that of the colder, thicker and more stable EAIS (Bindschadler 2007). The WAIS rests on a bed with an average elevation well below sea level, and slippery marine sediments deposited during warmer periods, along with high rates of geothermal heating, favour rapid ice flow (Bindschadler 2006). The WAIS has an high mass turnover, with relatively high accumulation rates and large ice discharge through fast-flowing ice streams which terminate as floating ice shelves (Bindschadler 2006; Ingolfsson 2007). The large discharge of ice to the ocean prevents the WAIS from reaching ice thicknesses above 2500 m. In contrast, the maximum ice thickness of the EAIS is 4780 m.

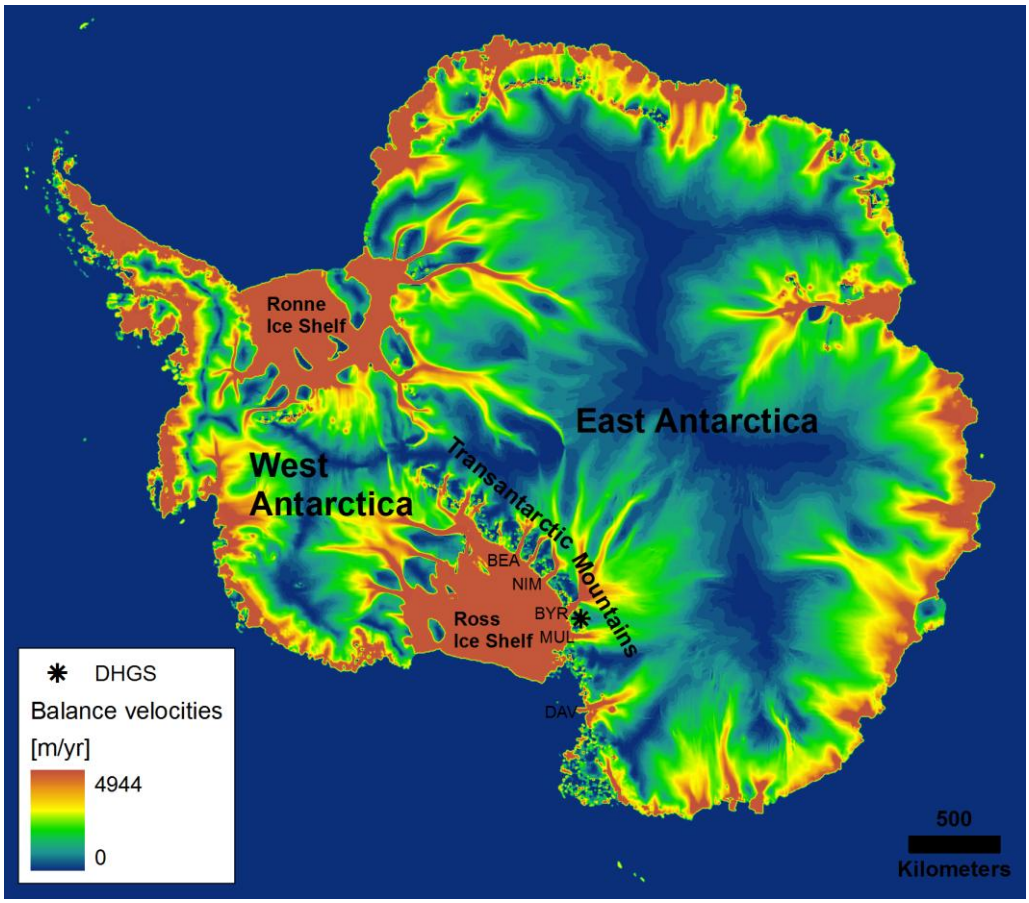

Figure 1.2. Map of Antarctica showing balance velocities from Bamber et al. (2000). Letters on the map indicate the location of major TAM outlet glaciers: Beardmore (BEA), Nimrod (NIM), Byrd (BYR), Mulock (MUL) and David (DAV) Glaciers.

The EAIS rests on thick continental crust and, compared to the WAIS, receives little precipitation (Ingolfsson 2007). Ice is primarily drained by a few fast-moving outlet glaciers which flow through deeply eroded bedrock troughs and typically terminate in the ocean (Waddington et al. 2007a, Figure 1.2). In addition to responding to climatic changes, ice thickness and flow dynamics of the EAIS have been influenced by an inferred 1-2 km Cenozoic uplift along the 3500 km long TAM towards its western margin (Kerr and Huybrechts 1999).

1.3 Current mass balance of the WAIS and EAIS

The Antarctic Ice Sheet has traditionally been considered a relatively stable feature of the cryosphere, but recent observations have shown that changes are occurring much more rapidly than previously thought possible (Truffer and Fahnestock 2007). These changes are thought to be controlled by a combination of recent climatic variations (Shepherd and Wingham 2007; Shepherd et al. 2004) and a grounding line retreat history which extends further back than the observational record (Jenkins et al. 2010).

Direct measurements of global mean surface temperature have shown a rise of 0.74°C during the last 100 years (1906-2005) (IPCC 2007). In Antarctica, air temperatures have been recorded since the late 1950s, and contrary to the observed global trend, they have remained relatively stable since recordings began, except for the Antarctic Peninsula where a significant temperature increase has recently occurred (Chapman and Walsh 2007; Comiso 2000; Turner et al. 2005). The global climate is expected to continue to warm and climate models predict an increase in overall Antarctic air temperatures of 2 – 3.5°C by the end of this century (Chapman and Walsh 2007). The predicted increase in temperatures is expected to result in greater levels of precipitation in Antarctica which will offset to some extent the effect of increased mass loss associated with higher air and ocean temperatures (Alley et al. 2007). Studies have documented a precipitation increase in the Antarctic Peninsula attributed to a change in atmospheric circulation (Turner et al. 2005), and a slight thickening of the EAIS is similarly thought to be driven by a precipitation increase (Davis et al. 2005). However, a more recent study by Monaghan and Bromwich (2008) has found no significant overall increase in Antarctic accumulation rates during the last five decades. It is therefore unlikely that the predicted accumulation increase will be able to completely offset the effect of increased air and ocean temperatures (Alley et al. 2007; Shepherd and Wingham 2007).

Although uncertainties remain high, most mass balance studies indicate that Antarctica is currently experiencing an overall net loss of mass caused largely by an accelerated discharge of ice into the oceans from the WAIS and the Antarctic Peninsula (Alley et al. 2007; Rignot et al. 2008; Rignot and Thomas 2002; Shepherd and Wingham 2007; Shepherd et al. 2004; Thomas et al. 2004). The recent accelerations demonstrate that glaciers and ice sheets are

capable of changing their dynamics much faster than previously assumed, profoundly affecting the mass budget of the Antarctic Ice Sheet (Rignot et al. 2008; Truffer and Fahnestock 2007). The mechanisms controlling these changes are not yet fully understood, but may be related to an instability of grounding lines located on upward-sloping beds (Jenkins et al. 2010) fuelled by increased surface and water temperatures (Shepherd and Wingham 2007; Shepherd et al. 2004) and the collapse of downstream buttressing ice shelves (Rignot et al. 2004). The stability of the Antarctic ice sheets and surrounding ice shelves have been examined through numerical modelling experiments which have found that a 5°C warming of the surrounding ocean is required for the WAIS to begin collapsing (Pollard and DeConto 2009b).

While large changes are observed in West Antarctica and the Antarctic Peninsula, the EAIS as a whole continues to remain relatively stable (Rémy and Frezzotti 2006; Shepherd and Wingham 2007). However, regional differences in mass balance exist with Filchner and Ross coastal sectors gaining mass, while Wilkes Land, which includes the northern part of the TAM, appears to be losing mass (Rignot et al. 2008). The behaviour of TAM outlet glaciers such as the DHGS is influenced by changes in both the WAIS and EAIS and the mass balance of these glaciers will be described in more detail in section 1.5.1.

1.4 Changes in the WAIS and EAIS since the LGM

During past glacial and interglacial periods, the extent of glaciers and ice sheets across the globe has varied significantly. Most recently the last glaciation culminated at the LGM, which in Antarctica occurred between 20,000 and 18,000 yr B.P. (Ingolfsson 2007). However, considerable regional differences exist in initial ice retreat from LGM ice configurations, which appear to have begun several thousand years later in the Ross Embayment (Conway et al. 1999, Figure 1.3). Since the LGM, the world's ice sheets and most glaciers, including the DHGS, have retreated and thinned considerably (Anderson et al. 2002; Hall 2009) resulting in a 120-135 m net increase in eustatic sea level (Clark and Mix 2002).

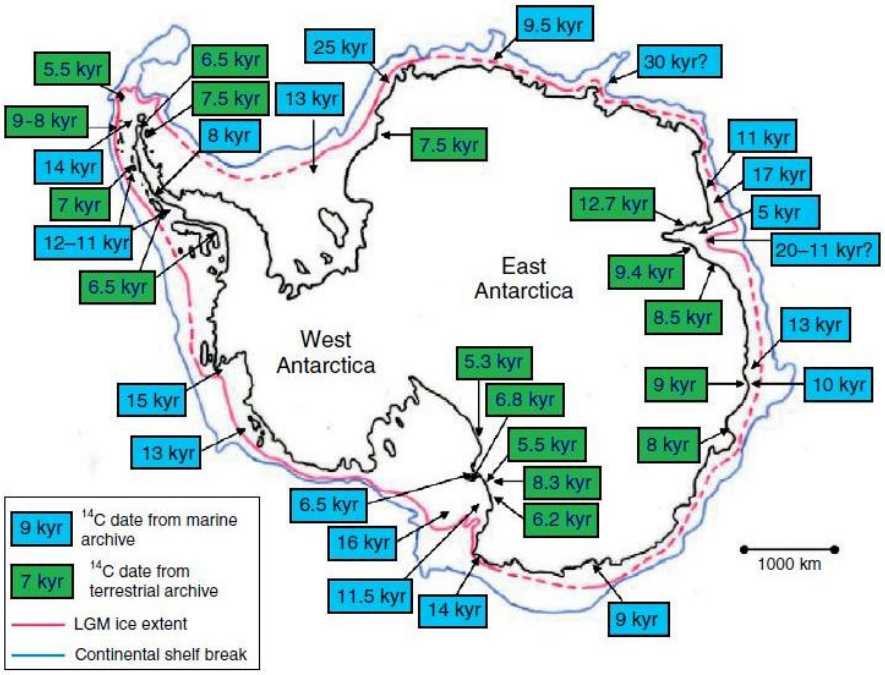

Figure 1.3. LGM ice sheet reconstruction with minimum ages for initial ice sheet retreat (Ingolfsson 2007). Red line shows the inferred LGM ice extent (dashed where uncertain) while the blue line shows the position of the continental shelf break.

Due to the difference in dynamics for the WAIS and EAIS described in section 1.2, the behaviour and responses of the two ice sheets to changing climatic parameters and global sea level have differed significantly in the past. For example, while the EAIS is known to have been present for approximately 40 million years (Waddington et al. 2007a), the WAIS almost completely disappeared at least once during the last 400,000 years (Bindschadler 2007). The LGM and subsequent termination provide the best opportunity to understand the dynamics of rapid change in Antarctica because of the quantity and quality of geological data recording these changes. However, as Figure 1.3 shows, considerable uncertainties (dashed red line) still exist in many regions, and estimates of LGM thickness and hence ice volume of the Antarctic Ice Sheet remain a focus of debate, including in the Darwin-Hatherton region (Storey et al. 2010).

1.4.1 Changes in the WAIS during and since the LGM

The Holocene change of the WAIS appears to have occurred both in response to increased global sea level and ocean temperature (Pollard and DeConto 2009b), and several authors have suggested that the deglaciation may initially have been triggered by a global sea level rise caused by the melting of Northern Hemisphere ice masses (Conway et al. 1999; Schoof

2007). Holocene surface elevation changes of the WAIS are thought to have been relatively small in the interior compared to coastal regions, although the scarcity of exposed bedrock for dating makes it difficult to accurately estimate the magnitude of change (Ackert et al. 1999; Waddington et al. 2005).

Of particular importance to past changes of the DHGS is the major advance of grounded ice into the Ross Embayment which occurred during the last glaciation (Figure 1.4). ^{14}C dates from lacustrine algae in proglacial lakes dammed by the grounded Ross Ice Sheet show that during the LGM, the WAIS grounding line was located more than 1000 km northward of the present-day position and remained close to its maximum position from at least 27,820 to 12,880 yr B.P. (Conway et al. 1999). At this time, estimates of the ice surface elevations of the Ross Ice sheet at the DHGS outlet range between 800 m (Anderson et al. 2004) and 1100 m (Bockheim et al. 1989) above present-day surface.

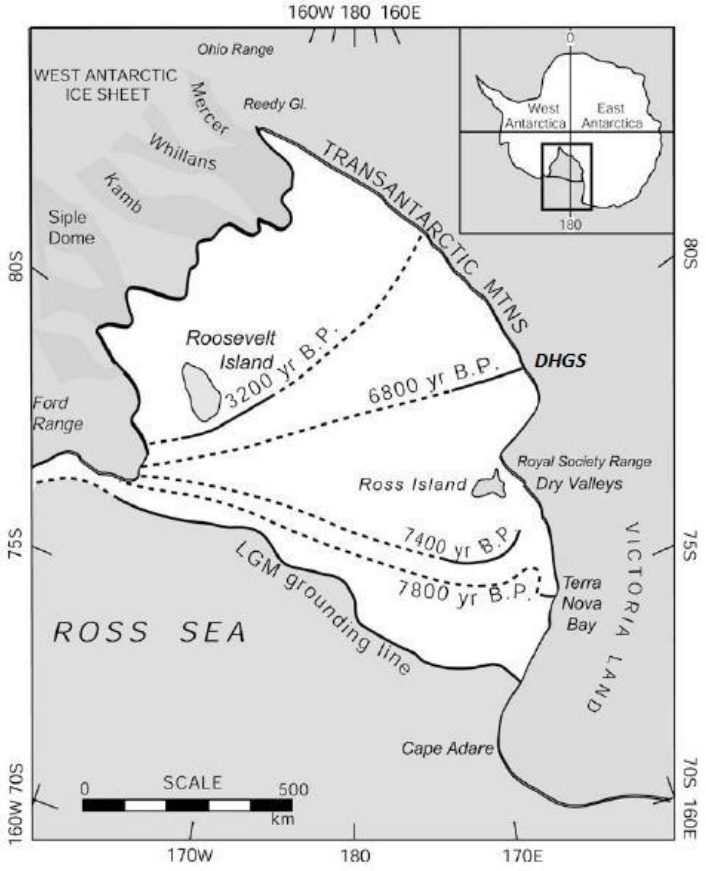

Figure 1.4. Swinging gate retreat of the grounding line of the Ross Ice Sheet following the LGM (Conway et al. 1999; Hall 2009).

In the Ross Embayment, a 'swinging gate' retreat of the WAIS has been suggested from geological evidence (Conway et al. 1999, Figure 1.4). The 6,800 yr B.P. retreat of the WAIS grounding line past the DHGS outlet (Figure 1.4), is based on ^{14}C dates from ice free valleys adjacent to the Hatherton Glacier indicating that the glacier was close to its present-day surface elevation no later than 6800-6550 yr BP (Bockheim et al. 1989). However, a later modelling study found that if the response time of the DHGS is accounted for, the grounding line would have retreated south past the Darwin Glacier outlet as early as 7,900-7,100 yr B.P (Anderson et al. 2004).

Overall, the retreat and thinning of the WAIS has been almost continuous since the LGM (Anderson et al. 2002; Hall 2009) and several authors argue that the ice sheet is still adjusting to the climate of the current interglacial (Conway et al. 1999; Rignot and Thomas 2002; Stone et al. 2003; Todd et al. 2010). If the ice sheet is still responding to the termination of the LGM, the changes presently observed (section 1.3) are a complex combination of this long-term trend and a response to the more recent increase in air and ocean temperature (Rignot and Thomas 2002).

1.4.2 Changes in the EAIS during and since the LGM

As with the WAIS, the largest changes in the EAIS since the LGM have occurred in the coastal regions, where evidence suggests that the ice sheet at its maximum extent terminated either mid-shelf or close to its present-day position (Anderson et al. 2002, Hall 2009, Figure 1.3). In the interior of the EAIS, past ice thickness has been inferred from ice cores (Augustin et al. 2004; Lorius et al. 1985; Steig et al. 2000) and modelling studies (Denton and Hughes 2002; Huybrechts 1990; Huybrechts and Oerlemans 1988; Pollard and DeConto 2009b). These studies generally show similar or slightly lower interior ice elevations during the LGM due to a precipitation decrease caused by lower air temperatures and increased distance to a moisture source. However, extrapolations of glacial drifts show that the ice sheet may have been elevated by as much as 35-40 m inland of the Beardmore Glacier and 100 m inland of the DHGS compared to present-day conditions (Denton and Hughes 2000).

1.5 Glaciers in the Transantarctic Mountains

The recent acceleration of ice discharge observed in the Antarctic Peninsula (section 1.3) demonstrates that changes in glacier dynamics can have a much more dramatic effect on the mass balance than more gradual changes in surface ablation and accumulation. Many of the TAM glaciers are partly grounded below sea level and terminate in the floating Ross Ice Shelf, and are therefore sensitive to the same influences as the glaciers in West Antarctica and the

Antarctic Peninsula. Attention has been focussed on the rapidly moving glaciers and ice streams draining the WAIS, while comparatively few studies have aimed to understand in detail the dynamics of the TAM glaciers, even though they drain a large proportion of the EAIS (Figure 1.2). Despite this lack of knowledge of response mechanisms and behaviour, geological evidence of former surface elevations of TAM outlet glaciers have been widely used to determine LGM thickness and subsequent change in both the EAIS and the WAIS. The following sections review the current knowledge of TAM glaciers, upon which the work presented in this thesis builds.

The TAM outlet glaciers can be divided broadly into categories of fast and slow moving glaciers (Giovinetto et al. 1964). The first group of glaciers have large catchment basins that extend into the interior of the EAIS, and ice velocities are high as the ice travels through the TAM in deep narrow valleys (Figure 1.2). The second type of outlet glaciers, to which the DHGS belongs, have considerably smaller catchment basins and their outflow from the EAIS is restricted by subglacial mountains (Denton 1979). The relatively few studies of the dynamic behaviour of TAM outlet glaciers have traditionally focussed on the group of larger and faster moving outlet glaciers (Giovinetto et al. 1964; Rignot and Thomas 2002; Stearns 2007; Swithinbank 1963; Wuite et al. 2009), while research in regions of the slower moving outlet glaciers have concentrated mostly on the surrounding ice free valleys (Bockheim et al. 1989; Hall et al. 2000; Staiger et al. 2006; Todd et al. 2010). However, recent studies of glacier dynamics on the slower moving Ferrar (Golledge and Levy 2011; Johnson and Staiger 2007; Kavanaugh et al. 2009b) and Taylor Glaciers (Kavanaugh and Cuffey 2009; Kavanaugh et al. 2009a; Kavanaugh et al. 2009b) have significantly improved our knowledge of this particular glacier type.

The TAM outlet glaciers span a large latitudinal range (Figure 1.5) and their behaviour varies accordingly. The outlet glaciers terminate either on land (generally west of McMurdo Sound), confluence with the Ross Ice Shelf (south of McMurdo Sound) or flow into the Ross Sea (generally north of McMurdo Sound). In addition, numerous smaller and entirely locally fed mountain glaciers are found in the TAM, particularly in the Dry Valleys where extensive ice free areas exist.

1.5.1 Mass balance

The TAM glaciers generally display a complicated surface pattern of snow-covered accumulation areas and blue ice ablation areas, as can be seen in Figure 1.5 on for example the Beardmore Glacier. Snow accumulation may occur throughout the year and has been shown to decrease with increased distance to open water (Fountain et al. 2006), resulting in inter-annual and seasonal variations in accumulation (Johnson and Staiger 2007). Surface

melting constitutes only a small fraction of the overall mass balance budget (Fountain et al. 2006) and mass loss from the surface is instead primarily controlled by strong katabatic winds from the polar plateau that, through wind scour and sublimation remove accumulated snow from the glacier surface (Denton et al. 1989a; Fountain et al. 2006; Johnson and Staiger 2007; Reusch and Hughes 2003). TAM glaciers terminating as floating termini experience considerable oceanic basal melting, especially if grounding zones are deep and come into contact with warm ocean water (Rignot and Thomas 2002). For the glaciers which terminate on land or directly in the Ross Sea as floating termini, mass is further lost through calving.

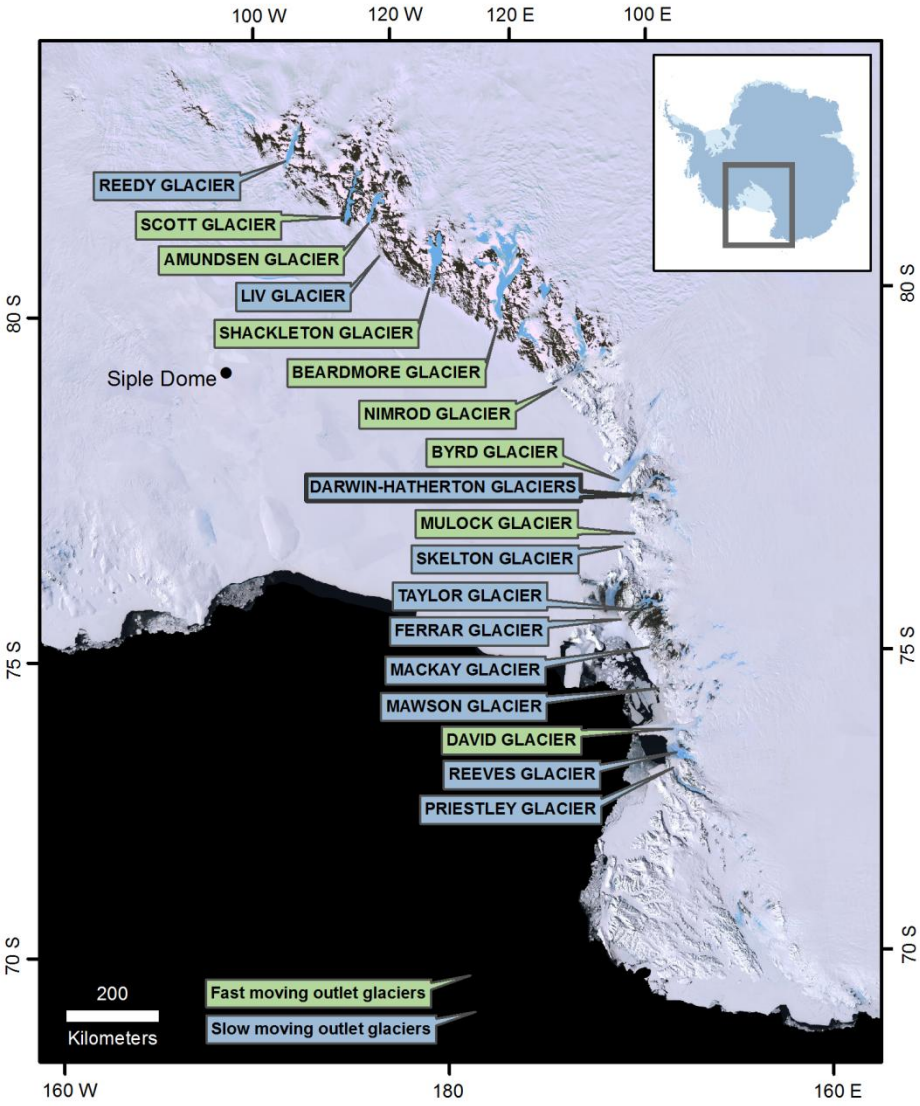

Figure 1.5. Map of the TAM and the location of the glaciers mentioned in the text (map based on LIMA, http://lima.usgs.gov).

The most recent large-scale studies of mass balance to include some TAM glaciers have showed that the Beardmore, Nimrod, Byrd and Mulock Glaciers (Figure 1.5) are currently experiencing a mass gain, while large glaciers north of McMurdo Sound such as the David Glacier, are losing mass (Rignot et al. 2008; Rignot and Thomas 2002). However, uncertainties in these studies are high, and Wuite et al. (2009) documented a long-term record of stable flow for the David Glacier (at least 1991-2000), while Stearns (2007) found the glacier to be currently gaining mass. Studies suggest that the Byrd Glacier is currently undergoing changes, which include an up to 20 km retreat of the grounding line between 1979 and 1997 (Stearns and Hamilton 2005), fluctuations in ice flow velocity (Stearns and Hamilton 2005; Stearns et al. 2008) and a surface elevation lowering of 0.4 to 1.2 m yr^{-1} below the grounding line between 1979 and 2004 (Schenk et al. 2005). The observed changes may be a response to changes in ocean circulation, increased ocean temperatures (Schenk et al. 2005) or changes in internal ice dynamics (Stearns et al. 2008).

Relatively little is known about the current mass balance of slower moving TAM outlet glaciers. An analysis of ice discharge from the Priestley, Reeves, Mawson and MacKays Glaciers (Figure 1.5) has found a positive mass balance for all glaciers, although uncertainties in accumulation rates may have led to an overestimation of mass gain (Frezzotti et al. 2000). In contrast, the southernmost Reedy Glacier continues to lower slowly (20 m in 1000 yr) in response to the end of the LGM (Todd et al. 2010). The mass balance of the Dry Valley glaciers have been investigated in more detail, and evidence suggest that these glaciers are likely to be in equilibrium with the current climate, and probably have been so at least since the beginning of the 20^{th} century (Chinn 1998; Fountain et al. 2006). Overall, the TAM glaciers appear to be fairly stable features of the present Antarctic landscape.

1.5.2 Characteristics of fast moving outlet glaciers

The following two sections provide a more detailed description of the two East Antarctic outlet glacier types. Although the DHGS belongs to the group of slower moving glaciers, several aspects of flow behaviour for the fast moving glaciers are of relevance, in particularly the ice-bed and ice-ocean interactions, which have been investigated in most detail for these glaciers. The velocities of the fast moving outlet glaciers range between more than 1000 m yr^{-1} for the fastest David and Byrd Glaciers to less than 300 m yr^{-1} for the slowest Shackleton Glacier (Table 1.1). Ice discharges are generally above 2 km^3 yr^{-1} with a maximum estimate of 24.3 km^3 yr^{-1} for the Byrd Glacier, although considerable discrepancies exist in estimates of ice flux for individual glaciers. This may reflect an actual change but more likely illustrates the large uncertainty that exists in regions where an adequate number of direct measurements is difficult to obtain.

Table 1.1. Measured surface ice velocities and ice discharges for fast moving TAM outlet glaciers listed from north to south. Values are described under 'Notes' using abbreviations for grounding line (GL), centre line (CL), grounded ice (GR), floating ice (FL), maximum (MAX), average (AVG). Numbers indicate: 1. ground based survey, 2. remote sensing study, 3. calculation of balance velocities, and 4. ice flow modelling.

Glacier name and publication	Ice velocity [m yr^{-1}]	Ice flux [km^3 yr^{-1}]	Notes
David Glacier:			
MacDonald et al. (1989)	670	-	GL, AVG, 2
Frezzotti et al. (1998)	68 – 553		GR to GL, 1, 2
Frezzotti et al. (2000)	461/560	6.9 ± 0.6	GL, AVG/MAX, 2
Rignot and Thomas (2002)	-	15.6 ± 1.0	GL, 3
Stearns (2007)	369	10.1 ± 1.0	GL, AVG, 2
Wuite et al. (2009)	150 – 1039		GR,2
	550-750		FL, 2
		5.0 ± 0.3	GL, 2
Mulock Glacier:			
Swithinbank (1963)	388	-	CL, GR, 1
Giovinetto et al. (1964)	290	2.8 ± 0.5	GR, AVG, 1
MacAyeal and Thomas (1986)	285	2.8	GL, AVG, 1, 4
Rignot and Thomas (2002)	-	6.8 ± 1.0	GL, 3
Humbert et al. (2005)	550	2.1	GL, AVG, 1, 4
Stearns (2007)	342	5.7 ± 0.6	GL, AVG, 2
Byrd Glacier:			
Swithinbank (1963)	843 ± 10	-	CL, FL, 1
Giovinetto et al. (1964)	740 ± 10	16.3 ± 10.6	FL, AVG, 1
Hughes (1977)	352	15.4	GL, AVG, 1
Hughes and Fastook (1981)	780 – 890	-	CL, GR to FL, 1
Brecher (1982)	580 – 875	-	CL, GR to FL, 2
Lucchitta and Ferguson (1986)	750 – 800	-	FL, 2
MacAyeal and Thomas (1986)	600	14	GL, AVG, 1, 4
MacDonald et al. (1989)	650	-	FL, AVG, 2
Rignot and Thomas (2002)	-	23.5 ± 2.0	GL, 3
Humbert et al. (2005)	1200	16.9	GL, AVG, 1, 4
Stearns and Hamilton (2005)	650 – 850	-	~GL, CP, 2
Stearns (2007)	672	24.3 ± 1.9	GL, AVG, 2
Stearns et al. (2008)	825 – 900	22.5 – 24.3	GL, 2
Nimrod Glacier:			
Swithinbank (1963)	226	-	CL, FL, 1
Giovinetto et al. (1964)	150	2.2 ± 0.7	FL, AVG, 1
MacAyeal and Thomas (1986)	250	2.7	GL, AVG, 1, 4
Humbert et al. (2005)	550	1.8	GL, AVG, 1, 4
Stearns (2007)	203	3.6 ± 0.2	GL, AVG, 2
Beardmore Glacier:			
Swithinbank (1963)	364	-	CL, FL, 1
Giovinetto et al. (1964)	330	5.8 ± 1.7	FL, AVG, 1
MacAyeal and Thomas (1986)	470	8.5	GL, AVG, 1, 4
Humbert et al. (2005)	700	4.0	GL, AVG, 1, 4
Schackleton Glacier:			
Giovinetto et al. (1964)	-	3.0 ± 0.6	FL, AVG, 1
MacAyeal and Thomas (1986)	170	0.9	GL, AVG, 1, 4
Humbert et al. (2005)	280	1.0	GL, AVG, 1, 4
Amundsen Glacier:			
Swithinbank (1963)	234 ± 10	-	CL, GR, 1
Giovinetto et al. (1964)	150 ± 10	3.3 ± 1.7	GR, AVG, 1
MacAyeal and Thomas (1986)	170	1.9	GL, AVG, 1, 4
Humbert et al. (2005)	700	1.9	GL, AVG, 1, 4
Scott Glacier:			
Swithinbank (1963)	256 ± 10	-	CL, GR, 1
Giovinetto et al. (1964)	180 ± 10	2.0 ± 0.4	GR, AVG, 1
MacAyeal and Thomas (1986)	170	1.9	GL, AVG, 1, 4
Humbert et al. (2005)	450	2.0	GL, AVG, 1, 4

The Byrd Glacier has a catchment area of 1,070,400 km^2 and is one of the largest Antarctic glaciers (Rignot and Thomas 2002; Schenk et al. 2005). The glacier supplies more ice to the Ross Shelf than any other ice stream or glacier and has a maximum ice thickness of ~3400 m (Reusch and Hughes 2003) which thins to about 1800 m at the grounding zone (Rignot and Jacobs 2002). Maximum measured velocities of the Byrd Glacier are higher than any of the West Antarctic ice streams draining into the Ross Embayment (Reusch and Hughes 2003). Surface velocity profiles resemble those of the West Antarctic ice streams, with a wide central zone of very high velocities and a narrow (<1 km) marginal zone of rapidly decreasing velocities (Stearns and Hamilton 2005; Swithinbank 1963). However, this does not appear to be a general characteristic of other fast moving outlet glaciers, and a more gradual decrease in ice flow velocities towards the margins has been documented for Mulock, Nimrod, Beardmore, Amundsen and Scott Glaciers (Swithinbank 1963).

Studies of the David, Mulock, Byrd and Nimrod Glaciers have shown that fast moving TAM outlet glaciers have high driving stresses (~250 kPa) that are primarily resisted by basal drag (~150 kPa), while lateral drag (~50 kPa) and longitudinal compression (~50 kPa) are less important (Scofield et al. 1991; Stearns 2007; Whillans et al. 1989). Ice flow is characterised by a high level of basal sliding, sustained by significant basal melting ranging between 6 mm yr^{-1} (Mulock Glacier) and 26 mm yr^{-1} (Byrd Glacier) for the grounded part of the glaciers (Stearns 2007). However, evidence of 'sticky spots' with increased basal drag found in particular on the David and Byrd Glaciers are thought to relate to the presence of alternating thawed and frozen subglacial conditions (Reusch and Hughes 2003; Stearns 2007; Whillans et al. 1989). Evidence suggests that changes in the flow behaviour of the Byrd Glacier is closely related to variations in the subglacial hydrology (Stearns et al. 2008).

Both the Byrd and David glaciers are grounded well below sea level for much of their extent (Frezzotti et al. 2000; Reusch and Hughes 2003), making them vulnerable to changes in ocean temperature and sea level. The grounding line of the Byrd Glacier is located 45 km upstream from its outlet and a substantial part of the glacier is exposed to rapid basal melting, calculated to 12 m yr^{-1} on average (Kenneally and Hughes 2004). Even more impressive, is the basal melt rate of ~29 m yr^{-1} calculated near the 3200 m deep grounding line of the David Glacier and which causes the glacier to lose 68% of its mass within 20 km downstream (Rignot and Jacobs 2002). Basal melting has been shown to account for 50% of total mass loss of the David Glacier compared to only 25% for the slower moving Reeves Glacier, which has a shallower grounding line at about 700 m depth (Frezzotti et al. 2000).

1.5.3 Characteristics of slow moving outlet glaciers

Velocities of the slower moving TAM outlet glaciers generally do not exceed 500 m yr^{-1} and ice fluxes are less than 2 km^3 yr^{-1} (Table 1.2). The glaciers drain only a minor part of EAIS and the catchment basin of for example the DHGS constitutes less than 1% of the Byrd catchment area. In-depth studies of glacier dynamics of slower moving TAM outlet glaciers are limited to the Taylor (Kavanaugh and Cuffey 2009; Kavanaugh et al. 2009b; Robinson 1984), Ferrar (Golledge and Levy 2011; Johnson and Staiger 2007; Kavanaugh et al. 2009b) and Darwin-Hatherton Glaciers (Anderson et al. 2004), for which characteristics differ considerably as they terminate on land, in McMurdo Sound and into the Ross Ice Shelf respectively.

Many of the smaller outlet glaciers are characterised by large blue ice areas which are more likely to develop when ice flow through ablation areas is slow (van den Broeke et al. 2006). Strong adiabatically heated katabatic winds are funnelled through the relatively steep and narrow valleys, and sublimation is generally the most important ablation process (Kavanaugh et al. 2009a; Robinson 1984). Oceanic melt rates are generally low, as the grounding lines are relatively shallow and therefore do not come into contact with deep warm water (Frezzotti et al. 2000).

One of the most prominent characteristics of the Taylor Glacier is the low ice velocity with which it travels despite relatively high driving stresses (~150 kPa) and ice thicknesses (Kavanaugh and Cuffey 2009). Although basal drag (~90-120 kPa) is the dominant resistive stress at the glacier, the effect of lateral drag (~20-50 kPa) is important, and may lead to velocity reductions of between 30 to 80% (Kavanaugh and Cuffey 2009). However, the low ice velocities are primarily the result of ice thicknesses below 1000 m leading to partly or completely frozen basal conditions and slowly deforming cold ice (Kavanaugh and Cuffey 2009).

Large undulations in subglacial bedrock topography have been documented for both the Taylor and Ferrar Glaciers, however, studies have disagreed on the effect of these on ice flow (Johnson and Staiger 2007; Kavanaugh et al. 2009b). Johnson and Staiger (2007) found that subglacial ridges acted to restrict ice flow in a manner which was later referred to by Kavanaugh et al. (2009b) as the 'trickle' model. According to the 'trickle' model, ice velocities are highest in bedrock troughs where ice thickness and temperature are increased (Johnson and Staiger 2007). However, later studies, which included remote and ground based velocity measurements (Kavanaugh et al. 2009b) and further modelling (Golledge and Levy 2011) have found no evidence to support the 'trickle' model, which appears to be a result of uncertainties in model input. New direct measurements and modelling results are instead in accordance with the more traditional 'cascade' theory, which predicts fastest ice flow in the

thinnest regions, where surface slopes and driving stresses are highest (Golledge and Levy 2011; Kavanaugh et al. 2009b).

Table 1.2. Measured surface ice velocities and ice discharges for slow moving TAM outlet glaciers listed from north to south. Values are described under 'Notes' using abbreviations for grounding line (GL), centre line (CL), equilibrium line (EQL), grounded ice (GR), floating ice (FL), maximum (MAX), average (AVG). Numbers indicate: 1. ground based survey, 2. remote sensing study, 3. calculation of balance velocities, and 4. ice flow modelling.

Glacier name and publication	Ice velocity [m yr^{-1}]	Ice flux [km^3 yr^{-1}]	Notes
Priestley Glacier:			
Frezzotti et al. (1998)	95-175	-	GR, 1, 2
Frezzotti et al. (2000)	93	0.77 ± 0.13	GL, AVG, 2
	130		GL, MAX, 2
Reeves Glacier:			
MacDonald et al. (1989)	520	-	FL, AVG, 2
Frezzotti et al. (1998)	110-252	-	GR to FL, 1, 2
Frezzotti et al. (2000)	109 – 113	0.52 – 0.9 ± 0.1	GL, AVG, 2
	200		GL, MAX, 2
Mawson Glacier:			
Frezzotti et al. (2000)	138	0.52 ± 0.07	GL, AVG, 2
	190		GL, MAX, 2
Mackay Glacier:			
Frezzotti et al. (2000)	265	0.33 ± 0.06	GL, AVG, 2
Taylor Glacier:			
Robinson (1984)	0.5 – 14.4	-	GR, 1
Kavanaugh et al. (2009b)	6 – 21		CL, GR, 1, 2
Kavanaugh et al. (2009a)		0.04	EQL, 1, 2
Ferrar Glacier:			
Scott, (1913)	12 – 16	-	GR, 1
Johnson and Staiger (2007)	<14	-	CL, GR, 4
Kavanaugh et al. (2009b)	2 – 40		CL, GR, 1, 2
Skelton Glacier:			
Wilson and Crary (1961)	88.7	0.8	GL, AVG, 1
Giovinetto et al. (1964)	90	0.8	FL, AVG, 1
Humbert et al. (2005)	350	1.34	GL, AVG, 1
Hatherton Glacier:			
Hughes and Fastook (1981)	30 – 50	-	GR, 1
Anderson et el. (2004)	< 20	-	CL, GR, 4
Darwin Glacier:			
Hughes and Fastook (1981)	40-60	-	GR, 1
	110 – 130		GR, MAX, 1
Anderson et el. (2004)	~325	-	GR, MAX, 1
Humbert et al. (2005)	350	1.03	GL, AVG, 2
Liv Glacier:			
Swithinbank (1963)	110 ± 10	-	CL, GR, 1
Giovinetto et al. (1964)	70 ± 10	0.5 ± 0.1	GR, AVG, 1
MacAyeal and Thomas (1986)	230	1.6	GL, AVG, 1
Humbert et al. (2005)	480	0.55	GL, AVG, 1
Reedy Glacier:			
Todd et al. (2010)	~170	~2	CL, GR, 1

The cold-based conditions which are typical of slower outlet glaciers are the result of inflow of cold ice from the EAIS, insufficient insulation by relatively thin ice and low levels of frictional heat from ice deformation (Higgins et al. 2000a; Hubbard et al. 2004). The effect of these factors varies within and between glaciers, and of the investigated glaciers, both the Taylor and Ferrar Glaciers are probably entirely cold-based (Higgins et al. 2000a; Johnson and Staiger 2007; Kavanaugh and Cuffey 2009) although a recent modelling study has found evidence of warm-based conditions in the deepest regions of the Ferrar Glacier (Golledge and Levy 2011). In contrast, the Darwin and Hatherton Glaciers may have larger warm-based parts (Anderson et al. 2004). The lack of basal sliding is thought to have a stabilising effect on the ice flow, and likely explains why the Ferrar Glacier has remained relatively static during the last ~4 million years (Johnson and Staiger 2007; Staiger et al. 2006). However, despite their stable appearance, the slow moving TAM outlet glaciers are capable of dramatic changes (see section 1.6 below).

1.6 Change of glaciers in the Transantarctic Mountains since the LGM

The behaviour of the TAM glaciers during and following the LGM has varied widely depending on the glacier type. Alpine glaciers, which terminate on land and are unaffected by changes in the EAIS and WAIS (section 1.4), have responded solely to variations in temperature and precipitation (Steig et al. 2000). The behaviour of East Antarctic outlet glaciers has been further influenced by variations in the EAIS, and when terminating in the ocean, by changes in ocean temperature and sea level (Denton et al. 1989a; Higgins et al. 2000a; Higgins et al. 2000b; Johnson and Staiger 2007). However, the outlet glaciers that have experienced the largest and most complex change are those that, in addition to the influences mentioned above, have been affected by restricted ice drainage into the Ross Embayment due to the advance of the WAIS grounding line during the LGM (section 1.4.1).

An out-of-phase behaviour with dammed outlet glaciers has been documented for the Taylor Glacier, which terminates on land and consequently fluctuated independently of the Ross Ice Sheet. Studies show that the glacier was less extensive than present during the LGM (Denton and Hughes 2000; Higgins et al. 2000b), has since experienced a significant advance and is now at its most advanced Holocene position (Denton et al. 1989b; Higgins et al. 2000a). This behaviour is similar to that of locally fed alpine glaciers in the Dry Valleys (Steig et al. 2000). Ice cores from the inland Taylor Dome reveal a history of ice thickening during warmer periods, which coincides with expansion of Taylor Glacier and local alpine glaciers (Higgins et al. 2000b). In contrast, the Mackay and Ferrar Glaciers, which also drain from the Taylor Dome but terminate in the Ross Sea and McMurdo Sound respectively, have experienced a retreat history similar to other outlet glaciers dammed by the grounded Ross Ice Sheet during

the LGM (Denton and Hughes 2000; Johnson and Staiger 2007; Staiger et al. 2006). The TAM glaciers affected by the expansion of the WAIS into the Ross Embayment have shown little if any response to the relatively minor EAIS changes. Instead, an extensive thickening occurred in the middle and lower reaches as these glaciers responded primarily to changes in the Ross Embayment (Bockheim et al. 1989; Bromley et al. 2010; Denton et al. 1989a; Denton and Hughes 2000).

The deglaciation of the TAM outlet glaciers affected by the advanced WAIS has been a gradual process controlled by the rate of southward retreat of the WAIS grounding line (Figure 1.4) and the response time of individual glaciers. The characteristic asymmetrical thinning has lead to steepening of the glacier profiles (Hall 2009; Todd et al. 2010). Initial retreat of the TAM outlet glaciers may have begun as early as 13,000 years BP (section 1.4) and is to some extent (<0.02 m yr^{-1}) still ongoing for the Reedy Glacier, which is the southernmost TAM outlet glacier to enter the Ross Embayment (Todd et al. 2010). Although some change may still be occurring, evidence suggests that the TAM outlet glaciers entering the Ross Embayment have remained stable for at least the last 1000 years and are at, or close to, dynamic equilibrium (Anderson et al. 2004; Fahnestock et al. 2000; Johnson and Staiger 2007; Todd et al. 2010).

1.7 Thesis outline

Each chapter of this thesis emphasises a different aspect of the characteristics of the DHGS. With the exception of the conclusion (Chapter 6), each chapter contains a self-contained introduction, methods (when appropriate), discussion of results and summary/conclusion. The final chapter brings together the main findings in the context of the aims described above. The contents of chapters 2 to 5 are detailed below.

Chapter 2, describes work which has previously been conducted in the Darwin-Hatherton region and is of relevance to the research presented in this thesis. The studies described constitute the foundation of this research, and references will be made to them continuously throughout this thesis.

Chapter 3 presents the results of the geophysical fieldwork. Ground-based and airborne radar measurements are combined to establish variations in ice thickness within the glacial system, and an analysis of internal layer stratigraphy provide evidence of the effect of undulating bedrock topography on ice flow behaviour (objective A.1). A GPR profile collected across the Darwin Glacier grounding line illustrates internal features and basal characteristics of this very complex zone, while an airborne radar profile facilitates calculations of deviations from hydrostatic equilibrium of the floating ice shelf downstream of the Darwin Glacier grounding

line (objective A.2). Undulations in shallow internal layers are utilised to examine the controls and magnitude of SMB variations within the glacial system (objective A.3). Lastly, the ice thickness data are combined with surface velocity measurements in calculations of ice discharge and oceanic melt rates downstream of the glacier grounding line.

Chapter 4 describes the compilation of configuration and climatological datasets of the DHGS and its surroundings to be used as input to the numerical ice-flow model presented in chapter 5. Three DEMs of varying resolution and spatial coverage are combined into one and the ice thickness and bedrock topography maps presented in Chapter 3 are merged with existing lower resolution datasets. In this process, artefacts of the interpolation routine used to construct the large-scale Antarctic configuration datasets are adjusted in order to produce more realistic gridded datasets. Meteorological datasets are used to examine controls on the SMB, and in combination with satellite imagery facilitate the construction of a new SMB map which accounts for the presence of large BIAs within the DHGS catchment (objective A.3). Lastly, mean annual air temperatures are successfully extrapolated from summer measurements and found to compare well with remotely sensed datasets of surface temperature.

Chapter 5 reports the process of fitting and applying the numerical ice-flow model to simulate the dynamic behaviour of the glacial system at present and at the LGM. Direct measurements and datasets presented in chapters 3 and 4 are applied to constrain and drive a numerical ice-flow model nested within an all-Antarctic model. Tuning of the nested model to present-day DHGS conditions offers additional constraint on the glacier SMB (objective A.3), while model output from a present-day simulation provide information on current variations in ice/base temperature and force balance within the glacial system (objective A.4). The LGM steady-state configuration and flow behaviour of the DHGS are investigated and compared to glacial drift boundaries in adjacent valleys (objective B.1), and the implications of the results to the ongoing debate about the Antarctic LGM ice thickness are discussed. In addition, the current mass balance of the DHGS will be discussed from evidence of ice discharge, SMB and model output (objective B.2).

In combination, the three results chapters provide a detailed description of current and past behaviour of the DHGS which contributes towards a better understanding of slow-moving TAM glaciers in general, as well as offering additional constraints on past changes in the EAIS and WAIS.

1.8 Summary

Studies of glacier dynamics in Antarctica have focused predominately on the faster moving components of the ice sheet, such as the ice streams and the large East Antarctic outlet glaciers. By contrast, little is known about the smaller and slower moving outlet glaciers draining from the EAIS through the TAM and into the Ross Embayment (Frezzotti et al. 2000). Due to their limited ice discharge and low SMB, these glaciers are often surrounded by ice-free valleys covered in glacial sediments, which provide evidence of previous ice surface elevations (Bockheim et al. 1989; Denton et al. 1989b). Extensive studies have mapped, dated and correlated glacial drift sheets in the Ross Sea Region, and the current knowledge of LGM thickness and extent of the two Antarctic ice sheets, as well as the subsequent timing and rate of retreat of the WAIS, rely primarily on interpretations of these results (Bromley et al. 2010; Conway et al. 1999; Hall 2009; Ingolfsson 2007).

The behaviour of the southernmost TAM outlet glaciers is complex, as they respond not only to variations in climatic parameters such as air temperature, precipitation, ocean temperature and global sea level, but also the level of inflow of ice from the EAIS and more importantly the damming effect of an advanced WAIS. All of these influences must be considered in order to accurately determine the current ice dynamics and the conditions that would have lead to the deposition of the glacial drift sheets in the past. Modelling experiments for the TAM outlet glaciers are hampered by the lack of direct measurements of bed morphology and ice velocity needed to constrain and drive the models, and so far, have yet to include the important interaction between glacier and ocean (Anderson et al. 2004; Johnson and Staiger 2007).

The research presented in this these aims to further investigate the present and past dynamic behaviour of the DHGS. This will lead to an increased understanding of slow-moving TAM glaciers and the results provide additional constraint to the magnitude of Holocene change of the WAIS and EAIS.

2 Introduction to the Darwin-Hatherton glacial system

The DHGS is located in the TAM between 152° and 161° E and 79.3° and 80.2° S. The Darwin Glacier extends from the EAIS to the Ross Ice Shelf in the Ross Embayment, whereas the Hatherton joins the Darwin Glacier below Junction Spur in the Darwin Mountains (Figure 2.1). The glacial system is surrounded by ice free valleys within which rare evidence of past changes in ice extent and thickness are preserved in the form of glacial drift sheets and moraines. This record makes the DHGS a key area for understanding the processes controlling the dynamic behaviour of TAM outlet glaciers today as well as in the past.

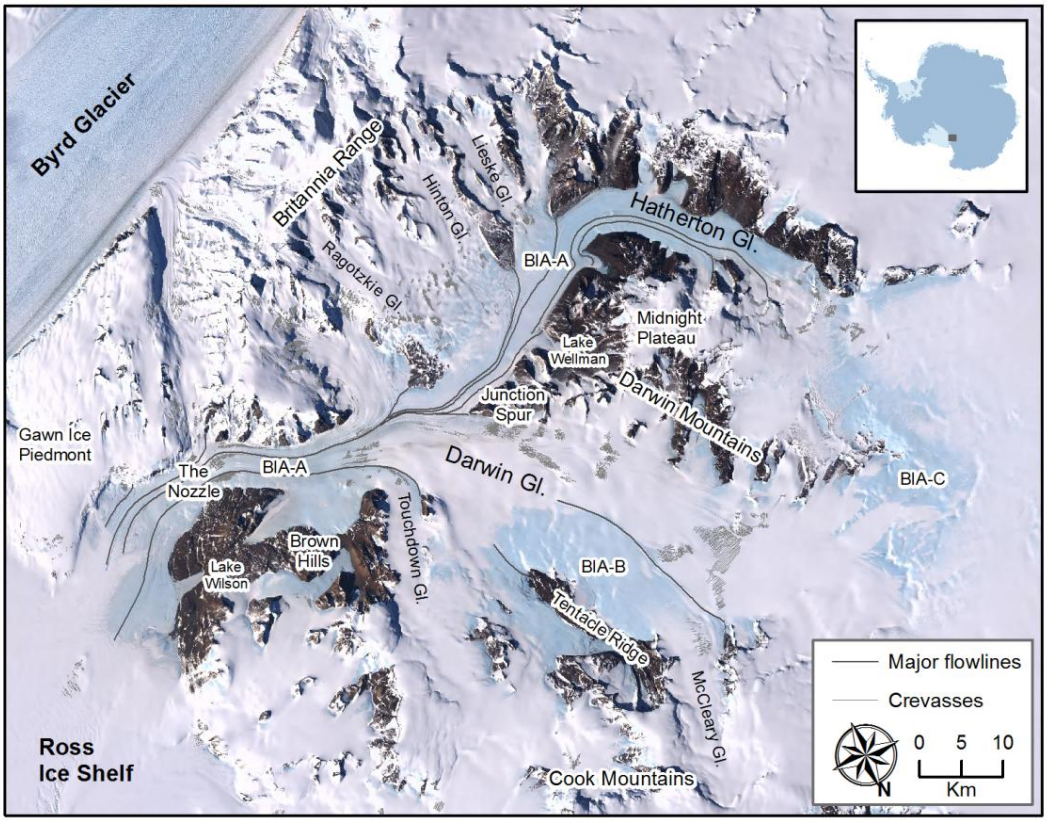

Figure 2.1. Satellite image of the study area with place-names mentioned in the text. Thick grey lines trace major flowlines visible in the blue ice areas and thin grey lines indicate the presence of crevasses.

Because of the valuable geological record, the DHGS has been the focus of several major research projects (Figure 2.2). Previous work include studies of ice velocity (Hughes and Fastook 1981), surface topography (Korona et al. 2009; LINZ 2010), regional meteorology (Zawar-Reza et al. 2010), mapping and dating of glacial sediments (Bockheim et al. 1989; Storey et al. 2010) and modelling of glacier behaviour (Anderson et al. 2004). In addition, several large scale continental maps of ice thickness (Lythe et al. 2000a), surface topography (Bamber et al. 2009b; Liu et al. 2001), surface air temperature (Comiso 2000), SMB (Arthern et al. 2006; van de Berg et al. 2006; Vaughan et al. 1999a), grounding line location (ADD-Consortium 2000; Scambos et al. 2007), and geothermal heat flux (Maule et al. 2005; Shapiro and Ritzwoller 2004) cover the DHGS at various resolutions.

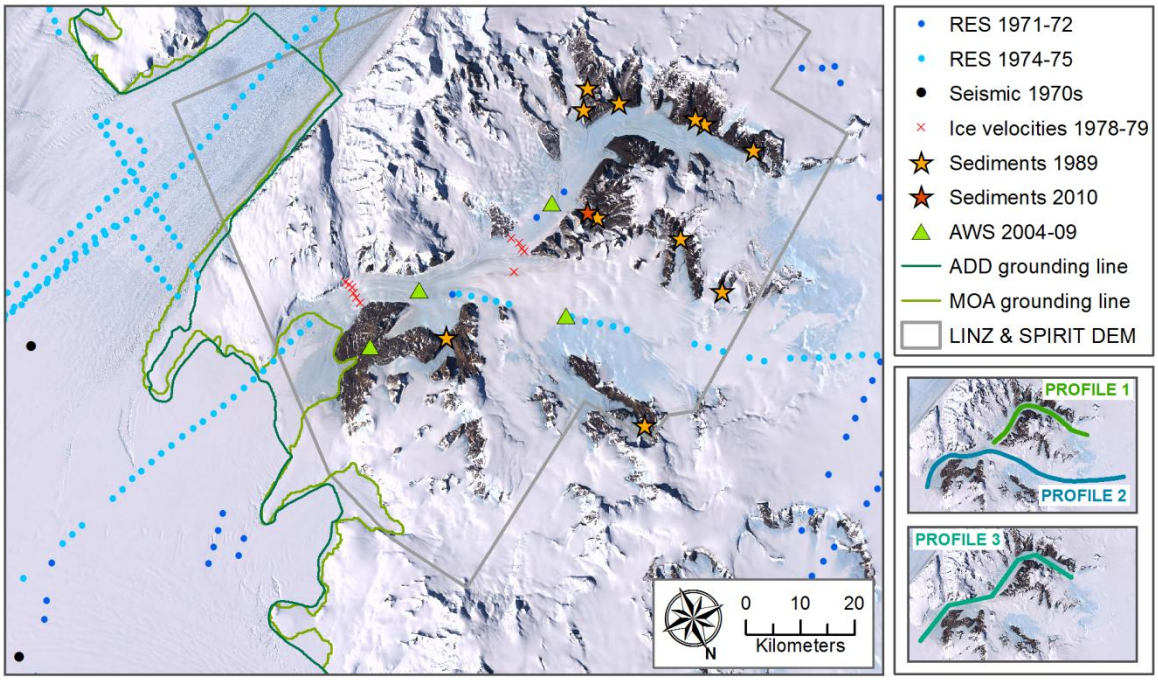

Figure 2.2. A map showing the location and nature of previous work in the region. Ice thickness and velocity estimates from glacier models are shown along profile 1 and 2 in Figure 2.4 and Figure 2.5 and from geological evidence along profile 3 in Figure 2.8 (map based on LIMA, http://lima.usgs.gov).

The first major study in the DHGS was conducted by Bockheim et al. (1989), who were the first to describe, map and date glacial drifts in the ice-free valleys. The results were subsequently correlated with glacial drifts present elsewhere in the Ross Embayment and utilised to develop and age-constrain the 'swinging gate' model (Conway et al. 1999, Figure 1.4). More recently, the study conducted by Anderson et al. (2004) on the behaviour of the Hatherton Glacier following the LGM, was the first to apply a numerical model to simulate the

effect of a grounded Ross Ice Sheet on a TAM outlet glacier. The establishment of the Latitudinal Gradient Project (LGP, www.lgp.aq) in 2003 has renewed interest in the Darwin-Hatherton region. Of particular importance to the work presented here has been the installation of several AWSs on the glacier surface (Zawar-Reza et al. 2010) and a new attempt to date the glacial drifts identified by Bockheim et al. (1989) using cosmogenic exposure dating (Storey et al. 2010).

2.1 Regional setting

The glacially eroded valleys, cirques and isolated nunataks of the Darwin-Hatherton area are characteristic features of a landscape which has been formed by uplift of the TAM through a pre-existing ice sheet (Denton 1979). During this uplift, deep glacially carved valleys formed in geologically weak zones, while shallow valleys became more and more isolated (Denton 1979). The DHGS is surrounded by two of the largest TAM outlet glaciers; the Byrd and the Mulock Glaciers which drain most of the East Antarctic ice immediately inland from the DHGS (Figure 1.2). A calculation of catchment area from early topographic maps has indicated a limited ice discharge from the EAIS through the DHGS (Anderson et al. 2004). However, a newer digital elevation model (DEM) constructed by Bamber et al. (2009b) is thought to describe the surface topography inland of the DHGS in more detail (section 4.1) and was used to recalculate the catchment outline. The result, which is shown alongside the old catchment basin in Figure 1.1, shows that the DHGS catchment boundary is likely to be located further inland than originally thought, resulting in a 15% increase in catchment area to 9150 km^2. Despite this, the DHGS drains a relatively small catchment that extends only ~180 km inland from the glacier outlet. The limited ice discharge from the EAIS suggests that the Hatherton and Darwin Glaciers flow in relatively shallow valleys with restricted inflow. This is inferred to be particularly true for the Hatherton Glacier, as the Darwin Glacier appears to capture the majority of the inland ice inside the catchment (Figure 1.1).

Within the catchment, the ice surface elevation ranges between a maximum of 2200 m above sea level (m a.s.l.) inland and a minimum of 50 m a.s.l. below the junction with the Ross Ice Shelf. The surface slopes are generally below 1% on the Hatherton Glacier and range between 1 and 3% for the Darwin Glacier. However, several steep regions with surface slopes of 7-10% exist on the Darwin Glacier, for example at The Nozzle, where the glacier narrows to a minimum width of 5 km before widening again towards the junction with the Ross Ice Shelf. The regions of high surface slopes correspond well with the outline of crevasse fields observed on the glacier surface in satellite images (Figure 2.1). Crevasses are indicative of zones of increased longitudinal stretching and document to the dynamic behaviour of the Darwin Glacier. In contrast, the low surface slopes and lack of surface crevasses on the Hatherton Glacier are characteristic of a less dynamic system.

2.2 Surface topography

The DHGS represents a challenge with regards to mapping, as the relatively flat glaciers are surrounded by steep mountains extending more than 1000 m above the glacier surface in many places and reaching more than 3000 m a.s.l. in the Britannia Range. The first topographic maps to cover the DHGS were produced by the U.S. Geological Survey (USGS) in the 1960s from reconnaissance aerial photographs (1:250,000 scale and 200 m contour intervals). Since then several DEMs of varying resolution and accuracy have covered the study area. Some of these models will be described in more detail below.

The first DEM to cover the Darwin-Hatherton area in relatively high resolution was published by Liu et al. (1999) as part of the Radarsat Antarctic Mapping Project (RAMP). The RAMP DEM combines altimetry datasets (ERS-1) with topographic data collected for Antarctica between 1940 and 1999 (primarily Antarctic Digital Database (ADD) and USGS maps). The DEM is gridded at 200 m pixel spacing and has a vertical accuracy of about ±100 m in the Darwin-Hatherton region (Liu et al. 2001; Liu et al. 1999). More recently, an all-Antarctic DEM has been produced by combining laser altimeter measurements with satellite radar altimetry data in order to obtain good vertical resolution as well as satisfactory spatial coverage (Bamber et al. 2009b). This DEM, which will be referred to as the Altimetry DEM throughout this thesis, has a pixel spacing of 1 km and a root mean squared error of 15 to ~40 m in steep mountainous areas such as the TAM (Griggs and Bamber 2009). Due to the coarse resolution of the model, it performs well in flat terrain, but fails to accurately resolve rapidly changing surfaces such as the mountains surrounding the DHGS. The two DEMs differ significantly, which is clear when comparing the DHGS catchment calculated from the RAMP DEM (USGS maps) with that of the Altimetry DEM (Figure 1.1).

The joint outline of two higher resolution DEMs that cover part of the DHGS is included in Figure 2.2. As part of the Latitudinal Gradient Project, Land Information New Zealand (LINZ) has produced a 20 m resolution DEM which covers the entire Hatherton Glacier and the majority of the Darwin Glacier (LINZ 2010). The LINZ DEM was constructed from a combination of ground based surveying and satellite imagery (ALOS) provided by the Japanese Earth Observation programme. In addition, a 40 m resolution DEM constructed as part of the SPOT 5 Stereoscopic survey of Polar Ice: Reference Images and Topographies (SPIRIT) project (Korona et al. 2009) covers regions of the glacial system towards the Byrd Glacier. Both the LINZ and SPIRIT DEMs accurately resolve the mountains surrounding the DHGS and compare well with each other in overlapping regions.

2.3 Climate and surface mass balance

An AWS installed in the Brown Hills (330 m a.s.l., Figure 2.2 and Figure 2.1) near the Ross Ice Shelf has been operating between 2004 and 2009 and provides the only medium-term record of meteorological parameters in the DHGS. More recently, several short-term AWSs have been installed at various locations on the glacier surface as part of a programme run by the University of Canterbury in New Zealand (Zawar-Reza et al. 2010). The two datasets suggest that the region is influenced by frequent katabatic winds descending from the polar plateau, with wind directions that are controlled by the surface topography. The Brown Hill data record shows a significant peak in wind speed in the winter periods with the summer months appearing calm in comparison. Mild periods may occur at the station throughout the year and are often associated with katabatic winds. As a consequence, the mean annual air temperature at the Brown Hill AWS is just above -20°C (LGP 2004), which is high compared to temperatures on the Ross Ice Shelf (Bockheim et al. 1989).

Few meteorological observations have been collected in the Darwin-Hatherton region and measurements of the spatial variations in temperature are instead limited to an all-Antarctic remote sensing study. Comiso et al. (2000) used infrared satellite data to produce a 1 km resolution gridded dataset of the annual mean surface temperature which has an accuracy of ~3°C compared to the long-term observational record in Antarctica. The dataset has been expanded since the initial publication and now includes averaged annual mean temperatures between 1982 and 2004 (Le Brocq et al. 2010b). The remotely sensed annual mean surface temperatures within the DHGS catchment range between -19.5°C at the glacier outlet and -38.2°C on the polar plateau (Comiso 2000).

Very little is known about the annual mean accumulation/ablation rates within the DHGS. Estimates of SMB have therefore traditionally been based on measurements on the polar plateau and on the Ross Ice Shelf (Anderson et al. 2004; Bockheim et al. 1989). The polar plateau near the head of the glacial system is thought to experience an annual accumulation rate of 10-15 cm water equivalent (w.e.) yr^{-1}. By contrast, accumulation rates are estimated at 20 cm w.e. yr^{-1} at the Ross Ice Shelf near the glacier outlet (Bockheim et al. 1989). Anderson et al. (2004) used these measurements to develop several SMB scenarios for the glacial system for use in a modelling experiment. The best fit scenario is shown in Figure 2.3 and accounts for the extensive blue ice areas (BIAs) present on the surface of the DHGS by combining a linear change in accumulation between the polar plateau and the Ross Ice Shelf with estimated ablation rates in BIAs (Robinson 1984) modified to fit the latitudinal location of the study area (Anderson et al. 2004). The SMB model proposed by Anderson et al. (2004) displays negative values up to an elevation of ~1600 m above which an annual accumulation rate of ~7.5 cm w.e. yr^{-1} was estimated.

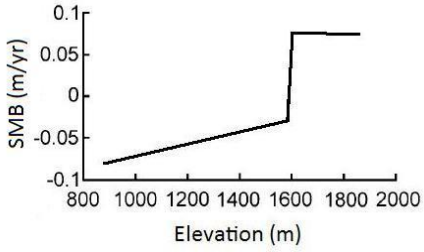

Figure 2.3. Best SMB scenario for the DHGS as determined by Anderson et al. (2004).

Several all-Antarctic maps of SMB have been constructed at various resolution and using a range of techniques. Vaughan et al. (1999a) and Arthern et al. (2006) interpolated between the poorly distributed in situ measurements by applying a background field derived from satellite data, while van de Berg et al. (2006) used output from a regional atmospheric climate model. However, as no direct measurements exist from the DHGS, and the 55 km resolution of the climate model is insufficient to resolve the BIAs in the glacial system, neither of these models accurately accounts for the variations in SMB which exists in the DHGS, and all models predict snow accumulation in BIAs within the catchment.

2.4 Ice surface features

As mentioned above, the surface of the DHGS is characterised by several large of BIAs. Most of the Hatherton Glacier surface as well as the northern and lowermost parts of the Darwin Glacier are covered by blue ice which comprise a total of ~18% of the catchment area (Figure 2.1). The BIAs are interspersed between snow-covered regions which are mainly located in the high elevation catchment areas and the southern half of the Darwin Glacier. BIAs have traditionally been divided into four categories (I. near exposed bedrock, II. on valley glaciers, III. on steep slopes, and IV. on lower parts of glaciers) based on their formation mechanisms and general characteristics (Bintanja 1999; Takahashi et al. 1992) and may be either open (inflow balanced by sublimation) or closed (inflow balanced by sublimation and outflow) types (Grinsted et al. 2003).

Numerous small closed type I BIAs no greater than 5 km^2 are present in the vicinities of exposed rocks within the DHGS catchment but because of their size are unlikely to play a major role in the overall SMB. Three much larger BIAs exist on the DHGS surface (BIA-A, BIA-B and BIA-C on Figure 2.1), the extent of which is thought to be closely related to the variable wind conditions that exist in the region (Zawar-Reza et al. 2010). The largest BIA-A extends from the upper Hatherton Glacier (~1650 m a.s.l.) through the Nozzle and to the glacier outlet

(~50 m a.s.l.) and covers a total of 900 km^2. BIA-A is confined by mountains on both sides and can be categorised as an open type II BIA.

The smaller BIA-B (306 km^2) surrounds the Tentacle Ridge which borders the northern side of the Darwin Glacier. During the December 2008 fieldwork a traverse of the Darwin Glacier from the snow-covered southern side and into BIA-B revealed a distinct increase in wind velocity in the BIA and its formation likely relates to katabatic winds channelled down the McCleary Glacier. Ice velocities are likely to be small in the vicinity of Tentacle Ridge, which may also act as a barrier to snowdrift from the plateau. Based on this evidence, BIA-B is likely to be a combination of type I and II BIA and as it experiences ice inflow as well as outflow, must be classified as an open type BIA.

BIA-C (~245 km^2) is located towards the polar plateau between ~1700 and 1900 m a.s.l. and has previously been described in detail by Brown and Scambos (2004). The protruding rocks downstream of BIA-C are likely to obstruct ice flow and it most probably owes its formation to a combination of snow ablation by katabatic winds and slow ice velocities. BIA-C is classified here as a type III with the parts close to the nunataks exhibiting the characteristics of a closed type. Other parts of BIA-C further away from the rocks appear to have some ice outflow and fall into the category of an open type III BIA.

Satellite imagery from the region show that at the height of summer, small supraglacial meltwater streams may form on the glacier surface and what appears to be supraglacial lakes of more than 100 m in diameter become visible immediately upstream from Lake Wilson. However, it is unlikely that the melting which occurs during at least some summers has a significant impact on the SMB, as the water probably refreezes within the surface layers when temperatures begin to lower (van den Broeke et al. 2009). The distributions of surface crevasses are also revealed on satellite images and appear to be primarily confined to the areas south-west of McCleary Glacier, north-west of Junction Spur and at The Nozzle (Figure 2.1). In contrast the Hatherton Glacier has a smooth surface without any detectable crevasse fields. As mentioned above, the distribution of crevasse fields provides evidence to variations in stresses, and their distribution within the DHGS illustrates a distinct difference between the flow behaviour of the Darwin and Hatherton Glaciers.

Flowlines and medial moraines are clearly visible in the BIAs and provide excellent indicators of the contributions to ice flow from various regions within the DHGS catchment (Figure 2.1). From the flowlines highlighted in Figure 2.1, it is clear that the Hatherton Glacier contributes very little to the total ice discharge at the junction with the Ross Ice Shelf. Ice flow through the Hatherton Glacier is governed partly by ice discharge from the EAIS, although as mentioned above, inflow is limited (Figure 1.1). In addition, a major part of the Hatherton

Glacier ice comes from local sources such as the Midnight Plateau in the Darwin Mountains, and the Lieske, Hinton and Ragotzkie glaciers in the Britannia Range. East Antarctic ice draining through the Darwin Glacier is the main source of ice for the DHGS (Figure 2.1). However, important inflow of ice occurs downstream of Junction Spur, where the Darwin Glacier is joined by the Touchdown Glacier, which drains from the Cook Mountains, and two unnamed glaciers draining from the Britannia Range.

2.5 Ice thickness

Prior to the Antarctic field season 2007/08, measurements of ice thickness in the DHGS were limited to the locations shown in Figure 2.2. These measurements were collected between 1971 and 1975 as part of airborne Radio Echo Sounding (RES) surveys carried out by the Scott Polar Research Institute (SPRI), the Technical University of Denmark (TUD) and the National Science Foundation (NSF). Also of importance is a set of seismic measurements conducted by the US Ross Ice Shelf Geophysical and Glaciological Survey in the 1970s (Lythe et al. 2000b). All of these measurements were included in the original BEDMAP dataset of ice thickness and bedrock topography of Antarctica (Lythe and Vaughan 2001; Lythe et al. 2000a). However, the accuracy of the RES data collected on the Darwin and Hatherton Glaciers is questionable, as the navigational uncertainty may be as high as 3 km (Lythe et al. 2000b) and side reflections from the nearby mountains may result in erroneous readings (Kavanaugh et al. 2009b).

Due to the lack of detailed ice thickness measurements, the modelling study conducted by Anderson et al. (2004) used an idealised trapezoid transverse valley shape to estimate ice thicknesses from calculations of balance ice fluxes. This method has uncertainties of several hundred metres, since the calculated balance flux used to determine ice thickness depends on the SMB and the degree of sliding and deformation, of which very little is known (Anderson et al. 2004). The inferred centreline bedrock topography was found to vary greatly, with the ice thickness reaching a maximum of ~1000 m in the lower part of the Hatherton Glacier and thinning considerably towards the EAIS (Figure 2.4).

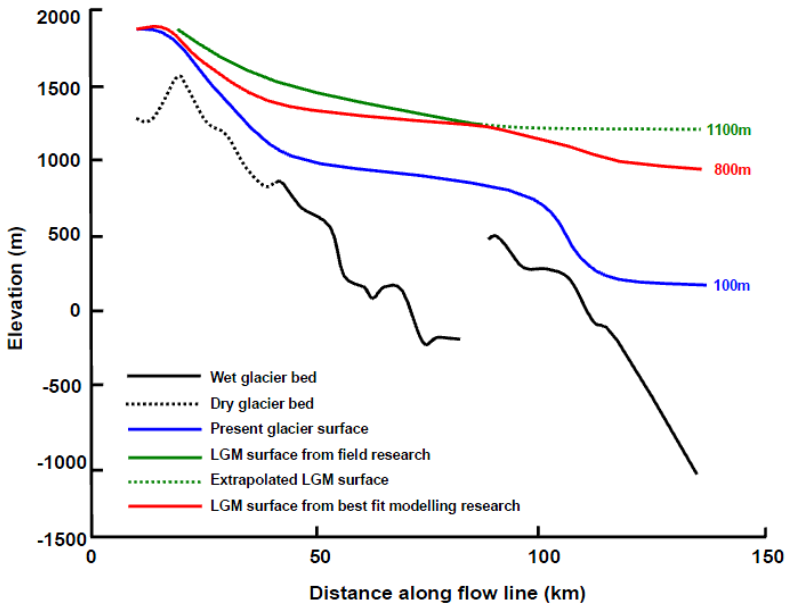

Figure 2.4. Surface profiles and bedrock topography along the Hatherton and lower Darwin Glacier centre flowlines shown in Figure 2.2 as profile 1 and 2. The modelled glacier configuration is shown by the bedrock topography (black line, full for warm-based and dashed for cold-based) and present glacier surface (blue line). The red and green lines show the LGM surface profiles determined through modelling (Anderson et al. 2004) and by extrapolation of drift sheet boundaries (Bockheim et al. 1989) respectively (Anderson et al. 2004).

2.6 Ice velocity

Ice velocities were measured near Junction Spur and at The Nozzle by Hughes and Fastook (1981) during their 1978/79 Antarctic fieldtrip to the Byrd Glacier (Figure 2.2 and Figure 2.5). Velocities at Junction Spur were measured to 40-60 m yr^{-1} and 30-50 m yr^{-1} on the Darwin and Hatherton Glaciers respectively, while a maximum velocity of 110-130 m yr^{-1} was measured at The Nozzle (Hughes and Fastook 1981).

Additional information on ice velocities were provided by the modelling study conducted by Anderson et al. (2004). Although the velocities measured by Hughes and Fastook (1981) were used to tune the flowline model to some extent, the continuous velocity profile offers new information about the magnitude of variations in ice velocity along the centre line (Figure 2.5). The model velocities compare well for the Darwin Glacier while velocities of the Hatherton Glacier are underestimated with values of less than 20 m yr^{-1}. A maximum velocity of ~325 m yr^{-1} is estimated by the model for the narrowest section of The Nozzle (Anderson et al. 2004).

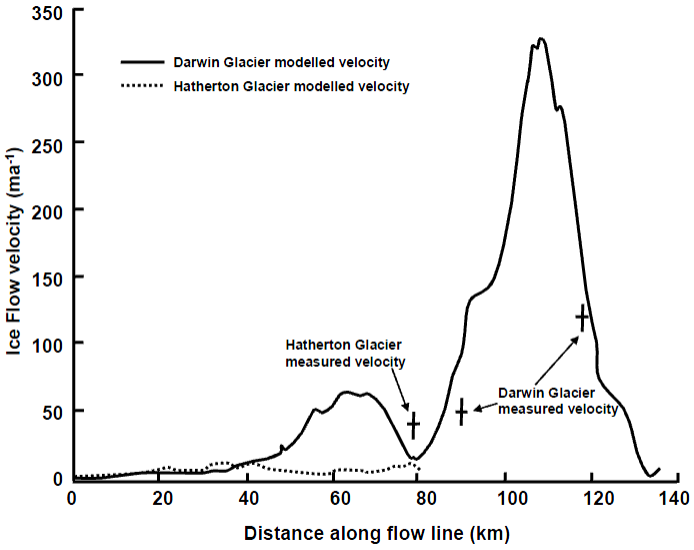

Figure 2.5. Ice velocities measured by Hughes and Fastook (1981) (crosses) and modelled by Anderson et al. (2004) along the centre flowline of the Hatherton (dotted black line, profile 1) and Darwin (full black line, profile 2) Glaciers. The locations of the flowlines are shown in Figure 2.2.

2.7 Grounding line position

Information on the Darwin Glacier grounding line position is provided by two studies which have applied two very different techniques to investigate the outline of the grounded Antarctic Ice Sheet (Figure 2.2). The ADD (http://www.add.scar.org) grounding line relies on interpretations of Landsat imagery and USGS maps (1:250,000 series) and has been revised by C. W. M. Swithinbank (ADD-Consortium 2000). The newer Mosaic of Antarctica (MOA, http://nsidc.org/data/moa/) grounding line map has been constructed from break-in-slopes in MODIS (Moderate-resolution Imaging Spectroradiometer) images, which are particularly sensitive to changes in slope (Scambos et al. 2007). The considerable difference (15-20 km, Figure 2.2) that exists between the Darwin Glacier grounding line location proposed by the two datasets is most likely unrelated to an actual change and instead relates to the increased detail provided by the MODIS imagery.

2.8 Basal properties

The conditions at the base of the DHGS constitute an important control on flow behaviour of the glacial system. The temperature of the base of the DHGS has been investigated by Anderson et al. (2004) utilising calculated ice thicknesses to apply the quadrature method described by Hindmarsh (1999). The results are shown in Figure 2.4 as the change from dashed (cold-based) to full black line (warm-based) for bedrock topography. The calculations

suggest warm-based condition for a substantial part of the glacier bed of both Hatherton and Darwin Glaciers, and while there are large uncertainties involved with the approach, cold-based conditions occur only in the thinnest regions.

The physical appearance of glacial sediments in the ice free valleys provides further evidence to past and possible present basal conditions. Boulders showing signs of striation, plucking and faceting (Figure 2.6) are present in particular in the lowermost and youngest glacial drifts, which have been exposed to post-deposition weathering for the shortest time span (Bockheim et al. 1989; Storey et al. 2010).

Figure 2.6. Two examples of stoss-and-lee shaped boulders with clear striations found close the Hatherton Glacier margin in the Lake Wellman area (Figure 2.1). Ice flow would have been from left to right for both boulders (Photo: M. Riger-Kusk).

The processes resulting in the observed erosional characteristics are normally associated with transport of sediments in the basal shear zone of warm-based glaciers where clasts lodged in basal till may become overridden by debris-rich ice (Benn and Evans 1998). Although several studies have shown that sliding as well as abrasion does take place under cold-based Antarctic glaciers (Atkins et al. 2002; Cuffey et al. 2000; Davies et al. 2009), the abundance of boulders showing signs of active glacial transport in combination with the large amount of sediments deposited in thick drift sheets and moraines, as a minimum indicate warm-based conditions for part of the glacial system at some time in the past (Storey et al. 2010).

2.9 Geomorphology and glacial history

The inland mountains surrounding the DHGS consist of Beacon sandstone and Ferrar dolorite intrusions, and only in the lower areas close to the Ross Ice Shelf can outcrops of basement granites be observed (Haskell et al. 1965). Granites are therefore erratic to the upper glacier area and have been used both to delineate glacial drift sheets (Bockheim et al. 1989) and for

cosmogenic exposure dating (Storey et al. 2010). As these drift sheet will be compared to the modelled LGM DHGS ice configuration presented in Chapter 5, their distribution and inferred ages will be described in detail below.

2.9.1 Glacial drift sheets

Glacial drift sheets and moraine features in the ice-free areas adjacent to the DHGS were initially described by Denton (1979) and Bockheim et al. (1989) and later by Storey et al. (2010). The drift sheets are best preserved in the Darwin Mountains and the Britannia Range surrounding the Hatherton Glacier (Figure 2.2) whereas only undifferentiated drift sheets have been identified in the lower parts of the Darwin Glacier (Bockheim et al. 1989). The regions surrounding the Hatherton Glacier are characterised by an abundance of granite erratic, perched boulders, terminal moraines, and boulders showing signs of active glacier transport (Figure 2.7).

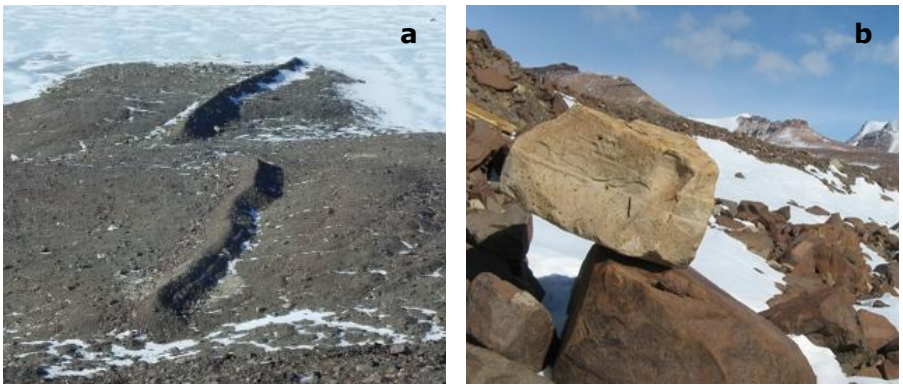

Figure 2.7. Photographs showing (a) a ~500 m long moraine close to the present-day glacier margin and (b) an example of a perched boulder (Photo: M. Riger-Kusk).

A total of five drift sheets were described by Bockheim et al. (1989) on the basis of soil morphology, chemistry, weathering rates and terminal moraine features (field sites shown in Figure 2.2). All except the youngest drift were found to show a pattern of increased distance between present-day ice surface and drift sheet boundary towards the glacial outlet (Figure 2.8). By comparison, drift sheet boundaries are closely spaced in the uppermost part of the glacial system and only minor ice thickness variations appear to have occurred in this region in the past (Bockheim et al. 1989).

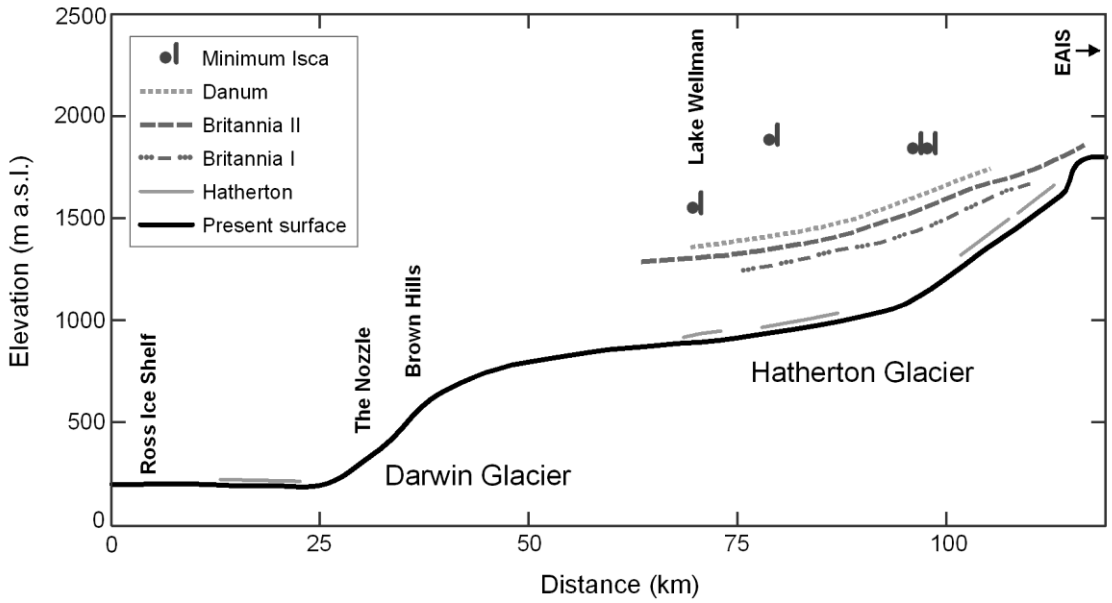

Figure 2.8. Elevation of present-day glacier surface and drift sheet boundaries along profile 3 in Figure 2.2. Figure modified from Bockheim et al. (1989).

The five drift sheets were named by Bockheim et al. (1989) in order of increasing ages as the Hatherton, Britannia I and II, Danum and Isca drift sheets. As the youngest drift, the Hatherton drift boundary is located closest to the present-day glacier margin whereas the oldest undifferentiated drift extends to a height of more than 750 m above present ice surface for the middle Hatherton Glacier (Bockheim et al. 1989). The drift sheets serve as excellent markers of former ice extent and thickness of the DHGS and have previously been used to constrain modelled LGM ice configurations of the Darwin and Hatherton Glaciers (Anderson et al. 2004).

2.9.2 Glacial history of the DHGS

The distribution of glacial deposits shows that during periods of growth the Hatherton Glacier expanded up slope into flanking valleys where it deposited large terminal moraines in positions of prolonged standstill. When conditions turned less favourable the ice retreated down slope, exposing the glacial drift sheets which cover many of the ice free regions. Because of the downward slope of the ice free valleys towards the present-day glacier margin, ice covered lakes are currently dammed by the glacier in several of the valleys previously occupied by glacier ice (Figure 2.1). In addition evidence exists in the Lake Wellman area of former lakes up valley from the current glacier margins. Proglacial lakes may therefore have continuously followed the glacier margin as it retreated down slope from its LGM position (Bockheim et al. 1989).

Bockheim et al. (1989) dated remnants of algae from the former lakes in an effort to determine the timing and rate of Holocene glacier retreat, while approximate ages of older drifts were determined through correlations with drifts identified and dated elsewhere in the Ross Embayment. More recently, Storey et al. (2010) have used cosmogenic surface exposure dating to determine the ages of the drift sheets identified by Bockheim et al. (1989) in the Lake Wellman area, with the aim of achieving a more precise dating of glacial events. The drift sheet ages found by Bockheim et al. (1989) and Storey et al. (2010) differ significantly (Table 2.1) and a brief discussion of the methods and results is given in the following sections.

Table 2.1. Ages of glacial drift sheets as determined by Bockheim et al. (1989) and Storey et a. (2010). The maximum age model proposed by Storey et a. (2010) was thought to be the most likely scenario of the two models. The ^{14}C ages have been calibrated using the calibration curves proposed by McCormac et al. (2004) for the youngest dates (11 – 0 cal kyr BP) and Reimer et al. (2004) for the oldest date.

Drift sheet	Bockheim et al. (1989) Minimum age [cal kyr BP]	Storey et al. (2010) Maximum age model [kyr BP]	Storey et al. (2010) Minimum age model [kyr BP]
Hatherton	5.96 ± 0.04 Early Holocene	15 – 20 MIS 2 (LGM)	0.5 – 3 Late Holocene
Britannia I & II	10.57 – 11.96 ± 0.17 MIS 2 (LGM)	40 – 30 MIS 3	23 MIS 2 (LGM)
Danum	140 – 160 MIS 6	230 – 630	77 MIS 4
Isca	?	2,200 – 395 Early – mid Pleistocene	130 MIS 6

Radio carbon dates show a more or less steady decrease in ages towards the present glacier surface (Bockheim et al. 1989). Ice recession from the Britannia II inferred LGM limit was shown to predate 10,570 – 11,960 cal yr BP with the ice surface reaching surface elevations close to present between 6450 and 6800 cal yr BP. Based on these dates, the Britannia I drift was thought to represent a major thickening during the general ice recession, whereas the Hatherton drift was assumed to be the result of an adjustment of the grounding line of the DHGS during the early Holocene (Bockheim et al. 1989). No dates exist from the Danum drift, which was instead correlated to the Marshall drift in the McMurdo Sound and inferred to be of a MIS 6 age.

The surface exposure dates described by Storey et al. (2010) from the Lake Wellman area suggest an entirely different glacial history for the Hatherton Glacier. Due to the large spread in ages and to account for various uncertainties, which will be mentioned below, two different age models were proposed (Table 2.1). In general, most evidence supports the model with the oldest measured exposure dates. According to the preferred interpretation of the dates, the

Isca drift is older than 2.2 M yr BP while the Danum drift was deposited either between 230 and 630 kyr BP (oldest ages) or at 77 kyr BP (youngest age). The most reliable results come from boulders collected from the Britannia drift sheets, which place the drift ages at 40 – 30 kyr BP and not at the LGM as was suggested by Bockheim et al. (1989). The Hatherton drift was dated as either a LGM (oldest ages) or late Holocene (youngest ages) deposit, which either way suggests a LGM thickness and ice extent of the glacial system considerably smaller than previously thought.

Both age datasets have various uncertainties associated with the results. When dating algae from former lakes as a means of dating the glacial retreat, accurate results can only be obtained if the disappearance of the lake is directly related to the retreat of the glacier margin. If on the other hand the lake exists for considerably time after the glacier has retreated down slope, the algae ages are not closely related to the glacier retreat. Therefore, at best, this method provides direct timing of glacier retreat, while at worst, it provides at set of minimum ages for ice recession from the former lake locations (Bockheim et al. 1989). Uncertainties of the surface exposure dates are partly related to the level of inherited surface exposure from multiple episodes of entrainment and exposure. This is particularly problematic in Antarctica, where cold-based basal conditions will limit erosion and deposition. A cold-based glacier advancing over an old drift sheet may, as a consequence, leave the older drift practically unaltered, while depositing few additional sediments (Sugden et al. 2005). If an erratic with an inheritance signal is sampled, the drift sheet age will be overestimated. Another concern with regards to the surface exposure technique is the potential re-positioning of glacial sediments in unstable terrain. Consequently, if the degree of exposure has not been continuous since the initial deposition, drift sheet ages will be underestimated (Storey et al. 2010). Most likely due to a combination of signal inheritance and re-positioning of sampled boulders, the dataset presented by Storey et al. (2010) does not show a consistent age-elevation relationship. The age model predicting the oldest ages was preferred because the error associated with re-positioning of sediments was thought to exceed that of signal inheritance.

2.9.3 Evidence from the DHGS on past changes of the Antarctic Ice Sheet

As a linkage between the EAIS and WAIS, the ice behaviour of the DHGS is influenced by changes in both ice sheets. The glacial drift sheets identified in the Darwin-Hatherton area provide evidence of several occasions where ice was significantly thicker, in particular in the lower parts of the glacier. In contrast only slight changes appear to have occurred in the upper reaches (Figure 2.8). Similar asymmetrical changes have been documented for a number of outlet glaciers in the TAM (section 1.6) and are likely the result of damming by a grounded Ross Ice Sheet leading to a progressive ice thickening of the lower parts of the southernmost

TAM glaciers (Bockheim et al. 1989; Denton et al. 1989a; Denton and Hughes 2000; Todd et al. 2010). By comparison, the minor increase (100 m for Britannia II drift sheet) in the uppermost reaches of the glacial system suggests near constant thickness of the interior EAIS during previous glacial events (Bockheim et al. 1989).

The geomorphologic evidence indicates a strong relationship between changes of the WAIS and those occurring in the DHGS. Estimates of LGM ice thickness at the DHGS outlet has consequently been used to infer the maximum thickness of the grounded Ross Ice Sheet during this time (Denton and Hughes 2000). However, the magnitude of change which occurred in the glacial system during the LGM remains uncertain, in particular with the new drift sheet ages proposed by Storey et al. (2010). Previous estimates of the LGM ice thickness at the DHGS outlet are based on an LGM age of the Britannia drift sheet and rely on a linear extrapolation of the drift boundary (Bockheim et al. 1989) and ice-flow model simulations (Anderson et al. 2004). Both studies predict a remarkable ice thickness increase ranging between 1100 m and 800 m for the extrapolation and model respectively (Figure 2.4). The ice thickness increase predicted by the model for the Hatherton Glacier compares reasonably well with the upper boundary of the Britannia drift and offers support to the inference that the change observed within the glacial system is primarily driven by ice conditions in the Ross Embayment (Anderson et al. 2004).

The 'swinging gate' model of the WAIS grounding line retreat from its LGM extent (Figure 1.4) was developed partly from the evidence presented by Bockheim et al. (1989) for the Darwin-Hatherton region (Conway et al. 1999). As mentioned in section 1.4.1, in this model, the grounding line retreats past the DHGS outlet at approximately 6800 years BP, which is when Bockheim et al. (1989) found surface elevations of the glacial system to be close to present-day levels (Figure 1.4). Therefore, the time it would take for the DHGS to adjust to the change in Ross Embayment ice conditions is not accounted for in the 'swinging gate' model. More recently Anderson et al. (2004) used a flow line model to investigated the dynamic response of the DHGS to the retreat of the WAIS grounding line. Results show that it would have taken approximately 1000 yr for the DHGS to adjust to this change, which would require the Ross Ice Sheet grounding line to retreat past the DHGS outlet as early as 7900 yr BP in order for the glacier surface to reach present-day levels by 6800 cal yr BP. The modelling study clearly illustrates the importance of accounting for glacier dynamics when interpreting former ice surface elevations from glacial drift sheet boundaries.

2.10 Summary

The DHGS belongs to a group of slower moving TAM outlet glaciers. It drains a limited catchment basin most likely because ice flow from the EAIS is restricted by subglacial

mountains. Calculations of basal temperature conditions suggest generally warm-based conditions, and only in the thinnest regions are temperatures expected to stay below the pressure melting point at depth (Anderson et al. 2004). The erosional characteristics of glacial sediments in surrounding ice free valleys further supports the presence of warm-based basal conditions at least at some time in the past (Storey et al. 2010). Like many of the TAM glaciers, the surface of the DHGS consists of a patchwork of blue ice ablation areas and snow-covered regions of net accumulation, although, the magnitude of ablation and accumulation is unknown.

The glacial system is surrounded by large ice-free valleys covered in glacial drifts and moraine features. A total of five drift sheets have been identified, extending to a maximum height of 750 m above the present-day elevation of mid-Hatherton Glacier (Bockheim et al. 1989). The distribution of the drift sheets indicate past episodes of significant thickening in the lower regions of the glacial system while little, if any, change has occurred towards the EAIS. The asymmetrical pattern is likely explained by an advance of the WAIS into the Ross Embayment during past glaciations leading to a damming of the southern TAM glaciers. The effect of such an advance on the DHGS has been simulated by a numerical ice-flow model and results compare reasonably well with the distribution of glacial drift sheets (Anderson et al. 2004). However, a recent study of drift sheet ages has questioned the LGM extent and thickness of the DHGS and consequently of the WAIS (Storey et al. 2010).

Prior to this thesis, knowledge of present-day ice dynamics of the DHGS was limited to the velocity measurements conducted by Hughes and Fastook (1981) in the late 1970s and the modelling study conducted by Anderson et al. (2004). The latter attempt of modelling the dynamic behaviour of the glacial system has resulted in some insight into the SMB, ice thickness, ice velocity variations and basal conditions as well as rate and magnitude of Holocene variations. However, the model was poorly verified due to the lack of direct measurements of key parameters. Considerable uncertainty to the magnitude of Holocene change of the DHGS has been introduced by recent effort to apply an alternative dating technique to the glacial drift sheets (Storey et al. 2010). These new results highlight the need to revisit the DHGS to obtain further information on present glacier dynamics and to revaluate its glacial history in the context of the WAIS.

The work presented in this thesis continues where earlier studies have ended by combining previous knowledge of the DHGS with new direct measurements of key parameters. This will not only advance our understanding of the current glacier dynamics of slower moving East Antarctic outlet glaciers but also provide a more accurate estimate of the magnitude of past changes.

3 Characteristics of the Darwin-Hatherton glacial system as determined from ground and airborne geophysical surveys

One of the main goals of this thesis is to improve the understanding of processes that influence the dynamic behaviour of the DHGS. In this chapter, the general characteristics and flow behaviour of the DHGS are investigated using GPR data collected between 15 November and 15 December 2008 and airborne radar measurements collected in January 2009. In addition, repeat GPS measurements offer information on ice surface velocities at a wide range of locations across the glacial system. The new measurements of ice thickness represent a significant improvement to the sparse data included in the 5 km resolution BEDMAP data series (Lythe and Vaughan 2001, section 2.5, Figure 2.2) and the new velocity measurements improve the spatial distribution of survey points (section 2.6, Figure 2.2).

The new radar measurements offer an opportunity to construct a new high quality map of ice thickness and bedrock topography (section 3.5) of the DHGS, and internal layers within the radar profiles provide evidence of the effect of rough bedrock topography on flow dynamics (section 3.6, objective A.1). A detailed GPR profile across the Darwin Glacier grounding line reveals interesting new insight into regions of this transition zone, which has previously been described only by low resolution airborne radar measurements (section 3.8, objective A.2). Shallow internal layers are utilised to infer variations in SMB and examine the cause of these changes (section 3.7, objective A.3). Finally, new ice velocity measurements facilitate calculations of ice discharge through cross profiles (section 3.9) which will be used in section 4.5.6 and 5.8 to examine the current SMB of the glacial system (objective B.3). In addition, ice discharge measurements facilitate the first calculation of oceanic melt rate below the Darwin Glacier grounding line (section 3.10).

3.1 The application of radar systems in glaciological research

Since the middle of the 1960s radar has been the preferred method for investigations of ice thickness and internal structures of polar glaciers and ice sheets due to the low attenuation of radar waves in cold homogeneous ice. RES systems have successfully been applied to airborne surveys of most of the Antarctic Ice Sheet, recording ice thicknesses of more than 4000 m in

places (Siegert 1999). For ground-based radar surveys, GPR is preferable to RES systems, mainly due to better vertical resolution and improved focussing of the radar beam, limiting the influence of above surface objects. However, the penetration depth of RES continues to greatly exceed that of GPR, which is restricted in power output and antenna gain (Arcone 2009; Plewes and Hubbard 2001).

A typical radar setup consists of a control system connected to transmitting and receiving dipole antennas. The frequency is controlled by the antenna length and typically ranges between approximately 10 and 500 MHz for glaciological applications. High frequency signals with short wavelengths and high vertical resolution will scatter from objects which are 'ignored' by lower frequency signals which have long wavelengths and poorer vertical resolution (Annan 2009; Plewes and Hubbard 2001). High frequency signals consequently lose energy more rapidly and when designing a radar survey it is therefore often a choice between high resolution and large penetration depth.

3.1.1 Propagation of electromagnetic waves in glacial environments

The velocity and attenuation of electromagnetic (EM) waves depends on the electric properties of the medium in which they are travelling, or more specifically the relative permittivity (ε_r) and the electrical conductivity (σ) (Table 3.1). EM waves will attenuate rapidly in materials with high conductivities, in which case an alternative method of investigation should be considered (Plewes and Hubbard 2001). Because the attenuation in pure cold ice is extremely low (Table 3.1) radar is the preferred method when investigating ice bodies.

The velocity of the radar waves in any given material is given by:

$$v = \frac{c}{\sqrt{\varepsilon_r}} \qquad (1)$$

where c = 300 m μs^{-1} and is the speed of light in vacuum. The values listed in Table 3.1 serve as guidelines for material properties, as the relative permittivity for ice, for example, may vary according to impurity and water content, crystal orientation, pressure and temperature (Plewes and Hubbard 2001). On Antarctic glaciers, the relative permittivity and consequently radar wave velocity will change considerably in the upper 40-100 m (van den Broeke et al. 2008) as the firn, which consists of a mixture of air and ice, compacts into pure ice. The dependency of the relative permittivity on firn density (ρ) can be described by the empirical formula proposed by Kovacs et al. (1995):

$$\varepsilon_r = (1 + 0.845\rho)^2 \qquad (2)$$

In radar surveys, velocity variations in the firn layer are generally accounted for by applying a constant radar firn correction to depths calculated using the radar wave velocity of pure ice. The magnitude of the radar firn correction is controlled by the density profile, which may vary according to temperature, wind speed and accumulation rate. Generally, radar firn corrections in Antarctica range between 7 (Ross Ice Shelf) and 15 m (Vostok Station) when the firn layer is fully developed (Dowdeswell and Evans 2004; van den Broeke et al. 2008).

Table 3.1. Relative permittivity, electrical conductivity, velocity and attenuation of materials found in the glacial environment (Annan 2001).

Material	Relative permittivity, ε_r	Conductivity σ [mS/m]	Velocity v [m μs^{-1}]	Attenuation α [dB/m]
Air	1	0	300	0
Fresh water	80	0.5	33	0.1
Sea water	80	3×10^3	10	10^3
Granite	4-6	0.01-1	130	0.01-1
Ice	3-4	0.01	168	0.01

Reflections of EM waves will occur whenever a contrast in relative permittivity is encountered. The depth (d) to observed reflectors can be calculated from the EM wave velocity (v) and the two-way traveltime (TWT) which is the time it takes for the EM wave to travel from the transmitting antenna to the reflector and back to the receiving antenna (Annan 2009).

$$d = \frac{v \cdot TWT}{2} \tag{3}$$

The strength of the reflected wave depends on the magnitude of the permittivity contrast, the interface roughness and the loss of power in the overlying material. Large contrasts, such as from ice to sea water (Table 3.1) are therefore expected to result in reflections of higher amplitude than smaller contrasts such as from ice to bedrock (Bogorodsky et al. 1985).

Reflections of EM waves originate not only from material boundaries, but also from boundaries of prominent internal layers in the ice which can be traced over distances of more than 100 km (Siegert 1999). Within dry snow, firn and ice, dielectric changes resulting in radar wave reflections are caused by variations in density, chemical composition and to a lesser extent crystal orientation (Plewes and Hubbard 2001; Siegert 1999). Density and chemical composition variations are thought to be the result of alternating climatic and atmospheric conditions at the time of deposition, and the layers can therefore be regarded as isochronous accumulation events (Richardson and Holmlund 1999; Siegert 1999; Vaughan et al. 1999b).

Reflections in the upper few 100 m are caused primarily by changes in ice density as the snow and firn compact into ice. Below the firn layer the ice-density remains roughly constant and internal ice reflections are caused predominantly by conductivity variations originating from atmospheric acid deposits from volcanic eruptions (Eisen et al. 2003; Siegert and Fujita 2001; Siegert et al. 2005). Furthermore, in areas of high ice shearing, layering of crystal orientation may become a significant source of reflections at ice thicknesses above 1000 m (Siegert and Fujita 2001).

Tracking of internal isochronal layers in firn and ice has many useful applications in glaciology. Depth-age relationships from firn and ice cores have been successfully correlated and extrapolated into areas without prior information (Rotschky et al. 2004; Siegert et al. 1998). Furthermore, the geometry of the layers has been used to determine spatial and temporal variations in surface accumulation rates (Sinisalo et al. 2003; Vaughan et al. 1999a; Waddington et al. 2007b) and as a means of establishing both current and past glacier dynamics (Hindmarsh et al. 2006; Leysinger Vieli et al. 2007; Siegert and Fujita 2001).

3.1.2 Evidence of SMB and glacier dynamics from internal reflections

As mentioned above, it is generally accepted that internal layers documented by radar surveys represent isochronal accumulation events. Variations in depth and distance between layer boundaries are initially caused by spatial differences in accumulation rates. As the layer is buried, however, several processes may lead to layer distortion. These processes were described by Siegert et al. (2001) and relate to layer deformation caused by undulating basal topography, strain rate variations near ice divides (Raymond bumps), converging or diverging ice flow, changes in glacier flow regime between sliding and no-sliding (the Weertman effect) and changes in rate of basal melting either caused by differences in geothermal heat flux or increased melting near grounding zones (Catania et al. 2005; Catania et al. 2010). In addition, post depositional changes in internal layer geometry may relate to surface ablation zones such as a BIAs, where internal layers will outcrop at the surface as the ice above them is removed (Siegert et al. 2003; Sinisalo et al. 2004).

The effect of post depositional processes on internal layer geometry must be accounted for when layers are located deeper than 1-2% of the total ice thickness, while variations in the uppermost internal layers can generally be attributed solely to changes in accumulations rates (Waddington et al. 2007b). However, several studies have found that influences from changes in glacier flow, basal melting or flow convergence may affect even near-surface internal layers (Leysinger Vieli et al. 2007; Pattyn 2002). Caution must therefore be taken when utilising changes in shallow internal layers to determine variations in accumulation rates in regions where a large change in any of these three factors is suspected.

3.1.3 Grounding zone characteristics

Most knowledge of grounding zones originates from airborne radar surveys. The grounding zone is defined as the transition of a glacier from fully grounded to freely floating conditions and may be several tens of km wide (between F and H in Figure 3.1, Fricker et al. 2009). Across this boundary, the controlling ice flow mechanisms change from vertical shear in the grounded part to longitudinal stretching and lateral shear where the ice is floating (Pattyn et al. 2006; Schoof 2007). Furthermore, the overall mass balance of the glacier is altered dramatically as the basal melting underneath the grounded ice due to frictional and geothermal heat increases from cm to m magnitude per year as the base comes into contact with relatively warm ocean water (Jenkins et al. 2006). Studies often refer to the grounding line, which is the point where the glacier begins to float (Schoof 2007, G in Figure 3.1). The magnitude of ice flux across a glacier's grounding line constitutes an important control on glacier mass balance, and changes in this flux may lead to dramatic thickness changes of the upstream ice (section 1.3, Rignot 2008). Studies have found that both oceanic basal melting and ice flux are positively correlated with and highly sensitive to ice thickness at the grounding line (Rignot and Jacobs 2002; Schoof 2007). The behaviour of the ice across the grounding zone is further complicated by the tidal influence which continuously migrates the grounding line and flexes the ice within the grounding zone (Sykes et al. 2009, Figure 3.1).

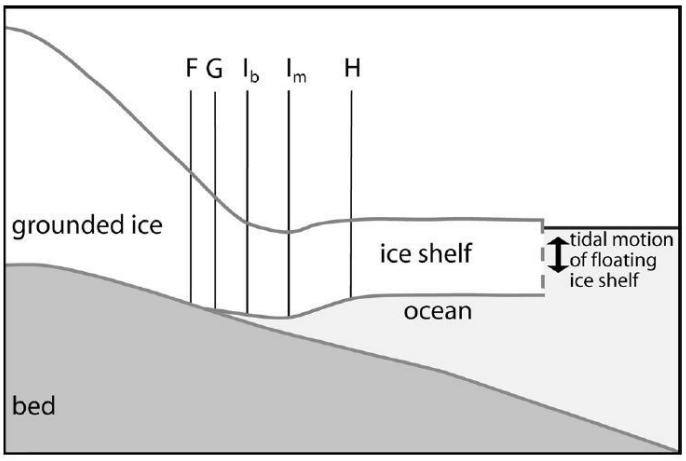

Figure 3.1. Identifying features that may occur across the grounding zone which extends between the landward (F) and seaward (H) limit of tidal flexing. The latter of which also represents the landward limit of hydrostatic equilibrium. G is the grounding line, I_b the break-in-slope and I_m the local elevation minimum (Fricker et al. 2009).

The location of a grounding line is determined by sea level, oceanic melting at the grounding line, the buttressing effect of downstream ice shelves and ice flux at the grounding line (Goldberg et al. 2009; Katz and Worster 2010; Schoof 2007). The latter depends on upstream SMB and ice flow dynamics which are also influenced by basal conditions, ice viscosity and bedrock topography. Over rough bedrock, several stable grounding line positions may exist for a certain combination of the influencing factors, as the glacier can undergo hysteresis. However, most studies agree that grounding lines are inevitably unstable on upward-sloping beds as an upstream retreat will result in an increase in ice thickness at the grounding line and hence ice discharge across it, acting as a positive feedback mechanism (Goldberg et al. 2009; Katz and Worster 2010; Pattyn et al. 2006; Schoof 2007; Weertman 1974). Conversely, this mechanism can result in rapid grounding line advances when conditions are favourable and the ice is grounded on an upward-sloping bed. Radar measurements of bedrock topography upstream of glacier grounding lines consequently provide valuable information about grounding line stability.

Direct measurements of grounding line locations are sparse and their positions are often determined remotely by applying various satellite techniques to either identify the break-in-slope, the change in velocity field or the limits of tidal flexing, all of which are features which often characterises the grounding zone (Figure 3.1). As this is a gradual transition, however, it is often difficult to accurately pin-point the grounding line, and estimates of grounding line position of for example the Evans Ice stream have differed by as much as 100 km depending on the method of choice (Fricker et al. 2009; Sykes et al. 2009). Ice thickness at the grounding line is often estimated from the surface elevation and the assumption that the ice is in hydrostatic equilibrium. This technique carries some uncertainty since DEMs are often inaccurate close to the break-in-slope if the terrain is steep and studies have shown that the ice surface may be depressed below equilibrium downstream of the grounding line (Fricker et al. 2009; Jenkins et al. 2006). Therefore, in order to further understand the mechanisms which determine grounding line changes, direct observations of grounding line locations and ice thicknesses are essential.

3.2 Data collection

Between 15 November and 15 December 2008, 300 km of GPR data were collected on the DHGS (Figure 3.2). In addition, in January 2009 an aerial radar survey completed as part of the IPY ICECAP project collected measurements along the centre flow-lines of the two glaciers as well as in the upper catchment areas.

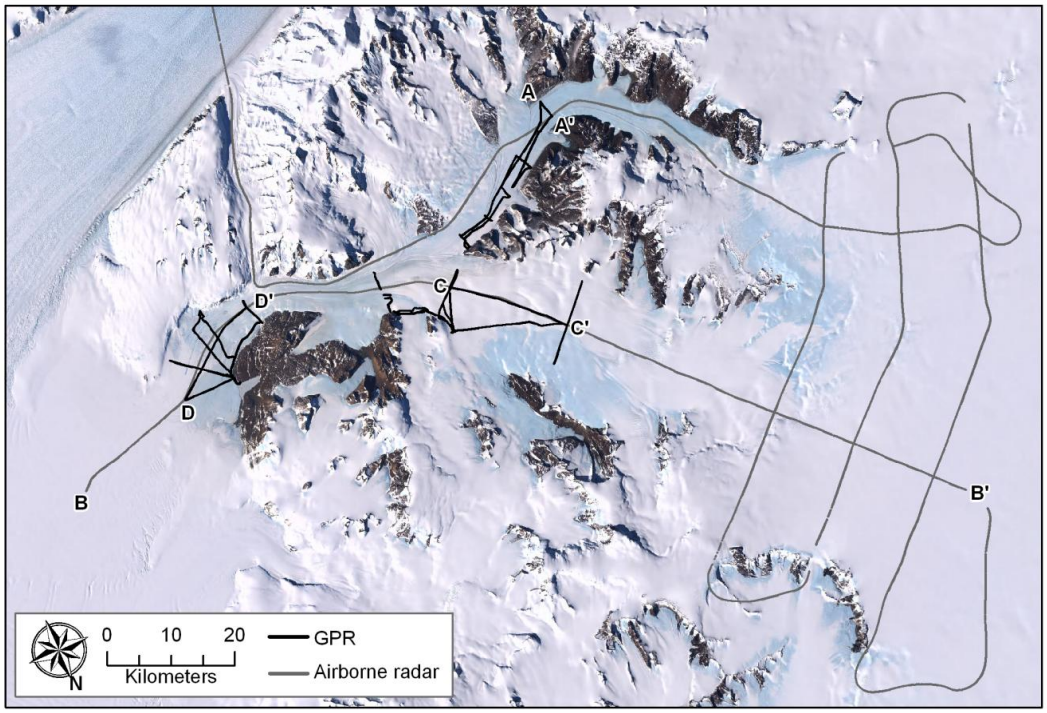

Figure 3.2. GPR survey tracks (black) and airborne radar flight path (grey). The start (e.g. A) and end (e.g. A') of transects referred to in the text are shown with capital letters.

3.2.1 Ground penetrating radar measurements

For the GPR survey, a new pulseEKKO PRO radar system was used in combination with an older set of unshielded resistivity loaded dipole antennas with a centre frequency of 25 MHz, both manufactured by Sensors and Sofware Inc. The pulseEKKO PRO radar system consisted of a separate receiver and transmitter connected to a Digital Video Logger (DVL) control unit by fibre optic cables which minimise noise from nearby conductors. The radar was run with a common-offset antenna configuration with an antenna separation of 3 m. The receiving and transmitting antennas were resting on the plastic skis of a purpose-built sled, oriented parallel to the direction of travel for practical reasons (Figure 3.3). Because of the directional character of the energy emitted by resistivity-loaded dipole antennas, GPR antennas should generally be oriented perpendicular to the direction of travel, so that the highest energy is focussed along the profile (Annan 2009). However, studies have found that when conducting a GPR survey on glaciers, the best penetration depth is expected when antennas are oriented parallel to the direction of ice flow, as this setup minimises the energy loss caused by the presence of surface crevasses (Navarro et al. 2005; Nobes 1999). The antenna setup chosen for the fieldwork consequently is ideal in relation to crevasse-orientation when travelling along the centre flow-line of the glaciers. However, increased scattering from crevasses and therefore decreased penetration depth were likely for profiles perpendicular to the ice flow direction as it was not practically possible to change between antenna setups. Surface contact of the sled was good

when travelling on snow but less so on the blue ice where the uneven surface resulted in severe rattling of the radar system during data acquisition. Great care was taken in limiting the influence of nearby conductors on the measurements, and no metal was used in the construction of the radar sled. Furthermore, the sled was towed 2 m behind a wooden Nansen sled carrying the DVL, GPS and batteries. The Nansen sled in turn was towed 6 m behind a snowmobile.

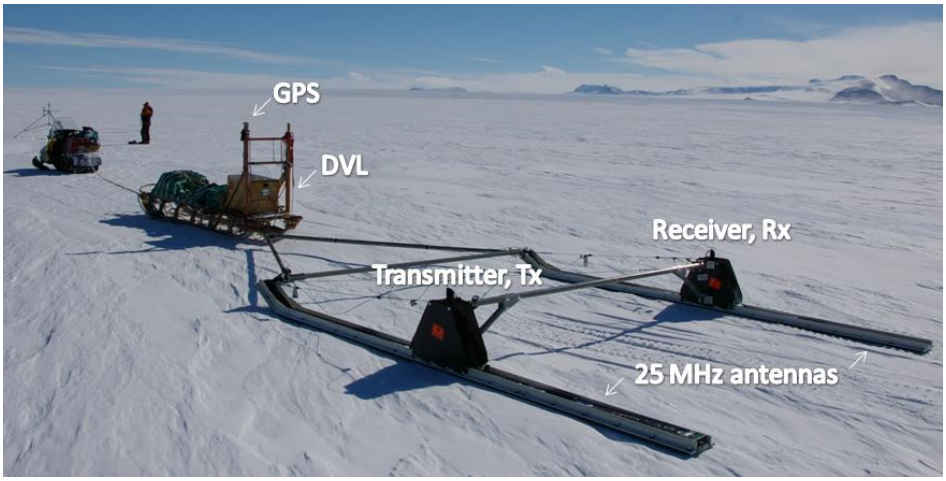

Figure 3.3. GPR data collection setup (Photo: M. Riger-Kusk).

An odometer wheel was initially employed to ensure a constant distance between ice thickness measurements (traces). However, despite attempts to increase the grip of the wheel, distance measurements proved unreliable on the icy surface and radar measurements were collected in continuous mode instead. The pulseEKKO DVL enables real time data display with basic processing (gain and DEWOW) and the length of the time window was regularly adjusted during data acquisition to enable the maximum number of individual measurements for specific measured ice thicknesses. Individual measurements were automatically stacked 4 times to improve the signal to noise ratio of the recorded trace. The towing snowmobile travelled with relatively constant speeds of between 6 and 10 km h^{-1} and stacked radar measurements were collected at intervals of approximately 1.5 to 3 metres, depending on both the travel speed of the snowmobile and the length of the time window. The GPR system configuration is shown in Table 3.2.

The radar system was connected directly to a Trimble GeoXM GPS (L1 only) which recorded positions to its internal memory every second as well as outputting position-stamps to the radar control unit every 5th trace. The GPS has a horizontal accuracy of between 1 and 3 m.

Table 3.2. GPR system configuration.

Transmitter voltage	1000 V
Antenna centre frequency	25 MHz
Antenna separation	3 m
Number of stacks	4
Sampling interval	3200 ps
Time window	12080 - 16960 ns
Points per trace	3775 - 5300

Despite real time basic processing of the radar traces during collection, basal reflections were weak and often not observed. In order to improve the chances of identifying weak reflections in the radargram, data collection was stopped every 1-2 km and the radar was left running for a period while stationary. These periods of stationary data collection were averaged during the following data interpretation in order to eliminate background noise at these locations.

3.2.2 Airborne radar sounding

In January 2009, a coherent radar onboard a fixed-wing aircraft was used to collect airborne measurements of ice thicknesses in the Darwin-Hatherton area as part of the IPY ICECAP project (D. Blankenship, unpublished, Figure 3.2). The flight tracks in the DHGS area were planned and adjusted in collaboration with UTIG (the University of Texas, Institute for Geophysics) in accordance with the ground-based GPR survey. The airborne measurements have been made fully available for use in this research (Appendix A.1). The transmitted pulse for the airborne survey had a centre frequency of 60 MHz with a 15 MHz bandwidth, which was converted by the receiver to an output signal ranging from 2.5 to 17.5 MHz. The measurements were not migrated, resulting in an effective horizontal along-track resolution of approximately 100 m. Positions of the radar traces were measured using a coarse acquisition code GPS (one frequency only). Further information on the radar equipment and setup used for the airborne radar survey can be found in Peters et al. (2005).

The airborne radar system measured ice thickness approximately every 20 m along a 650 km survey line, focussing on the centre flow lines of the DHGS and the upper catchment area. The coherent radar has a lower vertical resolution, but a higher penetration depth than the 25 MHz GPR setup and provides valuable information on ice thickness in the deepest areas of the DHGS where the GPR was unable to detect a basal reflection. The airborne radar measurements were processed and interpreted by UTIG.

3.2.3 GPS measurements of ice velocity

For the measurements of ice velocity, a repeat GPS survey of temporarily installed bamboo stakes was undertaken along Darwin Glacier cross profiles and the centrelines of the Darwin and Hatherton Glaciers. Static GPS measurements were conducted using Trimble 4700 receivers (L1 and L2) in fast static mode for postdifferential processing. Because of the expected low ice velocity and the limited time for the field survey, local base stations were installed on rocks at Roadend Nunatak, Lake Wellman, and Lake Wilson (Figure 3.5). Stake positions were recorded for 30 to 35 minutes at a 1 Hz data rate, and most of the stakes were re-measured after 3-5 days. The distance between base and field stations was, for the majority of the points, well below 20km.

Figure 3.4. GPS measurement setup on the glacier surface (Photo: W. Lawson).

The positions of the base stations were determined using the nearest two POLENET GPS Network stations at Butcher Ridge (79.1474° S, 155.89416° E) and Westhaven Nunatak (79.8457° S, 154.22012° E, http://facility.unavco.org/data/ftp.html). In addition, all base stations were postdifferentially corrected using the Automatic Precise Positioning Service (APPS; available at http://apps.gdgps.net/, making use of JPL's GIPSY-OASIS software Version 5), which resulted in an improved positional accuracy. All fast static points were analysed in Trimble Geomatics Office using a network analysis which included all available base stations within 100 km distance. The performance specification for horizontal precision with the chosen settings and a minimum of 5 continuously tracked satellites was ±5 mm + 1 ppm x baseline length (http://www.trimble.com/PRODUCTS/PDF/4700specs.pdf).

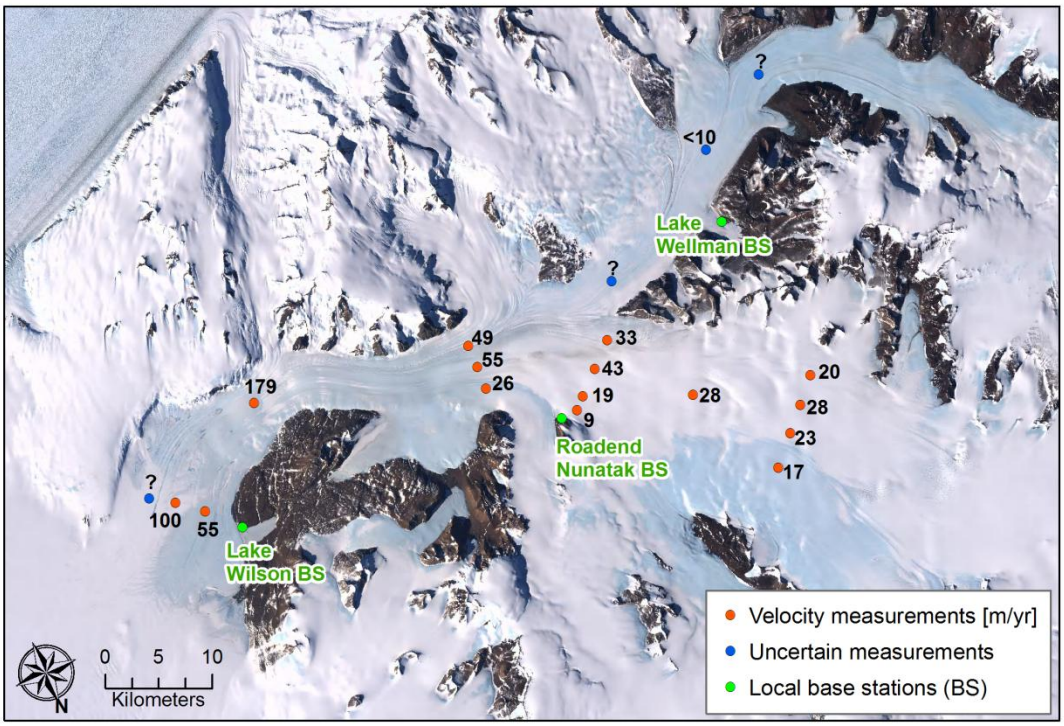

Figure 3.5. Position and magnitude of surface ice velocity measurements as well as the location of local base stations. Measurements have been extrapolated to yearly values.

On the Hatherton Glacier, the re-measurement time was only 2 days, and the measurement closest to the Lake Wellman base station was the only data point of a high quality. The measurement is uncertain though, as ice velocity is at the detection limit for the GPS setup. Various processing methods (with up to three base stations and, with and without network adjustment) yielded velocities of 2.3 – 11.8 m yr^{-1} in directions between north and east. The highest directional accuracy for ice flow (+23° compared to visible flowline) was achieved for the lowest velocity value using only the Lake Wellman base station during processing (2.3 ±6 m yr^{-1}; error accounting for a baseline length of 7 km and antenna/pole uncertainty). Therefore, from these measurements it is inferred that the mid-Hatherton Glacier travels with velocities of less than 10 m yr^{-1} (Figure 3.5).

3.3 Processing and accuracy of the GPR data

Considerable processing was required in order to facilitate and reduce the uncertainty of the GPR interpretation (Figure 3.6). Processing of the GPR data was done in EKKO_View Deluxe, the processing software developed by Sensors and Software Inc. for data collected with pulseEKKO radars. All interpretations were subsequently carried out in the seismic interpretation software KINGDOM (Seismic Micro-Technology).

3.3.1 GPR processing

As mentioned in Section 3.2.1, positions were recorded every 5th trace resulting in a location stamp every 7.5 – 15 m. GPS locations were added in EKKO_View Deluxe which automatically interpolates between GPS measurements so that each trace is assigned a unique position. In general, satellite coverage was good and a sample subset of 13315 raw GPS measurements (one GPS file from each day of data collection) shows an average of 7.9 satellites and an average horizontal dilution of precision (HDOP) of 1.21. The positioning of each individual measurement in relation to adjacent points is, however, much more accurate than the absolute positions (1-3 m accuracy), and was calculated as 0.10 ±0.05 m from GPS positions recorded during stationary periods. Base station data does not exist for all periods of GPR data collection, and as the horizontal resolution of the raw GPS positions is smaller than that of the horizontal resolution of the GPR (section 3.2.3), the GPS positions were not differentially corrected.

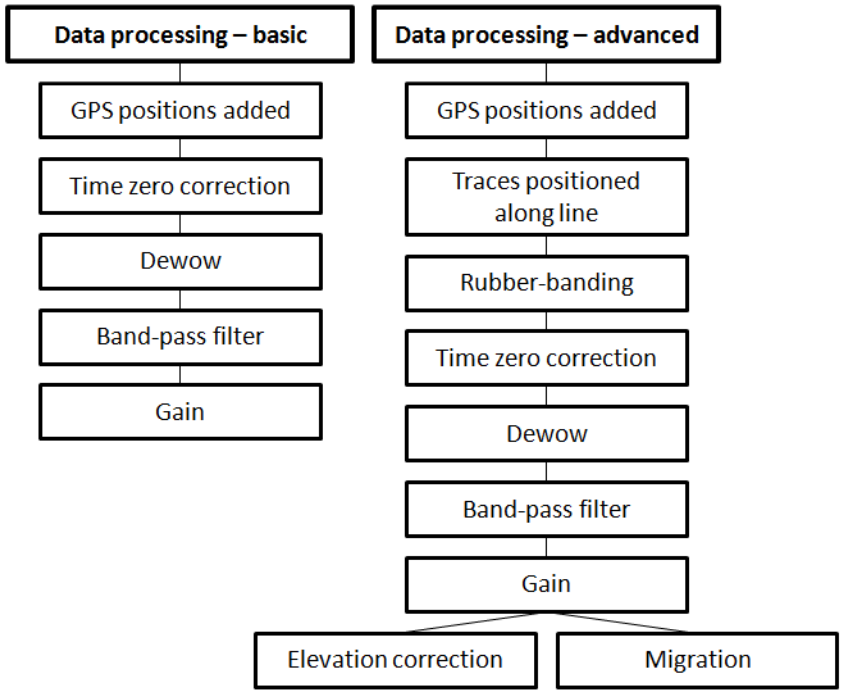

Figure 3.6. Examples of basic and more advanced processing flow. Most profiles were processed using the basic processing routine while more advanced processing was required for cross profiles (rubber-banding + migration), profiles used in the analysis of vertical changes in radar wave velocity (rubber-banding) and for illustrative purposes (rubber-banding + elevation correction).

For most of the GPR data, no further processing of GPS positions of the traces was required. However, for the analysis of radar wave velocity and firn correction (section 3.4) and when

migration is required, the traces have to be arranged at regular intervals along a straight line. Due to variations in the snowmobile travel speed, traces were collected at irregular sampling intervals. Furthermore, although great care was taken in following straight survey lines, the presence of crevasses at the surface necessitated some adjustments to the bearing during data collection. Some manipulation of the trace positions is therefore necessary in order to position them along a straight line. Two different approaches were taken to do this depending on the purpose of the investigation. For cross profiles, where the results would be used for calculations of cross section areas, each trace was projected onto the best fit straight line (method a in Figure 3.7) to maintain an accurate length of the cross section. All other profiles were corrected by maintaining the actual stepsize and 'stretching' the profile to a straight line (method b in Figure 3.7). Method b is thought to enable more accurate results when investigating reflection hyperbola shapes (section 3.4) as the distance between traces is maintained. For both methods, stepsizes smaller than 0.25 m were assumed to be related to GPS inaccuracy when stationary and assigned a stepsize of 0.005 m, the minimum allowed by the EKKO_View Deluxe software.

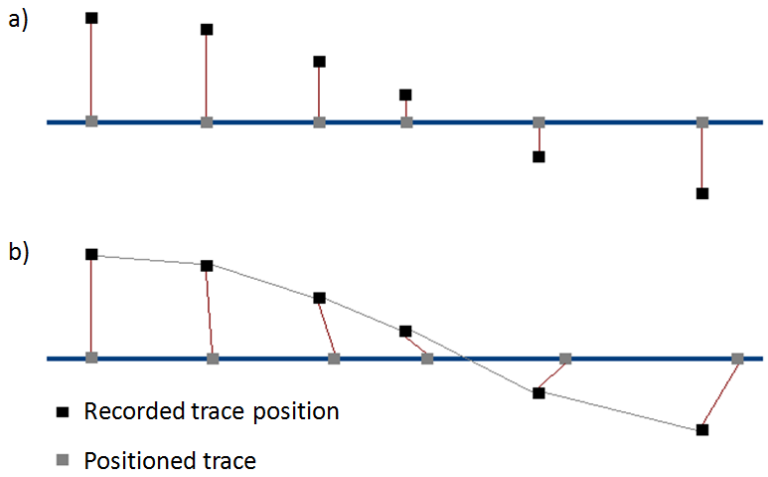

Figure 3.7. Illustrations of the two different approaches used for positioning traces along a straight line.

After assigning GPS positions to each GPR trace, rubber-banding was applied to eliminate stationary events and arrange radar traces at 2 m intervals. The assigned 2 m stepsize is similar to the actual distance between measurements so as to retain as much of the original data as possible. In places where measurements are more than 2 m apart, rubber-banding interpolates new traces, while traces are skipped when spaced less than 2 m apart. An example of the effect of rubber-banding can be seen when comparing the upper two radargrams in Figure 3.8. No noticeable discontinuities in reflectors were observed following

rubber-banding for any of the profiles, and the processing step is assumed to accurately place and interpolate traces along the survey lines.

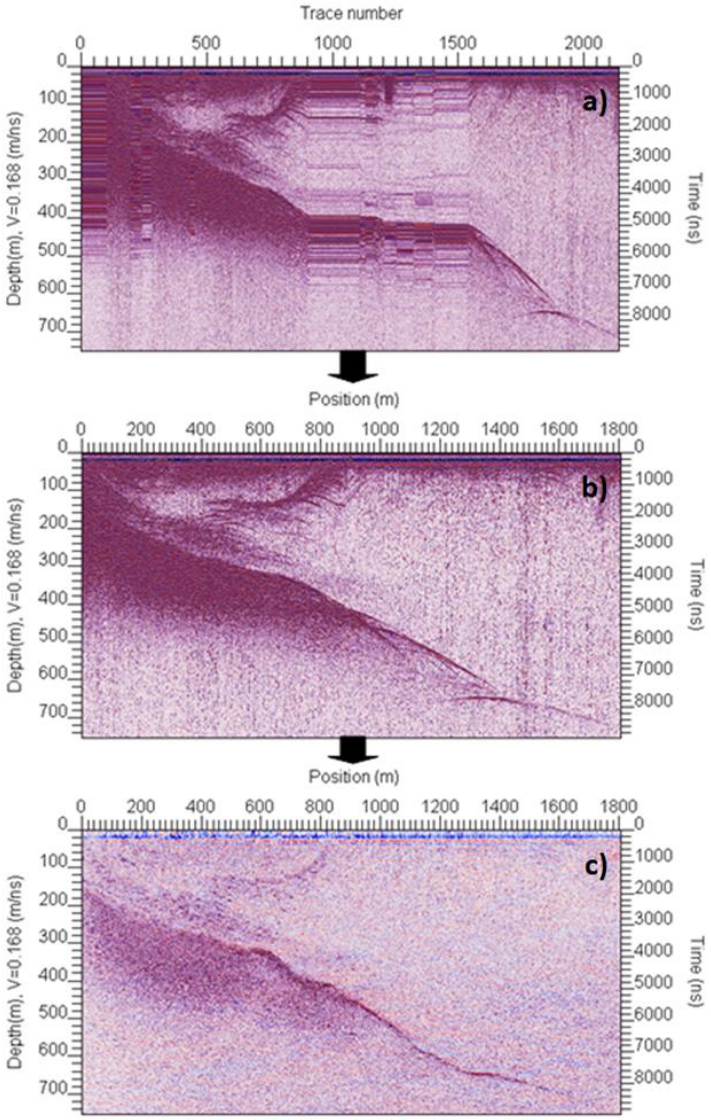

Figure 3.8. Example of a GPR profile at different stages of processing: (a) after basic processing and with the stationary events still present, (b) after rubber-banding and (c) after migration. The profile is located between A and A' in Figure 3.2.

After positioning the traces, all profiles were corrected for a potential drift in time zero and subjected to a Dewow and bandpass filter. The bandpass filter was chosen so that frequencies between 5 and 40 MHz were left unaltered while the influence of frequencies outside this range were gradually decreased towards 0 and 60 MHz. Frequencies above 60 MHz were completely removed from the data. Gain was subsequently applied to the traces using either a

SEC (spreading and exponential compensation) or AGC (automatic gain control) function depending on the nature of the following analysis. More advanced processing involved rubber-banding (described above), migration (for cross profiles with steeply sloping basal reflectors) and elevation correction (Figure 3.8).

In areas where a vague or no basal reflection was observed following processing, radar traces collected during stationary events were averaged in an attempt to improve the signal-to-noise ratio. This approach was a significant aid in accurately detecting the ice-bed interface in regions of weak reflections and on several occasions, a reflection was detected which would otherwise have been below the level of the background noise.

3.3.2 Accuracy of radar measurements

The overall accuracy, with which the depth to reflectors is determined, depends on the accuracy of the radar system and setup, the applied processing routine and subsequent interpretation, and the radar wave velocity assigned to convert from time to depth. The magnitude of error associated with the radar system, processing and interpretation will be considered is this section. Methods applied to reduce the error caused by variations in radar wave velocity will be investigated in section 3.4.

Radar theory predicts a vertical resolution of one-quarter of the pulse wavelength, which is a function of the radar wave velocity and the centre frequency of the transmitted wave (Annan 2009). However, in reality the vertical resolution of GPR systems has been found to vary between one-third to one-half of the wavelength (Plewes and Hubbard 2001) and values as high as one and a half wavelengths have been suggested for low frequency antennas such as the ones applied in this study (Eisen et al. 2002). Based on the above, a vertical resolution of between 2 and 10 m is expected for the 25 MHz antennas applied in this study. The horizontal resolution of a radar system depends on the wavelength as well as the distance to the reflector, and equals the Fresnel zone radius (Annan 2009). For the applied GPR system setup (Table 3.2) the horizontal resolution decreases from ~20 m at 100 m depth to ~60 m at 1000 m depth.

The uncertainty of the GPR and airborne datasets can be assessed by comparing the ice thicknesses measured at points where radar profiles cross (distance <10 m). The ice thicknesses recorded at the majority of the crossover points compare extremely well and the differences are generally well below 10 m (Figure 3.9). The basal reflection was strongest for the lower part of the glacial system where the recorded differences in ice thickness are less than 2 m for the GPR measurements. Considerable ice thickness differences of -75 m and -22 m exist for GPR crossover 9 and 12 respectively in Figure 3.9. At these two locations, ice

thicknesses measured for the longitudinal profile are much smaller than for the cross profile which can be explained by a steep bedrock topography. The cross profiles were migrated and hence corrected for the influence of steep topography, whereas more advanced post-processing is required to correct the longitudinal profile. At crossover 12 and 13 the GPR ice thickness exceeds the airborne measurement by 44 m and 64 m respectively. This discrepancy is most likely to be related to the steep surface and ice base topography in this region. The presence of steep reflectors will affect the quality of the airborne radar data more so than the GPR data because of the larger radar beam.

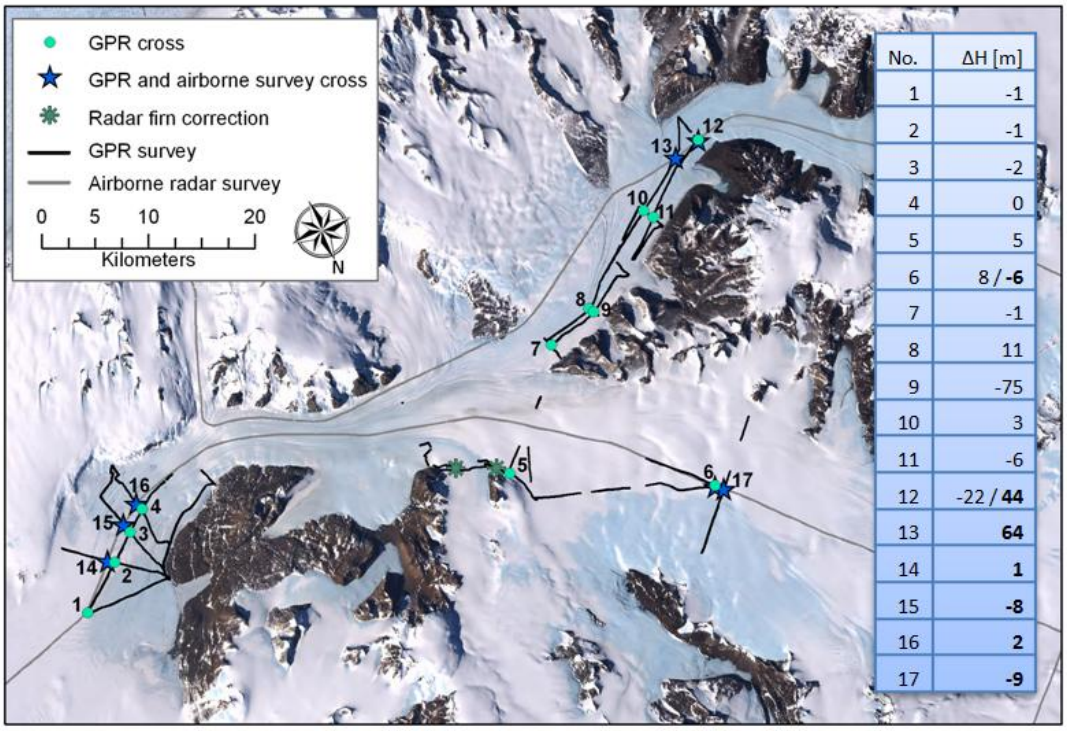

Figure 3.9. Radar profile crossovers (distance <10 m) used to evaluate the uncertainty of the depth measurements and list of corresponding ice thickness differences (ΔH). Comparison between GPR and airborne measurements are shown in the list in bold. Ice thickness differences are negative when the cross profile measurement exceeds that of the longitudinal profile or airborne measurement exceeds that of the GPR. The location of measurements utilised in the firn correction analysis presented in section 3.4.2 are also shown.

The above analysis in ice thickness uncertainties includes both the precision of the actual radar measurement as well as the accuracy of the processing and interpretation routine. The observed discrepancies in ice thickness illustrates: 1. the importance of travel direction on the accuracy of radar measurements, and hence the importance of collecting cross profiles when conducting surveys on glacier, 2. the value of migration as a processing step when measuring steeply dipping surfaces, and 3. the limitation of airborne radar surveys in steep terrain.

Based on the crossover analysis, the uncertainty in ice thickness for the two datasets is thought to be generally no more than 10 m and decreasing to less than 5 meters in regions where the bedrock topography is flat and the basal reflector strong. For regions with steep bedrock topography, the uncertainty in ice thickness may increase significantly. As all cross profiles were migrated and the majority of the remaining measurements were collected away from steep bedrock topography, it is reasonable to assume a general overall uncertainty in ice thickness measurements of less than 10 m.

3.4 Vertical variations in radar wave velocity

An accurate evaluation of radar wave velocity is essential in order to reduce the error when converting measured TWT to ice thickness (section 3.1.1). In regions where the firn layer is thought to have a uniform thickness and density profile, one common mid-point (CMP) velocity analysis is sufficient to accurately determine the vertical velocity profile. In a region like the DHGS, however, where several BIAs are interspersed between snow-covered surfaces, it is clear that the firn layer thickness must vary considerably from zero in BIA to a maximum in accumulation areas without prior history of erosion or ablation. It is therefore important to assess these variations and account for the uncertainties which are introduced as a consequence. In this section, several different approaches to determining the vertical velocity profile and subsequently the correction applied to the GPR data are combined in order to reduce the uncertainty associated with converting from TWT to ice thickness.

3.4.1 Analysis of radar wave velocity

During the fieldwork, one CMP survey was conducted with the 25 MHz antennas near the outlet of the DHGS. However, due to insufficient length of fibre optic cables, it was not possible to obtain an antenna separation large enough to facilitate a reliable velocity analysis of the subsurface and the results have been discarded from the further analysis of radar wave velocity.

An alternative, although less accurate way of obtaining information about the radar wave velocity is to examine the shape of hyperbolas in the radargrams at various TWT (Arcone 2002; Benjumea et al. 2003; Clarke and Bentley 1994). Hyperbolic reflections in radargrams are a result of scattering of the radar wave caused by discontinuities, heterogeneities and sharp folds (Arcone 2002; Clarke and Bentley 1994), and when observed in cold ice often relate to the presence of crevasses or rocks incorporated in the ice.

A total of 69 hyperbolas were identified in various rubber-banded radar profiles located on snow-covered surfaces. Care was taken in choosing only symmetric hyperbolas, which must originate either from a point source or from horizontal linear reflectors crossed by the survey line (Navarro et al. 2005). The average velocity of the firn and ice above the point reflector was determined by fitting theoretical hyperbolas calculated by EKKO_View Deluxe to the observed hyperbolas. The uncertainties associated with this method includes both imprecise positioning of radar traces during rubber-banding which may affect the shape of the hyperbolas, as well as inaccurate fitting of calculated hyperbolas. Through repeat analysis and a comparison between results obtained from traces positioned using method a and b in Figure 3.7, as well as coinciding data collected using the odometer wheel, the uncertainty associated with the velocity analysis was found to be up to ±10 m μs^{-1}.

The wave velocities found by examining the 69 hyperbolas range between 167 and 251 m μs^{-1} (Figure 3.10). Considerable variations exist in the average velocity at certain times, especially in the shallowest regions of the glacier (low TWT). Despite this large variability, the dataset clearly shows that the average wave velocities decreases with depth as expected and eventually approach the velocity of pure ice.

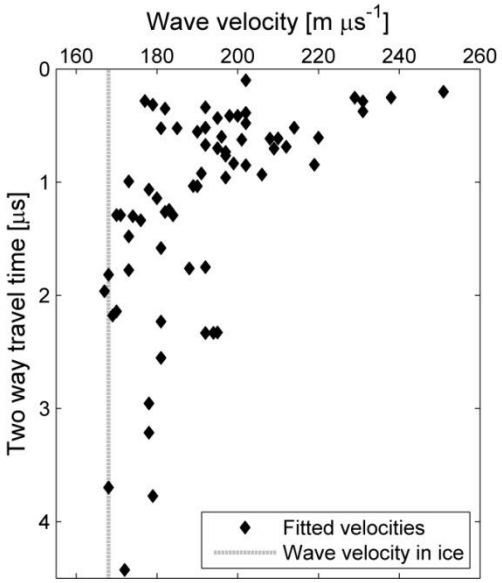

Figure 3.10. Average velocities of the firn/ice above 69 hyperbolic shaped reflections observed at different TWT in the GPR data. The vertical grey line shows the velocity of pure ice (168 m μs^{-1}).

The large spread in average velocities at any given TWT exceeds the uncertainty of ±10 m μs^{-1} and is likely caused by actual variations in density profiles above each reflector. Large spatial

variations in average velocities are expected in an area like the DHGS, where accumulation areas with fully developed firn layers are interspersed with thinner firn layers such as snow-covered ablation areas and accumulation areas downstream of BIA. However, the highest measured velocity of 251 m μs^{-1} far exceeds the radar wave velocities of less than 230 m μs^{-1} previously documented for near surface snow layers (Eisen et al. 2002; Hempel et al. 2000) and therefore cannot be explained by the presence of snow alone. Instead, the high velocities may either be a result of the radar wave travelling through air-filled crevasses (Clarke and Bentley 1994) or could be artefacts caused by point reflectors located to either side of the radar profile (Arcone 2002). Without further data it is not possible to establish the exact cause of the high velocities observed in the dataset.

The large observed spread in average radar wave velocity (Figure 3.10) is inferred to reflect variations in firn layer thickness and density within the study area. These variations are accounted for in section 3.4.2 by applying a variable radar firn correction to the ice thickness measurements (section 3.1.1).

3.4.2 Radar firn correction

The radar firn correction is assessed for the DHGS by combining evidence of maximum radar firn correction from the GPR data with the overall trend in near surface firn densities suggested by van den Broeke et al. (2008), and an assessment of ablation area boundaries from satellite imagery.

For the analysis of maximum radar firn correction, a subset of 25 of the original 69 data points (Figure 3.10) was chosen (Figure 3.11). The 25 hyperbolas originate from five different radargrams collected upstream of any known ablation areas and away from crevasse fields (Figure 3.9), where a fully developed firn layer is thought to exist. The radargrams display clear internal layers in the upper 100-150 m (Figure 3.15) which are likely related to density variations of a thick firn layer (section 3.1.1). The radar firn correction found at these locations is consequently likely to represent a maximum value within the DHGS.

The average radar wave velocities of the subset data range between 168 to 231 m μs^{-1} at TWT of up to 4.4 μs. A moving average filter was applied in order to minimise the level of the noise caused by the uncertainties discussed in section 3.4.1. Figure 3.11 shows that a change in velocity gradient occurs at approximately 1 μs, after which average velocities decrease at a much slower rate. A similar pattern has been documented by several other GPR studies (Clarke and Bentley 1994; Eisen et al. 2002; Hempel et al. 2000) and can be explained by a decrease in firn compaction rates with depth. A linear regression of the averaged data points in the top 1 μs (Figure 3.11) suggests a surface radar wave velocity of 224 m μs^{-1} which,

when using equation 1 in combination with equation 2, corresponds to a snow density of ~400 kg m^{-3}. This compares well with previous measurements of surface snow velocity and density in Antarctica (Eisen et al. 2002; Spencer et al. 2001) and provides confidence in the results. The very low average velocities observed at late TWT in Figure 3.11 are unrealistic if a thick firn layer is present above and are likely caused by the uncertainty introduced by individual data points (±10 m μs^{-1}) for times where few data points exist. In comparison, the upper half of the profile is relatively well constrained.

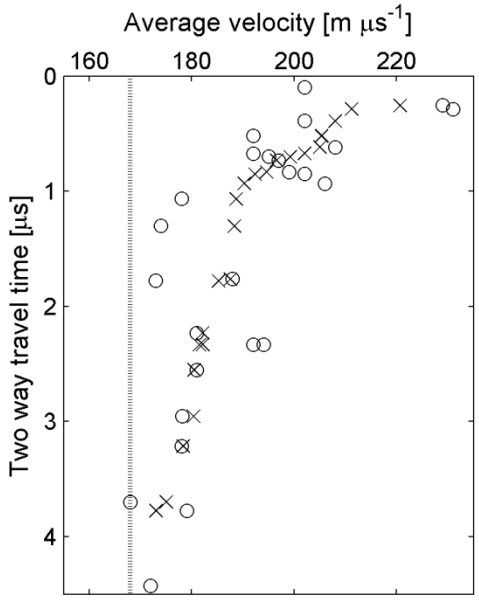

Figure 3.11. The subset of 25 average velocities (circles) and the moving average (spanning seven measurements) calculated from this dataset (crosses). The vertical grey line shows the radar wave velocity of pure ice (168 m μs^{-1}).

The radar firn correction is calculated as the difference between the depth found by assuming a constant velocity of 168 m μs^{-1}, and the depth calculated from the average fitted velocities (crosses in Figure 3.11). The results indicate that a gradual increase in radar firn correction between 0 and 65 m depths after which the correction remains roughly constantly at 11-12 m until 100 m depth. Radar firn corrections suggested by data points at lower depths vary considerably and generally exceed 12 m. As mentioned above, radar firn corrections of up to 15 m have been documented in the interior of the Antarctic continent where calm, cold and dry conditions slows the densification process of the snow (Dowdeswell and Evans 2004; van den Broeke et al. 2008) and it seems unrealistic that the radar firn correction should exceed 12 m in the DHGS accumulation areas.

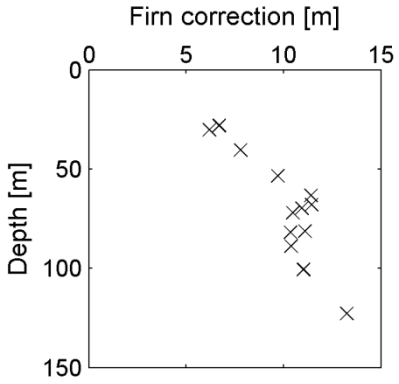

Figure 3.12. Calculated radar firn correction for the uppermost 150 m.

Variations in firn density profiles across the Antarctic continent have previously been investigated by van den Broeke et al. (2008) by combining the output from a regional atmospheric climate model with a firn densification model (van den Broeke et al. 2008). In this study, density differences were represented as changes in air layer thicknesses (h_{air}) defined as the difference between actual ice thickness (H) and the ice thickness if the firn layer was compressed to the density of pure ice (h_{ice}):

$$h_{air} = H - h_{ice} \tag{4}$$

The air layer thickness can be transformed into a radar firn correction (Z) as follows:

$$Z = \frac{\sqrt{\varepsilon_{ice}} - 1}{\sqrt{\varepsilon_{ice}}} h_{air} \tag{5}$$

(Horwath et al. 2006; Jenkins and Doake 1991), where ε_{ice} = 3.18 is the relative permittivity of ice. The air layer thicknesses modelled by van den Broeke et al. (2008) include zero corrections in BIAs, however, to the poor spatial resolution of the regional climate model (55 km), BIAs within the DHGS are not resolved. Within the DHGS, the air layer thickness map predicts values ranging between 9 m at the glacier outlet to 25 m at the polar plateau, equivalent of radar firn corrections of 4 and 11 m respectively. At the locations of the firn correction analysis (Figure 3.9) van den Broeke et al. (2008) calculated an air layer of 16.5 m thickness, which corresponds to a radar firn correction of 7.3 m. The value for firn correction found by van den Broeke et al. (2008) is therefore considerably smaller than the 11-12 m suggested by the GPR data. This discrepancy may be entirely explained by the resolution of the air thickness map, as blue ice areas exist in the immediate surroundings of the two survey locations.

Despite the uncertainties associated with the derived radar firn corrections, the result is more accurate at the survey locations than the average value predicted by the air layer thickness map within 55 km grid cells. However, as the air layer thickness map illustrates the general trend of the region, the two datasets can be combined with advantage to produce a map of radar firn correction which can be used to correct all measurements of ice thickness. The air thickness map was converted to a radar firn correction map using equation 5 and synchronised with the GPR results by adding a constant value of 4.7 m, which is the difference between measured radar firn correction (12 m) and the radar firn correction map (7.3 m) at this location. A constant shift of the entire map is justified by the poor spatial resolution of the gridded dataset leading to overestimations of radar firn corrections in BIAs and therefore a likely underestimation in nearby accumulation areas.

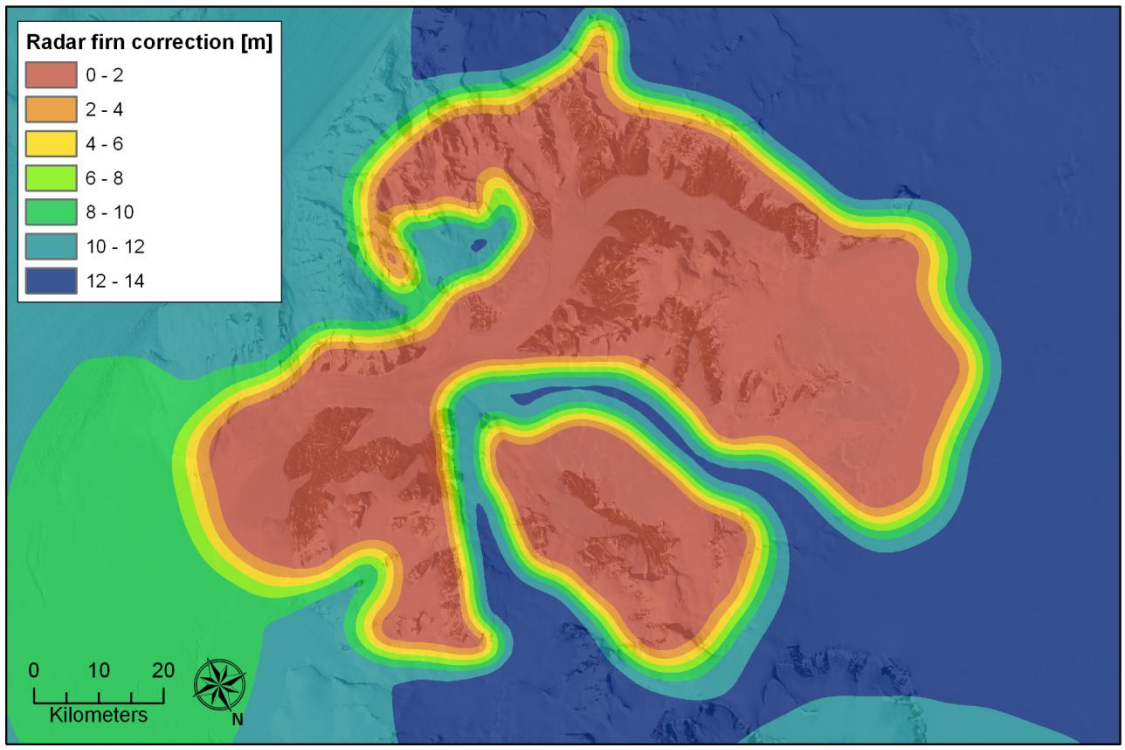

Figure 3.13. Interpolated map of radar firn correction for the DHGS.

The BIAs and rock outcrops were delineated from satellite images and a 5 km transition zone was introduced between regions of zero firn correction and values predicted by the adjusted radar firn correction map. The transition zones were extended to 15 km immediately downstream and upstream of major BIAs to account for snow-covered ablation areas (upstream of BIAs) and a more gradual increase of the firn layer thickness downstream of BIAs. The radar firn correction for the transition zones were interpolated in ArcMap using a

standard inverse distance weighted interpolation and the map was subsequently smoothed by calculating mean values within 3 km radius circles. The final result produces radar firn corrections ranging between 9.2 m at the glacier outlet to 13.6 m in the upper accumulation areas Figure 3.13. In section 3.8.4 it will be shown that the map accurately depicts surfaced conditions at the glacier outlet.

Although considerable uncertainties are associated with the construction of the radar firn correction map, it constitutes an informed assessment of the glaciological conditions of the DHGS, which will reduce the error associated with transforming TWT to measurements of ice thickness from the velocity of pure ice.

3.5 Ice thickness and bedrock topography

Variations in the ice thickness and bedrock topography within the DHGS will be investigated in this section by combining the GPR measurements with the airborne radar data. The two surveys complement each other well with the GPR offering detail and accuracy while the airborne survey has a better coverage and a higher penetration depth (section 3.1).

3.5.1 Cross sectional shape of the DHGS

The shape of the glacier valley provides evidence of the erosional power of the glacier and to some extent the basal conditions. In order to accurately resolve the DHGS valley shape, several GPR cross profiles were collected during the radar fieldwork. However, although a basal reflection was detected in most GPR profiles following processing, reflections were often weak and occasionally disappeared entirely when ice thicknesses exceeded ~700 m. As a consequence, gaps exist in the ice thickness measurements along most glacier cross profiles (Figure 3.14). Because of the high penetration depth of the airborne radar system, a basal reflector was observed in all traces (Figure 3.2).

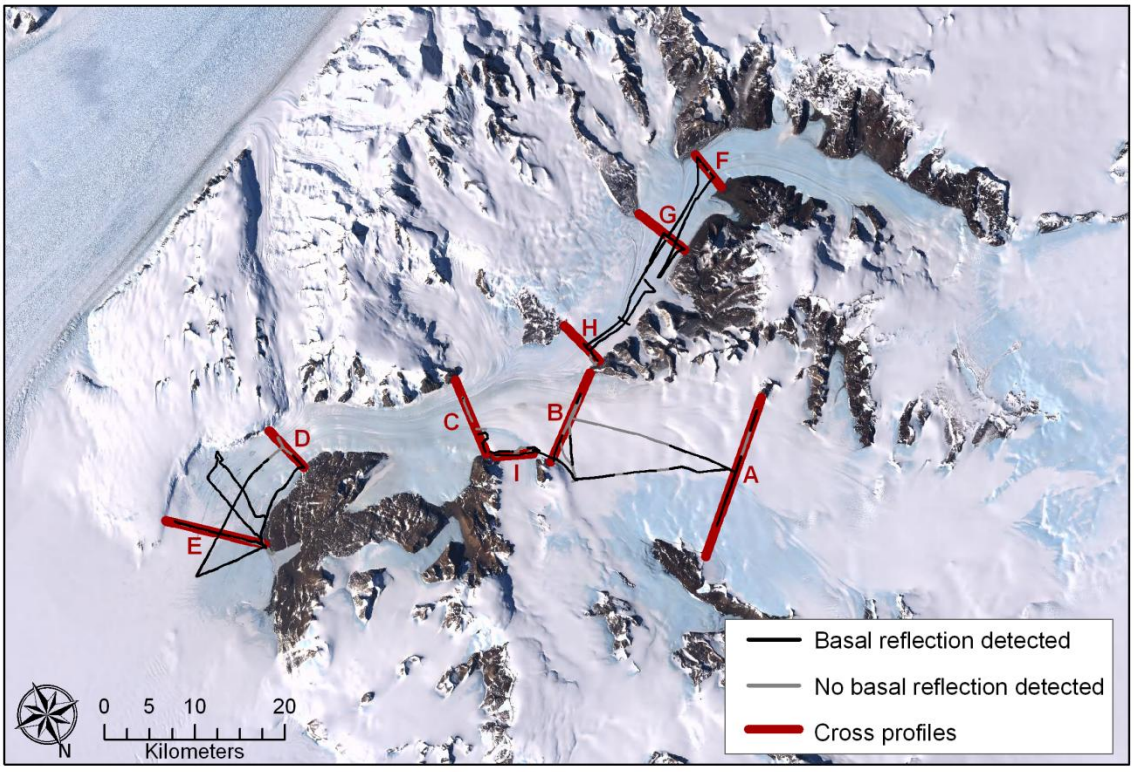

Figure 3.14. Map showing the GPR profiles where a basal reflection was detected as well as cross profiles mentioned in the text and shown in Figure 3.15 (profile I) and Figure 3.16 (profiles A to H).

The GPR profile collected across the Touchdown Glacier (profile I in Figure 3.14) was the only cross profile where ice conditions enabled a near complete transect and a continuous bedrock reflection was observed in the radargram (Figure 3.15). The thickness of the glacier at this profile is approximately 800 m in its deepest parts and the valley is particularly steep towards its true right margin (at 3500 – 4300 m distance). The profile shows a simple U-shaped valley which is typically associated with regions of considerable glacial erosion caused by warm-based conditions and basal sliding. The Touchdown Glacier valley shape is consequently indicative of present or past periods of warm-based conditions. Dipping internal reflections, although obscured to some extend by the applied gain and migration, are indicative of a change in the firn layer across the glacier. Evidence of this change can also be seen on satellite imagery as ice is exposed at the surface towards the true right margin, whereas the firn layer is likely fully developed towards the true left margin (at 0 – 2000 m distance).

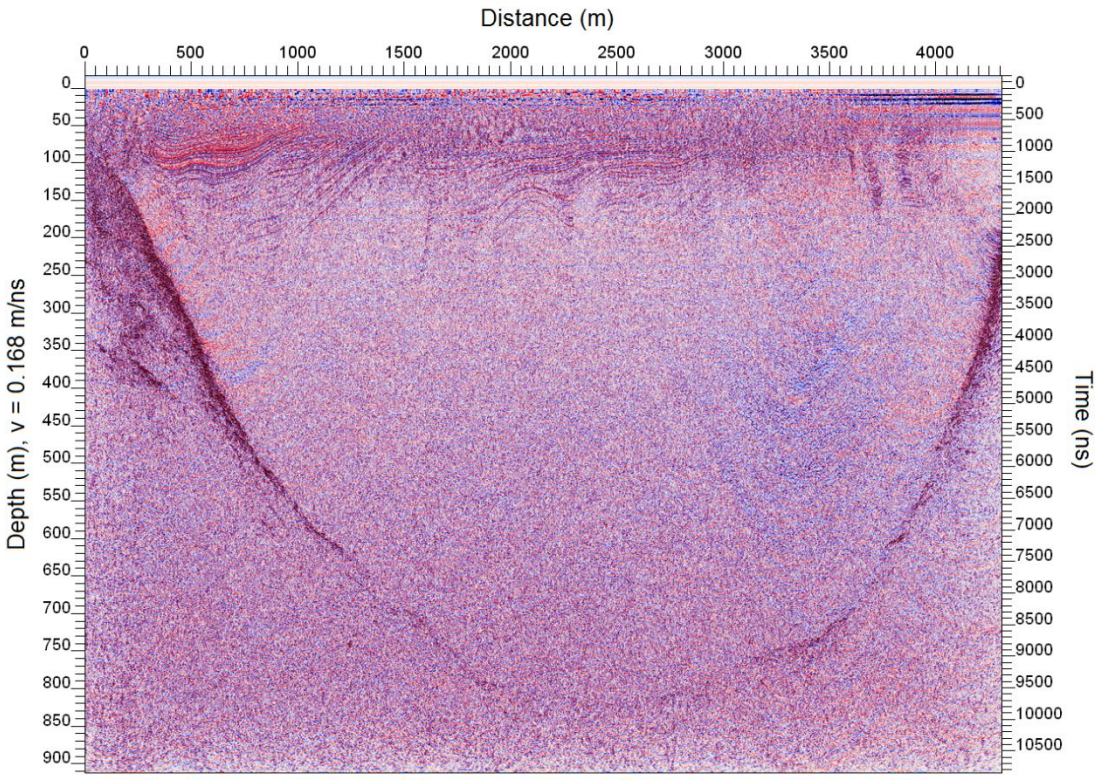

Figure 3.15. Radargram collected on the Touchdown Glacier (cross profile I on Figure 3.14) looking down glacier (north-westerly direction). The profile has been migrated (advanced processing in Figure 3.6). Hyperbolic shaped reflections present in the beginning of this profile (at 0 - 2000 m distance) prior to migration were included in the firn correction analysis described in section 3.4.2.

Other cross profiles are incomplete either due to impassable surface conditions or an undetected basal reflection (Figure 3.14). In order to create continuous cross profiles, the GPR measurements were combined with the airborne radar data and information on the glacier margin from satellite images, after which a cubic spline interpolation was used to interpolate ice thicknesses across data gaps (Figure 3.16). In addition, a DEM was used to guide and validate the valley shape found by the interpolation routine (Graf 1970; Stearns 2007).

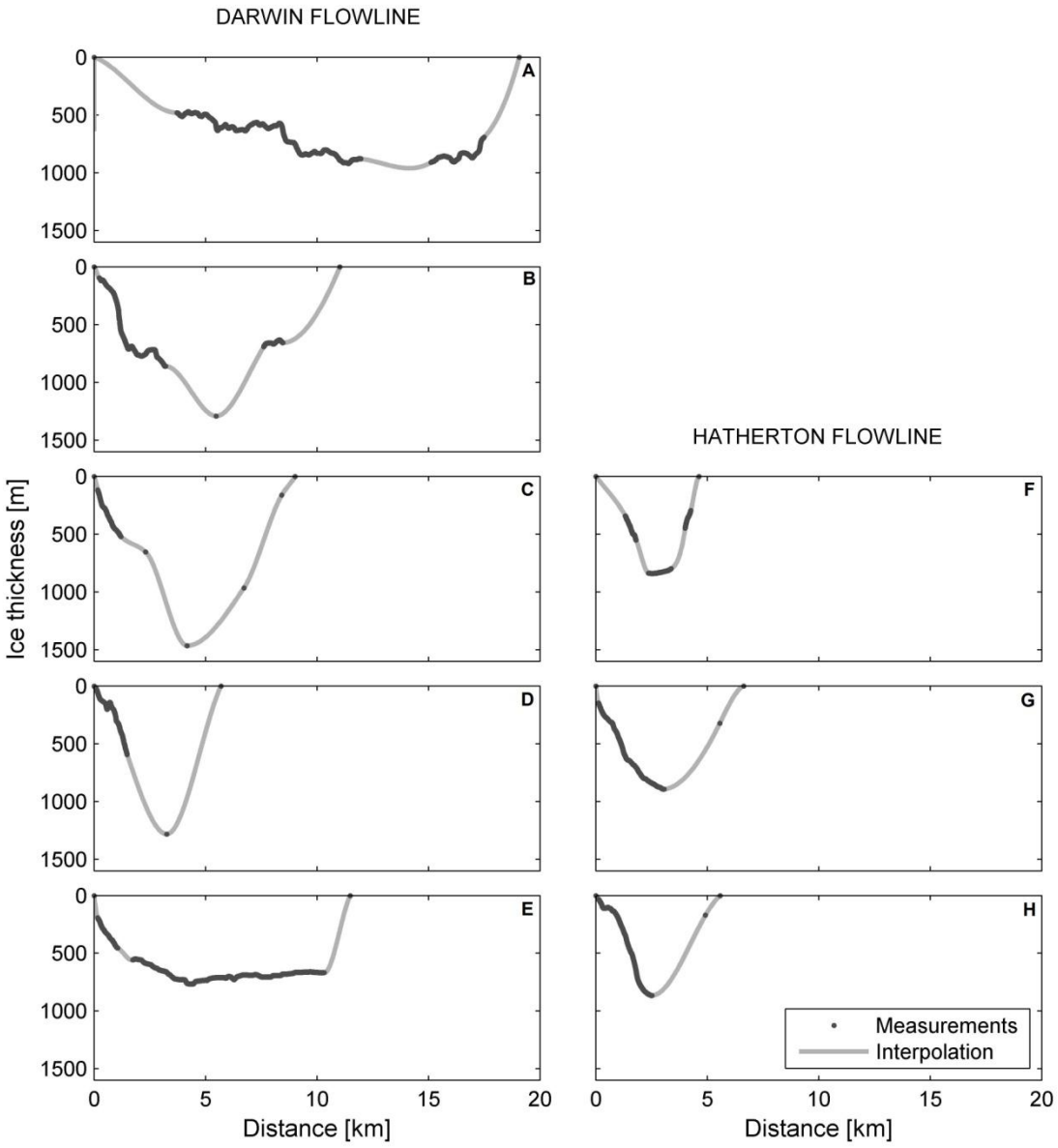

Figure 3.16. Variations in cross sectional shape of the Darwin and Hatherton Glaciers as determined from ice thickness measurements and a cubic spline interpolation routine. View is down glacier (easterly direction) and distances are from the true left glacier margin. The locations of the profiles are shown in Figure 3.14.

Compared to profile I (Figure 3.15), profiles A to G generally have a more complex valley geometry (Figure 3.16). Profiles A, B and C on the Darwin Glacier all have at least one major glacial bench at about 550-700 m depth, which is consistent with glacial tributaries joining the main glacier trunk. A general downstream change can be observed in the Darwin Glacier valley shape (profiles A to D), from a broad but relatively shallow basin with an irregular floor in the upper regions to a narrow and deeply incised trough in the lower parts. A similar pattern has been documented for the Taylor Glacier and is thought to reflect a gradient in glacial erosion

downstream and may be indicative of present or past warm-based conditions in the thickest regions (Kavanaugh et al. 2009b). At the lowermost profile on the Darwin Glacier (profile E) an almost horizontal basal reflection was observed between distances of 5 and 10 km. This characteristics base shape suggests that the glacier is detached from the bedrock and experiencing significant oceanic subglacial melting (section 3.8). Compared to the Darwin Glacier profiles, little change occurs downstream in the Hatherton Glacier valley shape.

Table 3.3. Calculated cross section areas for the profiles shown in Figure 3.14.

Cross profile	Cross section area [km^2]
A	12.17
B	8.03
C	7.31
D	3.93
E	6.97
F	2.24
G	3.65
H	2.45
I	2.62

The glacier cross section areas vary from 12.17 to 3.93 km^2 on the Darwin Glacier, and from 2.45 to 3.65 km^2 on the Hatherton Glacier (Table 3.3). The calculated areas depend strongly on the accuracy of the interpolated ice thicknesses and the cross section areas of profiles B, C, D, G and H are uncertain due to large gaps in recorded ice thickness (Figure 3.16). The interpolation routine generally predicts relatively narrow glacial troughs, and may therefore underestimate the cross section area for profiles where the largest ice thicknesses rely on one measurement only (profiles B, C and D). However, despite these uncertainties, the calculated cross sectional areas clearly illustrate one of the differences which exist between the Darwin and Hatherton Glaciers. While the Hatherton Glacier cross sectional area remains relatively constant, the cross sectional area of the Darwin Glacier decreases rapidly between profiles A and D as the ice velocity increases downstream (Figure 3.5). This change will be investigated further in section 3.9.

3.5.2 Longitudinal ice thickness of the Darwin Glacier

The undulating bedrock topography which exists underneath the Darwin Glacier is best illustrated by the continuous airborne radar profile located between the letters B and B′ in Figure 3.2. This radar profile was combined with the Altimeter DEM (section 2.2) and the

detailed analysis of the grounding zone presented in section 3.8 to construct an illustration of the longitudinal variations in ice thickness and bed topography of the Darwin Glacier (Figure 3.17).

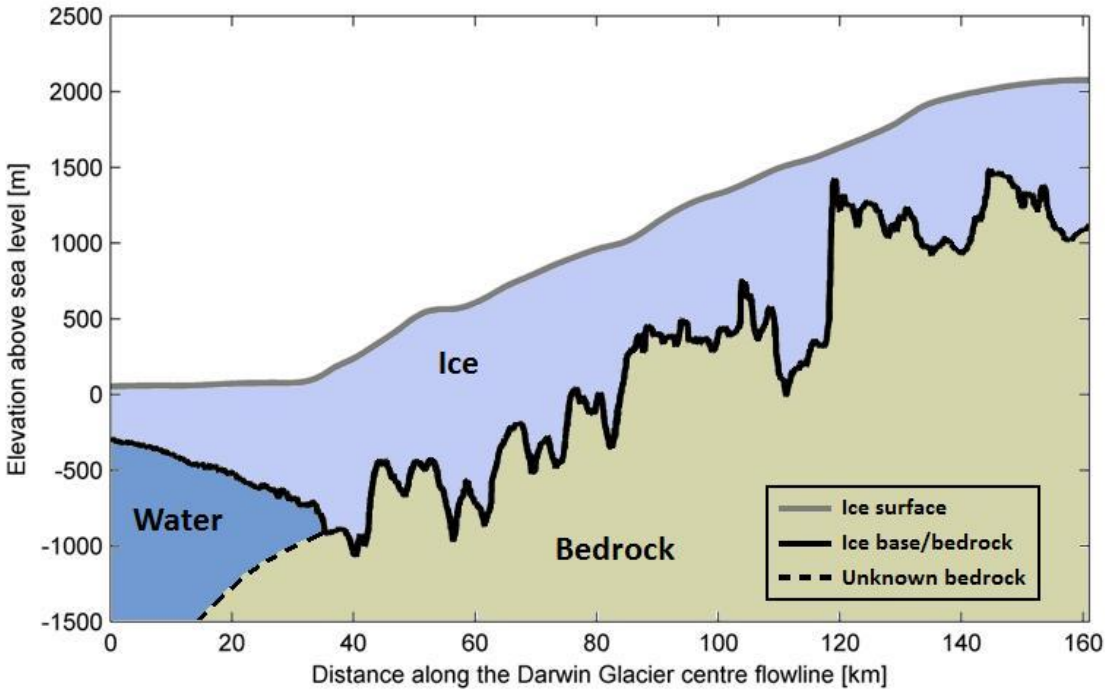

Figure 3.17. Longitudinal variations in ice thickness and bedrock topography of the Darwin Glacier from airborne radar data collected along the B-B' profile shown in Figure 3.2. The raw data is shown in Appendix A.1.

The radar profile (Figure 3.17) illustrates significant variations in ice thickness along the Darwin Glacier centre line with values generally exceeding the estimates of Anderson et al. (2004, Figure 2.4) and predicted by the BEDMAP ice thickness map (generally no more than 900 m). A maximum ice thickness of 1124 m was recorded by the GPR system towards the outlet of the glacial system, although ice thicknesses along the Darwin Glacier are close to 1500 m below Junction Spur (Figure 2.1) and in the upper regions. The Darwin Glacier is grounded below current sea level for more than 40 km upstream from the inferred grounding line. Several large steps are present in the bed topography, the largest of which occurs at a distance of 120 km, where the bed elevation can be seen lowering more than 1000 m over a distance of less than 2 km. At this particular bedrock step the airborne flight track borders the Darwin Glacier centre flow line and most of the East Antarctic ice drains through a deeply subglacial trough southwest of the profile (section 3.5.3). Previous studies have shown that the presence of subglacial bedrock steps have a significant influence on the glacier flow

dynamics (Kavanaugh et al. 2009b; Pattyn 2002). The effect of the observed bedrock steps on flow dynamics of the Darwin Glacier will be investigated in more detail in section 3.6.

3.5.3 3-D ice thickness and bedrock maps

In this section the GPR and airborne radar measurements of ice thickness are used to construct a 3-D interpolation map for the entire DHGS which, when combined with a DEM, facilitates the construction of a map of the bedrock topography. The previous measurements of ice thickness are not included in the final ice thickness interpolation map as they were collected in regions which are adequately covered by the newer and more accurate radar surveys (Figure 2.2 and Figure 3.2).

In order to ensure that the final ice thickness map includes ice in important tributaries not covered by the radar surveys, ice thicknesses were linearly interpolated between downstream measured values and an upstream exposed rock or line (Lythe and Vaughan 2001). Furthermore, an additional cross profile (J) was introduced to constrain the interpolation in the uppermost part of the Darwin Glacier (Figure A.3a). Ice thicknesses across this profile were interpolated (cubic spline) by assigning a maximum ice thickness equal to that measured by the airborne radar at this location. Finally, zero ice thicknesses were assigned to all rock outcrops within the glacial system. Appendix A.2 includes a map of the various inputs to the ice thickness interpolation map, a detailed description of the applied interpolation routine, and an evaluation of the accuracy of the ice thickness map.

Ultimately, to minimize the errors associated with the presence of a firn layer, the firn correction described in section 3.4.2 (Figure 3.13) was added to the interpolation in order to arrive at the final ice thickness map for the DHGS (Figure 3.18a). A map of ice base or bedrock topography when grounded (Figure 3.18b) was calculated from the ice thickness map and a compilation of various DEMs (described in section 4.1 and shown in Figure 4.3).

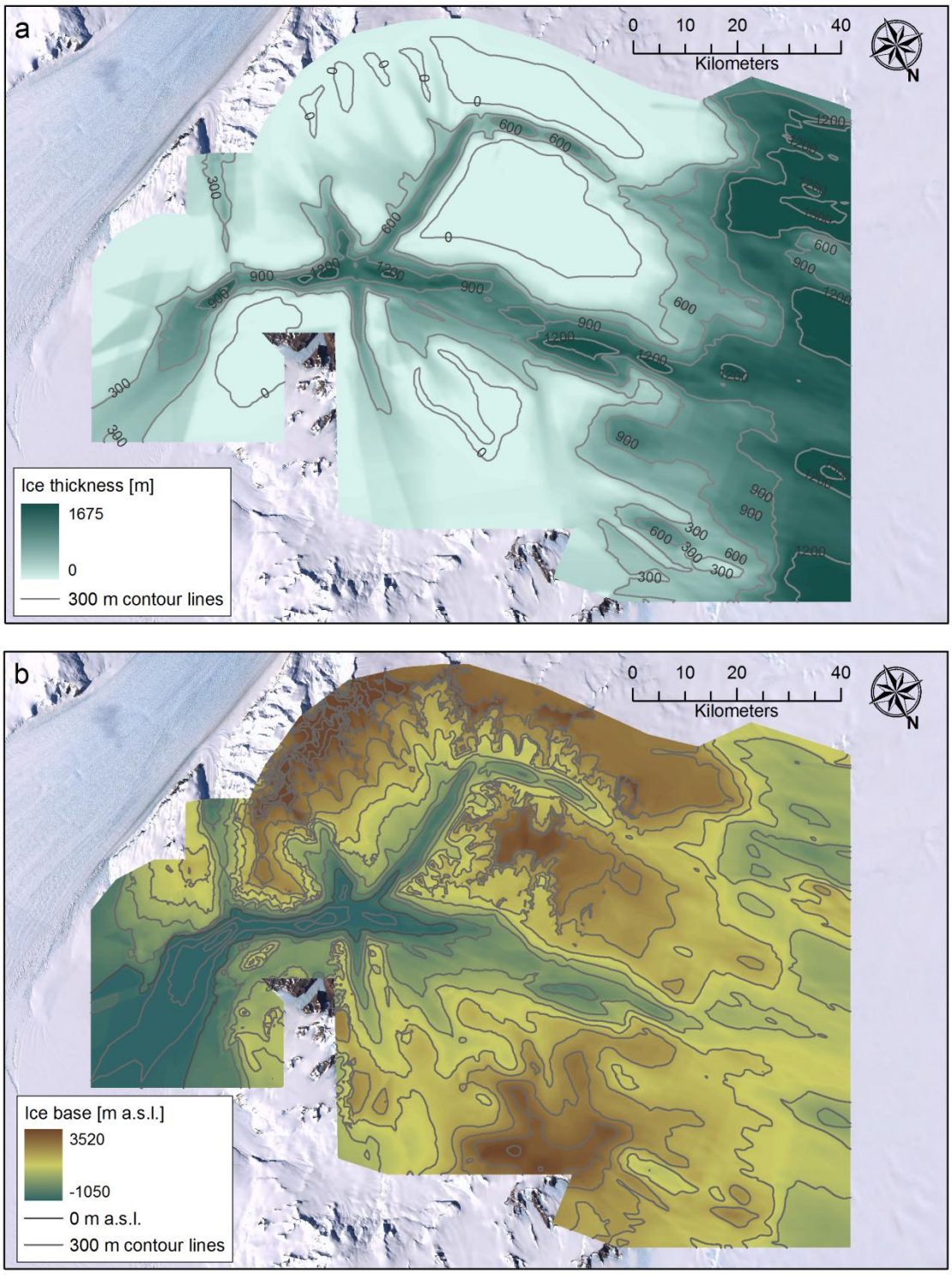

Figure 3.18. (a) Ice thickness at the DHGS. The radar data has been corrected for the presence of a firn layer. (b) Ice base elevation of the DHGS. The ice base equals the bedrock topography when the glacier is grounded, which is everywhere except at the glacier outlet.

The Darwin Glacier is by far the thicker of the two glaciers with ice thicknesses exceeding 1200 m at several locations (Figure 3.18a). Towards the glacier outlet, the ice thins dramatically from 1250 to 300 m within a distance of only 40 km as the glacier begins to float and is subjected to subglacial oceanic melting and lateral spreading. A maximum ice thickness of 1684 m was recorded by the airborne radar system in the catchment areas on the polar plateau upstream of the Darwin Glacier. The upper part of the Darwin Glacier is located in a relatively wide valley that gradually narrows and deepens towards the Ross Ice Shelf (Figure 3.18b). By contrast, the Hatherton Glacier flows in a continuously narrow valley with a low downstream gradient. The Hatherton Glacier is relatively thin, with ice thicknesses approaching 900 m only in the deepest regions although generally exceeding 600 m in the central valley (Figure 3.18a). The interpolation map shows that the Hatherton Glacier is generally thinner than suggested by Anderson et al. (2004, Figure 2.4). The limit of the DHGS which is grounded below sea level is shown in Figure 3.18b (dark gray line) to extend well above the confluence between the Hatherton and Darwin Glaciers.

Airborne radar cross profiles which constrain the ice thickness interpolation in the upper parts of the glacial system show that ice drains from the EAIS and into the Darwin Glacier through a <10 km wide and 1000 m deep valley surrounded by high subglacial mountains. Ice drainage into the Darwin Glacier is mostly confined to this trough and ice thins to less than 200 m as it passes over the surrounding mountains (Figure 3.17). Unlike the Darwin Glacier, the Hatherton Glacier has managed to carve only a minor valley towards the EAIS (Figure 3.18) suggesting limited ice discharge also in the past. The ice thickness of the Hatherton Glacier thins to less than 200 m at the subglacial saddle and an analysis of inland surface slopes suggests that the upstream catchment area is small (Figure 1.1).

The above analysis of ice thickness and bedrock topography of the glacial system has illustrated the differences which exist between the Darwin and Hatherton Glaciers. The ice thickness and bed morphology variations along the Hatherton Glacier are minor, while the Darwin Glacier experiences large downstream variations in both. Ice drains from the EAIS and into the Darwin Glacier through a deeply incised trough and inflow from the ice sheet is an important source of ice (section 2.4). In contrast, ice flow from the EAIS and into the Hatherton Glacier is restricted by a high subglacial ridge, and a 200 m lowering of the EAIS would isolate the glacier from inland ice sources. The Hatherton Glacier is consequently inferred to be particularly sensitive to potential in EAIS elevations and its dynamic response to variations in the EAIS may have differed significantly from that of the Darwin Glacier in the past. Another aspect of the bed morphology which may influence glacier dynamics is the grounding of the DHGS well below sea level for a considerable distance upstream from the grounding line. This is likely to cause the system to be sensitive to sea level rise, in particular

in the event of a removal of the Ross Ice Shelf and the buttressing effect it offers. The stability of the current Darwin Glacier grounding line will be discussed in more detail in section 3.8.5.

3.6 Evidence of flow dynamics from internal reflectors

Variations in deeper internal layers provide information on changes in flow dynamics (section 3.1.2). Generally, very few deep internal layers were observed in the GPR profiles and only on the Darwin Glacier upstream of the confluence with the Hatherton Glacier were layers observed below 200 m. Evidence of these layers are shown in Figure 3.19, which also illustrates the appeared transparency of the glacier ice at depths below ~500 m. Similarly, a GPR profile collected across the glacier grounding zone (Figure 3.22) shows almost no evidence of internal layers below 300 m depth. The airborne radar profile collected along the centre flowline of the Darwin Glacier (Figures A.1 and A.2 in appendix A.1) coincides with the GPR profiles shown in Figure 3.19 and Figure 3.22 (Figure 3.2). Despite the higher transmitted power, this data supports the findings of the GPR, and internal layers are only observed at depth in the uppermost catchment area. Previous RES studies in Antarctica have documented the presence of internal layers to several thousand meters depth (Siegert 1999) and the lack of internal layers has been used to infer zones where high internal stresses have distorted the layers beyond recognition (Karlsson et al. 2009; Siegert et al. 2004b). These zones are often associated with rapidly moving ice such as ice streams. The absence of internal layers on the relatively slow moving DHGS is surprising when the airborne data document their presence upstream in the upper catchment area. This suggests that even though the ice velocity is relatively low, the rough bedrock topography documented by the radar surveys leads to ice deformation large enough to distort the internal layers beyond recognition as the ice travels downstream.

Several prominent internal layers are observed in the GPR data parallel to the large-scale features of the underlying bedrock topography (Figure 3.19, marked 1-5). The nadirs of the synclinals, which develop in the internal layers as the ice flows in and out of the largest bedrock depression (at 15,500 – 9000 m distance), are extremely narrow and only resolved by the GPR system for one weak layer (not visible in Figure 3.19). In general, the variations of internal layers appear slightly more pronounced in deeper layers (marked 1 and 4) than shallower layers (marked 2 and 5), leading to an increased distance between layers over bedrock troughs and a decrease over crests. Similar patterns have previously been observed as ice travels over rough bedrock topography, and are related to variations in the longitudinal stresses as the ice compresses over troughs and stretches over crests (Irvine-Fynn et al. 2006; Pattyn 2002; Siegert et al. 2004a).

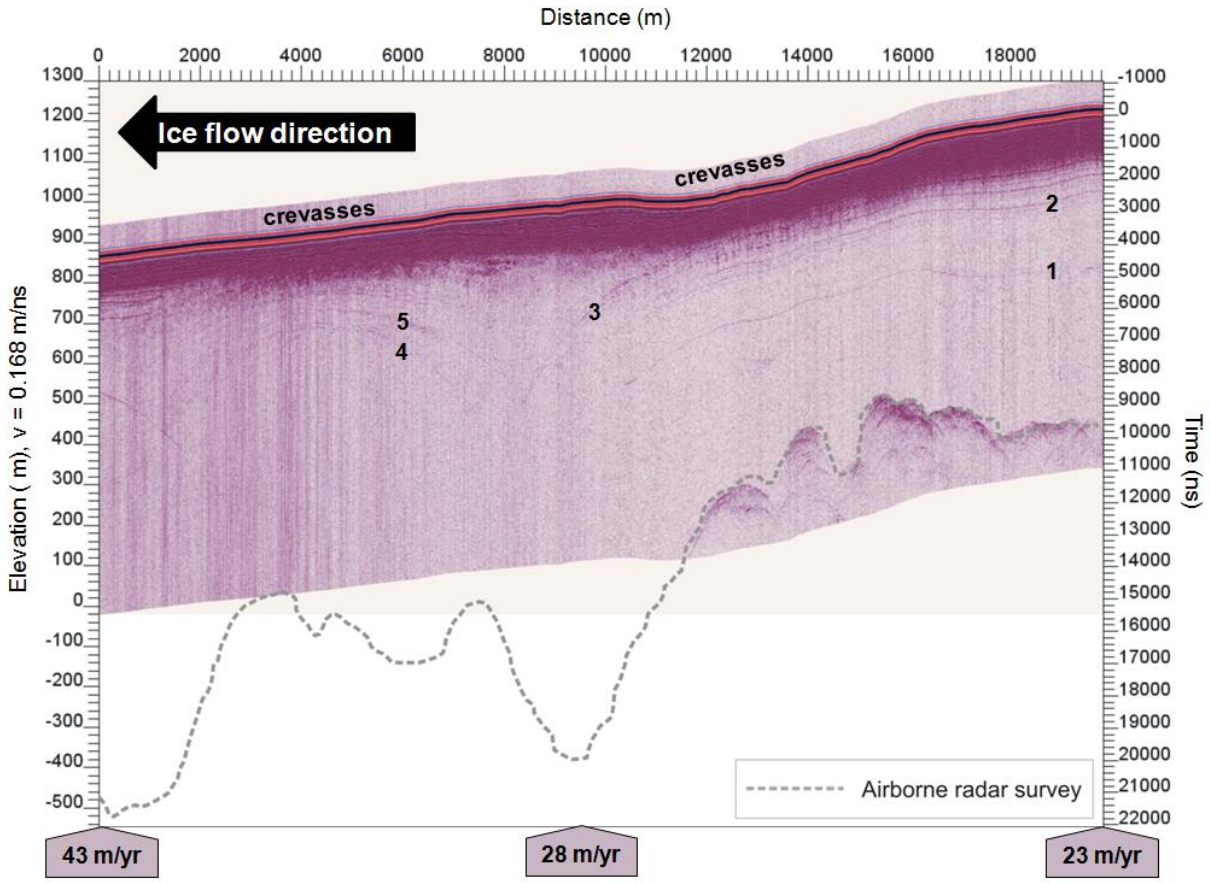

Figure 3.19. GPR profile collected along the centre flowline of the upper Darwin Glacier (profile C-C' on Figure 3.2). Ice flow is from right to left. Dashed grey line shows the ice bed interface as determined by the airborne radar system which travelled roughly along the same track. Prominent internal layers mentioned in the text are numbered between 1 and 5. The top 1500 ns of the profile is shown in greater detail in Figure 3.20. Measured ice flow velocities are shown in purple boxes below the radargram.

A distinct increase in surface slope occurs as the glacier begins to flow into the largest bedrock trough observed in Figure 3.19. The two upstream measured velocities indicate more or less constant ice movement (Figure 3.19), but evidence of crevasses in the GPR data as well as observations during fieldwork, suggest that the increase in surface slope is accompanied by a change in flow behaviour. Similarly, features in the GPR data suggest the location of another crevasse area over the downstream bedrock bump (at 2500 – 6500 m distance). Both of the inferred crevasse areas were characterised in the radargram by an abundance of near-surface hyperbolic reflections and disrupted internal layers below which deeper small-scale layer undulations occur (visible at distance 3000 – 6000 m, depth 30-60 m in Figure 3.20). Upstream and downstream of the crevasse regions, the same internal layers appear smooth, and the undulations are likely to be related to variations in radar wave velocities of shallower layers as opposed to actual undulations in the internal layers. The depths of the overlying crevasses were calculated from the size of the layer undulations to be no more than 7.5 m.

The location of the two confined crevasse areas (Figure 3.19) are in compliance with the theory proposed by Nye (1952), that crevasses perpendicular to the flow direction are likely to open during extending flow over convex parts the glacier bed and close again during compressive flow over concave beds. Previous studies of ice flow over undulating bedrock topography have shown that variations in ice velocity are primarily controlled by the surface slope, which are generally highest above bedrock bumps (Pattyn 2002). It is therefore possible that the ice flow velocity varies considerably between the three point measurements.

Compared to the large-scale variations described above, only minor if any changes occur in the elevation of the internal layers as they travel over the smaller bedrock undulations located upstream of the bedrock depression. The difference in the observed effect of bedrock undulations on the shape of internal layers compares well to the findings presented by Hindmarsh et al. (2006) showing that the glacier will override topographic undulations with wavelengths equal to or less than the ice thickness.

The internal features described above suggest that the rough bedrock topography observed along the Darwin Glacier centre flowline leads to some degree of longitudinal stretching (over bumps) and compression (over troughs) and consequently comprises a significant control on the overall glacier dynamics. The effect of the bed undulations on the ice flow is of importance to the general understanding of the processes governing ice flow of slower moving TAM outlet glaciers. In addition, it enables an evaluation of the applicability and accuracy of numerical ice-flow models. The shallow ice approximation (SIA), which is used in Chapter 5 to simulate the behaviour of the DHGS, will produce ice flow parallel to the bedrock topography independently of the size of bedrock undulations, and ignores the effect of variations in longitudinal stresses (Pattyn 2002). The reasoning behind choosing this particular model type despite these shortcomings will be discussed in more details in section 5.2.7.

3.7 Evidence for variations in surface mass balance

The surface patchwork of snow and ice which characterises the DHGS illustrates a high variability in SMB of which very little is known (section 2.3). As ice flux from the EAIS is relatively low (section 3.5), the local SMB is likely to be particularly important to the overall behaviour of the glacial system. In this section, undulations in shallow reflectors along the Darwin Glacier centre flowline (Figure 3.20) are utilised to investigate controls on changes in accumulation rates. The results reveal an interesting interaction between undulating bedrock topography and SMB, and the observations will be used to some extent in the construction of a SMB model (section 4.5.4).

The undulating character of the shallow internal layers (Figure 3.20) illustrates the large variability which exists even within short distances. Most conspicuously is the prominent synclinal, which occurs in the internal layers above the bedrock trough shown in Figure 3.19. From the synclinal, a downstream increase of more than 40 m occurs in the depth to individual layers. In general, the number of internal layers increases downstream. The observed variations in shallow (<25 m depth) internal layers likely reflect changes in accumulation rates, while the deeper layers are influenced to some extent by the longitudinal stretching and compression documented along this profile in section 3.6 (section 3.1.2).

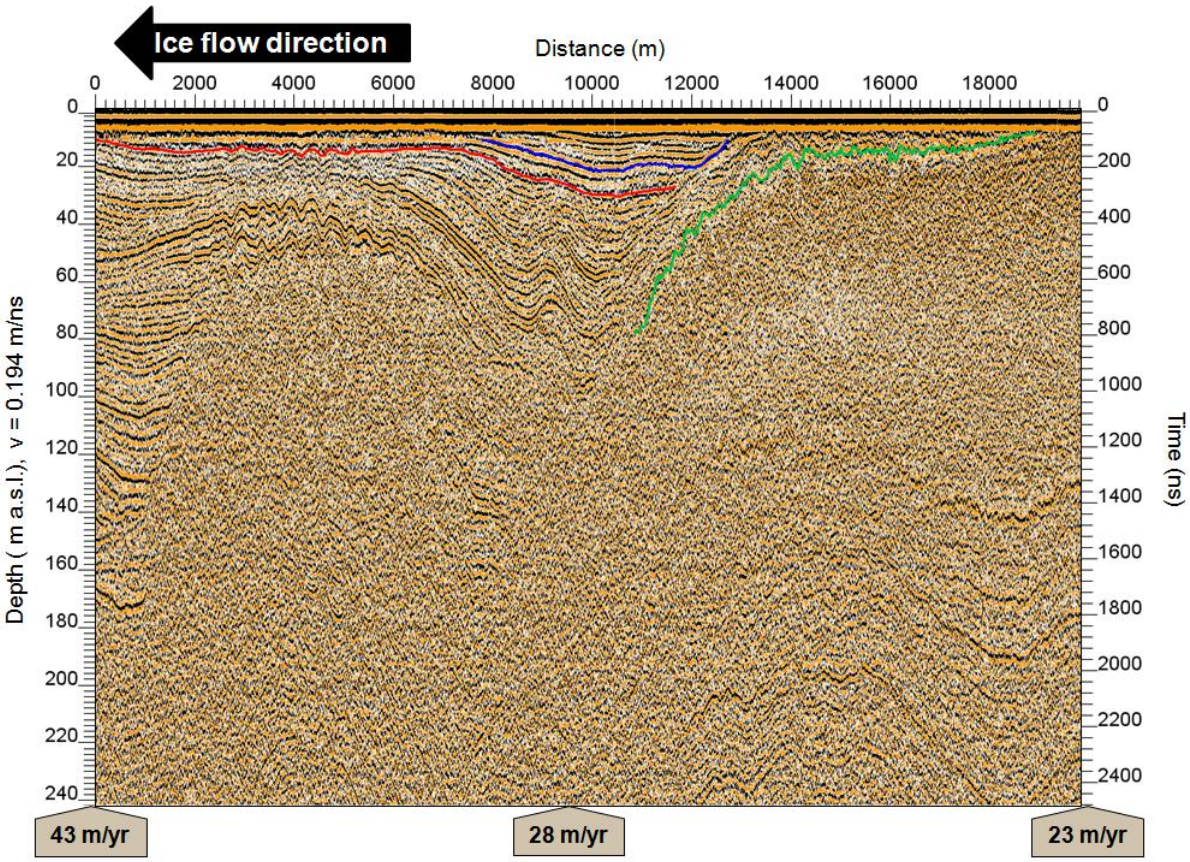

Figure 3.20. The top 1500 ns of the GPR profile collected along the centre flowline of the upper Darwin Glacier (profile C-C' on Figure 3.2). The three internal layer boundaries used in the SMB analysis are shown in blue, red and green. Measured ice flow velocities are shown in boxes below the radargram. TWT has been converted to depth using a constant radar wave velocity of 194 m μs^{-1}, which is inferred to be representative of the upper 1000 ns of the profile (Winther et al. 1996; Woodward and King 2009).

The preferred interpretation of the variations observed in Figure 3.20 is given in the following. As the GPR profile is located close to a BIA (Figure 3.2), a likely explanation for the lack of near-surface internal layers in the upstream part of the profile could be an almost complete

erosion of the firn layer where internal layers are generally most abundant (section 3.1.1). A sudden increase in firn density between new snow deposited onto an older and denser erosional surface would explain the particularly high strength of the reflector marked with green, as well as the presence of internal layers at shallower depths (section 3.1.1). The downstream dip in internal layers in the upstream part of the profile as well as the absence of outcropping layers further downstream suggests that the SMB is positive along the entire length of the radar profile. Accumulation rates are highest where the internal layers are furthest apart, and the syncline appears to be at least partly a result of a local increase in SMB.

The magnitude of change in accumulation rates occurring along the profile is investigated below in more detail by accounting for the effect of vertical changes in the radar wave velocity and layer thinning with depth (Sinisalo et al. 2004). No direct measurements of accumulation rates exist from the DHGS and none of the internal layers have been dated. In addition, due to the relatively poor vertical resolution of the 25 MHz antennas (section 3.3.2), reflections observed in the radargram are likely to originate from multiple layers located closely together. Information on annual accumulation rates therefore cannot be extracted from the dataset, and the analysis is restricted to relative changes in accumulation.

Three layer boundaries had to be utilised for the analysis because no single reflector could be traced throughout the entire GPR profile (Figure 3.20). Where layers overlap, the shallowest layer was utilised in the calculations. The depth to the shallowest layer never exceeds 2% of the total glacier thickness so as to minimise the influence of glacier dynamics on the internal layer structure (section 3.1.2). In order to arrive at an estimate of relative accumulation changes, the depth to the internal layers must first be established. As described in section 3.1.1, this requires knowledge of either the density or velocity profile (section 3.4.1) of the firn above the reflector in question. The depth (d) to reflectors is determined using the following equation derived by Robin (1955):

$$d = \frac{1}{2}\sqrt{(TWT \cdot v_0 - l_a \cdot 0.85\rho_{av})(TWT \cdot v_0 + 2l_a + l_a \cdot 0.85\rho_{av})} \cdot (1 + 0.85\rho_{av})^{-1} \qquad (6)$$

where v_0 is the velocity of the radar wave in air (300 m μs^{-1}), l_a is the antenna separation (3 m) and ρ_{av} is the average density of the firn above the reflection. As no knowledge of the density profile exists for this area, the average density above the layer was calculated from the model of firn densification proposed by Herron and Langway (1980). The density profile depends on the mean annual air temperature which varies between -26.6°C and -23.5°C along the profile (direct measurements, section 4.6.1), the initial snow density (400 kg m^3,

section 3.4.2), and mean annual accumulation rate (see below). Layer thinning with depth was accounted for by employing the one-dimensional model proposed by Nye (1963), which has been found to perform well for near surface internal layers (Sinisalo et al. 2004). The model predicts the age (T) of the firn with depth depending on the total ice thickness (H_{we}), annual mean accumulation rate (A_{we}) and the depth to the observed reflection (d_{we}) all of which are in water equivalent:

$$T = -\frac{H_{we}}{A_{we}} \ln(1 - \frac{d_{we}}{H_{we}}) \quad (7)$$

An initial assumption on accumulation rate allowed calculations of the density profile and subsequently the layer depth and age from equations 6 and 7 respectively. Downstream accumulation rates relative to the first upstream appearance of the green reflector (at ~19,000 m distance, Figure 3.20) were determined every 500 m by keeping the layer age constant while iteratively solving equations 6 and 7 and the mean density profile for varying accumulation rates.

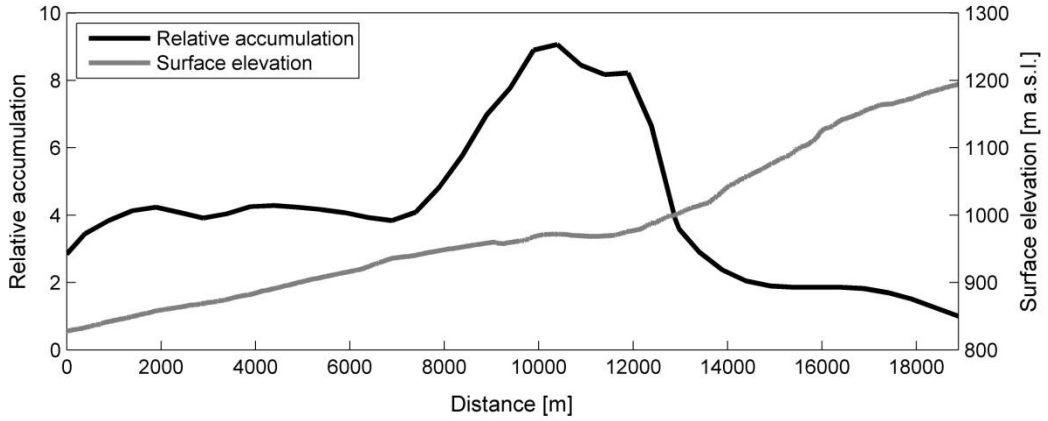

Figure 3.21. Relative accumulation rates and surface elevation along the GPR collected at the Darwin Glacier centre flowline (Figure 3.19 and Figure 3.20) (Relative accumulation rate = 1 at 18890 m distance).

An overall downstream increase in accumulation rates occurs along the GPR profile upon which is superimposed a distinct accumulation maximum, where values reach levels of more than nine times the accumulation rate at the upstream end of the GPR profile (Figure 3.21). The accumulation peak is located on a narrow reversed slope immediately downstream of a particularly steep part of the Darwin Glacier, which section 3.6 showed arises from ice flow into a large bedrock trough. Variations in surface accumulation have been shown to closely relate to changes in surface slope due to their effect on erosion and deposition of snow by the

wind (King 2009; Vaughan et al. 1999b; Woodward and King 2009). Measurements of wind direction and speed from an AWS installed on the upper Darwin Glacier (section 4.5) show that katabatic winds travelling parallel to the GPR transect dominate at wind speeds >5 m s^{-1} (Figure 4.9) which is an approximate lower limit for snow drift over snow-covered surfaces (Bintanja 2001; Bintanja et al. 2001). As the katabatic wind encounters the downwind foot of the steep slope (at 11,500 m distance, Figure 3.21), the change in surface slope causes a deceleration and snow is deposited from suspension (King 2009; Vaughan et al. 1999b; Woodward and King 2009). The local accumulation maximum is consequently ultimately caused by the underlying bedrock topography and its effect on the glacier surface.

As the GPR profile is located in a region where variations in longitudinal stresses affect the ice flow (section 3.6), the potential error associated with attributing variations in shallow internal layers to accumulation variations only should be evaluated (section 3.1.2). Findings by Pattyn (2002) for similar bedrock undulations suggest a ~1% overestimation of accumulations rates over bedrock troughs and a ~7% underestimation over bumps for layers at 50 m depth (2.5% of total ice thickness). Uncertainties of this magnitude do not affect the inference of a distinct local accumulation increase, and the above analysis of internal layer variations is thought to illustrate well the way in which bedrock topography may ultimately influence the glacier SMB. Such variations are generally unaccounted for in SMB models and may lead to uncertainties in the overall glacier mass budget.

3.8 Grounding zone description

Grounding zones are immensely complex regions of great importance to the glacier SMB and flow dynamics (section 3.1.3). Past studies of grounding lines have relied on low frequency and often airborne radar systems which have identified a downstream increased power of the basal reflection, an abundance of hyperbolic shaped reflections interpreted as bottom crevasses close to the grounding line (Frezzotti et al. 2000; Jezek and Bentley 1983; Uratsuka et al. 1996), and downwarping of internal layers as the ice begins to float (Catania et al. 2005; Catania et al. 2010). Presented in this section is a GPR profile illustrating in great detail the variations which occur across the Darwin Glacier grounding zone (Figure 3.22).

The GPR profile shows the presence of a weak horizontal basal reflection furthest upstream (at 13,500 – 15,000 m distance, Figure 3.22). The basal reflection is detected to 1124 m depth (maximum ice thickness recorded by the GPR) before falling below the level of the background noise. Immediately downstream of this deep reflector the location of the ice base becomes indistinct due to the abundance of hyperbolas (at 11,000 – 13,500 m distance). When a clear basal reflector is registered again, a dramatic decrease in ice thickness has occurred. Further downstream the ice thickness decreases much more gradually. The dramatic change in ice

thickness coincides with the break-in-slope at ~12,000 m distance which is often used to approximate the grounding line location (Figure 3.1, section 3.1.3).

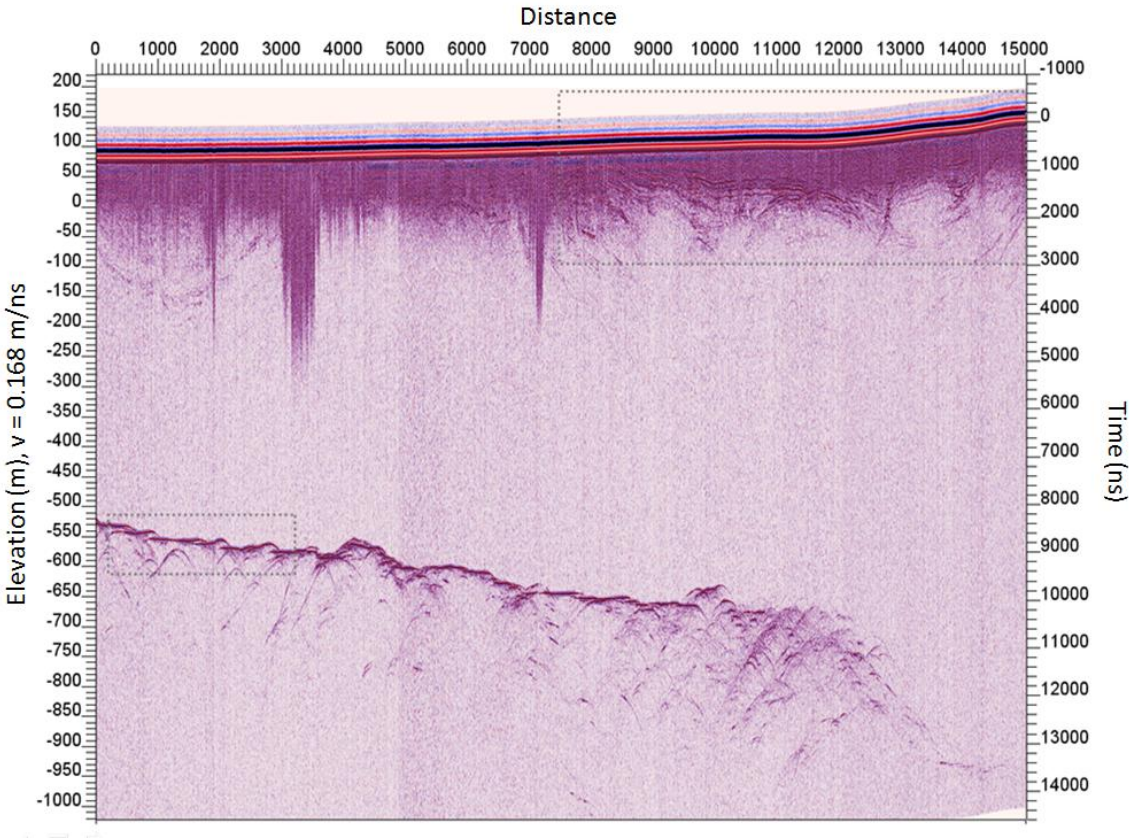

Figure 3.22. GPR profile along the centre flowline up across the Darwin Glacier grounding line (profile D-D' on Figure 3.2). The two squares show the location of two sections of the radargram which are shown in greater detail in Figure 3.23 and Figure 3.24. The profile has been topographically corrected using the Altimeter DEM.

Several factors such as the change in basal reflection and ice thickness, the presence of reflection hyperbolas as well as the change in surface slope suggest that the Darwin Glacier grounding line is located at approximately 13,500 m distance in Figure 3.22. At this location an ice thickness of ~1050 m was recorded by the GPR and the bed elevation is at ~925 m below sea level. The general characteristics of the grounding zone will be described in more detail in the sections below.

3.8.1 Subsurface ponds

Prominent 'cone' shaped features of enhanced reflectivity are observed extending from the surface in the GPR profile (Figure 3.22). The largest of these features has a width of more

than 500 m and extend to a depth of 400 m. The features were observed in the data during fieldwork and appeared to coincide with smooth ice surfaces beneath which water was observed at more than one occasion. Similar features have been described previously in GPR data and relate to a reverberation of the radar wave in an underlying water layer (Irvine-Fynn et al. 2006). The presence of subsurface pools of water is well documented in Antarctica low-elevation blue ice areas, where the low albedo of blue ice leads to a high absorption of shortwave radiation (Brandt and Warren 1993; Rasmus 2009; Winther et al. 1996). Consequently although the subsurface ponds documented by the GPR are characteristic features of the Darwin Glacier grounding zone, their formation is unrelated to any change in glacier behaviour which may occur across the grounding zone.

3.8.2 Downwarping of shallow internal layers

Internal layers at various inclinations were observed in the uppermost 200-300 m of the radar profile. A clear downwarping of the internal layers can be observed between distances of 0 and 3000 m as well as 8000 and 15,000 km (Figure 3.22 and Figure 3.23). The downwarping furthest upstream coincides with the break-in-slope and cannot be explained by changes in the bedrock topography or SMB. The internal layers become obscured downstream, and it is not immediately clear whether they taper or truncate at the surface.

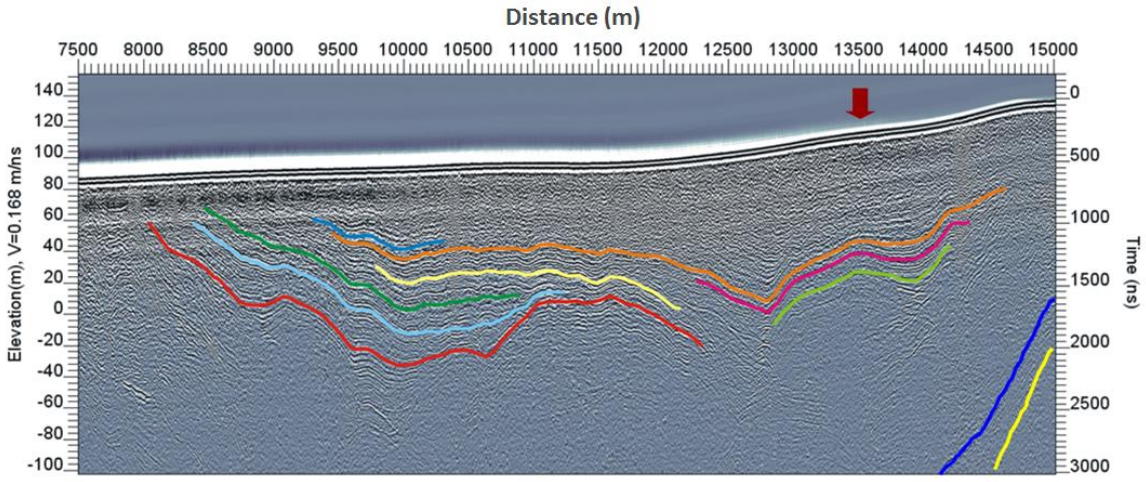

Figure 3.23. Enlarged image of variations in internal layers across the grounding zone for the radargram shown in Figure 3.22. The red arrow indicates the inferred grounding line position.

Downwarping of internal layers has previously been documented by RES studies across both current and relict grounding lines, and are thought to be indicative of the increased basal melting which occurs within the first few km downstream of the grounding line (Catania et al.

2005; 2010). If basal melting is indeed responsible for the pattern observed in the radargram (Figure 3.23), deep downward dipping internal layers should be truncated at the ice base. Unfortunately no deep internal layers were observed in any of the radar data (GPR and airborne) collected across the Darwin Glacier grounding line and the cause of the downwarping can therefore not be confirmed. Studies have shown that not all grounding lines display downwarping of internal layers and they are thought to develop only when ice flow is slow or the oceanic basal melting high and the grounding line position stable (Catania et al. 2010). Since surface velocities of more than 100 m yr^{-1} were measured across the grounding zone (section 3.2.3), the downwarping of internal layers is probably the result of high basal melting near the grounding line when adopting the explanations proposed by Catania et al. (2005; 2010).

3.8.3 Character of the ice base interface

As explained in section 3.1.1, the strength of the ice base reflector depends on the permittivity contrast between the glacier ice and the underlying material. For the floating portion of GPR profile, the high contrast between glacier ice and the conductive sea water should result in a strong reflection and a rapid attenuation of the remaining energy. In accordance with the theory, the strongest basal reflection recorded by the GPR was observed downstream the inferred grounding line in the GPR profile (Figure 3.22). As the distance to the grounding line increases, the strength of the basal reflector increases and clear near horizontal steps of 10 m height with widths of up to 1 km emerges (Figure 3.24). The linearity of the basal reflection between steps provides evidence of the extremely smooth character of the ice base. Numerous hyperbolas can be seen below the basal reflection. Because of the rapid attenuation of the radar wave in sea water mentioned above, the hyperbolas must originate from discontinuities in the basal ice to either side of the survey line and consequently reflect the condition of the surrounding ice base.

The presence of bottom crevasses and cracks is characteristic for floating ice and they are rarely observed on grounded glaciers (van der Veen 1998). Calculations and observations suggest that bottom cracks are more likely to form at or close to the grounding line due to a combination of tidal flexure and shear stresses (Catania et al. 2010; Jezek and Bentley 1983; Peters et al. 2005; Rist et al. 2002). This corresponds well with the increased scattering of the radar wave observed immediately downstream of the proposed grounding line (Figure 3.22). As the distance to the grounding line increases downstream, the number of hyperbolas observed in the radargram decreases, the ice base becomes smoother and the vertical steps become more defined. The gradual change observed at the ice base suggests that certain basal features are able to continue to grow whereas others are melted away or smoothed by accretion of marine ice.

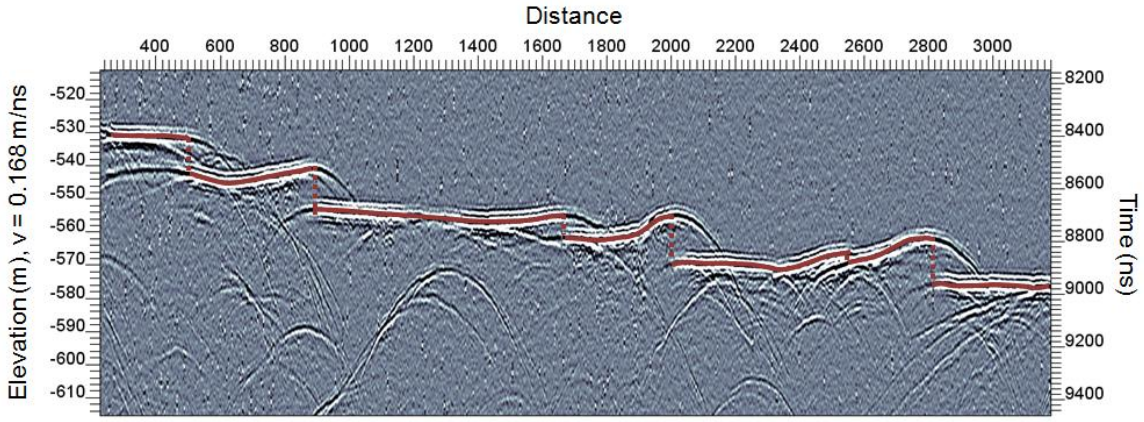

Figure 3.24. Detailed view of the interface between ice and sea water below the grounding line. Dashed red lines show proposed abrupt changes in basal reflector.

The horizontal steps appear to end in single-sided hyperbolas (Figure 3.24), which in the current setting are likely to be associated with either a sudden vertical change in basal topography (Jol 2009), rough-walled bottom crevasses (Clarke and Bentley 1994) or bottom crevasses with a crevasse plane oriented at an angle to the GPR profile (Catania et al. 2010; Jezek et al. 1979). If a crevasse is of a sufficient size compared to the radar footprint, hyperbolas may be observed both from the crevasse tip and the two crevasse edges (Jezek et al. 1979). This may explain the observed single sided hyperbolas (upper edges) followed by a full hyperbola (crevasse tips). However, where the upstream edges of the basal features appear extremely steep, the downstream slopes are much less inclined and no hyperbolas are observed at the lower limits. This indicates that the shape of the features observed at the ice base is distinctly asymmetrical, and hence not typical of crevasses. Similar 10 m ice thickness changes were observed by Peters et al. (2005) immediately downstream of the Ice Stream C grounding line and were inferred to be evidence of a jumble of ice blocks created by rapid basal melting as the ice begins to float. The vertical steps observed in the GPR profile are thought to reflect a complex interaction between crack formation due to tidal flexure and basal melting/freezing.

3.8.4 Calculations of hydrostatic equilibrium

As mentioned in section 3.1.3, assumptions on hydrostatic equilibrium at the grounding line are normally made in order to remotely infer the ice thickness at this location. When ice thickness measurements exist, these can be compared to the calculated ice thickness to provide evidence of variations from hydrostatic equilibrium below the grounding line. In

addition, analysis of freeboard height can be used to indirectly determine variations in firn thickness when the ice is in hydrostatic equilibrium (Horwath et al. 2006). In the following analysis the assumption of hydrostatic equilibrium along a part of the airborne radar profile collected across the Darwin Glacier grounding line is investigated (Figure 3.25).

In order to accurately compare ice thickness calculated from the surface elevation with measured ice thickness, the surface elevations along the profile must first be established. No accurate measurements of surface height exist along the floating portion of the ice. However, as it is reasonable to assume that the ice is in equilibrium at the Ross Ice Shelf end of the radar profile (at 0 m distance and 34,500 m downstream of grounding line), the surface elevation was calculated from the first radar firn corrected ice thickness measurement. The calculated surface elevation (55.9 m a.s.l.) compare well with the elevation suggested by the Altimeter DEM (53.3 m a.s.l., referenced to the OSU91A geoid) which was constantly shifted along the profile to account for this discrepancy.

The total ice thickness (H) for ice in hydrostatic equilibrium was calculated along the radar profile from equation 8 (Horwath et al. 2006):

$$H = \frac{\rho_{water}}{\rho_{water} - \rho_{ice}} h - \frac{\rho_{ice}}{\rho_{water} - \rho_{ice}} h_{air} \qquad (8)$$

where ρ_{ice} is the density of ice (917 kg m^{-3}), ρ_{water} is the density of ocean water (1029 kg m^{-3}), h is the surface elevation, and h_{air} is the air layer thickness which was calculated from the varying radar firn correction interpolation (section 3.4.2). The ice thickness was used to calculate the elevation of the ice base which can be readily compared to the measured elevation (Figure 3.25). Floating ice shelves generally reach hydrostatic equilibrium within few kilometres of the grounding line (Horwath et al. 2006) and the downstream part of the radar profile can consequently be used to evaluate the accuracy of the radar firn correction map (Figure 3.13).

The calculated ice-base elevation and the radar firn corrected measurements generally compare well between distance 0 and 32,000 m (Figure 3.25). The similarity between calculated and measured ice-base elevation both in regions where the firn layer is thick (at 0-10,000 m distance) and completely absent (at 25,000 – 30,000 m distance) suggests that the maximum radar firn correction (section 3.4.2) is accurate for the region. The discrepancies observed between the two curves as the air layer decreases upstream appear to be directly related to changes in the air layer thickness. This suggests that the firn layer develops more gradually than predicted by the firn correction interpolation and at a constant rate before reaching its full regional thickness at ~12,000 m distance (~18.5 km downstream of the BIA boundary).

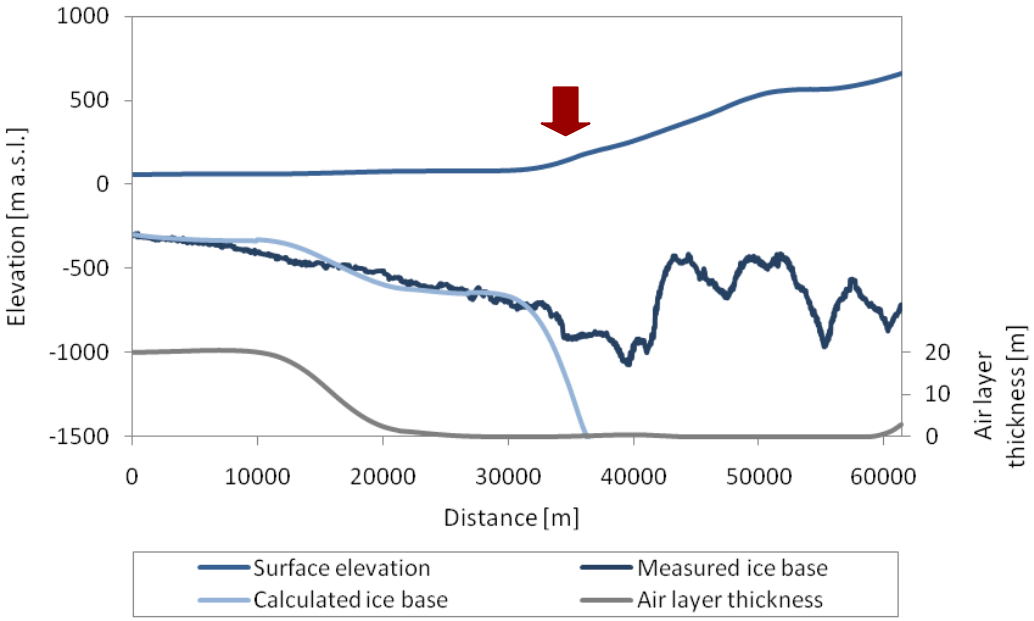

Figure 3.25. Surface elevation and measured as well as calculated ice base along part of the airborne transect crossing the Darwin Glacier grounding line (profile E-E' on Figure 3.2). The grey line shows the change in thickness of the air layer along the radar profile. The red arrow indicates the position of the inferred grounding line.

Upstream of 32,000 m it becomes clear that for the ice to reach the given surface elevation, it cannot be floating freely and eventually must be grounded. The discrepancy begins ~2500 m downstream (at ~32,000 m distance) of the proposed grounding line (at ~34,500 m distance) as the surface slope begins to increase. Upstream of the break-in-slope which is located ~1500 m downstream (at ~33,000 m distance) of the inferred grounding line, the difference between measured and calculated ice base increases dramatically. Breaks-in-slopes are most often found some way downstream of grounding lines (Figure 3.1) as it takes time to adjust to the large change in flow dynamics (Fricker et al. 2009). It is therefore normal for the ice to be elevated above hydrostatic equilibrium between the grounding line and the break-in-slope, as is observed for the Darwin Glacier. From the analysis it is clear that if the break-in-slope had been used to remotely determine the grounding line position, it would have lead to inaccuracies ~1500 m and the grounding line ice thickness could have been underestimated by approximately 150 m. There is no evidence in Figure 3.25 of an elevation minimum (I_m in Figure 3.1) and apart from the first ~2500 m, where the surface is elevated above hydrostatic equilibrium, the ice appears to be close to hydrostatic equilibrium downstream of the grounding line.

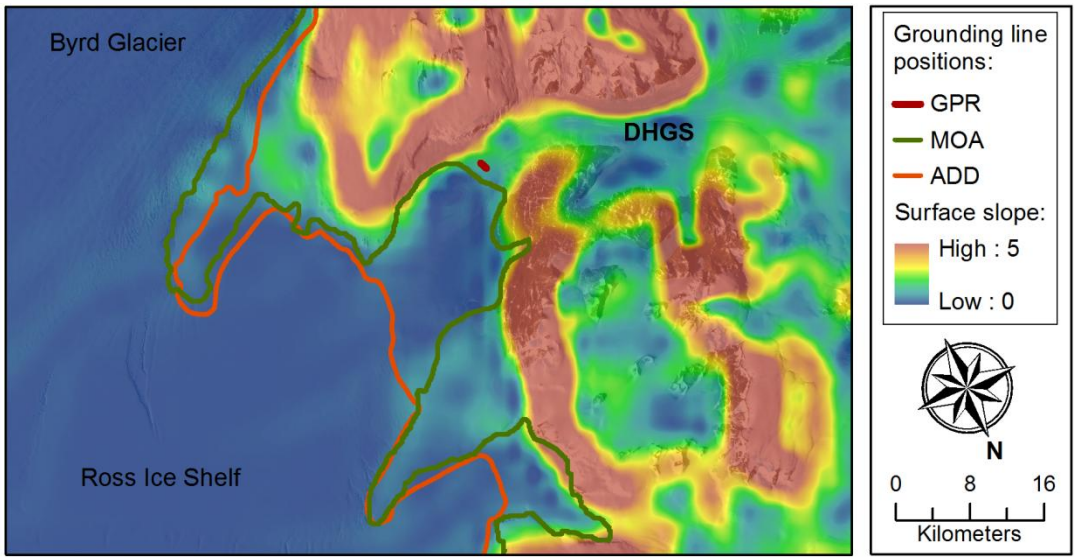

Figure 3.26. Comparison of grounding line positions from the ADD (orange) and MOA (green) datasets as well as measured by the GPR (red). The colour shading shows the average surface slope in degrees calculated from the Altimeter DEM over 2 km distances.

Two maps of Antarctic grounding lines cover the Darwin Glacier outlet (section 2.7), the Antarctic Digital Database (ADD, http://www.add.scar.org) and the more recent Mosaic of Antarctica dataset (MOA, http://nsidc.org/data/moa/). As described in section 2.7, the ADD and the MOA grounding line maps were determined remotely from Landsat imagery and break-in-slopes in MODIS respectively, and a comparison with the measurements presented above provide evidence of the uncertainties associated with these methods for the Darwin Glacier (Figure 3.26). The ADD grounding line is positioned more than 20 km downstream of the grounding line location measured by the GPR and consequently performs badly in this region. The MOA grounding line coincides with the break-in-slope suggested by the Altimeter DEM and consequently compares better with the radar results. However, as the above analysis showed this results in a ~1.5 km error in the grounding line position because the glacier is elevated above equilibrium at this location.

3.8.5 Stability of the Darwin Glacier grounding line

The slope of the bed immediately upstream of the grounding line is one of the main controls on grounding line stability (section 3.1.3). The DHGS is grounded well below current sea level for more than 40 km upstream of the present-day grounding line, and the underlying bedrock is characterised by several large bumps and troughs (section 3.5, Figure 3.17). The grounding line is currently positioned on a slightly downward-sloping bed and is therefore most likely in a stable position. Forces acting to stabilise the Darwin Glacier grounding line include the

buttressing effect of the Ross Ice Shelf and the stabilising effect of the narrow valley which the system drains through (Katz and Worster 2010). In its current state, the Darwin Glacier grounding line is most likely resistant to minor perturbations of influencing factors such as oceanic melt rates, ice shelf buttressing and SMB (section 3.1.3). However, as several regions of the bed which is currently below sea level are upward-sloping, an irreversible and rapid grounding line retreat or advance could take place for these sections if large changes were to occur in for example the ice shelf buttressing offered by the Ross Ice Shelf.

3.9 Ice discharge through Darwin Glacier cross profiles

The ice discharge of the DHGS at the Darwin Glacier grounding line has previously been estimated at 1.03 $km^3\ yr^{-1}$ (Table 1.2). However, the value is highly uncertain as it relies on rough assumptions of grounding line ice thickness and velocity from a comparison of the Darwin Glacier width to other TAM outlet glaciers where measurements exist (Humbert et al. 2005). Consequently, the ice flux values presented below represents the first calculation of ice discharge based on direct measurements of ice thickness and surface velocity. The catchment wide SMB is established from ice discharge measurements, and will be used to validate the SMB model applied in the numerical ice-flow model presented in Chapter 5 (section 4.5.5).

The ice flux is calculated across Darwin Glacier profiles A, B, C, D and E (Figure 3.14) from the associated ice velocity measurements (Figure 3.5) and the interpolated ice thickness (Figure 3.16). For each cross profile, a continuous velocity profile is fitted to the point measurements using either a piecewise cubic or a spline interpolation routine. For profile A and B, where few velocity measurements exist, additional points are introduced to guide the interpolation routine (Nye 1965). The total ice flux through each cross profile (Φ) was calculated as the sum of flux through 1 m segments (ΔL) from the equation:

$$\Phi = \sum_{L} 0.87 \cdot U_{surface} \cdot H \cdot \Delta L \qquad (9)$$

where $U_{surface}$ is the surface velocity, H is the ice thickness and 0.87 is the surface velocity factor ($U_{average}/U_{surface}$), which is an estimate of the ratio between the depth-averaged ice column velocity and the surface velocity (Fricker et al. 2000). A value of 0.87 has previously been utilised in Antarctica (Budd and Warner 1996; Fricker et al. 2000), where the ratio is thought to vary between 0.85 in the interior to 0.92 at the coast (Budd et al. 1971).

Table 3.4. Calculated ice flux from measurements of ice thickness and surface velocity. The location of the profiles are shown in Figure 3.14.

Profile:	A	B	C	D	E
Ice flux [$km^3\ yr^{-1}$]	0.22	0.23	0.27	0.52	0.55

The calculated ice fluxes increase downstream from 0.22 $km^3\ yr^{-1}$ at cross profile A to 0.55 $km^3\ yr^{-1}$ at cross profile E as tributaries join the Darwin Glacier (Table 3.4, Figure 3.14). Ice flow through profile C and D carries the largest uncertainty, as the ice thickness is not well resolved along these profiles (Figure 3.16). In particular the ice flux through profile C seems unrealistically small, as large tributaries join the Darwin Glacier between profile B and C. A possible underestimation of ice flux through profile C could be explained by the lack of ice thickness measurements across this profile, or might indicate that the short-term velocity measurements do not reflect the annual values well. A considerable inflow of ice from the Gawn Ice Piedmont (Figure 2.1) occurs between the inferred grounding line and profile E (section 3.10) and the grounding line ice discharge is likely to be close to the ice flux of 0.52 $km^3\ yr^{-1}$ calculated for profile D. This result clearly shows that the ice discharge of 1.03 $km^3\ yr^{-1}$ proposed by Humbert et al. (2005) significantly overestimates the actual DHGS discharge.

3.10 Oceanic melt rates near the Darwin Glacier grounding line

Oceanic melting underneath floating ice generally constitutes the largest negative component in the mass balance close to the grounding line (Frezzotti et al. 2000; Rignot and Jacobs 2002), and affects the ice shelf thickness and grounding lines location (Pollard and DeConto 2009b). Consequently, values of oceanic melt rates are an important input variable for the numerical model used to simulate the behaviour of the DHGS in Chapter 5.

The Darwin Glacier grounding line is located approximately halfway between profile D and E (Figure 3.14 and Figure 3.26). A calculation of the average rate of oceanic melting between the two profiles involves quantifying inflow of ice from the Gawn Ice Piedmont (Figure 2.1), SMB and basal melt rates under the grounded ice. Ice flux through the section of profile E which originate from the Gawn Ice Piedmont (outlined by clear flowline in Figure 2.1) shows that the piedmont contributes approximately 0.10 $km^3\ yr^{-1}$. No more than 0.001 $km^3\ yr^{-1}$ is lost to surface ablation (MB-1, section 4.5.5), while basal melting under the grounded ice is unlikely to exceed 0.01 $km^3\ yr^{-1}$ (Joughin et al. 2009). The 0.52 $km^3\ yr^{-1}$ ice flowing through profiles D is consequently reduced to 0.45 $km^3\ yr^{-1}$ (0.55 $km^3\ yr^{-1}$, less 0.10 $km^3\ yr^{-1}$) at profile E. Subtracting the part of this reduction which is due to basal melting underneath grounded ice (0.01 $km^3\ yr^{-1}$) and ablation at the glacier surface (0.001 $km^3\ yr^{-1}$) suggests that

0.059 km^3 yr^{-1} melts from the base of the ice between the grounding line and profile E (63.8 km^2). These estimates of ice loss/gain between profile D and E result in a calculated average oceanic melt rate of ~0.9 m yr^{-1} for the first 7 km downstream of the Darwin Glacier grounding line.

The magnitude of oceanic melt below the Darwin Glacier grounding line compares well with previous estimates of 1 m yr^{-1} oceanic melt rates near the fjord entrance of the David Glacier (Frezzotti et al. 2000; Wuite et al. 2009). Oceanic melt rates of more than 10 m yr^{-1} have been documented near deep grounding lines of fast moving TAM outlet glaciers (section 1.5.2) and the comparatively low value downstream of the Darwin Glacier grounding line is likely to be a result of the proximity of the fjord entrance and the relatively shallow grounding line position at ~925 m below sea level (section 3.8). In addition, the oceanic melt rates may be influenced by supercooled water (Wuite et al. 2009) entering the Ross Embayment from underneath the deep Byrd Glacier grounding line. Oceanic melt rates generally decrease with increased distance from the glacier grounding line, and a modelling study has found an average oceanic melt rate of 0.1 m yr^{-1} for the Ross Ice Shelf (Reddy et al. 2010).

3.11 Conclusion

Prior to this study, knowledge of the glacier characteristics of the DHGS was limited and insufficient to facilitate a detailed modelling study of the present and past dynamics of the glacial system. The high quality of the field data collected in December 2008 and January 2009 has enabled a range of information to be deduced about diverse aspects of the DHGS as a complex and dynamic system. This includes surprising information on glacial geomorphology and dynamics, SMB and grounding zone characteristics. The main results will be summarised briefly below.

The data show a particularly rough bedrock topography located well below sea level more than 40 km upstream of the grounding line. The grounding zone was captured in detail by the GPR which measured a grounding line ice thickness of ~1050 m and associated bed elevation of ~925 m below sea level. The Darwin Glacier is close to 1500 m thick at the narrow Nozzle and ice thicknesses approach 1700 m at the upper catchment area on the polar plateau. Changes in the valley shape of the Darwin Glacier suggest increased glacial erosion downstream, possibly related to a change in the basal temperature regime. The glacial behaviour and characteristics of the Darwin and the Hatherton Glacier differ significantly (section 2.4). On the basis of the radar survey it is inferred that this is at least partly related to a difference in inflow of ice from the EAIS. The radar measurements show that inflow of ice from the EAIS to the Hatherton Glacier is restricted by a high subglacial ridge, whereas the Darwin Glacier has carved a deep subglacial trough of at the threshold to the polar plateau. Ice above the

mountain threshold to the Hatherton Glacier is less than 200 m thick and the glacier is consequently likely to be particularly sensitive to ice thickness changes of the EAIS.

Large variations in SMB exist across the region illustrated on satellite imagery as BIAs interspersed between snow-covered surfaces. Evidence of these changes was also observed in the GPR data as variations in near surface internal layers and discrepancies between calculated and measured ice thickness below the grounding line. An in-depth analysis of near surface internal layers along the Upper Darwin centre profile showed that local changes in accumulation rates may be explained by changes in the surface slope (related to the bedrock topography) and deposition of snow by katabatic winds. In addition, features observed in the radargrams provide evidence of zones of longitudinal stretching and compression caused by ice flow over bedrock bumps and troughs respectively. It is clear that the rough bedrock topography has a significant influence on the flow dynamics as well as on the SMB of the DHGS.

The grounding zone was captured in great detail by the GPR system which revealed a zone characterised by:

- An abundance of bottom crevasses and a rapid decrease in ice thickness immediately below the grounding line
- A particularly strong and smooth basal reflector below the grounding line with evidence of 10 m high, 1 km wide ice blocks
- Downwarping of shallow internal layers above the grounding line due to increased basal melting at this location
- Hydrostatic equilibrium of the floating ice except for the first ~2.5 km downstream of the grounding line where the ice surface was elevated above hydrostatic equilibrium

Ice velocities were measured at several locations on the Darwin and Hatherton Glacier. Velocities are low in the wide upper regions of the Darwin Glacier (<30 m yr^{-1}) but an acceleration occurs downstream as the glacier trunk gradually narrows. A maximum measured velocity of 179.0 m yr^{-1} was recorded at The Nozzle (Figure 2.1) where the glacier is narrowest and steepest. Although the measurement was of a high quality at one location on the Hatherton Glacier, the time between repeat surveys was too short to accurately determine the slow velocity with which this glacier flows. The measurement does however suggest that ice flow velocity of the mid-Hatherton Glacier does not exceed 10 m yr^{-1}.

Ice discharge through cross profiles on the Darwin Glacier increase downstream from 0.22 km^3 yr^{-1} in the uppermost regions to 0.55 km^3 yr^{-1} 7 km downstream of the grounding line. The grounding line discharge was inferred to be close to the ice flux of 0.52 km^3 yr^{-1} measured 5 km further upstream. From these calculations of ice discharge, an average oceanic melt rate of

~0.9 m yr^{-1} was found between the grounding line and a cross profile located 7 km further downstream.

4 Integration of new geophysical data sets as input for the nested ice sheet-shelf model

As a result of the radar surveys presented in Chapter 3 and a number of local high resolution DEMs (section 2.2), the surface elevation, ice thickness and bedrock topography are now relatively well constrained for the DHGS. In this chapter, these datasets and measurements of meteorological parameters will be integrated with existing gridded datasets to produce input of the physical and climatological setting for the nested ice sheet-shelf model presented in Chapter 5. The results presented in this chapter therefore indirectly contribute towards meeting objective B.1.

The measures taken to prevent discontinuities as several datasets are combined to produce maps of surface elevation (section 4.1), ice thickness (section 4.2), water column thickness (section 4.3), and bedrock topography (section 4.4, objective A.1) are outlined below. In addition, the climatological setting is characterised from data collected by AWSs. Previous estimates of the climatological setting within the DHGS have relied on measurements from outside the glacial system (Anderson et al. 2004) and the AWS data consequently provide valuable new insight into the surface conditions of this very complex region.

The SMB of the DHGS is one of the fundamental controls on the behaviour of the glacial system, and an in-depth understanding of the way in which variations in air temperature, precipitation, sublimation and wind erosion interact to shape this landscape is important (objective A.3). In section 4.5, direct measurements are combined with existing datasets of Antarctic SMB to arrive at an improved estimate of SMB within the DHGS, which can be used as input to the nested ice sheet-shelf model. In addition, the applicability within the Darwin-Hatherton region of an already existing gridded dataset of remotely determined Antarctic surface temperatures is assessed (section 4.6).

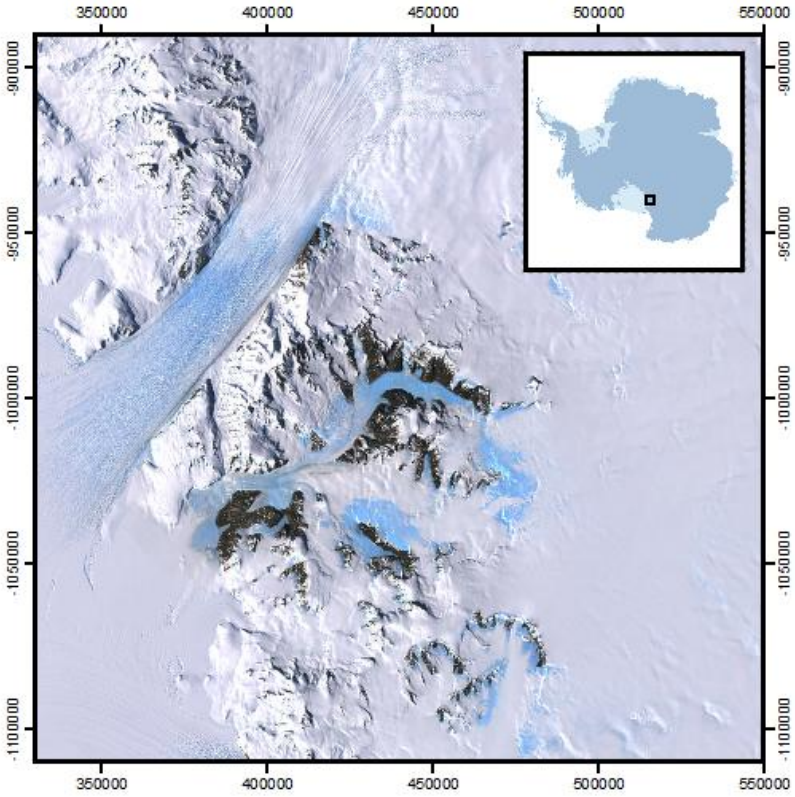

Figure 4.1. Location and outline of the nested model domain (1 km resolution) within the all-Antarctic model domain (insert map, 20 km resolution).

The model setup applied in Chapter 5 involves the nesting of a 1 km grid resolution model within an all-Antarctic 20 km grid resolution model (centred at the South Pole, Figure 4.1). The location of the nested grid was chosen so that the entire DHGS catchment (Figure 1.1) is included and the nested grid boundaries upstream and downstream of the DHGS are located in flat terrain, in order to minimise the error associated with the resolution change. The physical and climatolocical grids required for the nested model are 220 x 220 km in size and are in Polar Stereographic Projection (central meridian, 0°, standard parallel, 71° S) with the lower left corner easting/northing at 330000 m/-1110000 m (Figure 4.1). Maps of surface elevation and bedrock topography were referenced to the OSU91A geoid.

4.1 Surface elevation

Several DEMs of various resolutions cover parts or whole of the nested model domain (Figure 4.2, section 2.2). In this section, the DEMs which best depict the surface topography in any given region are combined to construct one consistent DEM which covers the entire nested model domain. This DEM enables the construction of a map of bedrock topography which is

used to describe variations in glacier morphology within the DHGS (section 3.5.3) and as input to the ice sheet-shelf model (Chapter 5).

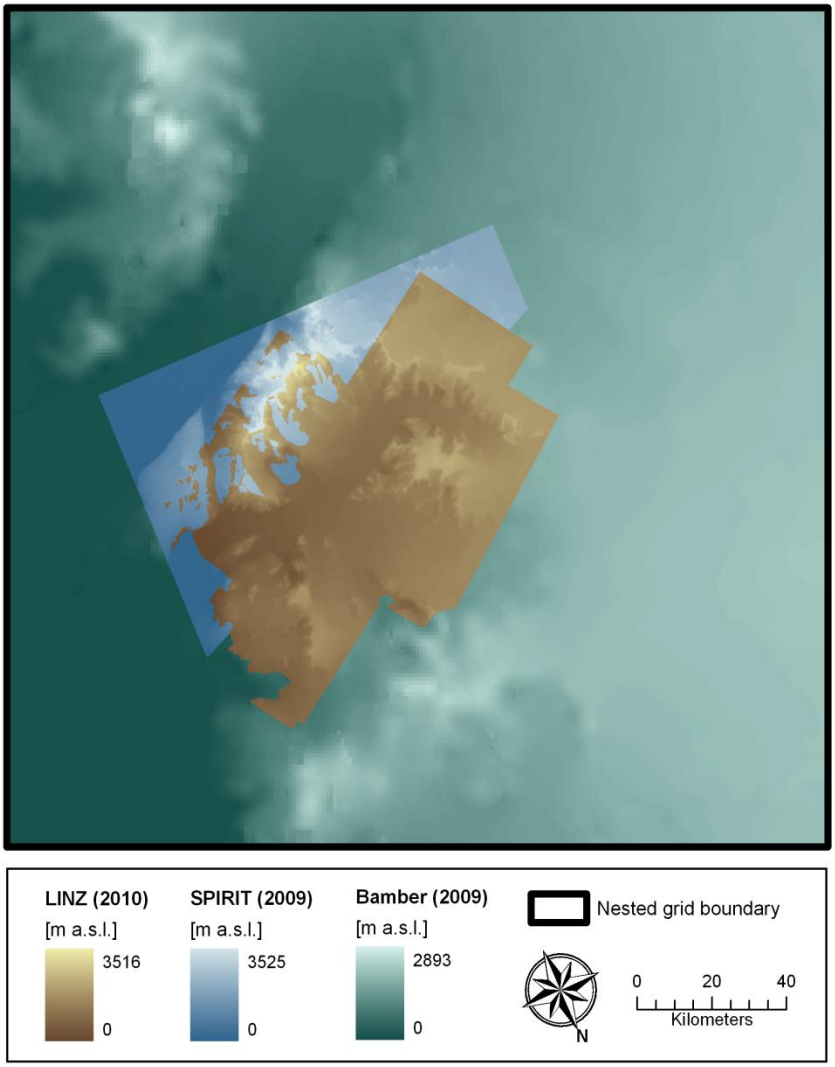

Figure 4.2. Overview of the coverage of the three DEMs utilised to produce the final model of surface elevations within the nested grid.

The DEMs that cover the DHGS were described in detail in section 2.2. Of the two high-resolution models, the LINZ DEM (LINZ 2010) includes the most detail and the SPIRIT DEM (Korona et al. 2009) is consequently only used in regions which were not covered by the LINZ model. Outside the area covered by the two high-resolution models, one of the lower resolution models is applied. The performance of the RAMP DEM (Liu et al. 2001) and the Altimetry DEM (Bamber et al. 2009a) were evaluated by comparing them to the LINZ DEM in overlapping regions. The RAMP DEM performs best in hilly terrain but poorly over the ice

surface, while the Altimetry DEM significantly underestimates the surface elevation in steep terrain but performs much better than the RAMP DEM on the flat glacier surface. The surface topography inland of the DHGS is consequently likely to be best described by the Altimetry DEM and this model was therefore used together with the LINZ and SPIRIT DEMs to produce a new elevation model (Figure 4.2). The DHGS catchment basins calculated from the RAMP and Altimetry DEM (Figure 1.1) differ significantly. The above analysis shows that the catchment area calculated from the Altimetry DEM is likely to be most accurate.

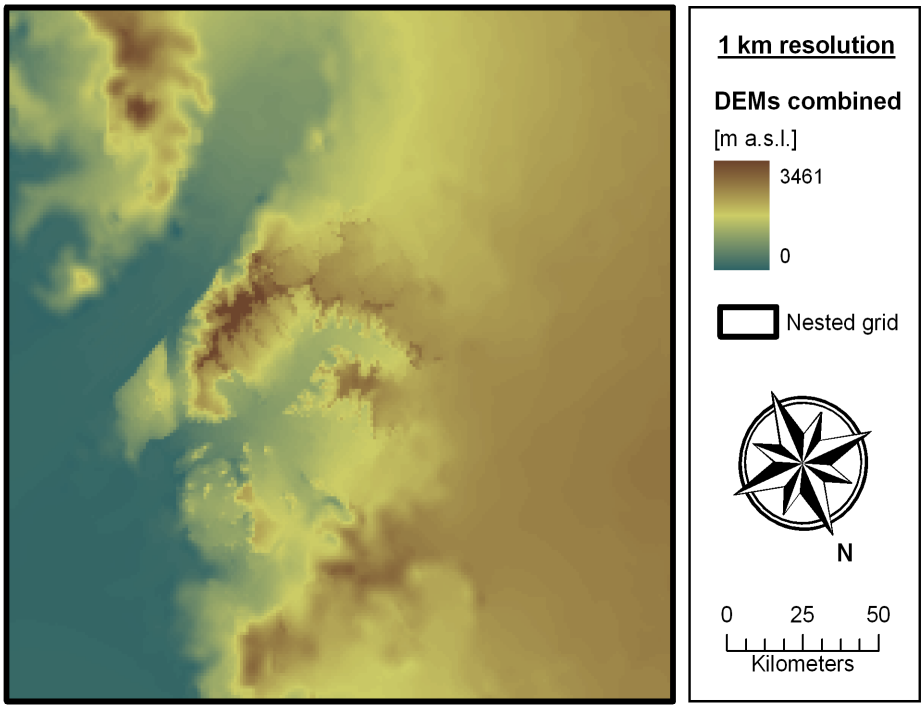

Figure 4.3. DEM for the nested grid constructed from the LINZ, SPIRIT and Bamber et al. (2009a) datasets.

In order to merge the DEMs, all models were resampled to 50 m cell size using a cubic convolution. No systematic deviations exist between the three DEMs, and generally only minor discrepancies are observed at the boundaries despite the differences in data quality and resolutions. Therefore, to preserve as much of the original models as possible, surface elevations were adjusted only in narrow zones of ±1 km at boundaries between the LINZ and SPIRIT DEMs, and zones of ±2 km at boundaries between the LINZ/SPIRIT and Altimetry DEMs where larger initial discontinuities exist. At the boundaries between the LINZ and SPIRIT DEM the transition was smoothed by calculating mean values within 100 m radius circles, except at the glacier mouth where 500 m radius circles had to be applied. At the Altimetry DEM boundaries, the transition was smoothed by calculating mean values within 500 m radius

circles and by using a weight based algorithm to blend the DEMs across 1 km overlapping regions.

The final 50 m resolution DEM was used to calculate the detailed map of bedrock topography (Figure 3.18) described in section 3.5.3. The DEM was resampled to a 1 km cell size by cubic convolution to produce the map of surface elevation required to calculate elevations of the ice base within the nested model domain (Figure 4.3). Almost no evidence of the original model boundaries remains following the merging and local smoothing. The steep topography and valleys adjacent to the Hatherton Glacier are well resolved by the new DEM, which is of importance when comparing model output with currently exposed moraines and glacial drift limits. In contrast rock outcrops at the margin of the Byrd Glacier, which are covered by the Altimetry DEM, have a much smoother appearance. By combining three datasets into one coherent DEM, the steep topography surrounding the DHGS is preserved in a model which covers the entire surveyed regions and nested model domain.

4.2 Ice thickness

In order to produce a map of ice thickness which covers the entire nested grid, the high resolution interpolation map of the immediate DHGS area (Figure 3.18) was merged with an existing map of Antarctic ice thicknesses produced by (Le Brocq 2010a, ALBMAP). The ice thickness interpolation outside the DHGS region relies on few direct measurements (Lythe et al. 2000a) and large discontinuities exist at the boundaries between the two datasets. Consequently, considerable smoothing and interpolation was required to combine the two maps.

The two datasets were resampled by cubic convolution from their original resolutions of 50 m (Figure 3.18) and 5 km (Le Brocq et al. 2010a) to the 1 km nested model resolution. In order to make the boundary as smooth as possible, a 7 km data gap was introduced between the new ice thickness interpolation and the older ice thickness map. Values across the data gap were found by applying an inverse distance weighting interpolation, after which the region was smoothed by calculating mean values within 3 km radius circles.

The general characteristics of the DHGS and the surrounding ice free regions are preserved in the merged map (Figure 4.4). Ice thickness variations in the surrounding regions are smoothed, reaching peak ice thicknesses of up to 2700 m at the head of the Byrd Glacier valley. According to the map, ice thickness of the DHGS exceeds that of the Byrd Glacier at the glacier outlet. The maps merge smoothly on the Ross Ice Shelf where the low resolution ALBMAP is well constrained by ice thickness measurements, while evidence of the map boundary remain on the polar plateau where uncertainties are higher.

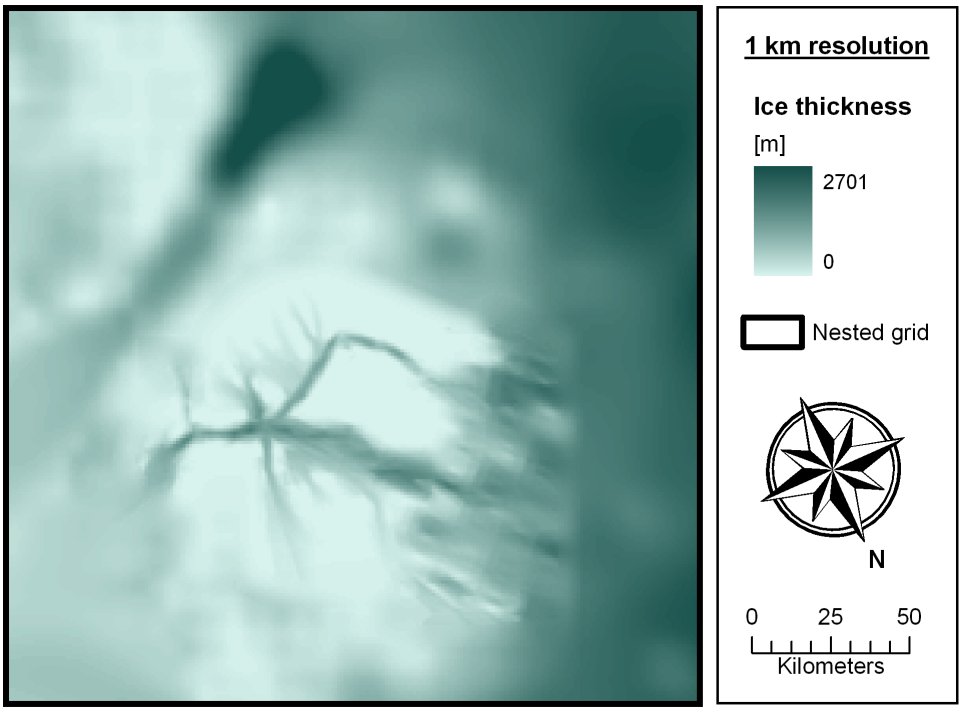

Figure 4.4. Final 1 km ice thickness interpolation map for the nested model domain constructed by compiling new data (Figure 3.18) with the ALBMAP interpolated map.

4.3 Water column thickness

In order to calculate the bedrock topography underneath the floating ice shelf in the lower left corner of the nested grid, water column thickness should be accounted for. However, the ALBMAP water column thicknesses are low at the DHGS mouth and when applying these together with surface elevation (Figure 4.3) and ice thickness (Figure 4.4) to calculate bed elevation, a large bedrock bump appears below the Darwin Glacier grounding line (Figure 4.5a).

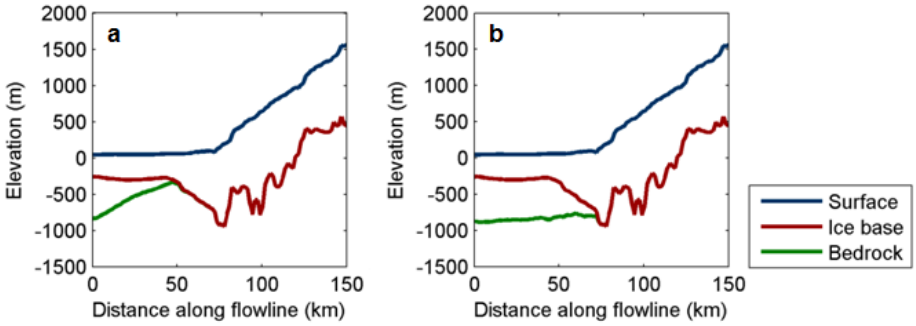

Figure 4.5. Surface elevation, ice base and bedrock elevation (a) before and (b) after removing the bedrock bump. The Darwin Glacier grounding line is located at ~75 km distance.

As radar waves do not penetrate below the base of the floating ice (section 3.1.1), the ALBMAP interpolation relies on two seismic measurements only in this region, both of which are located downstream of the bump (Figure 2.2). It seems unlikely that a bedrock bump of this size would be located below the Darwin Glacier grounding line without leading to a significant grounding line advance (section 3.8) and as the presence of the bump is not supported by direct measurements, it is more likely a result of the interpolation routine utilised to construct ALBMAP. Consequently, the water column thickness was adjusted so that the bedrock topography changes gradually between the bed elevations measured at the Darwin Glacier grounding line by the GPR and the downstream seismic measurement (Figure 4.5b). Following these corrections, the water column thickness reaches peak levels of 625 m downstream of the DHGS.

Although there is evidence to suggest the presence of similarly unsubstantiated shallow water downstream of the Byrd Glacier grounding line (Figure 4.6), the water column thickness was adjusted downstream of the DHGS only. This is likely to lead to inaccurate model simulation of the Byrd Glacier behaviour. However, it is beyond the scope of this study to correct these uncertainties.

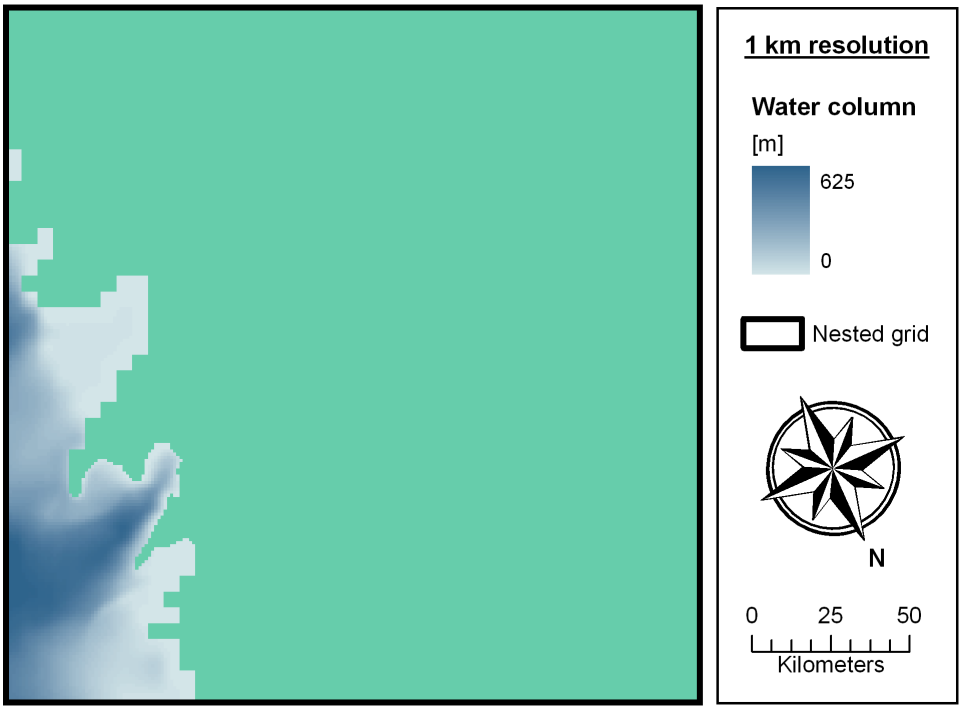

Figure 4.6. Adjusted water column thickness map. Green colour indicates regions within the grid where the ice is grounded.

4.4 Bedrock topography

The elevation of the bed (Figure 4.7) was calculated by subtracting the ice thickness (Figure 4.4) and water column thickness (Figure 4.6) from the surface elevation (Figure 4.3). Both the glaciated and non-glaciated valleys adjacent to the Hatherton Glacier are well resolved (Figure 4.7) in the resulting map and the bedrock topography changes gradually below the Darwin Glacier grounding line. The lowest bed elevations of close to 1990 m below sea level are found at the head of the Byrd Glacier. Further downstream, bed elevation underneath the Byrd Glacier increase rapidly and are significantly higher than measured at the Darwin Glacier grounding line (Figure 3.17).

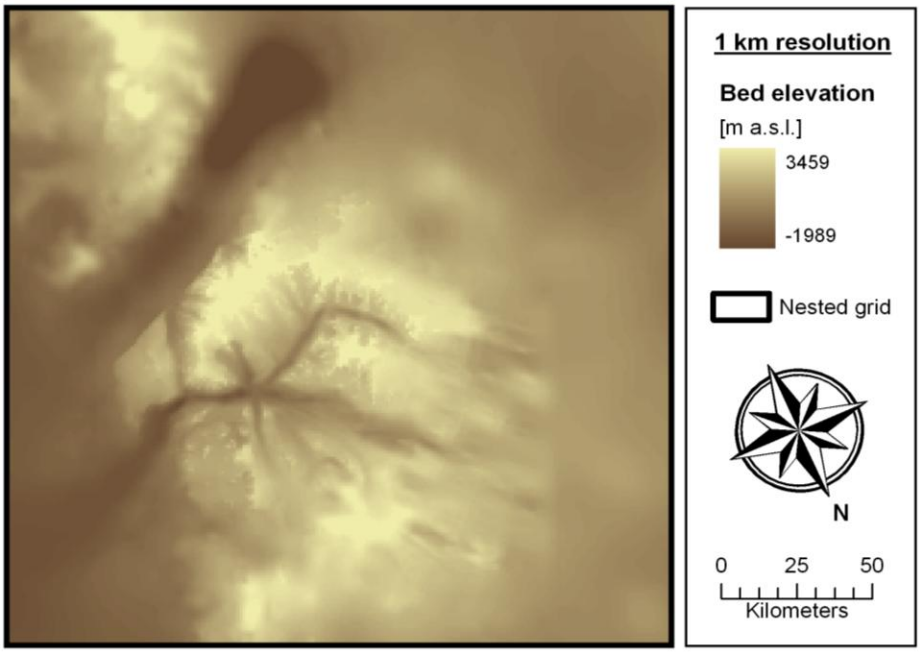

Figure 4.7. Bedrock topography calculated from the surface elevation (Figure 4.3), ice thickness (Figure 4.4) and the adjusted water column thickness map shown in Figure 4.6.

4.5 Surface mass balance

In situ measurements of SMB are rare in Antarctica and for large parts of the continent no measurements exist at all. As a consequence, maps of Antarctic SMB are currently produced by applying remote sensing techniques to control the interpolation routine between in situ measurements (Arthern et al. 2006; Vaughan et al. 1999a) or from regional climate models which are becoming more and more reliable as the model algorithms improve (van de Berg et al. 2006). The poor spatial resolution of regional climate models and the sparse number of in situ measurements, however, means that these maps do not capture the small scale variability in SMB which characterises DHGS and mountainous regions of Antarctica in general. As a consequence of these uncertainties, comparison of Antarctic SMB maps to ice flux of large TAM outlet glaciers have found evidence to suggest that current maps overestimate SMB in low accumulation regions (Frezzotti et al. 2000; Stearns 2007). The lack of accurate SMB maps has lead to considerable uncertainties in mass balance and modelling studies (Anderson et al. 2004; Golledge and Levy 2011; Stearns 2007).

In this section, the processes which influence SMB of the DHGS are investigated in detail after which direct measurements of sublimation will be combined with existing SMB maps to produce an improve gridded dataset for the DHGS.

4.5.1 Automatic weather stations

Four AWSs installed in the Darwin-Hatherton region constitute the first continuous measurements of meteorological parameters in the area (Figure 4.2). The Lower Darwin, Upper Darwin and Hatherton AWSs operated during summer months only between 2006 and 2008 (Zawar-Reza et al. 2010). Brown Hills AWS, which is operated by the National Institute of Water and Atmosphere (NIWA), is the only year round weather station in the region and has been operational since November 2004 (Table 4.1). The Upper Darwin, Lower Darwin, Hatherton and Brown Hills AWSs are resting on surfaces of snow, blue ice (possible melt influenced), blue ice (smooth) and rocks respectively. In addition the Mary and Mulock AWSs operated by the University of Wisconsin (http://amrc.ssec.wisc.edu/) are located approximately 100 km north of the DHGS and are the two closest continuous year round weather stations. The Mulock AWS is located high on the Mulock Glacier in a similar setting to the Upper Darwin AWS while the Mary AWS is situated on the ice shelf downstream of the glacier outlet. These two stations are used in section 4.6 to investigate mean annual air temperatures (MAAT) within the DHGS.

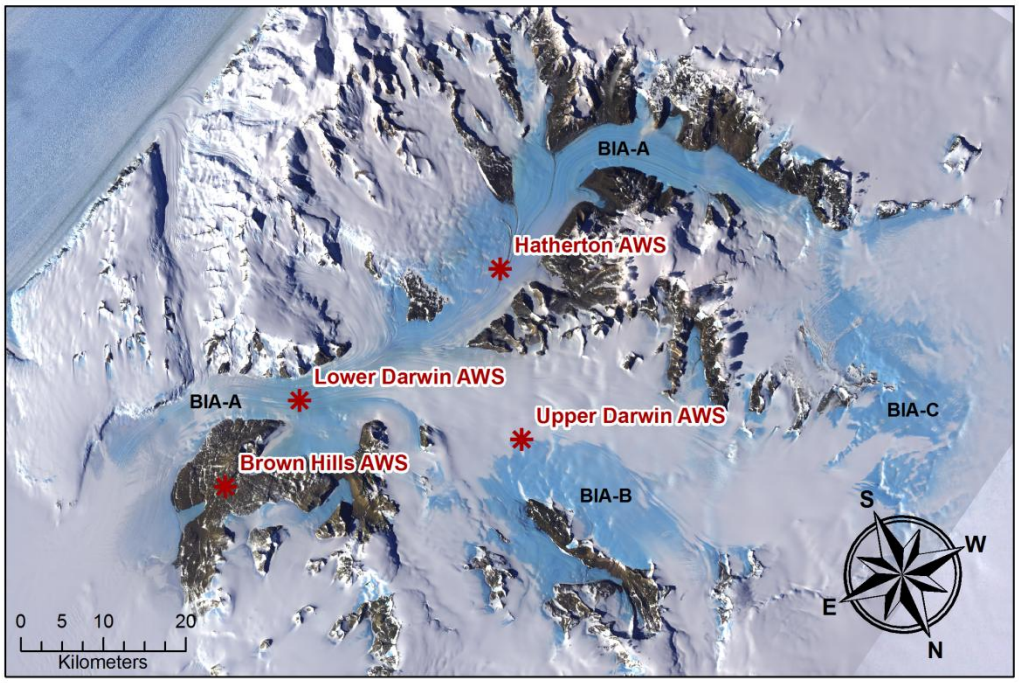

Figure 4.8. Locations of various AWSs in the Darwin-Hatherton region and the three largest BIAs described in section 2.4. Map based on ASTER images (https://lpdaac.usgs.gov/).

The analysis of SMB is based primarily on measurements of changes in relative surface height collected by the two SR50A sonic ranging sensors (measurement accuracy of ±1 cm, Cambell

Scientific Inc.) which were installed at the Upper Darwin and Hatherton AWSs during two summer seasons. The sonic sensors measure the shortest distance to an uneven surface. Surface heights were measured every 10 minutes and automatically corrected to the influence of air temperature on the speed of sound. A recording of data quality was logged for every data point and unreliable measurements are observed in the dataset during precipitation events and periods of inferred snow drift. To minimise the influence of noise in the dataset, poor quality data were removed and data gaps were filled by linear interpolation, after which the hourly mean surface elevations were calculated.

Table 4.1. Overview of weather stations in the proximity of the DH region.

AWS	Position	Elevation [m a.s.l.]	Operation period	Data
Lower Darwin	79.89 S 158.69 E	586	05-12-06 – 30-01-07 17-11-08 – 27-01-09	Air temperature Ice temperature Relative humidity Pressure Wind speed Wind direction
Upper Darwin	79.76 S 157.48 E	969	17-11-07 – 22-01-08 10-11-08 – 29-12-09	Air temperature Ice temperature Relative humidity Pressure Wind speed Wind direction Short-wave (down) Net radiation Relative surface elevation
Hatherton	79.95 S 157.19 E	927	17-11-07 – 22-01-08 10-11-08 – 27-01-09	As for Upper Darwin
Brown Hills	79.84 S 159.32 E	330	16-11-04 – present	Air temperature Relative humidity Wind speed Wind direction
Mulock	78.92 S 159.00 E	1000	01-10-06 - present	As for Lower Darwin
Mary	79.31 S 162.99 E	58	01-10-06 - present	As for Lower Darwin

Surface lowering will occur when mass is lost by sublimation, wind erosion or melting and when the snowpack is subjected to densification. In low accumulation regions, snowpack densification may range from 1 to 27% of the annual accumulation, most of which occurs during the summer when air temperatures are highest (Eisen et al. 2008). Considerable uncertainties are consequently involved with converting variations in relative surface height to change in SMB in snow-covered regions where snow densities are unknown (Takahashi and Kameda 2007). A surface increase can be caused by accumulation from synoptic events,

riming as well as by snow-drift deposition by wind. Due to the variety of possible explanations for the measured variations, the data are best interpreted in combination with measurements of other meteorological parameters.

The remainder of the meteorological parameters were checked for outliers before mean hourly values were calculated to reduce noise. The Mulock AWS dataset of air temperature was found to be particularly noisy, and a median filter (over three consecutive measurements) was applied before the hourly averaging.

4.5.2 Surface climatology at the Upper Darwin and Hatherton AWSs

A subset of measurements of meteorological parameters at the Upper Darwin and Hatherton AWSs is presented below in order to examine the processes which influence SMB within the DHGS in detail (objective A.3).

In the satellite image from December 2002 shown in Figure 4.8, the Hatherton and Upper Darwin AWSs are located on blue ice and snow-covered surfaces respectively. Calculations of surface albedos for the two summer periods following the same approach as Zawar-Reza et al. (2010) show that values at the Hatherton (0.62) and Darwin AWS (0.78) remain at levels characteristic of blue ice and snow-covered surfaces. This suggests that the Hatherton AWS is located on exposed blue ice with insignificant periods of snow cover, whereas the Upper Darwin AWS is located on a surface which is constantly snow covered. It is consequently inferred that the BIA outlines shown on the satellite image accurately depicts the general conditions of the DHGS surface.

The variations of meteorological parameters (hourly averages) shown in Figure 4.9 reflect the differences in surface conditions observed between the two weather stations. Although the two AWSs record similar meteorological conditions overall, a number of differences can be distinguished. For example, the air temperature at the higher elevation Upper Darwin AWS is constantly lower with a more pronounced diurnal cycle (Figure 4.9a). Winds are generally stronger and more stable at the Hatherton AWS (Figure 4.9b), and may change within a few hours between relatively calm anabatic (up-slope) winds (~60°) and powerful katabatic winds (~240°). The wind patterns at the Upper Darwin appear more chaotic, and katabatic winds (~320°) are less developed (Figure 4.9c). The mechanisms controlling wind behaviour at the DHGS have been discussed by Zawar-Reza et al. (2010) and will not be dealt with in more detail here. Calculated relative air humidity is generally low during katabatic winds, particularly at the Hatherton AWS where the winds are most developed (Figure 4.9d).

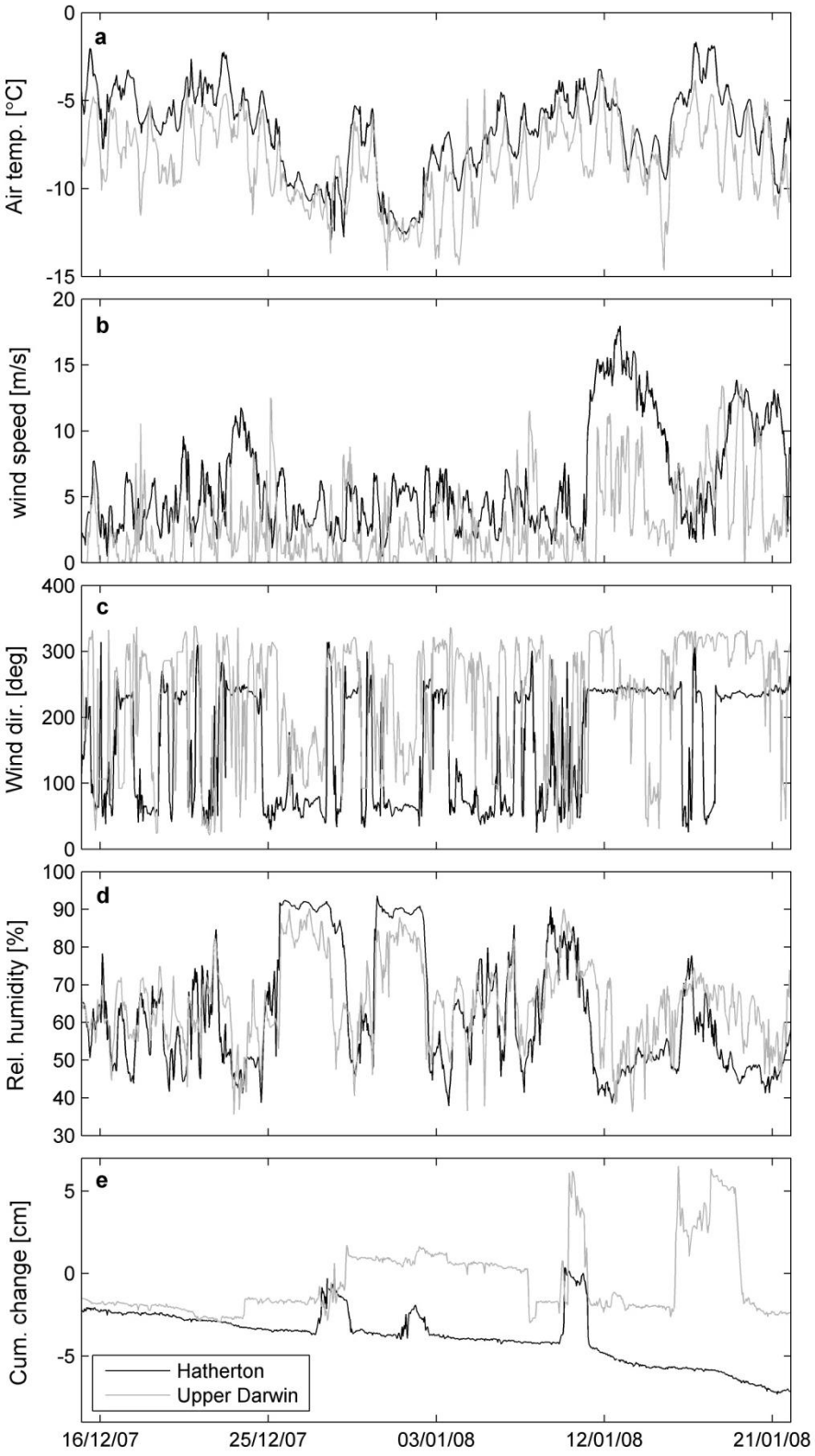

Figure 4.9. Hourly mean values of (a) air temperature, (b) wind speed, (c) wind direction, (d) relative air humidity and (e) cumulative change in surface height. The surface elevation is 0 m on 17 November 2007 when measurements began.

The measured changes in surface height (Figure 4.9e) indicate episodes of surface accumulation (precipitation, snowdrift deposition), ablation (sublimation, snow erosion) and possibly snow densification. In general, observed timing and magnitude of major changes in surface height differ significantly between the two locations. At the Hatherton AWS, three distinct episodes of accumulation (surface height gain) of between 2 and 5 cm are superimposed on an overall gradual decrease in surface height. The accumulation events coincide with periods of high relative humidity and low wind speeds, and as source areas of snow for drifting are sparse in the Hatherton catchment, these events are likely to reflect precipitation and not snow drift deposition. The termination of precipitation events are indicated by drops in relative humidity, after which the snow is rapidly removed from the glacier surface, by what is inferred as wind erosion. Ablation by sublimation will appear in the record as a much more gradual decrease in surface height than snow erosion (Reijmer and van den Broeke 2003) and is thought to explain the observed overall decrease in surface height between accumulation events. Evidence of the main drivers of ablation over BIAs in the DHGS can be observed between 11-14 January and between 18–21 January at the Hatherton AWS. During these two periods, increased surface lowering coincides with particularly strong and dry katabatic winds (wind speeds >10 m/s) and relatively high air temperatures, characteristic of conditions favourable for sublimation (Bintanja and Reijmer 2001). As air temperatures peak during the intermediate period of low sublimation rates, katabatic winds are likely to be the main driver of sublimation on the Hatherton Glacier.

The changes in surface height observed at the Upper Darwin AWS are much more dramatic than at the Hatherton AWS. Four prominent and several smaller episodes of snow accumulation occur at the surface during the period shown in Figure 4.9e. Several of these are unaccounted for in the Hatherton record and may relate to local snowdrift deposits or precipitation events at the Upper Darwin AWS, or immediate snowdrift erosion of precipitated snow at the Hatherton AWS. Either way, they document the large variability which exists within the DHGS. Accumulation events are not only more abundant at the Upper Darwin than at the Hatherton AWS, but also lead to larger height gain. The maximum accumulation event recorded during the two summer seasons occurred at the Upper Darwin AWS on 30 November 2007 when the surface height increased by 12.5 cm in 24 hours, during which time no change was registered at the Hatherton AWS. Once snow has been deposited it tends to remain on the surface at the Upper Darwin AWS for a relatively long period before being rapidly removed by the wind. This differs from observations at the Hatherton AWS and the difference is likely to be a result of the generally lower wind velocities and the increased surface roughness over snow at the Upper Darwin AWS, which acts to limit snow erosion at lower wind speeds (Bintanja 2001; Bintanja et al. 2001). In between the rapid stepwise changes in surface elevation observed at the Upper Darwin AWS, a gradual decrease in surface height occurs, which likely reflects either sublimation or densification of the snowpack.

The rate of change in relative surface height is similar during the two summers at the Hatherton AWS, but differs significantly at the Upper Darwin AWS (Table 4.2). The latter measurements consequently fail to provide an unequivocal result of the SMB at this location.

Table 4.2. Average daily changes in relative surface height during the two AWS measurement periods and in brackets the number of days that each station was operational.

AWS	Surface change 2007/08 [cm day^{-1}]	Surface change 2008/09 [cm day^{-1}]
Upper Darwin	-0.04 (*67*)	+0.05 (*50*)
Hatherton	-0.11 (*67*)	-0.10 (*79*)

In summary, the AWS data indicate that the Hatherton AWS is located on exposed blue ice which experiences significant surface sublimation driven primarily by dry katabatic winds. Snow accumulates for short periods only, before being eroded away by strong winds. By contrast, the Upper Darwin AWS is situated on a surface of snow and experiences more frequent and larger accumulation events (precipitation/snowdrift deposition), most of which are removed by eroding winds. The Upper Darwin AWS is located close to the lower equilibrium line of BIA-B and annual snow accumulation at this location is therefore expected to be low. This is reflected in the small surface lowering which occurs in 2007/08 and equally small height increase in 2008/09. Consequently, the above analysis of controls on SMB does not cover the regions within the DHGS which are characterised by high accumulation rates. Nevertheless, it does describe the main processes responsible for accumulation and ablation in the DHGS and the variations that may exist even within short distances.

4.5.3 Annual SMB at the Hatherton AWS

The nested ice sheet-shelf model requires as input a map of present-day SMB. In this section, the relative surface elevation changes observed at the Hatherton AWS are converted into annual SMB based on seasonal patterns in sublimation observed for year round AWSs in other Antarctic regions. As the Upper Darwin AWS is located on a predominantly snow-covered surface (section 4.5.2), and the changes in surface height varies considerably between the two summer seasons, the measurements are not utilised in this analysis. The Hatherton AWS point estimate of SMB is used to establish a relationship between elevation and sublimation in DHGS BIAs (section 4.5.4), as has previously been documented for other Antarctic ablation areas.

To arrive at an estimate of annual SMB at the Hatherton AWS location, the data from the two summer periods must be extended to the remainder of the year. Potential changes in accumulation patterns must first be evaluated, as several studies have found that atmospheric accumulation in Antarctica demonstrates a slight peak during the winter (Bintanja and Reijmer 2001). It was demonstrated in section 4.5.2 that snow is unlikely to remain at the Hatherton Glacier surface during the summer. Furthermore, the wind velocities within the DHGS are generally stronger during the winter (section 2.3), which suggests that snow would also be unlikely to stay on the glacier surface for extended periods during this time. The influence of snow accumulation on the annual SMB at the Hatherton AWS is consequently assumed to be negligible.

In contrast, seasonal variations in sublimation rates are likely to have a significant influence on the annual SMB at the Hatherton AWS. Rates of sublimation are enhanced during warm, dry and turbulent conditions, and in general the majority of total annual surface sublimation occurs during the 3–4 months of Antarctic summer when incoming solar radiation and air temperature are at their highest (Bintanja 1999; Bintanja and Reijmer 2001; Fountain et al. 2006; Hoffman et al. 2008). Winter sublimation is primarily associated with the development of strong gravity-driven katabatic winds (Bintanja 1999; Fountain et al. 2006; Hoffman et al. 2008).

In order to account for sublimation outside the measurement period (see Table 4.1 for dates), several assumptions were made. The measurements were collected between mid November and late January and therefore only span part of the Antarctic summer. No distinct decrease in the rate of surface lowering was observed at the end of the data collection periods, and the recorded average daily surface change (Table 4.2) was applied from the end of the data collection period (Table 4.1) until 1 February. An intermediate sublimation rate of half the measured average rate was assumed between 1 November and the data collection start date, as well as throughout all of February, to account for a seasonal transition.

Sublimation rates at a BIA in Dronning Maud Land (type I) with similar summer temperatures as the Hatherton AWS were such that 70% of the annual sublimation occurred in the period between 1 November and 1 March (Bintanja and Reijmer 2001). Annual sublimation rates at the Hatherton AWS are calculated under the assumption that a similar relationship exists between summer and winter sublimation at this location. Annual sublimation rates at the Hatherton AWS were calculated at -13.6 cm w.e. (2007/08) and -12.8 cm w.e. (2008/09). The measured surface lowering of 6.5 cm w.e. (17 Nov 2007 to 11 Jan 2008) and 7.0 cm w.e. (10 Nov 2008 to 27 Jan 2009) constitute roughly half of the calculated annual value.

Despite the shortcomings of this approach, the annual values for the Hatherton AWS fit well within the framework suggested by previous studies, such as the 13 cm w.e. found for a BIA in Dronning Maud Land further north (74.6° S, Bintanja and Reijmer 2001) and 0.17 – 0.23 cm w.e. found for a BIA near the Reedy Glacier further south (86° S, Todd et al. 2010). However, the extrapolation of summer measurements is highly uncertain as differences exist between BIA type, latitude and surface elevations. Very little is known about the valley type BIAs (type II, Takahashi et al. 1992) present on the DHGS surface, and the area is located further south of most well-studied ablation areas. It is possible that because the BIAs in the Darwin-Hatherton region are closely related to the presence of strong katabatic winds, which persist throughout the year, they may experience proportionally more winter sublimation than a typical type I BIA. Alternatively, the fact that the DHGS BIAs are located further south of other well studied areas and are sheltered by steep topography should work to reduce incoming solar radiation and consequently summer sublimation. Despite the uncertainties associated with the above calculation, it currently represents the best estimate of annual sublimation rate at the Hatherton AWS and will be used below to infer sublimation rates in other DHGS BIAs.

4.5.4 SMB variations with elevation in DHGS ablation areas

In order to determine the DHGS SMB, the point measurement described above must be extrapolated to the surrounding ablation areas (regions of negative SMB). Due to the uncertainties surrounding this extrapolation, a range of SMB models are constructed in this section, and subsequently tested with the nested ice shelf-sheet model (section 5.5.5). In all models, a SMB of zero is assigned to regions of exposed bedrock and at the downstream equilibrium line of large BIAs (ice-snow boundary). In addition, as the GPR data presented in section 3.7 document a positive SMB close to the lateral limit of BIA-B (Figure 4.8), a positive SMB was inferred from the western BIA-B boundary (Figure 4.10).

The first SMB model (MB-1) includes snow-covered ablation areas. Based on simple approximations of ice velocity, average ablation rates and firn layer thickness and density (van den Broeke et al. 2006), the upstream equilibrium lines (SMB = 0) of BIA-A, B and C (Figure 4.8) were inferred to be located 15 km upstream from exposed blue ice. The outline of the MB-1 ablation area is shown Figure 4.10 (orange line).

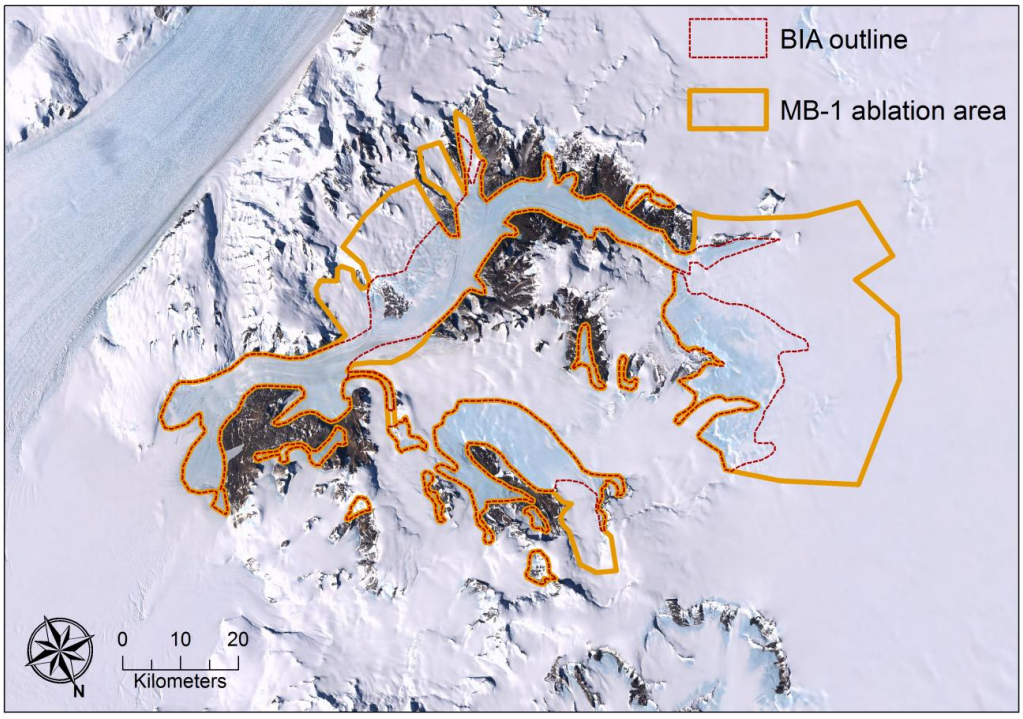

Figure 4.10. Outline of the MB-1 ablation areas (orange line) and the largest DHGS BIAs (dashed red line) which also delineate the extent of the ablation areas of MB-2, MB-3 and MB-3A, as well as the region of zero SMB in MB-4. The remaining snow covered regions were inferred to exhibit a positive SMB while rock outcrop have SMB of zero.

Ablation rates within the DHGS ablation areas are expected to change in relation to variations in snow accumulation and sublimation, the latter of which depends strongly on the annual air temperature and consequently altitude of the BIA (Bintanja 1999; Robinson 1984). To accommodate inferred regional changes in sublimation rates, the MB-1 ablation areas were divided into three categories based on surface elevation (Figure 4.11). For BIAs upstream of the confluence of the Hatherton and Darwin Glaciers (720 m a.s.l.) and downstream of the uppermost part of the Hatherton Glacier (1300 m a.s.l.), SMB was assumed to increase with increased elevation as the magnitude of sublimation decreases in response to lower air temperatures (Figure 4.11). In these regions, the elevation lapse rate of sublimation measured at the similar Taylor Glacier ablation area (2.2 cm w.e. per 100 m) was applied (Robinson 1984). For BIAs and snow-covered ablation areas above 1300 m a.s.l. the SMB was assumed to increase less steeply towards 0 cm w.e. yr^{-1} at 2090 m a.s.l., which is the elevation of the uppermost equilibrium line for MB-1 (Figure 4.10).

It is generally accepted that atmospheric precipitation increases from the dry Antarctic polar plateau towards the Ross Ice Shelf (Bockheim et al. 1989; van den Broeke et al. 2006). In the DHGS more snow is generally observed on the glacier surface downstream of the Hatherton

and Darwin glacier confluence (720 m a.s.l.), and downstream of the glacier outlet (lowermost section of equilibrium line at ~50 m a.s.l.) the glacier surface becomes permanently snow covered (Figure 4.8). For MB-1 it is therefore assumed that below 720 m a.s.l. SMB increases linearly from the minimum value of -17 cm w.e. yr^{-1} to 0 cm w.e. yr^{-1} at the down-flow equilibrium line of BIA-A (Figure 4.11).

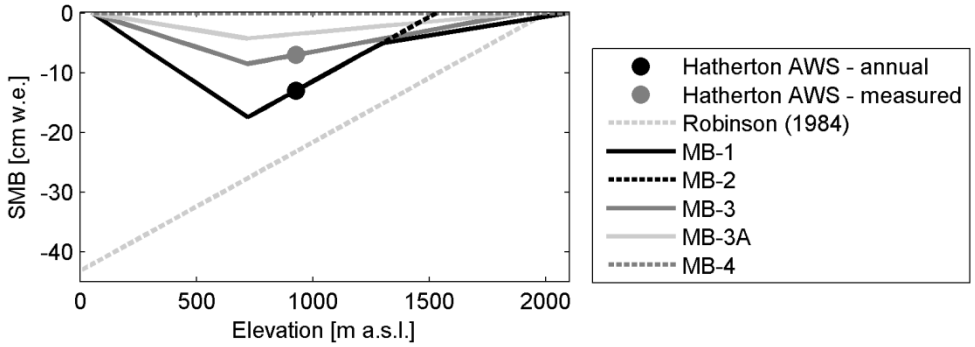

Figure 4.11. Variation in SMB for ablation areas between 50 and 2090 m a.s.l. as predicted by the three SMB scenarios. The black circle shows the calculated annual ablation at the Hatherton AWS while the grey circle illustrates measured ablation during the longest data record (2008/09). The light gray dashed line shows the relationship between elevation and annual SMB measured by Robinson (1984) for the Taylor Glacier ablation area.

The second SMB model (MB-2, Figure 4.11) assumes a much steeper SMB gradient between blue ice and accumulation areas by ignoring the effect of snow-covered ablation areas (ablation area outline shown with dashed red line in Figure 4.10). MB-2 differs from MB-1 only above 1300 m a.s.l. where MB-2 continues to increase linearly with increasing elevations, reaching 0 cm w.e. yr^{-1} at 1530 m a.s.l. To include ablation in BIA-C which is located at elevations above 1530 m a.s.l., a constant SMB of -5 cm w.e. yr^{-1} was assumed for this BIA.

The third SMB model (MB-3, Figure 4.11) differs considerably from both MB-1 and MB-2 in that sublimation outside the recorded period is ignored. This model therefore recognises that little is known about the seasonal changes in SMB for valley type BIAs, and that the DHGS BIAs are located further south than other well-studied Antarctic BIAs. Due to these uncertainties, it is possible that sublimation outside the recorded period may be less important than is suggested in the above analysis. In MB-3 a linear increase in SMB is assumed between the Hatherton AWS and the highest elevated BIA (~1900 m a.s.l., 0 cm w.e. yr^{-1}) resulting in a more gentle SMB gradient than documented for the Taylor Glacier (Figure 4.11, Robinson 1984). Maximum ablation is still assumed to occur at the glacier confluence (720 m a.s.l.), from which the SMB increases linearly to 0 cm w.e. yr^{-1} at the BIA equilibrium line at 50 m

a.s.l. Snow covered ablation areas are ignored in MB-3 and the ablation area outline is similar to MB-2 (Figure 4.10).

In order to test the full range of SMB models with the nested ice sheet-shelf model, a simple end-member model (MB-4, Figure 4.11) was constructed by assuming a SMB of zero in all BIAs and by ignoring the presence of snow-covered ablation areas. If snow accumulation is accurately determined in regions of net mass gain, this SMB model represents an absolute maximum for the SMB within the DHGS under present-day conditions.

4.5.5 Surface mass balance maps

Because of the lack of reliable direct measurements of snow accumulation rates within the DHGS, the estimates of ablation within the ablation areas (section 4.5.4) were combined with existing gridded datasets of Antarctic accumulation rates (Arthern et al. 2006; van de Berg et al. 2006) to produce a range of SMB maps which cover the entire nested model domain.

The annual SMB in DHGS ablation areas were calculated by combining the elevation lapse rate of SMB suggested by the four models shown in Figure 4.11 with the DEM presented in section 4.1. In order to account for a gradual decrease in ablation towards ablation area boundaries not explained by any of the relationships shown in Figure 4.11 (for example the western BIA-B boundary), the SMB was gradually increased towards these boundaries across a 5 km transition zone. The estimates of ablation area SMB were integrated with the van de Berg et al. (2006) and Arthern et al. (2006) datasets by imposing a 5 km wide transition zone of gradually increasing accumulations rates from assumed equilibrium lines. This zone was increased to 15 km downstream of BIA-A and towards the EAIS, where SMB gradients are thought to be smaller than in regions where changes in SMB are influenced by nearby exposed bedrock (Brown and Scambos 2004). SMB in the transition zones were interpolated using a regularised spline interpolation routine and the resulting interpolations were subsequently smoothed by calculating mean values within 3 km radius circles.

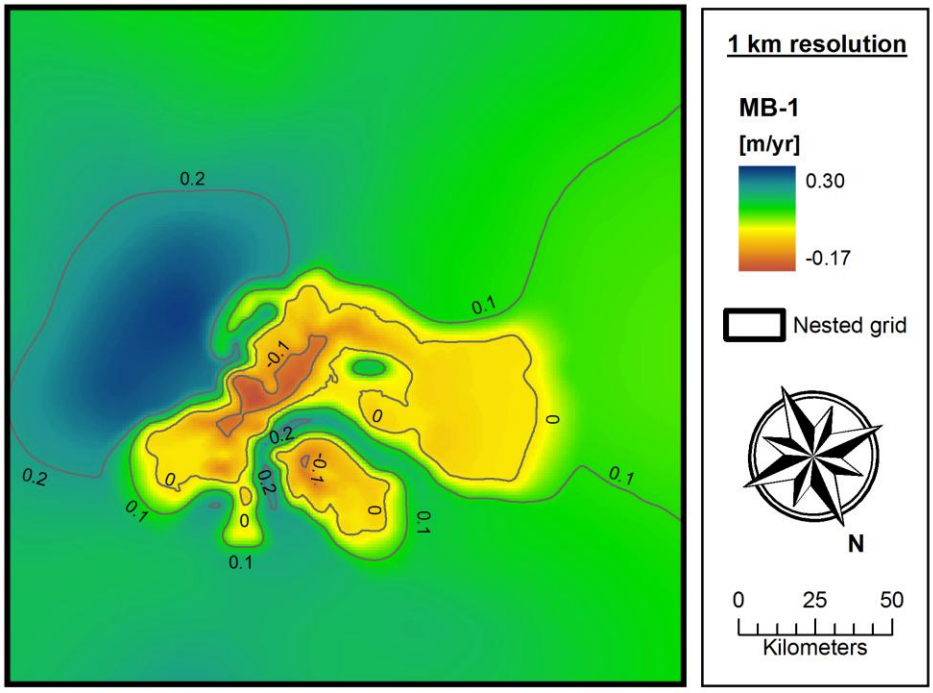

Figure 4.12. MB-1 with Arthern et al. (2006) accumulation rates within the nested model domain.

A total of eight different SMB maps were produced by combining MB-1 to MB-4 with existing large-scale datasets of Antarctic SMB (Arthern et al. 2006; van de Berg et al. 2006). The resulting SMB map inferred from the MB-1 scenario (Arthern et al. (2006) accumulation rates, Figure 4.12) predicts annual SMB between a minimum of approximately -0.17 m w.e. yr^{-1} at the confluence of the Darwin and Hatherton Glaciers to maximum accumulation rates of ~0.30 m w.e. yr^{-1} at the mouth of the Byrd Glacier. As the MB-1 scenario accounts for winter sublimation and includes snow-covered ablation areas, the map is likely to most realistically reflect annual SMB at the Hatherton AWS and DHGS ablation area outlines. However, without further direct measurements, the error associated with the temporal and spatial extrapolation of the summer measurements at the Hatherton AWS is unclear. By accounting for the presence of BIA and realistic ablation rates within these, the new SMB maps represent a significant improvement to existing gridded datasets, despite the uncertainties involved.

4.5.6 Validating the SMB scenarios

The DHGS is likely to be close to, or in, equilibrium with the current climate (section 1.5.1), and the calculations of ice discharge near the Darwin Glacier grounding line presented in Table 3.4 therefore provide evidence of the upstream cumulative catchment-wide SMB. As a result,

the accuracy of the various SMB scenarios can be assessed by comparing the catchment-wide SMB to estimates of the grounding line ice discharge (Table 4.3).

Table 4.3. Catchment-wide annual SMB within the DHGS calculated from the eight SMB models described above. For comparison, the last row lists the value suggested by the original van de Berg et al. (2006) and Arthern et al. (2006) models.

Model	SMB [$km^3\ yr^{-1}$] *van de Berg (2006)*	SMB [$km^3\ yr^{-1}$] *Arthern et al. (2006)*
MB-1	0.17	0.29
MB-2	0.31	0.43
MB-3	0.36	0.48
MB-4	0.43	0.58
MB-3A	0.34	0.46
Original SMB map	1.12	1.43

In order to compare calculated grounding line discharge with the SMB models, the degree of basal melting underneath the grounded ice should be accounted for. As basal melting only occurs for a small fraction of the DHGS catchment (section 5.6.2), it is unlikely to exceed 0.02 $km^3\ yr^{-1}$ (6 mm yr^{-1} (section 1.5.2) beneath a third of the catchment area). In section 3.9 it was inferred that ice discharge at the grounding line is best approximated by calculated ice flux through profile D (0.52 $km^3\ yr^{-1}$, Figure 3.14 and Table 3.4). Comparing the estimated grounding line discharge to the upstream catchment-wide SMB, corrected for the estimated basal melt rate (0.02 $km^3\ yr^{-1}$), suggests that MB-1 and MB-2 significantly underestimate the SMB within the DHGS, while the two large-scale maps of SMB overestimates the SMB by more than 100%. The large discrepancy between grounding line discharge and catchment-wide SMB for MB-1 and MB-2 suggests an overestimation of ablation in these models. This in turn implies that winter sublimation within the DHGS is less important than for other Antarctic BIA. However, it is also possible that the differences reflect other uncertainties in accumulation areas or the applied extrapolation routine.

MB-4 with van de Berg (2006) accumulation rates seems to underestimate the catchment-wide SMB, despite the fact that ablation in BIA and snow-covered regions are ignored. This suggests that the van de Berg (2006) model underestimates accumulation rates in DHGS accumulation areas although the model performs better than the Arthern et al. (2006) in its original form. If the DHGS is in equilibrium with the current climate, the DHGS catchment-wide SMB appears to be best represented by either MB-4 or MB-3 with Arthern et al. (2006) accumulation rates. MB-3 also compares better than MB-1 and MB-2 with previous modelling-based investigations of SMB (Figure 2.3, Anderson et al. 2004). It seems incongruous that MB-

4 (no ablation, Arthern et al. (2006) accumulation rates) with a catchment-wide annual SMB of 0.58 km^3 yr^{-1} (~0.56 km^3 yr^{-1} grounding line discharge) provides the best fit with the grounding line discharge. This suggests that accumulation rates predicted by the Arthern et al. (2006) dataset, as with that of van de Berg (2006), underestimates the SMB in accumulation areas within the DHGS.

Experiments conducted with the nested ice-flow model and described in more detail in section 5.5.5, suggest that the best present-day model simulation was achieved by halving the ablation rates predicted by MB-3 (Arthern et al. (2006) accumulation rates), and decreasing snow accumulation in high altitude accumulation areas adjacent to the Hatherton Glacier (MB-3A, Figure 4.11, Table 4.3). MB-3A predicts a catchment-wide annual SMB of 0.46 km^3 yr^{-1} (~0.44 km^3 yr^{-1} grounding line discharge) which implies that the DHGS could presently be losing mass. However, there are considerable uncertainties, and even when accounting for the interannual variations in air temperature which are documented below in Table 4.7, it seems unlikely that the sublimation rate at the Hatherton AWS is on average half of the measured value. This inference is supported by meteorological measurements which illustrate that sublimation rates peak during strong katabatic winds (section 4.5.2) and that these winds persist during the winter period (section 2.3). It consequently seems unlikely that winter sublimation would be negligible in the DHGS. Therefore, although MB-3 and MB-3A may reflect the overall SMB best, they certainly underestimate annual ablation rates at the Hatherton AWS. Instead, the difference between catchment-wide SMB and grounding line ice discharge could reflect uncertainties in the extrapolation routine, which above 720 m a.s.l. relies on a primary dependency of ablation rates on annual air temperature (surface elevation). As illustrated by the meteorological data (section 4.5.2), the development of katabatic winds are important to ablation rates on the Hatherton Glacier, and the relationship between SMB and surface elevation may be less straightforward than suggested by Robinson (1984). This is confirmed by a comprehensive dataset of new SMB measurements conducted on the Taylor Glacier, which illustrates large variations in the relationship between ablation and surface elevation (Kavanaugh et al. 2009a). Other uncertainties include accumulation rates proposed by the original SMB maps, uncertainties in the model simulation. In addition, the Hatherton Glacier may still be adjusting to the termination of the LGM, which will be discussed in more detail in section 5.8.

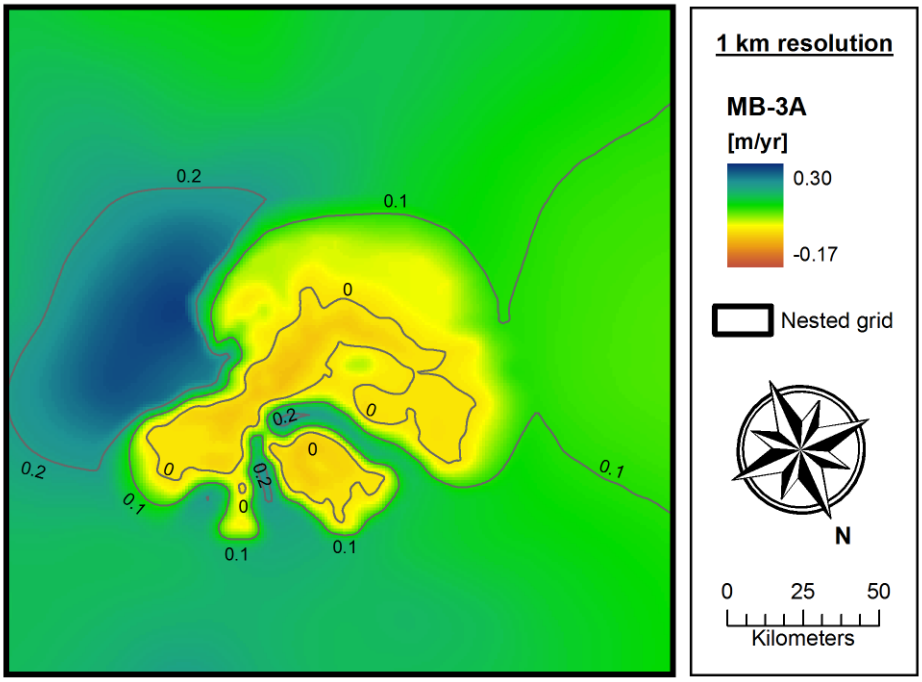

Figure 4.13. MB-3A with Arthern et al. (2006) accumulation rates. The model simulations presented in Chapter 5 utilises MB-3A as input.

Due to the complexity of the terrain which surrounds the DHGS, it is difficult to accurately resolve the spatial variation in SMB within the system. Only a few direct measurements of SMB exist for the area, but the variations in internal layers observed in the GPR (Figure 3.21) testify to the large change in SMB which may occur within few kilometres. The models presented above serve as good first estimates of SMB within the glacial system, although considerable uncertainties remain. A comparison between Darwin Glacier grounding line discharge and upstream catchment-wide SMB predicted by the SMB scenarios suggests that ablation rates are overestimated within the DHGS when accounting for winter ablation. The SMB scenario which compares best with the estimated grounding line discharge while maintaining some ablation in BIAs (MB-3, Arthern et al. (2006) accumulation rates), implies that all sublimation was measured at the Hatherton AWS and consequently ignores the effect of winter sublimation. The presence of relatively low annual ablation rates within the DHGS BIAs were further supported by nested model experiments (section 5.5.5), where the best results were achieved when applying a SMB scenario with significantly reduced ablation rates (MB-3A, Arthern et al. (2006) accumulation rates). However, it is possible that the applied reduction in ablation rates compensates for inaccuracies in accumulation areas.

4.6 Surface and air temperature

An input map of mean annual surface (skin) or air temperature for the DHGS is required for the nested ice sheet-shelf model in order to accurately determine ice temperature and changes in SMB over time (section 5.2.3). Although distinct diurnal differences exist between air and surface temperature, long term averages generally compare well, and air temperature measurements are often used to validate remotely sensed data of surface air temperature (Comiso 2000; Jin et al. 1997). In this section, short-term measurements of air temperature from AWSs within the glacier system (Table 4.1) are used to calculate MAAT at the four locations shown in Figure 4.8. These values are subsequently compared to the Comiso et al. (2000) gridded dataset of averaged remotely determined mean annual surface temperatures (MAST, section 2.3) in order to assess the applicability of the dataset in the DHGS area.

4.6.1 Deriving the MAAT from summer measurements

This section examines the correlation between the summer AWSs (Hatherton, Upper and Lower Darwin AWSs) and the year round stations (Brown Hills, Mulock and Mary AWS) during overlapping data recording periods. This is done in order to establish whether any such relationship can be applied to extrapolate the measured summer record to the winter period and facilitate calculation of MAAT at the location of the three temporary AWSs (Joyce et al. 2001).

The correlation between individual datasets was assessed by calculating correlation coefficients (R) and p-values for hourly (e.g.1300h to 1400h) and daily (midnight to midnight) averages, as well as daily maximum and minimum temperatures during the two summer season. The best correlation was found between mean daily air temperatures, and the calculated correlation coefficients between all datasets are shown in Table 4.4. Mary AWS correlates least well with the other weather stations, most likely due to its position low on the ice shelf (Table 4.4). In contrast, both Brown Hills and Mulock AWSs correlate very well with most of the summer weather stations. As expected, the Lower Darwin temperature record shows most similarities with the Brown Hills station, which is located only 14 km away, while the Upper Darwin measurements show a much better correlation with the Mulock AWS which is located in a similar setting 100 km north of the DHGS. The correlation between Mulock and the Lower Darwin AWS is greater than between the Brown Hills and Upper Darwin dataset. The best correlation for the intermediate Hatherton AWS is less obvious although the station compares slightly better to the Mulock than the Brown Hills AWS during the summer of 2008/2009.

Table 4.4. The correlation coefficient (R) between datasets of daily mean air temperature for 2007–2008 (n = 60) and 2008–2009 (n = 42). All correlations have p-values <0.01.

08/09 \ 07-08	Lower Darwin	Upper Darwin	Hatherton	Brown Hills	Mulock	Mary
Lower Darwin		-	-	-	-	-
Upper Darwin	0.95		0.96	0.92	0.98	0.92
Hatherton	0.96	0.98		0.95	0.95	0.91
Brown Hills	0.98	0.91	0.92		0.92	0.88
Mulock	0.95	0.96	0.95	0.93		0.93
Mary	0.94	0.90	0.91	0.94	0.93	

Based on the above initial analysis, the Mulock AWS is preferred for extrapolation of summer temperatures over the Brown AWS due to the slightly better overall correlations with the summer stations and its location on the Mulock Glacier surface. However, the above analysis is based on summer measurements only and as the Mulock AWS is located ~100 km north of the DHGS, it might not record local weather phenomena throughout the year. In order to establish whether the Mulock station accurately reflects the conditions at the Darwin-Hatherton over longer periods of time, the annual temperature records of the Mulock and Brown Hills AWSs were compared (Figure 4.14 and Table 4.5). This comparison shows that a close relationship exists between daily mean air temperatures at the Brown Hills and Mulock weather stations throughout the year (R = 0.98), with summer correlations (1 October – 31 March, R = 0.98) exceeding winter correlations (1 April – 30 September, R = 0.93).

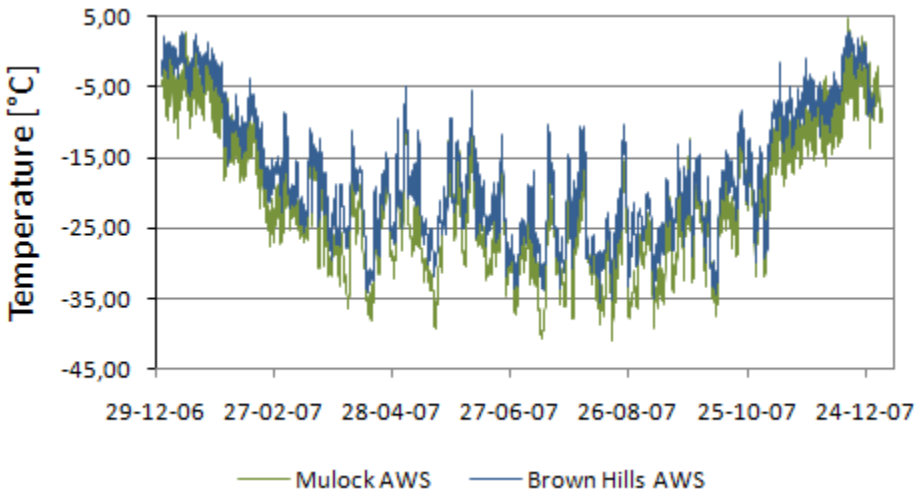

Figure 4.14. Variations in daily average air temperature during 2007 as recorded by the Brown Hills and Mulock AWSs.

Calculations of the optimal concordance correlation coefficient (ρ_c, Table 4.5) and corresponding temperature correction represent an ideal way in which to quantify the constant temperature shift which will lead to the best agreement between two temperature datasets (Joyce et al. 2001; Lin 1989). In order to determine the temperature correction which will lead to the highest similarity between datasets, corrections were iteratively applied to summer station temperatures until the maximum concordance correlation coefficient was found between these and the Mulock dataset. However, the method can only be utilised to extrapolate summer temperatures into the winter period if the relationship between air temperatures at the different weather stations does not change during the winter season. The potential error introduced by a seasonal change was investigated by comparing the optimal temperature correction between the Mulock and local Brown Hills AWSs for winter and summer period (Table 4.5). The calculated optimal temperature corrections (Table 4.5) suggest that the Brown Hills is between 3.3°C and 4.2°C warmer than the Mulock station during the summer and the winter periods respectively and that a difference of 3.8°C exists throughout the year.

Table 4.5. Summary of the comparison of daily mean air temperatures measured during 2007 by the Mulock and Brown Hills AWSs (Figure 4.14) and the optimal temperature correction of the Mulock dataset to fit the Brown Hills dataset.

Period	R	p-value	Correction [°C]	ρ_c
All 2007 (n = 360)	0.98	< 0.01	+3.8	0.98
1 January - 31 March (n = 89)	0.98	< 0.01	+3.7	0.98
1 April – 30 September (n = 183)	0.93	< 0.01	+4.2	0.93
1 October – 31 December (n = 88)	0.98	< 0.01	+3.3	0.98

To further test the accuracy of the approach, the listed temperature corrections were applied to the Mulock dataset and from these the MAAT was calculated for the Brown Hills location. Calculated mean temperatures range from -17.9°C (Mulock +3.3°C) to -17.0°C (Mulock +4.2°C) compared to the measured value of -17.5°C. The above analysis suggests that seasonal variability in the degree of correlation between the Mulock and Brown Hills temperature records are of minor importance, leading to errors of only ±0.5°C in the calculated MAAT. However, these errors are likely to increase to some extent for datasets with shorter overlapping records. The above analysis shows that the Mulock AWS can be used to depict seasonal variations in air temperature in the DHGS, and it was therefore chosen as the best year round AWS against which to correlate the three summer weather stations. Consequently, a concordance correlation coefficient analysis between the summer weather

stations and the Mulock AWS was carried out in order to determine the relationship between the AWSs for overlapping data records (Table 4.6 and Figure 4.15).

Table 4.6. Comparison of daily mean air temperatures observed by summer weather stations with temperatures recorded by Mulock AWS.

Dataset	Correction [°C]	ρ_c
2007-2008:		
Upper Darwin	-3.1	0.98
Hatherton	-1.0	0.93
2008-2009:		
Upper Darwin	-4.0	0.96
Hatherton	-1.5	0.94
Lower Darwin	+0.2	0.94

Optimal temperature corrections of the summer weather stations range from +0.2°C for the Lower Darwin AWS to -4.0 for the coldest Upper Darwin station (Table 4.6). Some variation in temperature correction seems to occur between the two summer periods. Both the Hatherton and Upper Darwin AWSs have larger magnitude temperature corrections with the Mulock AWS during the 2008/09 summer period, during which there was also a larger spread in the mean daily temperature values (Figure 4.15) than the previous summer (decreased ρ_c in 2008/09, Table 4.6). The systematic change in data spread with temperature (Figure 4.15) indicates that datasets from the Hatherton and Upper Darwin weather stations are best correlated with the Mulock temperature record during warmer days.

To test the performance of each calculated temperature correction, daily mean temperatures for the three summer weather stations were corrected by the optimal temperature and compared to the daily mean temperature record for the Mulock AWS. Temperature differences between the corrected datasets and the Mulock record all have means of 0.0°C and standard deviations range from 0.7°C for the best correlated 2007/08 Upper Darwin record to 1.2°C for the 2008/09 Hatherton and Lower Darwin record. The standard deviation range is a good indicator of the magnitude of the error associated with the method.

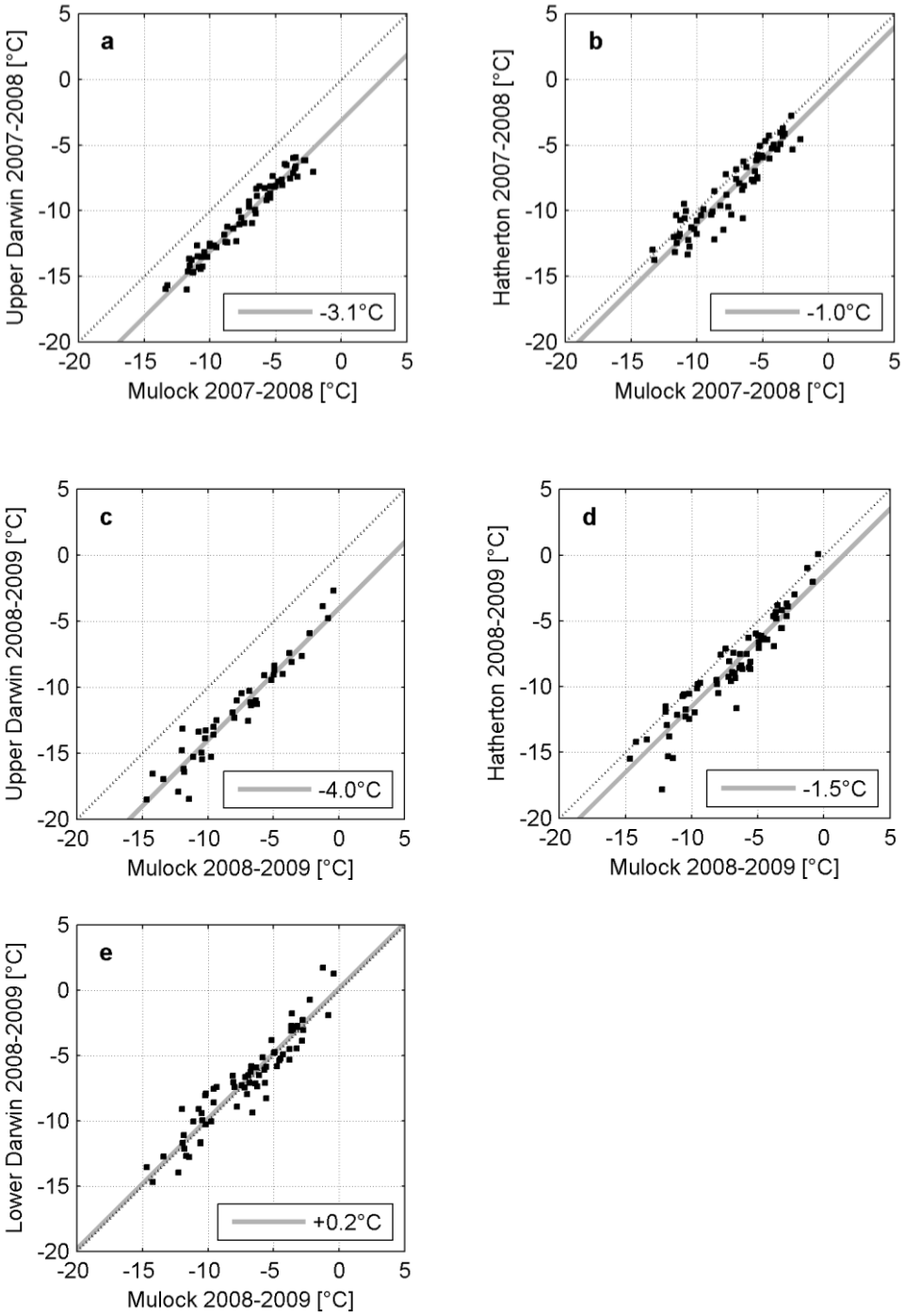

Figure 4.15. Daily mean air temperature comparison between Mulock AWS and Upper Darwin, Lower Darwin and Hatherton AWSs (a, b) during the summers of 2007/08 and (c, d, e) 2008/09. Grey lines indicate the line of the optimal concordance correlation coefficient while the dashed line illustrates the line of perfect concordance. Temperature pairs between Mulock and summer stations vary between 65 (Lower Darwin and Hatherton) in 2008/09 to 45 (Upper Darwin) and 70 (Lower Darwin and Hatherton) in 2008/09.

To determine the MAAT at the summer AWSs, a mean of the temperature correlations from 2007/08 and 2008/09 was applied for the Upper Darwin and Hatherton locations resulting in a temperature correction of -3.6°C and -1.3°C respectively. Since the Mulock AWS temperature record for 2008 is incomplete, temperature observations for 2007 were utilised for the extrapolations of daily temperatures at the locations of the Upper Darwin, Lower Darwin and Hatherton locations. To evaluate whether the 2007 temperature record is representative for the region, yearly average temperatures were compared. As the Mulock AWS has only been operating between 2007 and 2009 and was out of order for most of the winter 2008, the Brown Hills temperature record was used to determine potential variations in MAAT (Table 4.7).

Table 4.7. Measured yearly average air temperature from the Brown Hills AWS.

Year	Average temperature [°C]	Difference from average [°C]
2005	-18.2	0.0
2006	-18.8	-0.6
2007	-17.5	+0.7
2008	-18.1	+0.1
2009	-18.3	-0.1
Average	-18.2	0.00

The five year temperature record from Brown Hills AWS (Table 4.7) suggests that 2007 was a particularly warm year in this region, differing by as much as 0.7°C from the five year average annual temperature. The MAAT found for the three AWSs in the DHGS were therefore reduced by 0.7°C to account for this. This results in final MAAT at Brown Hills, Lower Darwin, Hatherton and Upper Darwin of -18.2°C (measured), –21.7°C, -23.2°C and -25.5°C (calculated) respectively. Daily mean air temperatures at the four locations reach a summer maximum of 1.4°C at the Brown Hills and a winter minimum of -43.3°C at the Upper Darwin.

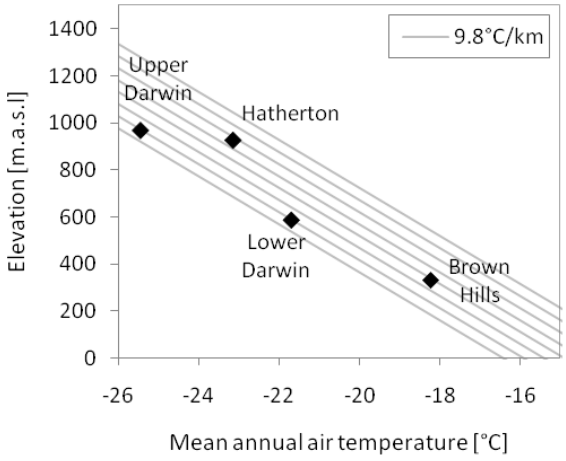

Figure 4.16. Calculated (Hatherton, Upper Darwin and Lower Darwin) and measured (Brown Hills) MAAT at different elevations within the DHGS. Grey lines illustrate the gradient of the dry adiabatic lapse rate of 9.8°C km^{-1}.

Together, the four calculated MAAT illustrate that a more or less gradual decrease in temperature occurs with increased surface elevation (Figure 4.16) and that the rate of decrease approaches the dry adiabatic temperature lapse rate (9.8°C km^{-1}). The Hatherton MAAT appears to be relatively warm for its high elevation (Figure 4.16). This is likely to be a summer phenomenon caused by increased solar absorption by the low albedo blue ice which characterises the Hatherton Glacier surface (Bintanja 1999, 2000; Bintanja 2001). Since the extrapolation of the temperature record relies on data from the summer season only, the calculated value does not account for a potential seasonal change in lapse rate up the Hatherton Glacier, and the final MAAT at this location might therefore be slightly overestimated.

4.6.2 Surface temperature interpolation

In order to assess the performance of the remotely sensed dataset of Antarctic surface temperature which covers the DHGS (Comiso 2000), the four values of MAAT from the DHGS were compared with the MAST at overlapping 5 km grid cells (ALBMAP, Table 4.8). The MAAT values compare extremely well with the corresponding average grid cell values, and the differences are well within the 3°C uncertainty associated with the MAST values (Comiso 2000).

Table 4.8. Calculated (Hatherton, Upper Darwin and Lower Darwin) and measured (Brown Hills) MAAT compared to values of MAST found by Comiso (2000) for corresponding grid cells.

AWS	Measured / calculated MAAT [°C]	Comiso (2000) MAST [°C]	Difference [°C]
Upper Darwin	-25.5	-25.3	-0.2
Hatherton	-23.2	-24.5	+1.3
Lower Darwin	-21.7	-21.4	-0.3
Brown Hills	-18.2	-19.6	+1.4

The similarity of the two sets of results confirms the MAAT in the DHGS through two independent methods and suggests that the map of surface temperatures published by Comiso (2000) accurately depicts spatial variations in air temperature over the range of surfaces present within the DHGS. The ALBMAP 5 km resolution Comiso (2000) map of averaged MAST (Le Brocq et al. 2010a) was consequently used as input to the numerical ice-flow model in its original form (Figure 4.17). Within the nested model domain, this map predicts surface temperatures ranging between a maximum value of close to -40°C high on the polar plateau and minimum values of close to -15°C on the Ross Ice Shelf.

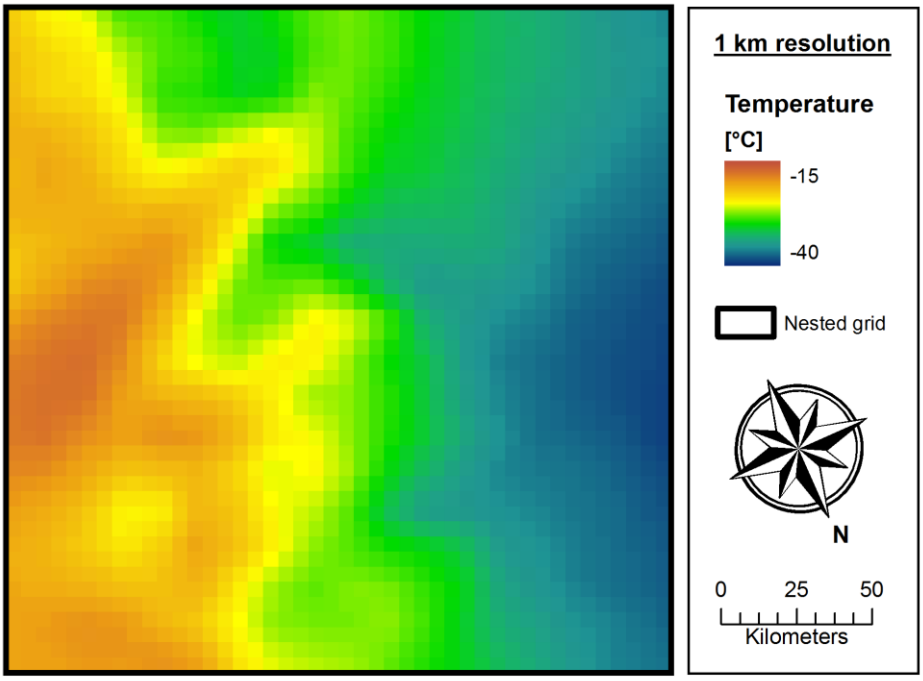

Figure 4.17. Average surface temperature variations within the nested model domain Comiso (2000).

4.7 Conclusion

The six gridded datasets described above set the framework for the nested ice sheet-shelf model. The maps incorporate new direct measurements of ice geometry and meteorological parameters and consequently represent a significant improvement to previous large-scale datasets that cover the region. With their added degree of accuracy, the new maps enable more realistic model simulation of the past and present DHGS behaviour (objectives A.3 and B.1).

In section 4.5 direct measurements of surface climatology and SMB were combined with existing gridded datasets of Antarctic SMB in order to arrive at an appropriate SMB scenario within the nested model domain. Direct measurements of surface meteorology presents evidence of the main controls on SMB variations within the DHGS and also provide a first estimate of the magnitude of spatial change (objective A.3). The Upper Darwin AWS, which is located on snow near BIA-B, is characterised by large episodes of snow accumulation, the majority of which are eventually removed by wind erosion. In contrast, at the Hatherton AWS, which is located on blue ice, snow is eroded quickly from the glacier surface and summer sublimation rates are high (~0.1 cm day^{-1}) and appear to be controlled primarily by the development of katabatic winds. The point measurement of summer ablation at the Hatherton AWS was used to develop several SMB scenarios. The results suggest that the applied temporal and spatial extrapolation of sublimation rates overestimate annual ablation rates in DHGS BIAs. The SMB scenario that compares best with grounding line ice discharge does not include ablation in BIAs (MB-4, Arthern et al. (2006) accumulation rates), which indicates that sublimation rates are generally much lower than suggested by the Hatherton AWS measurement, and/or that accumulation rates are underestimated in surrounding accumulation areas. This result is further supported by tests with the nested ice sheet-shelf model, which show that the best results are achieved when ablation rates are reduced by 50% from the measured summer magnitude (MB-3A, Arthern et al. (2006) accumulation rates). Given the poor resolution of the Antarctic large-scale SMB maps, it is likely that snow accumulation near ablation areas is underestimated.

Annual air temperatures were successfully calculated from a dataset of summer air temperatures measured on the DHGS. MAAT on the DHGS surface range between -21.7°C at the Lower Darwin AWS (586 m a.s.l.) to -25.5°C at the Upper Darwin AWS (969 m a.s.l.) with the temperature lapse rate close to the dry adiabatic lapse rate. The dataset of MAAT within the DHGS compares well with a remotely sensed map of averaged MAST (Comiso 2000), and the original MAST map (ALBMAP) was applied in the nested ice sheet-shelf model without adjustments. The extrapolation routine applied to derive MAAT values from seasonal

measurements has a wide application in Antarctica, where logistical concerns and the harsh environment often restrict direct measurements to the summer season.

5 Model simulations of ice dynamics in the Darwin-Hatherton glacial system

5.1 Introduction

Geological evidence of former surface elevations of TAM outlet glaciers have been widely used to infer past variations in EAIS and WAIS, even though the dynamic response of the outlet glaciers themselves is poorly understood (section 1.4.1 and 2.9). In this chapter a numerical ice-flow model (section 5.2) is used to simulate present and past dynamic behaviour of the DHGS. The high-resolution model is nested within an all-Antarctic lower resolution model in order to account for the effect of the EAIS and WAIS on ice flow within the glacial system (Figure 4.1, section 5.4). The modelling experiments will provide new insight into the present-day ice-flow dynamics of the DHGS and of slow-moving TAM glaciers in general (section 5.6, objective A.4). In order to establish Holocene change within the DHGS (section 5.6.3), the model is applied to simulate the LGM ice thickness and extent of the glacial system (objective B.1). In addition, the model results are used to infer whether the DHGS is currently in a steady state or continues to adjust to the termination of the LGM (objective B.2).

The modelling experiments presented in this chapter represent a significant improvement to previous modelling efforts, which were hampered by the lack of measurements of ice thickness, ice velocity and grounding line location (Anderson et al. 2004). The few previous modelling studies, which have investigated past changes in the TAM outlet glaciers have used flow-line models (Anderson et al. 2004; Golledge and Levy 2011) or flow-band models (Johnson and Staiger 2007). By applying a high-resolution 3-D nested model to simulate present and past behaviour of the DHGS, this study will account for the complexity introduced by numerous tributary glaciers and a large spatial variability in ice thickness and SMB within the glacial system.

5.2 Ice sheet-shelf model description

The ice sheet-shelf model used for the simulations of present and past glacier dynamics of the DHGS builds upon standard ice sheet model equations (shallow ice and shallow shelf approximations) and also includes:

1. A scaled transition zone across glacier grounding lines where equations for sheet and shelf flow are heuristically combined (Pollard and Deconto 2009a).
2. A freely migrating grounding line where ice velocity is calculated from ice thickness using the analytical solution developed by Schoof (2007).
3. A parameterisation to account for ice shelf buttressing caused by bedrock rises of sub-grid resolution (Pollard and DeConto 2009c).

In the model, three dimensional ice temperature calculations include vertical heat diffusion and shear heating, and the model accounts for lithospheric flexure and relaxation of the asthenosphere towards isostatic equilibrium (Pollard and DeConto 2009b). The model is run with 10 vertical layers on a finite-difference grid, where horizontal velocities are staggered by half a grid cell in relation to ice thickness, bedrock elevation and ice temperature.

Of particular importance for simulations of the DHGS is the possibility offered by the ice sheet-shelf model to nest high-resolution simulations of the glacial system (nested model, at 1 km resolution) within a relatively low-resolution model covering all of Antarctica (all-Antarctic model, at 20 km resolution). The all-Antarctic and nested model simulations are both conducted with the same ice sheet-shelf model although physical parameters and input datasets may differ between the two model setups as described in section 5.5. The nesting enables high-resolution simulations of ice dynamics in complex regions, such as the DHGS, that are significantly influenced by the behaviour of the surrounding ice sheet (section 1.6 and section 2.4).

Another main reason for choosing the ice sheet-shelf model for the DHGS nested simulations is its proven ability of capturing grounding line behaviour, which is a very important aspect of the DHGS dynamics. The ice sheet-shelf model has been tuned and validated specifically for Antarctic conditions and previous modelling results compare well with the modern ice sheet configuration and geological evidence of past glacier variations (Huybrechts 2009; Naish et al. 2009; Pollard and DeConto 2009b). The model is described in further detail below and in the papers of Pollard and Deconto (2009a; 2009b, c).

5.2.1 Model applications of the shallow ice and shallow shelf approximations

The ice sheet-shelf model has been designed to simulate the Antarctic Ice Sheet, where floating ice shelves fringe the continent, and consequently accounts for the change in flow dynamics which occurs at the glacier grounding line, as well as the buttressing effect offered by floating ice shelves (Pollard and Deconto 2009a; Pollard and DeConto 2009b, c).

In regions where the ice is grounded and friction at the bed is substantial, ice deformation occurs predominantly by vertical shear (Greve and Blatter 2009), which in the model is determined locally from the driving stress, τ_d:

$$\tau_d = \rho_i g H \alpha \tag{10}$$

The driving stress depends on the ice thickness (H), surface slope (α), ice density (ρ_i) and the gravitational acceleration (g), and in these regions is balanced completely by the basal drag (τ_b) which represents the degree of friction at the bed. The influence of lateral drag and longitudinal stretching on ice flow is ignored leading to a simplified set of equations describing ice flow, known as the zero-order, or SIA. The SIA is appropriate in regions where vertical variations in horizontal ice velocity far exceed longitudinal variations, which includes regions away from ice divides where the ice is thin compared to the lateral extent of the ice body (Greve and Blatter 2009). The SIA is preferred to the full set of stress equations in large-scale ice sheet models because it produces comparatively good results in most regions and has a relatively short computational time (Pollard and Deconto 2009a; Vacco et al. 2009). However, several studies have determined that the SIA is incapable of accurately simulating ice flow in regions where basal sliding is significant and/or large undulations occur in the underlying bedrock topography (Hindmarsh et al. 2006; Johnson and Staiger 2007; Pattyn 2002, 2003). Its applicability in the DHGS will be discussed in more detail in section 5.2.7.

For the floating ice shelves, the influence of basal friction is insignificant, and horizontal velocities are assumed constant with depth. Longitudinal variations in horizontal velocity far exceed vertical variations, and the effect of vertical shear on ice flow can consequently be ignored (Greve and Blatter 2009). The set of ice flow equations which describe only the effect of longitudinal stretching is known as the shallow shelf approximation (SSA) and is applied by the ice sheet-shelf model for floating ice shelves. In the SSA the ice velocity at any location is influenced by the ice thickness distribution of the entire ice shelf (Greve and Blatter 2009).

One of the main challenges for numerical ice-flow models in Antarctica has been to accurately simulate the gradual transition in ice dynamics which occurs towards the glacier grounding line (Schoof 2007). Ice flow may be significantly influenced by longitudinal stresses for a considerable distance upstream from the grounding line, in particular if the basal stress is small and sliding is important (Pattyn 2003; Pattyn and Naruse 2003). In the ice sheet-shelf model, the zones of complex ice flow are simulated by heuristically combining scaled equations for sheet and shelf flow (Pollard and Deconto 2009a). Because of the increased computation time associated with solving the scaled equations, this particular feature of the ice sheet-shelf model is included only in regions where sliding is important, which are determined by the magnitude of the basal sliding coefficient (section 5.2.2). Although both sets of flow equations

constitute approximations to the full stress solution, the scaled approach to simulating ice flow in complex regions has been found to produce good results (Hubbard 2000; Pollard and Deconto 2009a).

Flow enhancement factors are included in the ice flow equations for sheet (E_{SIA}) and shelf (E_{SSA}) flow in order to account for the potential influence of crystal orientation and impurities on the ice strain rate (Hooke 2005; Ma et al. 2010). Variations in any of these factors may affect the rate of ice deformation, which is accounted for in the ice sheet-shelf model by adjusting the temperature-dependent flow rate factor in Glen's flow law by the respective enhancement factors. Very little is known about the magnitude of the sheet and shelf enhancement factors. In general however, the enhancement factor for sheet flow has been found to vary between values of 1 and 10 (Greve and Blatter 2009). In addition to describing variations in ice strain rate, enhancement factors may reflect approximations in ice-flow models, such as the disregard of basal sliding (Hooke 2005) or violations of the assumptions underlying the SIA. In the ice sheet-shelf model, sheet and shelf flow enhancements factors of 5 and 0.5 respectively have been determined empirically to produce the most realistic results (D. Pollard, personal communication). These values compare well with a modelling study of the effect of ice anisotropy (Ma et al. 2010), where values of 4.5 – 5.6 and 0.58 – 0.71 were found for sheet and shelf flow enhancements factors respectively and a E_{SIA}/E_{SSA} relationship of between 5 and 10 was recommended.

5.2.2 Model treatment of basal sliding

Of particular importance to the ice velocity and grounding line position is the degree of basal sliding which, in the model, is controlled by prescribed sliding coefficients (B). The magnitude of the coefficient depends on the basal temperature (no sliding when basal ice temperature is below the pressure melting point), and the presence of subglacial deformable sediments (present when rebounded ice free bedrock topography is below sea level). The relationship between basal sliding velocities (u_b) and the basal stress (τ_b) is given by equation 11 where m = 2 (Pollard and DeConto 2009c).

$$\vec{u}_b = B\left|\tau_b\right|^{m-1}\vec{\tau}_b \qquad (11)$$

In general B values of 10^{-5} – 10^{-6} m a^{-1} Pa^{-2} are expected for soft deformable sediments, 10^{-10} m a^{-1} Pa^{-2} for hard bedrock and 10^{-20} m a^{-1} Pa^{-2} when bed temperatures are below the pressure melting point (no sliding). The combined set of sheet and shelf equations are solved when the basal sliding coefficient for grounded ice exceeds 10^{-8} m a^{-1} Pa^{-2}, while below this threshold only the SIA is applied (section 5.2.1). To account for the buttressing of floating ice shelves by sub-grid pinning to underlying bedrock highs, the basal sliding coefficient is linearly

decreased downstream from 15% of the grounded ice value at the grounding line, to zero at 300 m water depth (Pollard and DeConto 2009c).

5.2.3 Temperature and surface mass balance equations

Present-day SMB and surface temperature as described in section 4.5 and 4.6 for the nested model are input to the ice sheet-shelf model when the simulations are initiated. Past variations in surface temperature and SMB are calculated from these datasets using a simple empirical parameterization of the Vostok temperature record (SeaRISE 2009) and the insolation records (Laskar et al. 2004).

In the ice sheet-shelf model, the mean annual surface temperature, T (°C) is calculated for each grid cell by accounting for the potential effect of a changing surface elevation (Δh_s) and the temperature difference from modern value (ΔT_{Vostok}).

$$T = T_{present} + \Delta T_{Vostok} - 0.009 \cdot \Delta h_s \qquad (12)$$

where $T_{present}$ is present-day input surface temperature (Figure 4.17) and 0.009 °C m^{-1} is the temperature lapse rate.

A clear relationship exists between air temperature and Antarctic precipitation rates (section 1.4) and the SMB within each grid cell is calculated from the present-day value ($SMB_{present}$) adjusted for the difference from present-day temperature (ΔT). In addition, a positive degree day (PDD) model accounts for surface melting ($MELT$) and separates precipitation in accumulation areas into components of snow and rain ($RAIN$).

$$SMB = SMB_{present} \cdot 2^{\Delta T / 10} - MELT - RAIN \qquad (13)$$

The PDD model is driven by the calculated surface temperature and a seasonal sinusoidal temperature cycle with an amplitude determined by the difference between average January and July insolation for the respective year at latitude 80° S (Laskar et al. 2004; Pollard and DeConto 2009b). For the simulations of present-day and LGM conditions presented in this chapter, the levels of melting and liquid precipitation are insignificant, and the PDD calculations are superfluous. Consequently if a temperature decrease occurs, equation 13 predicts a decrease in SMB in accumulation areas ($SMB_{present} > 0$) and an increase in SMB in ablation areas ($SMB_{present} < 0$), while the opposite occurs if the air temperature increases compared to present-day values.

Temporal changes in sublimation rates within Antarctic ablation areas are poorly understood as they depend on complex interactions between sublimation rates (dependent on air temperature), accumulation rates and surface elevation in relation to nearby exposed bedrock (Bintanja 1999; Bintanja and van den Broeke 1995; Brown and Scambos 2004; Sinisalo and Moore 2010). During a temperature decrease, the accompanying decrease in sublimation rates (section 4.5.4) are thought to be outweighed by the effect of decreased precipitation rates, and BIAs are likely to increase in size, except if the surface elevation difference to exposed bedrock is reduced by a significant ice thickness increase (Sinisalo and Moore 2010). Geological evidence from the DHGS region shows that considerable increases in ice thickness have occurred during past glacial periods (section 2.9.2). Therefore although temporal changes in ablation area extent are not accounted for by equation 13, it correctly depicts a decreased importance of ablation areas to the overall SMB during glacial periods (high ice thickness) and vice versa during warm periods. However, the rate of change predicted by equation 13 in ablation areas is highly uncertain.

5.2.4 Basal melting underneath grounded and floating ice

The magnitude of basal melt of grounded ice is controlled by ice temperature and geothermal heat flux (Hooke 2005), while oceanic melt rates beneath floating ice shelves depend on the temperature of the water which comes in contact with the ice (Rignot and Jacobs 2002). The ice sheet-shelf model includes the effect of basal melting for grounded ice when temperature at the ice base exceeds the pressure melting point, but the model ignores both the presence of non-ocean water underneath the grounded ice and the advection of liquid water (D. Pollard, unpublished notes). Water produced as the basal ice melts is assumed to drain freely, either through subglacial channels or the underlying sediments. The errors associated with this simplification are thought to be of minor importance, as large bodies of water are unlikely to exist beneath the glacial system.

Oceanic melting underneath ice shelves is important, not only to the overall mass balance of the glacial system, but also to the location of the grounding line. This has been illustrated in sensitivity studies conducted by Pollard and DeConto (2009b, c), which clearly show that for the ice sheet-shelf model, changes in oceanic basal melting are more important than variations in global sea level, ice temperature and basal slipperiness in driving glacier retreat or advance. The model prediction of oceanic melting relies on a simple parameterisation of three shelf conditions (protected, exposed and deep-ocean), depending on the access and distance to open water as well as the depth of the ocean water column. For the nested model domain shown in Figure 4.1 all ice shelf grid cells are classified as protected. The magnitude of oceanic melt is varied through time using a heuristically-determined simple parameterisation (depending on difference from modern day sea level and average January insolation at 80° S)

of extreme interglacial, modern interglacial and full glacial conditions (Pollard and DeConto 2009b).

5.2.5 Modelled bedrock elevation

Model solutions for changes in bedrock elevation take into account both the effect of elastic lithospheric flexure and relaxation of the asthenosphere towards isostatic equilibrium (Pollard and DeConto 2009b). Both of these calculations work well for the all-Antarctic model, but when nesting the relatively small (220 x 220 km) high-resolution region within the all-Antarctic model, considerable errors are introduced by the equations for lithospheric flexure. These errors arise because the bed elevations outside the nested grid are constrained along the nested boundary and are therefore unable to respond to, and properly affect, variations within the nested grid. This error is particularly pronounced for the DHGS nested grid where the grid size is comparable to the 100 km 'radius of influence' utilised in the calculations of bedrock elevation (D. Pollard, personal communication). Consequently for the nested model, variations in bedrock elevation are calculated from a locally relaxing asthenosphere only. The errors associated with this simplification are minor and all-Antarctic and nested bedrock elevations compare well along the boundaries of the nested grid.

5.2.6 Original and adjusted nesting approach

The location of the 220 x 220 km region chosen for the high-resolution nested model simulations and the grid setup used in the ice sheet-shelf model was described in detail in the introduction to Chapter 4 (Figure 4.1). A grid cell resolution of 1 km was applied so that the glacial system is appropriately resolved at The Nozzle and upper parts of the Hatherton Glacier, where the glacial system narrows to a minimum width of ~5 km (Figure 2.1). This horizontal resolution is the same order of magnitude as the ice thickness and no higher resolution was considered. The ice dynamic time step was determined by trial and error and set to 0.005 yr for the nested model and 0.25 yr for the all-Antarctic model. The ice sheet-shelf model has up until now never been run at such high resolution, and considerable effort was put into reducing the artefacts introduced by the nesting routine to a minimum.

Because of the relatively small size and high resolution of the nested grid, the grid boundary must be treated carefully. In the nested model, boundary values of ice thickness, bedrock elevation and ice velocity are interpolated bilinearly from the four closest 20 km all-Antarctic grid cells (section 5.4.2). Even minor uncertainties in the assigned constant boundary ice flux result in significant discrepancies between modelled and measured present-day ice elevations, as well as between surface elevations of the constant boundary cells and the evolving adjacent nested cells (section 5.5.1). The all-Antarctic model resolves only the largest TAM outlet

glaciers and it is therefore not surprising that modelled ice velocities differ somewhat from the actual values as will be described in more detail in section 5.4.2. Nested model simulations conducted at a range of times suggest that the magnitude of these inaccuracies vary and consequently cannot be adjusted by a constant value.

In order to account for these uncertainties, various adjustments were made to the original nesting routine. The best results were achieved when ice velocities were varied at the boundary, depending on the difference in surface elevation between the all-Antarctic boundary grid cell and the adjacent evolving nested cell. The boundary ice velocities from the all-Antarctic simulation are consequently replaced by varying velocities, which keeps the nested grids cells at the surface elevation suggested by the all-Antarctic model output. The adjusted boundary conditions were applied downstream (south-eastern nested boundary) and upstream (north-eastern nested boundary) of the DHGS. Compared to the original ice velocities proposed by the all-Antarctic model, these adjustments lead to an overall decrease in ice flux into the nested grid from the EAIS, and outflow to the Ross Ice Shelf/Sheet. Ice shelf thickness and grounding line locations are sensitive to the decreased pull at the floating south-eastern boundary and the model output is significantly improved following the changes described above. Assigning the new boundary conditions to the nested model implies that the EAIS acts as a perfect source (or sink) of ice to the DHGS, while the Ross Ice Shelf/Sheet is a perfect sink (or source). The applied changes are justified by the uncertainties associated with the all-Antarctic ice velocities (section 5.4.2) and the lack of feedback between the all-Antarctic and nested model output in the original nesting routine. The adjustments were required in order to produce realistic simulations of the DHGS flow dynamics and illustrate the additional challenges involved with nesting relatively small high-resolution models within low-resolution models.

5.2.7 Applicability of the ice sheet-shelf model in the Darwin-Hatherton area

The DHGS represents a considerable modelling challenge with regards to accurately accounting for:

1. The present and past influence of the EAIS and the Ross Ice Shelf/Sheet (section 2.9.2).
2. The interactions between two main glaciers with different characteristics (section 2.4).
3. Ice flow over a rough bedrock topography (section 3.6).
4. The changing flow dynamics across the glacier grounding line (section 3.8).
5. The effect of a complex SMB (section 4.5).

As described in the above sections, the ice sheet-shelf model includes a number of features, which take most of these issues into consideration. However, utilising a SIA model (section 5.2.1) to model a valley glacier where longitudinal and lateral stresses are likely to be of importance (section 1.5.3) and evidence exists of extending and compressive flow (section 3.6) carries some uncertainty. These uncertainties may be reflected in the model results as inaccuracies in glacier dynamics (Hubbard 2000; Schäfer et al. 2008). However, the glacier geometry proposed by SIA models generally compares well with measurements and fuller stress model output, even for glaciers with higher aspect ratios and bed slopes than the DHGS (Greuell 1992; Hubbard 2000; Pattyn 2002; Vacco et al. 2009). The proposed experiments could not have been conducted within a realistic timeframe using a higher order model and the ice sheet-shelf model is preferred due to its numerical stability and relatively short computational time.

5.3 Modelling approach and experimental design

The present-day characteristics of the DHGS and LGM configuration will be investigated with two versions of the ice sheet-shelf model, the all-Antarctic and nested model, using the workflow illustrated in Figure 5.1.

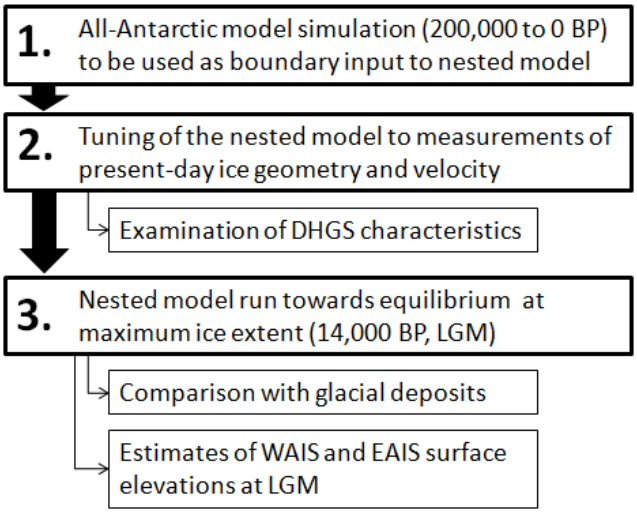

Figure 5.1. Outline of the modelling approach, experimental design and expected outcome.

The modelling approach involves creating input boundary conditions for the nested model from a simulation with the all-Antarctic model (step 1 in Figure 5.1, section 5.4), after which the nested model is tuned to DHGS conditions (step 2 in Figure 5.1, section 5.5). The nested

model is then applied to simulate present-day characteristics of the DHGS in order to investigate current flow behaviour (section 5.6). The tuned nested model is subsequently used to simulate LGM conditions in the DHGS, which will clarify existing discrepancies on glacial drift sheet ages (Table 2.1) as well as provide further constraint on the configurations of the WAIS and EAIS during the LGM (step 3 in Figure 5.1, section 5.7).

5.4 All-Antarctic model setup and results

The boundary conditions specified by the all-Antarctic model for the nested model act as a primary control on the evolution of the nested grid. This section describes the setup of the all-Antarctic model and the accuracy of the present-day simulation of ice thickness and surface velocity. In addition, the simulated late Quaternary change in ice configuration of the EAIS and WAIS suggested by the all-Antarctic model is evaluated. Simulations of the late Quaternary changes in the Ross Embayment have previously been conducted with the ice sheet-shelf model (Pollard and DeConto 2009b, c). The experiments were repeated here in order to produce the files required to conduct the nested experiments.

5.4.1 All-Antarctic model setup

The all-Antarctic model was run with the default setup (Table 5.1 and 5.2) and started at 200,000 yr BP to allow for the two Antarctic ice sheets to fully build-up before the initiation of the last glaciation. Some parameters and physical constants are consistent between the all-Antarctic and nested models (Table 5.1), while others (Table 5.2) are varied in the nested model during the tuning process described in section 5.5.

The all-Antarctic model requires input of certain gridded datasets in order to account for spatial variability in bedrock topography, ice thickness, SMB, temperature and geothermal heat flux (Table 5.2). In addition, past changes in temperature, solar insolation and sea level are used to drive the model either directly or through parameterisation of SMB (section 5.2.3) or oceanic melt rates (section 5.2.4). The input datasets are primarily sourced from a data compilation produced by the SeaRISE community (Sea-level Response to Ice Sheet Evolution, http://websrv.cs.umt.edu/isis/, version 0.7), which aims to improve the comparability of modelling results by offering common input datasets. These datasets are continuously updated, and includes the newest published data and modifications.

Table 5.1. Parameters, physical constants and time series which are consistent between the all-Antarctic and nested model runs.

Parameters, physical constants and time series	All-Antarctic and nested model
Thermal conductivity of ice [m^{-1} K^{-1}]	2.1
Density of ice [kg m^3]	910
Heat capacity of ice [J kg^{-1} K^{-1}]	2009
Latent heat of fusion of ice [J kg^{-1}]	3.35×10^5
Triple point of water [K]	273.15
Pre-exponential constant, Arrhenius law (cold) [Pa^{-3} s^{-1}]	3.615×10^{-13}
Pre-exponential constant, Arrhenius law (warm) [Pa^{-3} s^{-1}]	1.735×10^3
Pressure dependence of melting [K m^{-1}]	8.66×10^{-4}
Activation energy for creep (cold) [J mol^{-1}]	13.4×10^4
Activation energy for creep (warm) [J mol^{-1}]	6.0×10^4
Universal gas constant [J mol^{-1} K^{-1}]	8.314
Glen's flow law exponent	3
Present-day surface temperature	Comiso (2000)
Present-day geothermal heat flux	Maule et al. (2005)
Temperature time series	Vostok $\delta^{18}O$, SeaRISE
Insolation time series	Laskar et al. (2004)
Sea level time series	SPECMAP, SeaRISE

Table 5.2. Parameters and input datasets specific to the all-Antarctic model. Table 5.3 lists equivalent model parameters and input datasets for the nested model.

Parameters and input datasets	All-Antarctic model
Dynamic timestep [yr]	0.25
Enhancement factor (sheet)	5
Enhancement factor (shelf)	0.5
B (bed below sea level, warm-based) [m yr^{-1} Pa^{-2}]	10^{-5} – 10^{-7}
B (bed above sea level, warm-based) [m yr^{-1} Pa^{-2}]	10^{-10}
B (frozen base) [m yr^{-1} Pa^{-2}]	10^{-20}
B threshold for inclusion of SSA [m yr^{-1} Pa^{-2}]	10^{-8}
Present-day oceanic melt rates (protected) [m yr^{-1}]	0.1
LGM oceanic melt rates (protected) [m yr^{-1}]	0
Bedrock topography	BEDMAP1_plus, SeaRISE
Ice thickness	BEDMAP1_plus, SeaRISE
Surface mass balance	Vaughan et al. (1999a)

5.4.2 Comparison of the all-Antarctic model output to present-day ice conditions

The past and present behaviour of the DHGS is influenced by both the WAIS and EAIS (section 2.9.2). In order to achieve realistic nested model results, it is therefore important that the all-Antarctic model accurately simulates ice configurations of both the Antarctic ice sheets. The all-Antarctic model performance is evaluated by comparing measured and modelled present-day ice configuration along two transects covering regions of importance to the DHGS behaviour (Figure 5.2). The EAIS inland of the DHGS covered by profile A influences the upper DHGS catchment basin, while profile B shows the WAIS and the Ross Ice Shelf along which large changes have had a considerable impact on past ice thickness variations in the lower reaches of the glacial system (section 2.9.2). The all-Antarctic model performs reasonably well along the two transects (Figure 5.2), although some discrepancies exist which may impact the accuracy of the nested simulation. Of particular importance to the nested model is the increased surface elevation of the EAIS close to the TAM (at 3200 – 3800 km distance in profile A). The build-up of ice upstream of the mountain range is likely related to the 20 km resolution of the all-Antarctic model, which is insufficient to resolve the TAM outlet glaciers that drain the inland ice (Fyke et al. 2011). The largest discrepancies between modelled and measured ice configurations are observed along profile B (Figure 5.2b) where the model appears to significantly underestimate the WAIS ice thickness (at 0 – 500 km distance). Probably as a result of this, the thicknesses of the ice shelves (floating ice base shown with green lines) along both transects are generally too low and the WAIS grounding line is located further inland than is actually the case (arrows along profile B). The uncertainties of the all-Antarctic model output will be discussed further in section 5.4.3. However, although the model output presented here is inaccurate in certain regions, the ice sheet-shelf model performs reasonably well near the DHGS as demonstrated below. This provides some confidence in terms of the focus of this research.

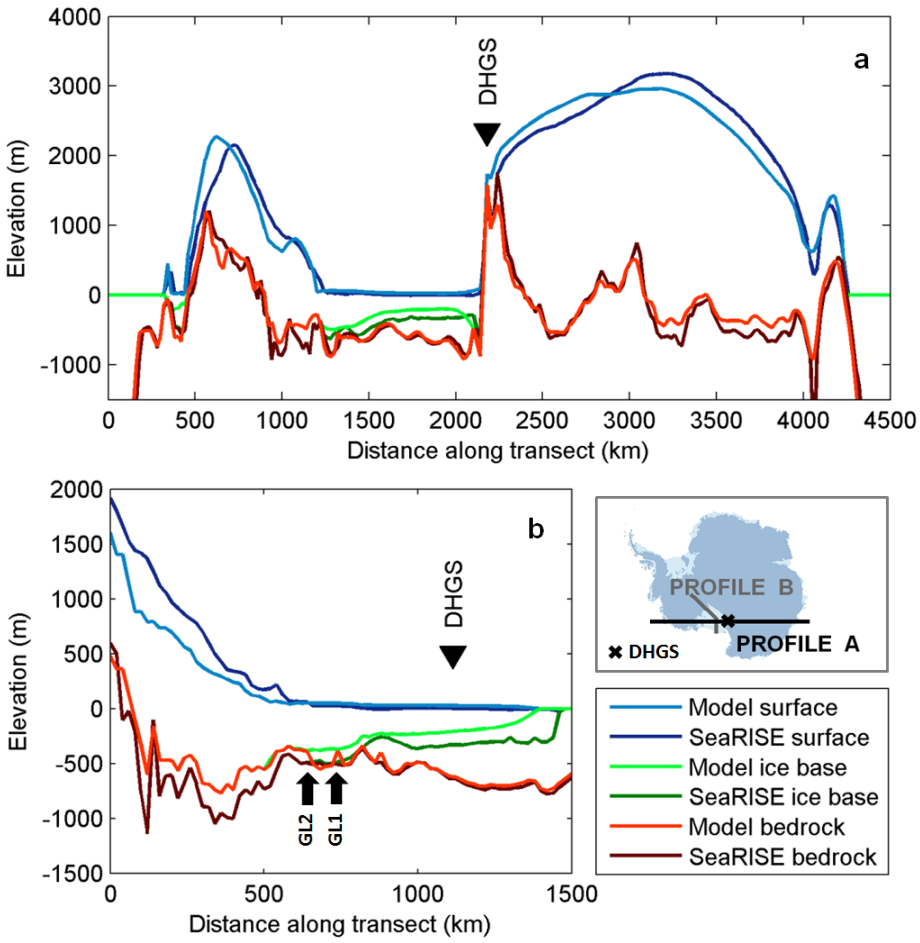

Figure 5.2. Comparison between gridded dataset of surface elevation, ice base (when floating) and bedrock elevation based on measurements (SeaRISE 2009) and the modelled all-Antarctic present-day ice sheet configuration along (a) profile A and (b) profile B. Arrows along profile B indicate the measured (GL1) and modelled (GL2) grounding line location. The location of profile A and profile B are shown on the inset map.

Because of the relatively small nested model domain, the nested results are highly sensitive to uncertainties in the all-Antarctic model output (section 5.2.6 and 5.5.1). Consequently, before the performance of the nested model can be properly evaluated, the accuracy of the all-Antarctic output in the region surrounding the nested grid boundary values must be investigated. This is done below by comparing the ice thickness and ice velocity computed by the model with the 5 km resolution SeaRISE gridded datasets of ice thickness and calculated Antarctic balance velocities (Bamber et al. 2000).

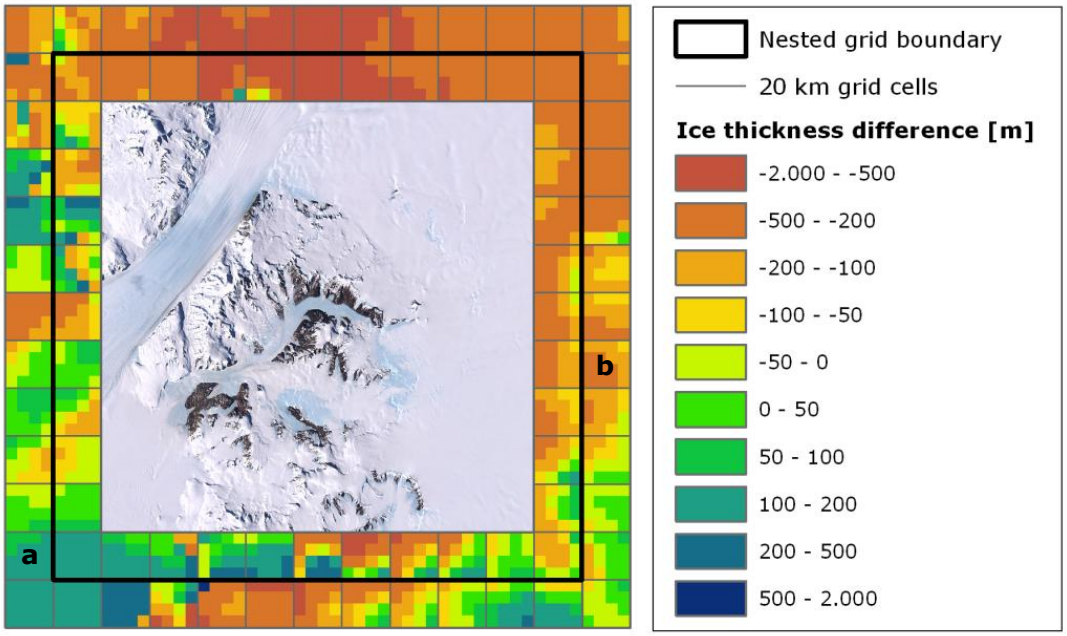

Figure 5.3. Map showing the difference in ice thickness between the SeaRISE ice thickness dataset and the model output for the all-Antarctic 20 km grid cells (grey lines) used for the calculation of nested boundary values. Values are negative when model thicknesses exceed those given by the SeaRISE dataset. The letters a and b refer to grid cells investigated in more detail in Figure 5.7.

Overall, the all-Antarctic model produces reasonably good results in the regions located upstream and downstream of the DHGS, where modelled ice thicknesses generally vary less than ±200 m from the SeaRISE dataset (~10% of the total upstream ice thickness, Figure 5.3). As was also shown in Figure 5.2a, ice thicknesses are generally overestimated by the model upstream of the DHGS, while it underestimates the thickness of the downstream ice shelf. Of less importance to the simulation of the DHGS are the large discrepancies in ice thickness observed where the nested grid boundary intersects steep terrain near the Byrd Glacier (Figure 5.3). It is clear that the nested grid should be positioned differently if the Byrd Glacier was to be accurately simulated by the nested model.

A comparison between balance velocities (Bamber et al. 2000) and model output from the all-Antarctic model indicates that the average ice velocities found by the model differ by as much as ±5 m yr^{-1} upstream of the DHGS, where modelled depth averaged velocities range between 5 and 20 m yr^{-1}. This suggests that ice velocities in the region carry significant uncertainties, which nested model results confirm (section 5.5.1). As a consequence, the nesting routine was altered (section 5.2.6), so that the exact all-Antarctic ice velocities are only applied at the upper and lower nested boundaries.

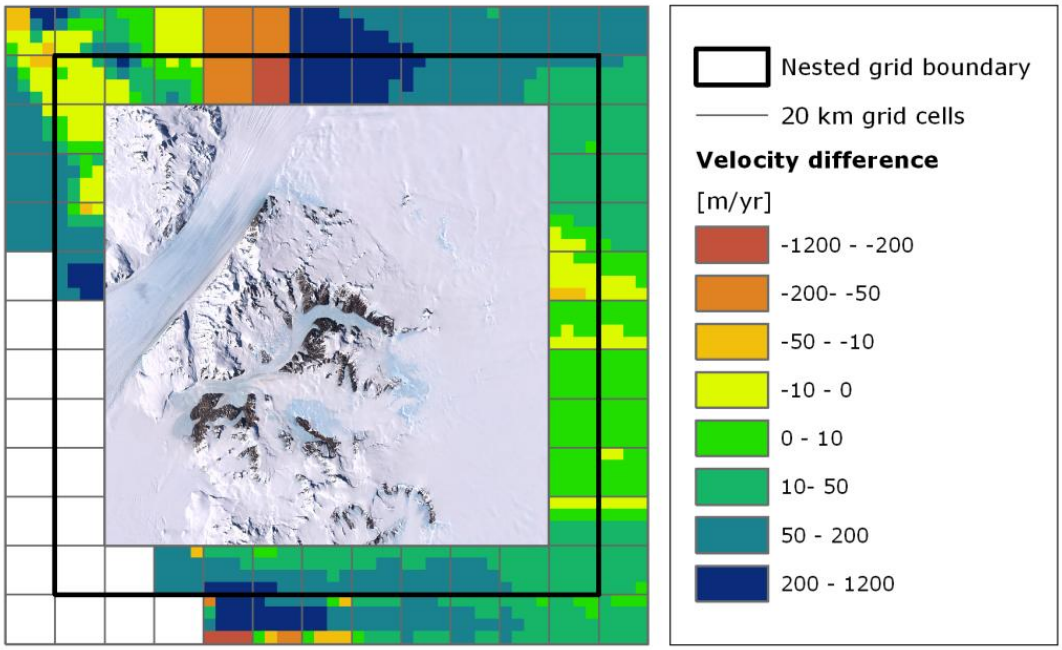

Figure 5.4. Map showing the difference between balance velocities (Bamber et al. 2000) and the vertically averaged model output for the all-Antarctic 20 km grid cells (grey lines) used for the calculation of nested boundary values. Values are negative when model velocities exceed the calculated balance velocities. White areas indicate regions which are not covered by the balance velocity dataset.

5.4.3 Late Quaternary changes as simulated by the all-Antarctic model

The modelled ice thickness and extent of both the all-Antarctic and nested model changes over time in response to variations in global sea level, oceanic melt rates (section 5.2.4) and SMB, the latter of which is related to variations in air temperature (section 5.2.3). In addition, the nested model responds to changes in ice flux and temperature across the model domain boundary from the all-Antarctic model. Changes in surface temperature and global sea level during the past 40,000 years (SeaRISE 2009) used as input to both model experiments (Table 5.2 and Table 5.3) are shown in Figure 5.5. The figure illustrates the dramatic increase in air temperature (~8.5°C) and global sea level (~130 m) associated with the last deglaciation.

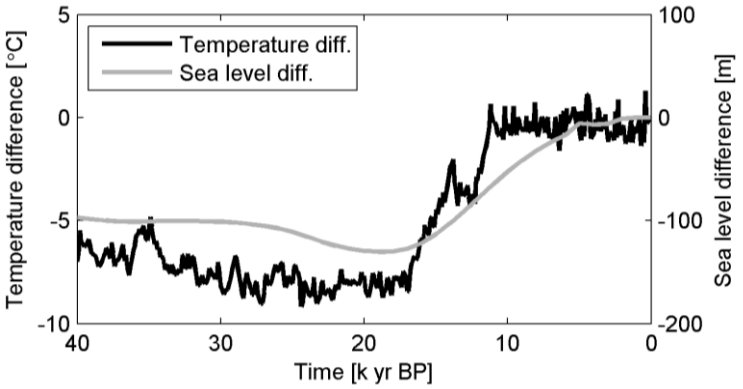

Figure 5.5. Temperature (Vostok) and sea level (SPECMAP) variations during the past 40,000 years in relation to present-day values (SeaRISE 2009).

As described in section 1.4.1, the more dynamic WAIS experienced the largest variations in the past of the two Antarctic ice sheets (Bindschadler 2007), and the advance and retreat of the WAIS grounding line is thought to be the main driver of ice thickness variations in the DHGS (Anderson et al. 2004; Bockheim et al. 1989). According to the all-Antarctic model, the WAIS grounding line advance occurred primarily between 24,000 and 14,000 yr BP, passing north of the DHGS outlet at approximately 20,000 yr BP (Figure 5.6a). The rapid advance of the grounding line coincides with a ~30 m sea level lowering between approximately 30,000 and 20,000 yr BP as shown in Figure 5.5. The all-Antarctic model predicts a maximum ice extent at 14,000 yr BP, after which the grounding line retreats rapidly, passing the DHGS between 10,000 and 9000 yr BP, reaching its current position at ~5000 yr BP (Figure 5.6b).

The influence of the WAIS and EAIS on the DHGS can be illustrated in more detail by studying the evolution in ice conditions at grid cells located at the nested grid boundary. Significant changes occur towards the Ross Embayment (Figure 5.7a), where ice thickness and surface elevation can be seen increasing dramatically between 25,000 and 14,000 yr BP. Ice is grounded at this location until 11,000 yr BP, after which it rapidly thins and the ice velocity increases. The early grounding of this grid cell is caused by an advance of TAM glaciers, probably in response to the low global sea level (Figure 5.5). Before the advance of the WAIS grounding line past the DHGS outlet (Figure 5.6a), ice flow downstream of the DHGS is consequently controlled by the neighbouring Carlyon and Byrd Glaciers (Figure 1.1). According to the all-Antarctic model, the maximum ice thickness occurred at 14,000 yr BP and since then, ice thickness downstream of the DHGS has decreased 1300 m and the surface elevation has lowered almost 750 m (Figure 5.7a). For other grid cells along the south-eastern boundary of the nested grid, the change in surface elevation varies between 600 and 750 m. Surface velocities are low (<15 m yr^{-1}) when the ice is grounded, in particular when the WAIS dams

the glacier outlet (<5 m yr^{-1}), but increase rapidly as the WAIS grounding line retreats south past the glacier outlet and the ice begins to float (Figure 5.6a).

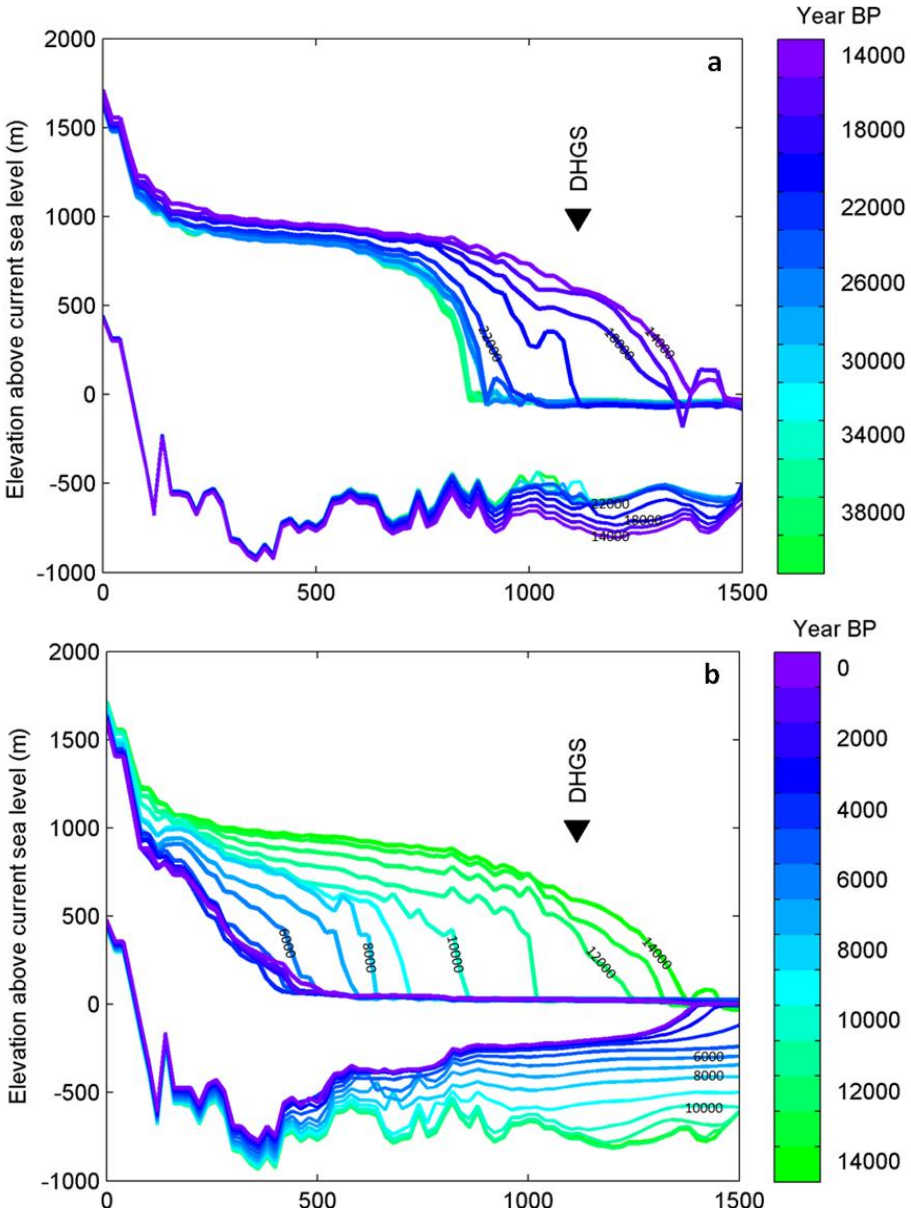

Figure 5.6. All-Antarctic model output of glacier geometry (ice surface and corresponding ice base) along transect B (Figure 5.2), during (a) the advance and (b) retreat of the Ross Ice Sheet grounding line to and from its maximum extent at 14,000 year BP. The position of the grounded ice base varies in the plot according to the weight of the overlaying ice.

Although the largest changes in ice thickness, surface elevation and velocity occur towards the Ross Ice Shelf, the all-Antarctic model predicts some variations in ice conditions on the East Antarctic plateau. Towards the EAIS (Figure 5.7b) ice thickness and surface elevation increase

80 m for the period between 25,000 and 13,000 yr BP. In other regions of the EAIS, the predicted ice thicknesses are lower than present-day during the last glaciation due to lower snow accumulation rates. For other grid cells along the north-western boundary of the nested grid, the increase in EAIS surface elevation ranges between 0 and 80 m. The period of increased ice thicknesses at the LGM observed upstream of the DHGS is a local effect, which appears to be caused by the damming of ice flow through the TAM as the Ross Embayment fills with grounded ice. Velocities are generally very low (<10 m yr^{-1}), in particular just before the deglaciation (~5 m yr^{-1}) when an advanced WAIS likely restricted ice flow through the TAM.

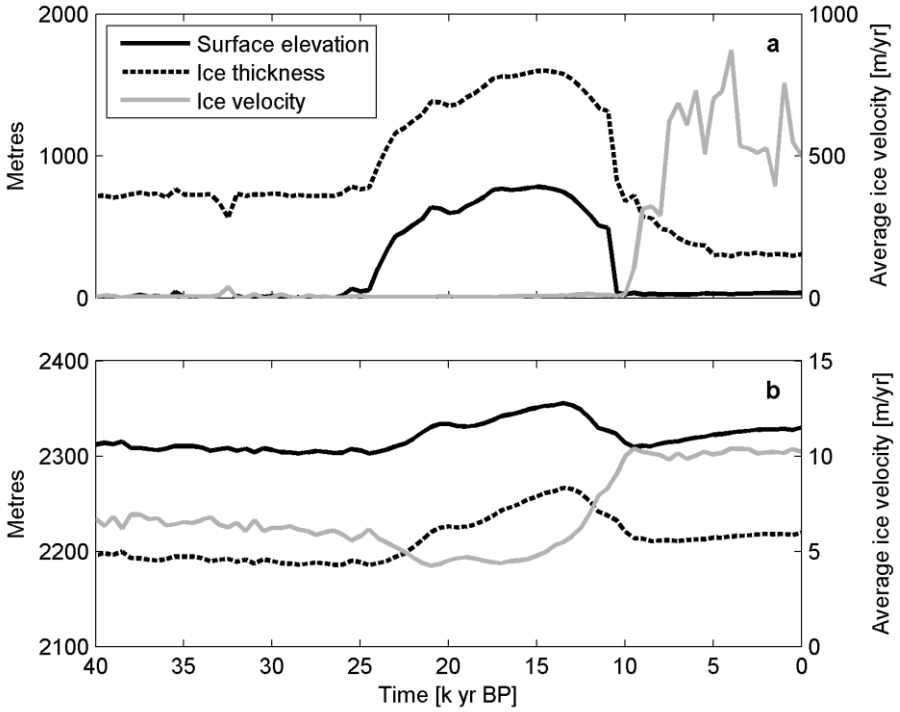

Figure 5.7. Surface elevation (m above present-day sea level), ice thickness and average ice column velocity variations from two all-Antarctic model grid cells located immediately (a) downstream and (b) upstream of the nested grid (exact locations shown in Figure 5.3).

The results produced by the all-Antarctic model differ to some extent from the general consensus about the Ross Ice Sheet ice thickness and in particular the timing and rate of grounding line advance and retreat (section 1.4.1, Figure 1.4). As described in section 1.4.1, interpretations of the geological evidence suggests that the Ross Ice Sheet was close to its maximum position at least between 27,820 and 12,880 yr B.P. (Conway et al. 1999), that the grounding line retreated south past the DHGS outlet at ~6800 yr BP and that the surface elevation at the glacier outlet has lowered 1100 m since then (Bockheim et al. 1989; Conway

et al. 1999). Compared to this evidence the maximum ice thickness and extent of the WAIS occurs late in the all-Antarctic model, and as a result, the Ross Ice Sheet has little time to thicken in the northernmost regions. In addition, the subsequent retreat takes place at a faster rate than suggested by the geological evidence. A previous modelling study of the DHGS has found evidence to suggest that the WAIS grounding line may have retreated south of the outlet as early as 7900 yr BP and that the surface of the Ross Embayment ice has lowered only 800 m ±100 m since then (Anderson et al. 2004). This study consequently compares better with the LGM ice thickness and retreat history proposed by the all-Antarctic model.

The present-day ice configuration and Holocene retreat of the WAIS illustrated by the all-Antarctic model output differs somewhat from previously published simulations with the ice sheet-shelf model (Pollard and DeConto 2009c). The development of the all-Antarctic model is ongoing, and the discrepancies are likely to be a result of changes in model setup between the various versions of the model. In particular, a change in datum of input configuration datasets (SeaRISE referenced to WGS-84) could explain the late advance of the WAIS into the Ross Embayment observed in the all-Antarctic output. The newest version of the ice sheet-shelf model is run with the newer ALBMAP dataset (referenced to the EIGEN-GL04C geoid, Le Brocq 2010) and derives a large-scale basal roughness map using a crude inversion method, and perhaps as a consequence simulates the most recent glaciation and subsequent deglaciation in good accordance with the geological evidence (D. Pollard, personal communication). Due to time constraints imposed on the research presented in this thesis, it was not possible to account for the uncertainties associated with the all-Antarctic simulation presented above.

From the above discussion, it is clear that the results produced by the all-Antarctic model differ somewhat from the general consensus of change in the Ross Embayment during the last glaciation. In particular, the timing of the advance of the WAIS does not compare well with geological evidence. Despite these uncertainties, the timing of the LGM in the Ross Embayment, as well as the thickness of the Ross Ice Sheet downstream of the DHGS at this time appear realistic. In addition, the all-Antarctic model output of present-day ice conditions in the regions surrounding the DHGS is reasonably good given its low resolution. Consequently, the uncertainties introduced by conducting static nested runs with the present-day and LGM all-Antarctic boundary conditions are thought to be minor.

5.5 Tuning the nested model to the DHGS

The ice sheet-shelf model has already been successfully applied to present-day Antarctic conditions and validated against past evidence of changes in the Antarctic Ice Sheet (Pollard and Deconto 2009a; Pollard and DeConto 2009b). However, initial nested simulations of present-day DHGS conditions with original all-Antarctic settings (section 5.4.1) significantly

underestimate ice thickness, overestimate ice velocities on the Darwin Glacier and position the grounding line too far upstream. Several studies have illustrated how the slow moving TAM outlet glaciers differ from the 'average' large and fast moving Antarctic outlet glaciers which control the mass balance of the Antarctic Ice Sheet (Figure 1.2). It is therefore not unexpected that the nested model requires considerable tuning to accurately simulate the flow dynamics of the DHGS (step 2 in Figure 5.1).

As is often the case with model simulations, no prior knowledge exists for a range of parameters of importance to the ice flow dynamics. The tuning, which will be described in more detail below, involved varying the basal slipperiness, the enhancement factors for sheet flow, the SMB and the subglacial oceanic melt rate until the nested model accurately simulate the present-day DHGS behaviour. All of these parameters are site-specific and changing them within reasonable limits is standard modelling practise. The nested model is tuned towards present-day measurements of:

1. Ice surface elevation (Figure 4.3)
2. Ice thickness (Figure 4.4)
3. Surface velocity (section 2.6 and 3.2.3)
4. Grounding line location (section 3.8)

Together, the datasets listed above allow for a robust fitting of the ice sheet-shelf model to DHGS conditions. Ultimately, the model variables and SMB model chosen for the final model setup are those which (in order of importance):

1. Create the most accurate surface elevation of the DHGS
2. Maintain some degree of ablation in the BIAs
3. Produce reasonable ice flow velocities
4. Accurately position the grounding line
5. Produces reasonable ice shelf thickness

5.5.1 Modifications of the all-Antarctic boundary ice flux

As discussed above, ice thickness upstream of the DHGS is generally overestimated by the all-Antarctic model (Figure 5.2, 5.3 and 5.4, section 5.4.2). Within the nested model, this leads to an unrealistic build-up of ice upstream of the DHGS. To acquire more accurate results within the nested grid for the present-day simulation, all-Antarctic model output of ice thicknesses were lowered to present-day levels along the north-western boundary of the nested model domain. In addition, ice flow out of the nested grid towards the upper catchment of the Carlyon Glacier (Figure 1.1) was decreased to avoid drawn-down of the ice surface in this

region. These changes recognise that some inaccuracies exist in the all-Antarctic model output, to which the simulation of the DHGS is sensitive towards, and the nested modelling results are improved following the changes. As these inaccuracies are likely to reflect a general problem caused by the low-resolution of the all-Antarctic model compared to the size of TAM outlet glaciers, the constant changes applied to the present-day all-Antarctic boundary values were maintained for the LGM simulation also. Therefore, if the all-Antarctic model predicts a change from present-day levels, the size of this change is maintained.

5.5.2 Enhancement factors

The significance of the flow enhancement factors in the ice sheet-shelf model was described in section 5.2.1. When the nested model is run with the default sheet and shelf flow enhancement factors of 5 and 0.5 respectively (Table 5.2), ice velocities on the Darwin Glacier are too high and surface elevations are generally too low for the entire glacial system. Through testing it was found that no accurate surface elevation and ice velocity of the DHGS could be obtained with reasonable basal slipperiness and SMB model when applying the all-Antarctic sheet enhancement factor. The best fit surface elevation, grounding line position and ice shelf thickness were obtained when maintaining a shelf flow enhancement factor of 0.5 but lowering the sheet flow enhancement factor to 2. In addition, a change from 5 to 2 of the sheet enhancement factor significantly improves the fit between measured and modelled surface velocities on the Darwin Glacier. However, modelled velocities are significantly lower than measured velocities on the Hatherton Glacier, while they still appear to be somewhat overestimated on the Darwin Glacier. When applying these settings to the nested model, the Byrd Glacier thickness increases and grounded ice advances to the boundary of the nested grid. This affects the Darwin Glacier grounding line position and downstream ice shelf thickness and was accounted for by adjusting the basal slipperiness, as described in more detail below.

5.5.3 Basal sliding coefficient

The magnitude of the modelled basal sliding velocity is related to a basal sliding coefficient as was described in section 5.2.2. However, as very little is known about the basal conditions underneath Antarctic glaciers, values have to be determined heuristically, which is also the case for the ice sheet-shelf model (Pollard and DeConto 2009b). A range of basal sliding coefficients was tested for the DHGS and eventually a value of 10^{-7} m a^{-1} Pa^{-2} for the bedrock where the rebound elevation is below sea level was found to produce the best fit grounding line position and surface elevation in the lower regions of the glacial system. For rebounded bedrock above sea level and frozen basal conditions, all-Antarctic basal sliding coefficients of 10^{-10} and 10^{-20} m a^{-1} Pa^{-2} respectively (Table 5.2) were maintained. The magnitude of the best

fit basal sliding coefficient in the region below the Darwin and Hatherton Glacier confluence suggest the presence of subglacial deformable sediments (section 5.2.2), although the effect of these sediments on the basal sliding velocity is significantly reduced compared to the all-Antarctic model.

In order to counteract the effect of the unrealistic ice conditions at the Byrd Glacier described above, a high basal sliding coefficient of 10^{-4} m a^{-1} Pa^{-2} was assigned to this region of the nested grid. Although the Byrd Glacier is still poorly simulated by the nested model, the increased basal sliding coefficient improves the ice thickness and grounding line position significantly and most importantly produces more realistic ice condition for the floating regions of the nested grid downstream of the DHGS.

5.5.4 Oceanic melt rate

The grounding line position and ice shelf thickness are sensitive to variations in oceanic melt rates, and tuning therefore involved varying the basal melt rate until the correct ice configuration is achieved near the grounding line (Figure 3.22). Following this procedure, an oceanic melt rate of 2 m yr^{-1} was found to produce the most accurate present-day grounding line position. When applying this basal melt rate, the ice shelf thickness immediately downstream of the grounding line is underestimated by the nested model. This suggests that although the assigned melt rate positions the Darwin Glacier grounding line reasonably well, it overestimates the basal melting further downstream where melting is likely significantly reduced (Frezzotti et al. 2000).

A calculation of basal melt rates near the DHGS grounding line presented in section 3.10 suggests an average melt rate of ~0.9 m yr^{-1} for the first 7 km downstream of the grounding line. It is consequently not unrealistic that the grounding line oceanic melt rate would be of the magnitude suggested by the model. As the modelled ice shelf thickness is uncertain primarily due to inaccuracies in simulations of the Byrd Glacier, a correct Darwin Glacier grounding line location was prioritised over a better agreement between measured and modelled ice shelf thickness. The ice shelf thickness and magnitude of best fit oceanic melt rate are sensitive to applied downstream boundary conditions (section 5.2.6), and the realistic oceanic melt rate suggested by the modelling experiments provides confidence in the model treatment of the Darwin Glacier grounding line as well as in the altered nesting routine.

5.5.5 Surface mass balance

Because of the lack of knowledge of SMB within the DHGS, several potential SMB models were proposed in section 4.5.5. All of these were tested with various nested model setups, the

results of which showed that the Hatherton Glacier, in particular, is sensitive to changes in SMB. An initial surface lowering of both the Darwin and Hatherton Glaciers occurs to various degrees when applying the proposed MB-1, MB-2 and MB-3 (Table 4.3). In contrast, MB-4 (zero SMB in BIA) produced reasonably good results for the Darwin Glacier, while ice thicknesses were overestimated on the Hatherton Glacier. Consequently, to limit the surface lowering of the Hatherton Glacier observed with MB-3 while maintaining some degree of ablation, the ablation rates proposed in MB-3 (Arthern et al. (2006) accumulation rates) were halved (section 4.5.6). In addition, accumulation rates in the high-elevation Hatherton accumulation areas were reduced to limit unrealistic build-up of ice in these regions. The resulting SMB model was referred to as MB-3A (Arthern et al. (2006) accumulation rates) in section 4.5.6. The crude adjustment of the proposed SMB is justified by the considerable uncertainties involved with the construction of the map (section 4.5).

5.5.6 Final nested model setup

Based on the above tuning process, the nested model setup which best simulates DHGS behaviour is summarised below in Table 5.3. When starting the nested model from the present-day ice configuration, steady state conditions are reached within 2000 yr except on the Hatherton Glacier and in steep high altitude catchment basins where minor changes continue to occur. On the Hatherton Glacier, a slow surface lowering takes place in response to the negative SMB (section 5.5.5), while the surface elevation of surrounding mountain glaciers increase above the DEM surface. Eventually the mountain glaciers begin to affect ice thickness on the Hatherton Glacier and after 10,000 yr, when the surface changes have begun to slow down, the modelled surface elevation of the Hatherton Glacier exceeds measurements by 40 - 200 m. Although snow accumulation was significantly reduced in high accumulation regions surrounding the Hatherton Glacier (section 5.5.5), the elevated ice surface is primarily the result of excess inflow of ice from adjacent mountain glaciers. Various attempts to stabilise the Hatherton Glacier through variations in model setup or SMB were unsuccessful, and illustrate the challenges involved with accurately simulating the behaviour of the Hatherton Glacier and the surrounding mountain glaciers. Local tributaries are thought to be particularly important in maintaining the low discharge of the Hatherton Glacier (section 2.4), which may explain why the glacier has posed a greater modelling challenge than the Darwin Glacier. As the observed changes appear to have a minimal affect on the simulated temperature and velocity fields, the model was run for 2000 yr only for the present-day simulation presented in section 5.6. Simulations of LGM ice extent have to be run for more than 10,000 years to allow for the glacial system to respond realistically to an advanced WAIS (section 5.7). Consequently in the LGM experiments, the uncertainties illustrated by the long present-day simulation are likely to have some influences on the overall result.

Table 5.3. Parameters and input datasets for the nested model. Table 5.2 lists equivalent model parameters and input datasets for the all-Antarctic model.

Parameters and input data	Nested model
Dynamic timestep [yr]	0.005
Enhancement factor (sheet)	2
Enhancement factor (shelf)	0.5
B (bed below sea level, warm-based) [m yr^{-1} Pa^{-2}]	10^{-4} and 10^{-7}
B (bed above sea level, warm-based) [m yr^{-1} Pa^{-2}]	10^{-10}
B (frozen base) [m yr^{-1} Pa^{-2}]	10^{-20}
B threshold for inclusion of SSA [m yr^{-1} Pa^{-2}]	10^{-8}
Present-day oceanic melt rates (protected) [m yr^{-1}]	2.0
LGM oceanic melt rates (protected) [m yr^{-1}]	0
Bedrock topography	Figure 4.7
Ice thickness	Figure 4.4
Surface mass balance	Figure 4.13

The tuning process has revealed interesting differences between the flow behaviour of the DHGS and the Antarctic Ice Sheet in general, as simulated by the all-Antarctic model. The nested model results are particularly sensitive to variations in the sheet flow enhancement factor, which had to be reduced considerably to produce accurate surface profiles and reasonable surface velocities (section 5.5.2). This relatively low value (section 5.2.1) may reflect: 1. an actual decrease in ice strain rate caused by differences in general flow characteristics between the DHGS and faster moving components of the Antarctic Ice Sheet, and/or 2. the influence of lateral drag from the valley walls, which are unaccounted for in the SIA (section 5.2.1). In either case, the low sheet flow enhancement factor reflects a low tendency of the DHGS to flow, despite relatively high ice thicknesses and driving stresses.

5.6 Modelled present-day DHGS characteristics

The nested model simulation of present-day DHGS provides information about the general characteristics and flow behaviour of the glacial system (objective A. 4 in section 1.1). In this section, the accuracy of the the present-day ice configuration and ice dynamics of the DHGS as simulated by the tuned nested model (section 5.5) will be evaluated (section 5.6.1). Section 5.6.2 presents modelled variations in force budget and basal temperature which are discussed in relation to flow behaviour of the Darwin and Hatherton Glaciers. The model results are compared to previous work on slow-moving TAM outlet glaciers (section 5.6.3) and

ultimately contribute towards a better understanding of the dynamic behaviour of this particular glacier type.

5.6.1 Accuracy of the present-day simulation

The nested model appears to simulate the behaviour of the DHGS well. The outline of the modelled catchment area differs only slightly from the catchment area calculated from the Altimetry DEM (Figure 1.1) and the modelled grounding line discharge of 0.44 km^3 yr^{-1} compares well with the catchment-wide (delineated from DEM) annual SMB of input map MB-3A (0.46 km^3 yr^{-1}, Table 4.3). Measured ice discharge close to the glacier grounding line (0.52 km^3 yr^{-1}) exceeds these two values, which suggests that either the DHGS is currently losing mass and/or MB-3A underestimates the overall SMB within the DHGS. Although it is possible that the DHGS is still adjusting to the termination of the LGM, it seems unlikely that the glacial system should be experiencing the relatively large negative mass balance suggested by the grounding line discharge discrepancy. Given the uncertainties of the SMB map (section 4.5), it is more likely that at least part of this difference is caused by an underestimation of the catchment-wide SMB predicted by MB-3A.

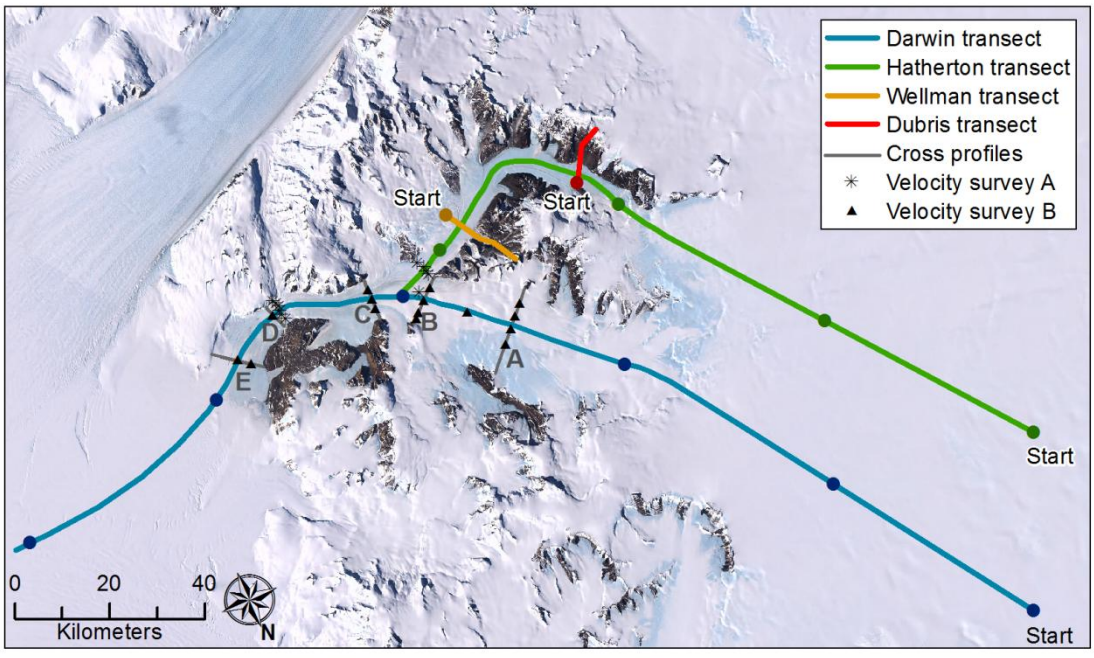

Figure 5.8. Map showing the location of the Darwin, Hatherton, Wellman and Dubris transects utilised to display model output. Coloured circles divide each transects into 50 km segments from its starting point. Velocity survey A was conducted by Hughes and Fastook (1981) while velocity survey B was presented in section 3.2.3.

The tuned nested model simulates variations in surface elevation on both the Darwin and Hatherton Glaciers reasonably well (Figure 5.9 and Figure 5.10). Differences between measured and modelled ice thickness are less than 100 m (<10% of total ice thickness) along the Darwin transect, except near the grounding line (at 185 km distance) where discrepancies between modelled and measured grounding line configuration lead to larger differences. The gradual ice shelf thickness increase found by the model towards the nested grid boundary (at 220-250 km distance) is caused by inaccuracies in the all-Antarctic simulation. The modelled Hatherton Glacier surface shows a better fit than the Darwin Glacier surface, and the ice thickness generally differs by no more than 50 m (~5% of total ice thickness). In general, surface elevations appear to be slightly underestimated on both the Darwin and Hatherton Glaciers, while the surface elevation of the EAIS is overestimated upstream of the Hatherton Glacier.

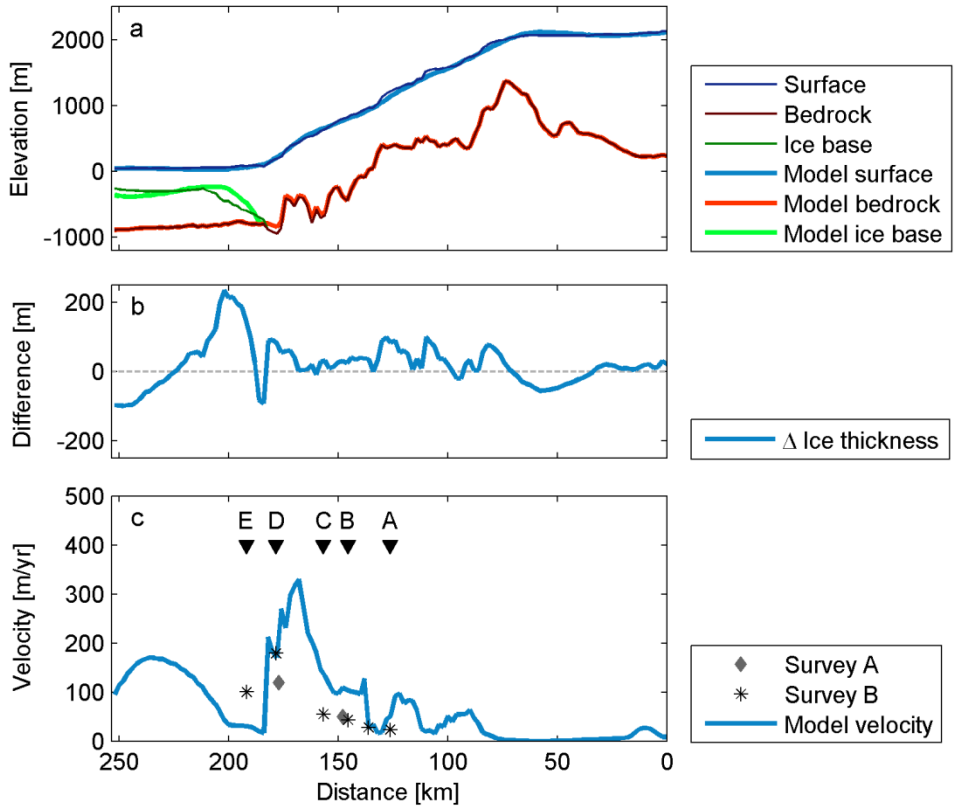

Figure 5.9. (a) Measured and modelled glacier configuration, (b) the difference between the two, and (c) ice velocity along the Darwin transect (Figure 5.8). Modelled surface velocities are compared with measured conducted by Hughes and Fastook (1981) (survey A) and the new measurements presented in section 3.2.3 (survey B). Capital letters show the locations of cross profiles (Figure 5.8).

The Darwin Glacier travels with velocities of up to 130 m yr^{-1} until below profile C (Figure 5.9c), after which a significant increase occurs to maximum values of ~330 m yr^{-1} at The Nozzle (Figure 2.1). In contrast, the modelled ice velocity of the Hatherton Glacier is extremely low, with values generally below 2 m yr^{-1}. Measured and simulated ice velocities compare well in the upper parts of the Darwin Glacier and at The Nozzle (Figure 2.1), while significant differences were observed at profile B, C and E (Figure 5.9c), and on the Hatherton Glacier (Figure 5.10c). Despite these uncertainties, the general downstream increase in measured flow velocities of the Darwin Glacier is captured well by the model. The difference observed at profile E is a result of the underestimation of modelled ice thickness which occurs at this location (Figure 5.10c).

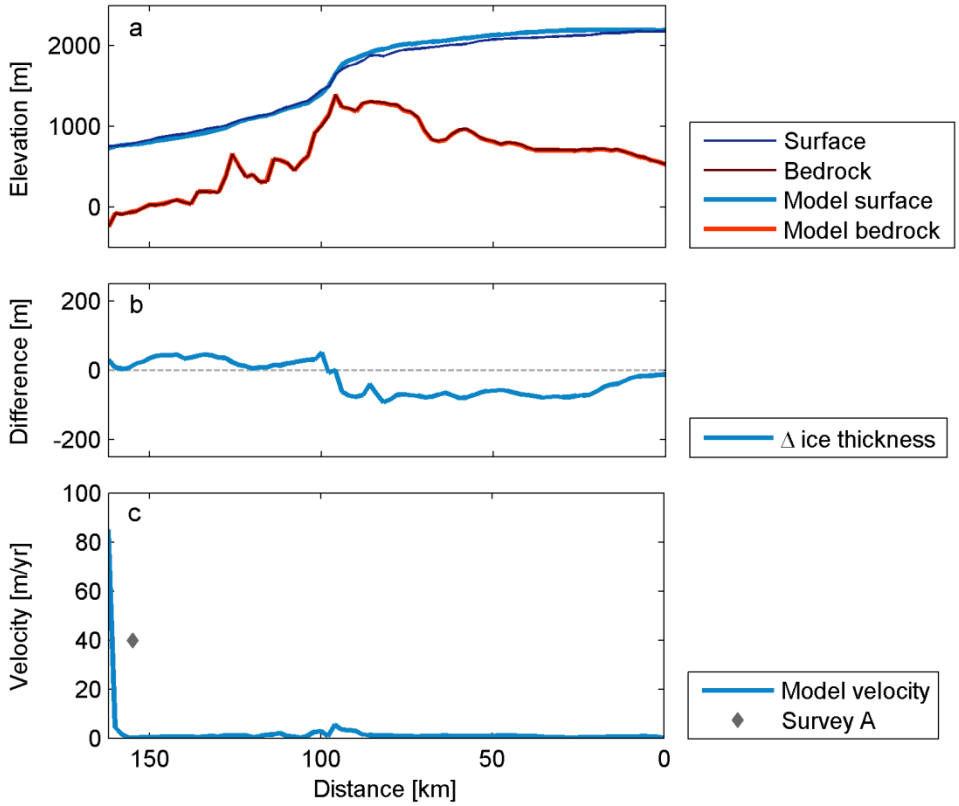

Figure 5.10. (a) Measured and modelled glacier configuration, (b) the difference between the two, and (c) ice velocity along the Hatherton transect (Figure 5.8). Modelled surface velocities are compared with measured conducted by Hughes and Fastook (1981) (survey A). Capital letters show the locations of cross profiles (Figure 5.8).

The low velocities suggested by the model on the Hatherton Glacier compare poorly with the ~40 m yr^{-1} measured in the lowermost part by Hughes and Fastook (1981, Figure 5.10c). A similar discrepancy between modelled and measured surface velocity has been documented by

previous modelling results (Figure 2.5, Anderson et al. 2004), which suggests that the low velocity indicated by the new velocity survey (section 3.2.3) provide a more realistic estimate of the Hatherton Glacier flow behaviour. The velocity measurements presented in section 3.2.3 (survey B in Figure 5.9c) are thought to be of reasonable quality, however, both these and the previous velocity measurements (survey B in Figure 5.9c and Figure 5.10c, Hughes and Fastook 1981) are all short-term, and it is unclear how well the measured velocities reflect annual values. Such uncertainties may explain the poor comparison between the two surveys at cross profile D.

Due to the nature of the velocity measurements and the potential uncertainties in ice flow dynamics associated with SIA models (section 5.2.7), the surface geometry is preferred as an indication of model performance. Given the complexity and uncertainties of the SMB, bedrock topography and nested boundary ice flux, the nested model output reflects the behaviour of the DHGS well. This suggests that the model is capable of accurately simulating the present and past dynamic behaviour of the glacial system.

5.6.2 Modelled flow dynamics of the DHGS

The nested ice sheet-shelf model facilitates 2-D illustrations of the large spatial variations which exist in ice characteristics across the DHGS (Figure 5.11). The Darwin Glacier is considerably thicker than the Hatherton Glacier, has higher driving stresses, exhibits partially warm-based conditions and as a consequence has the higher flow velocities (Figure 5.11). The map of surface velocities illustrates the extent of the DHGS catchment area and the proportions of inland ice captured by the Darwin and Hatherton Glaciers respectively. Although the nested model simulates flow behaviour of the Byrd Glacier poorly (section 5.5.2 and 5.5.3), the model output clearly shows the differences which exist between the DHGS and the much thicker, entirely warm-based and rapidly moving Byrd Glacier. Small isolated regions of high surface velocities and ice temperature visible at the head of ice flowing from the Britannia Range (figure 2.1) relate to steep mountainous regions where ice dynamics are poorly simulated.

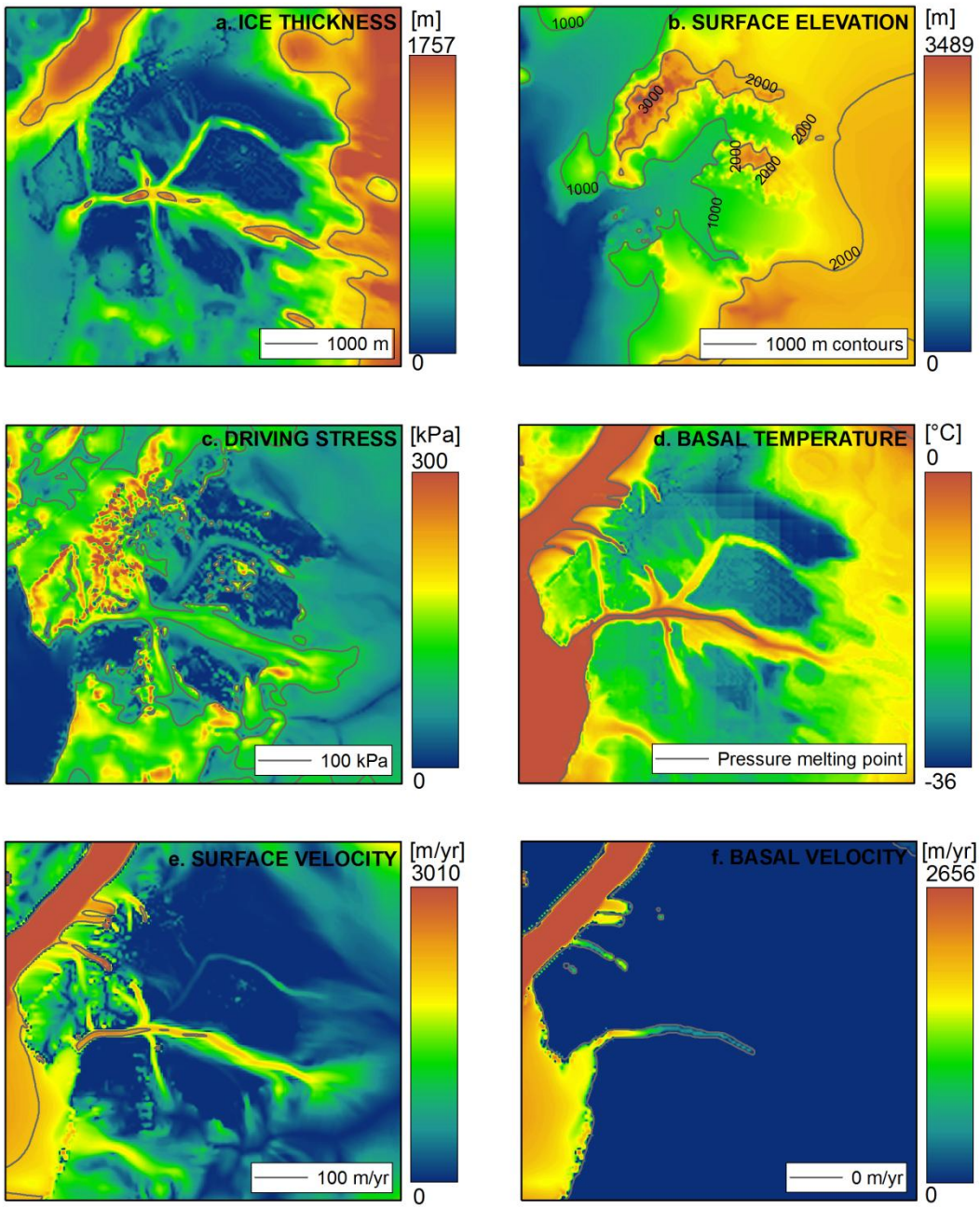

Figure 5.11. Present-day (a) ice thickness, (b) surface elevation, (c) driving stress, (d) basal temperature, (e) surface ice velocity, and (f) basal velocity within the nested model domain.

The variations in the force budget, ice temperature and ice velocity along the Darwin and Hatherton Glaciers are shown in more detail in Figure 5.12 and Figure 5.13. Variations along the two transects in the force budget are illustrated from modelled driving stress, basal shear stress and longitudinal stress, which is the residual of the two (Figure 5.12b). Driving stresses are generally high (~150 kPa) for the Darwin Glacier and reach values of 170 – 185 kPa below the head of the Darwin Glacier (at 85 km distance) and at The Nozzle (at 170 – 180 km

distance) where ice thickness and surface slopes are high (Figure 5.12b). Driving stresses are resisted by basal stresses for the upper half of the glacier (at 0 - 150 km distance), where only the SIA is applied. A decrease in basal stresses and resulting increase in longitudinal stresses occurs rapidly at a distance of ~150 km as the basal sliding coefficient increases above the critical values for inclusion of the SSA (section 5.2.2, Table 5.3). Although longitudinal stresses dominate further downstream, basal drag continues to be of importance until the grounding line, which is located at 185 km distance. The spike in basal stresses which occurs at ~180 km distance appears to relate to inflow of cold ice from the valley which traverses the Britannia Range towards the Byrd Glacier (Figure 2.1). Downstream of the grounding line, water column thickness rapidly increases to more than 300 m, and the basal stress is quickly reduced to zero (section 5.2.2). The driving and longitudinal stresses decrease more gradually as the slope of the floating ice shelf declines.

Driving stresses are considerably lower for the flatter and thinner Hatherton Glacier (Figure 5.13b). Values do generally not exceed 85 kPa except at the steep threshold towards the EAIS (at 95 km distance) where a maximum value of 190 kPa occurs. Because of the relatively high bed elevation and frozen basal condition, the SIA alone is applied throughout the profile, and driving stresses are continuously balanced by basal drag. On both the Darwin and Hatherton Glaciers, variations in driving stress are associated primarily with changes in surface slope, and increased values are generally observed at and just downstream of bedrock bumps where the ice thickness is relatively low. This relationship is most clear on the Hatherton Glacier where the valley width remains relatively constant. On the Darwin Glacier, ice velocities are furthermore affected by narrowing (velocity increase) and widening (velocity decrease) of the glacier width (Figure 5.11e).

Basal sliding occurs in regions where the ice base temperature reaches the pressure melting point (Figure 5.11d and f). However, ice flow within the DHGS is predominantly by internal ice deformation, and a significant level of basal sliding occurs only in the lower part of the Darwin Glacier (at >155 km distance, Figure 5.12c). Downstream of the grounding line (at >185 km distance), the internal ice deformation approaches zero and the basal velocity equals the average ice column velocity. In general, variations in ice flow velocities appears to be controlled primarily by changes in the driving stress, and peak velocities along the Darwin and Hatherton transects occur over and immediately downstream of bedrock bumps, where the driving stresses are highest.

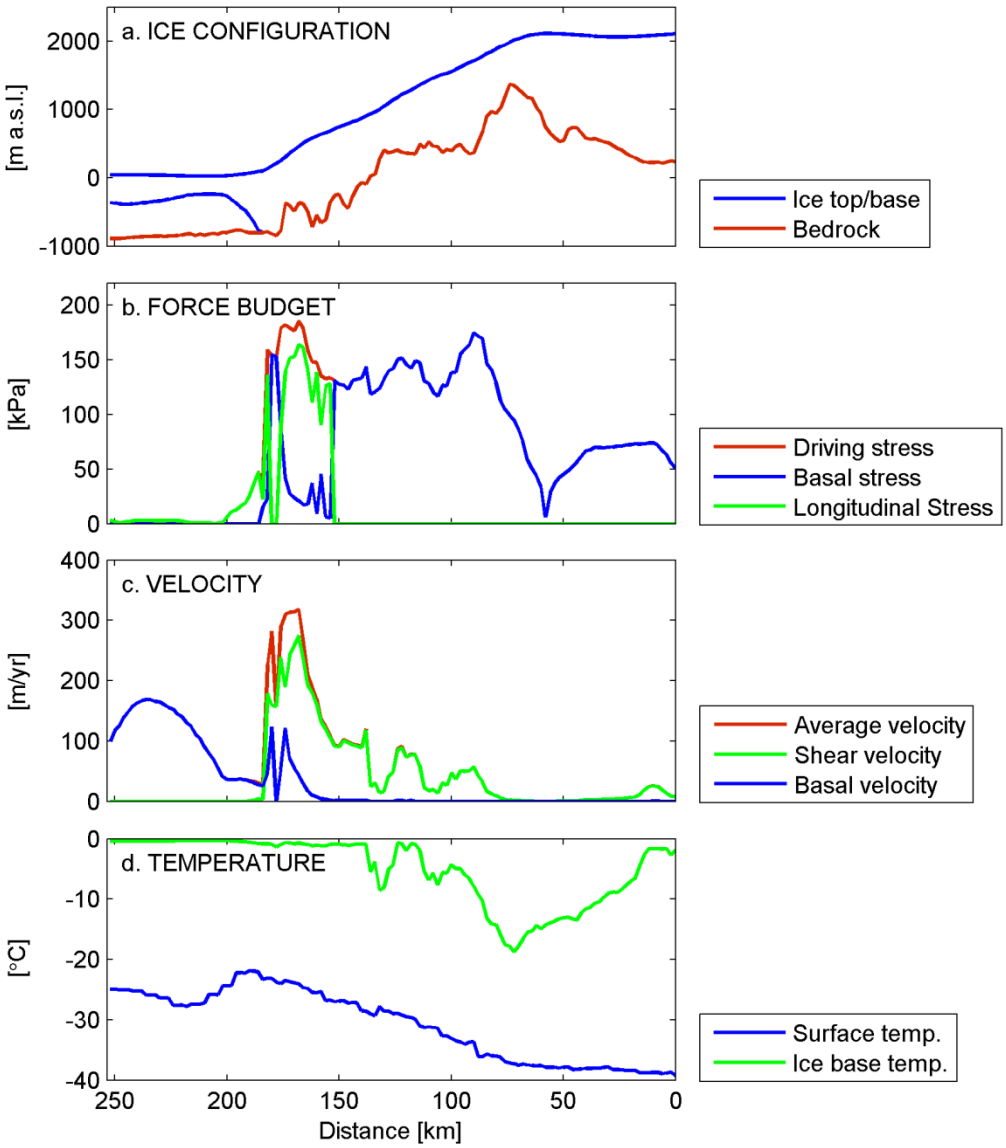

Figure 5.12. Summary of glacier characteristics along the Darwin centre transect as determined by the nested model. Where the basal temperature is below the pressure melting point, the driving stress is identical to the basal stress and the average velocity is identical to the shear velocity.

Both the Darwin and Hatherton Glaciers are significantly influenced by inflow of cold ice from the EAIS, and both are cold-based towards the polar plateau (Figure 5.11, Figure 5.12e and Figure 5.13e). Regions which are characterised by high basal/driving stress and ice velocities generally have increased basal temperatures, except at the head of the Hatherton Glacier (at 95 km distance, Figure 5.12e), where the ice is too thin to effectively insulate the base from the colder surface temperatures. The Hatherton Glacier bed remains below the pressure melting point throughout its extent, while the thickest regions of the Darwin Glacier are warm-based (Figure 5.11, Figure 5.11f and Figure 5.12). The downstream change from cold- to

warm-based conditions and increase in ice velocity observed on the Darwin Glacier corresponds well with the gradient in glacial erosion suggested by the gradual change in cross sectional valley shape identified in section 3.5.1.

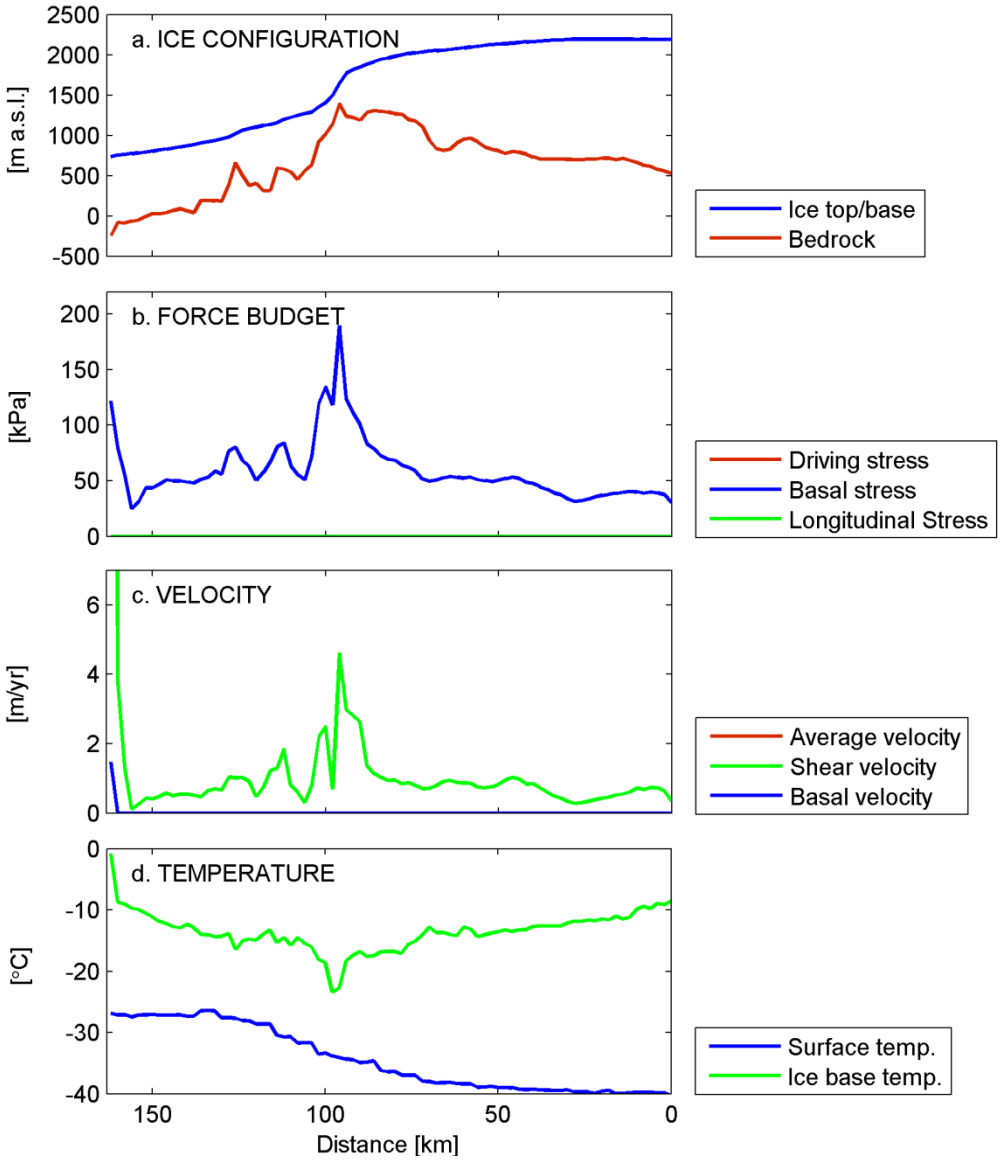

Figure 5.13. Summary of glacier characteristics along the Hatherton centre transect as determined by the nested model. As the basal temperature is constantly below the pressure melting point, the driving stress is identical to the basal stress and the average velocity is identical to the shear velocity.

5.6.3 DHGS characteristics in relation to outlet glaciers in the Transantarctic Mountains and other glacier types

The flow-tendency of various glacier types were compared by Kavanaugh and Cuffey (2009) from calculations of flow indexes ($U/\tau_d H$) from typical values of ice velocity (U), driving stress and ice thickness (Figure 5.14). Calculations of flow indices for the Darwin and Hatherton Glaciers show that the Hatherton Glacier as modelled by the nested model has an extremely low tendency to flow. The flow index for the Darwin Glacier is low compared to other glacier types of similar thickness, but significantly higher than both the Hatherton and Taylor Glaciers.

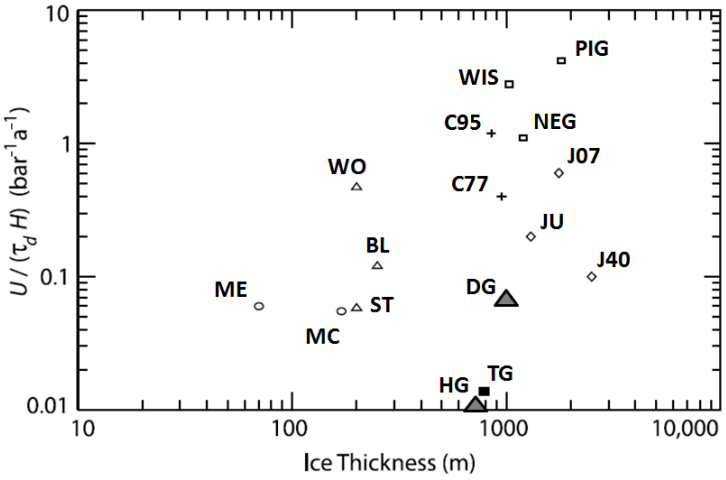

Figure 5.14. Flow index in relation to ice thickness for a range of glacier types such as slow moving TAM outlet glaciers (Darwin Glacier, DG; Hatherton Glacier, HG; Taylor Glacier, TG), alpine polar glaciers (McCall Glacier, MC and Meserve Glacier, ME), alpine temperate glaciers (Storglaciären, ST; Blue Glacier, BG; Worthington Glacier, WO), a temperate tidewater glacier (Columbia Glacier, C77 – 1977, and C95 – 1995), strong-bedded polar ice streams (Jakobshavn Isbræ, J07 - 7 km from terminus, and J40 - 40 km form terminus), and weak-bedded polar ice streams (Whillans Ice Stream, WIS; Pine Island Glacier, PIG; Northeast Greenland Ice Stream, NEG). Figure modified from Kavanaugh and Cuffey (2009).

The present-day model simulation provides new insight into the processes which control flow dynamics of the DHGS and slow moving glaciers in general. The findings distinguishes the glacial system from faster moving TAM outlet glaciers (section 1.5.2) where a high level of basal sliding and melting occurs, and instead compare well with the general characteristics of slow moving TAM glaciers (section 1.5.3). The findings offer support to the traditional 'cascade' model (section 1.5.3) which predicts highest velocities where surface slopes and driving stresses are highest (Kavanaugh and Cuffey 2009). The nested model found ice flow velocities of less than 5 m yr^{-1} for the Hatherton Glacier, which is entirely cold-based similar to the Taylor and Ferrar Glaciers (Johnson and Staiger 2007; Kavanaugh et al. 2009b). In

contrast, a significant proportion of the Darwin Glacier is warm-based and ice velocities reach several 100 m yr^{-1} in the narrowest and steepest regions. The Darwin and Hatherton Glaciers consequently belong to the fastest and slowest portion respectively of the slow moving TAM outlet glaciers behaviour spectrum (Table 1.2).

5.7 LGM characteristics of the DHGS

As a linkage between the EAIS and WAIS, variations in ice configuration within the DHGS can be used to constrain changes in the both of the Antarctic ice sheets (Chapter 1). In this section, the LGM ice extent and thickness of the DHGS as simulated by the nested model are compared to geological evidence of former ice configurations in order to establish the Holocene change of the glacial system (section 5.7, objective B.1). This analysis will provide new information on the response mechanisms of slow-moving TAM outlet glaciers, and will test the degree of change induced by the ice configuration of the EAIS and WAIS suggested by the all-Antarctic model (section 5.4.3).

The accurate simulation of present-day geometry and dynamics of the DHGS provides confidence that the nested model will be able to simulate past changes equally well. The Holocene change of the DHGS is investigated by varying the all-Antarctic input as well as the surface temperature, global sea level, SMB and the oceanic melt rate (section 5.2.3 and 5.2.4). The optimal settings for the nested model derived in section 5.5 were maintained during the simulations of the LGM ice configuration.

In order to investigate the LGM configuration of the DHGS, the nested model was run from present-day ice configuration with boundary conditions corresponding to the maximum ice extent (14,000 BP, section 5.4.3) and associated climatic conditions until a steady state was achieved (step 2 in Figure 5.1). The Darwin Glacier adjusts relatively quickly (~2000 yr) to LGM conditions (Figure 5.15a) whereas it takes 15,000 yr for the Hatherton Glacier to reach a LGM steady state. The all-Antarctic model output suggests that maximum ice thickness of the WAIS was only maintained for ~5000 yr (Figure 5.7) and although geological evidence indicates that this period was considerably longer (~15,000 yr, section 5.4.3), it seems unlikely that the Hatherton Glacier reached equilibrium during the LGM. This is in good correspondence with geological evidence from the Reedy Glacier, which suggests that this glacier similarly did not reach its equilibrium state during the LGM (Todd et al. 2010). Furthermore, at 15,000 yr the glacier surface is elevated between 50 and 120 m above the Britannia II drift sheet at levels above the Danum drift sheet in the middle regions (Figure 2.8). Previous studies have determined that the Danum drift sheet was deposited no later than 77,000 yr BP and more likely earlier than 140,000 yr BP (Table 2.1, Bockheim et al. 1989; Storey et al. 2010) and it is unlikely that the Hatherton Glacier was elevated above the

Britannia II limit during the LGM. The LGM simulation show that changes in the surface elevation of the Ross Ice Sheet has a significant impact on the Hatherton Glacier surface, and illustrates that it is unlikely that the glacier reached equilibrium during the LGM, even with the relatively low surface elevations of the Ross Ice Sheet suggested by the all-Antarctic model (section 5.4.3).

It is clear from the shape of the modelled glacier surfaces that the Hatherton drift sheet is unlikely to represent the LGM limit (Figure 5.15b) as has recently been proposed from surface exposure ages (Storey et al. 2010). If the Hatherton drift sheet was to represent the LGM limit, the ice thickness in the Ross Embayment would have had to have been significantly lower than predicted by the all-Antarctic model. Given that the all-Antarctic model has been run with a high basal sliding coefficient in the Ross Embayment (Table 5.2) and produces a low slope Ross Ice Sheet profile (Figure 5.6), it seems unlikely that surface elevation was significantly lower than that modelled at the LGM. Instead the general downstream decrease in elevation above the current glacier surface suggests that this particular drift sheet relates to a change in the upper regions, and may reflect a reduction in ice discharge from the EAIS into the Hatherton Glacier. In contrast, modelled surfaces compare well with the former glacier profiles outlined by the older and higher drift sheets (Figure 2.8), in particularly the Britannia II drift, which was proposed as the LGM limit by Bockheim et al. (1989). Consequently, the modelled surface profile which compares best with the Britannia II drift limit was chosen as the likely LGM limit (Figure 5.15b). It takes the Hatherton Glacier 12,500 yr to reach this level from its present-day ice configuration and at this point, the ice surface change has begun to slow down over most of the glacier. Although this is significantly longer than the ~5000 yr period of maximum WAIS thickness proposed by the all-Antarctic model, it compares reasonably well with the longer period of maximum ice extent suggested by geological evidence (section 5.4.3). The good match between modelled glacier surface elevation and the Britannia II drift limit elevation along the Hatherton Glacier (Figure 5.15b) suggests that the chosen surface profile correctly depicts the LGM ice configuration in the DHGS.

The LGM simulation of the DHGS illustrates the way in which the DHGS responds to changes in ice thickness in the Ross Embayment and of the EAIS as proposed by the all-Antarctic model. According to the all-Antarctic model, ice elevation along the south-eastern boundary (50 km from the Darwin Glacier outlet) of the nested grid was elevated 600-750 m above the present-day level. At the north-western boundary (~80 km from the head of the Hatherton and Darwin Glaciers) the ice surface was slightly elevated near the Byrd Glacier (~80 m) but similar to present-day values further north (section 5.4.3).

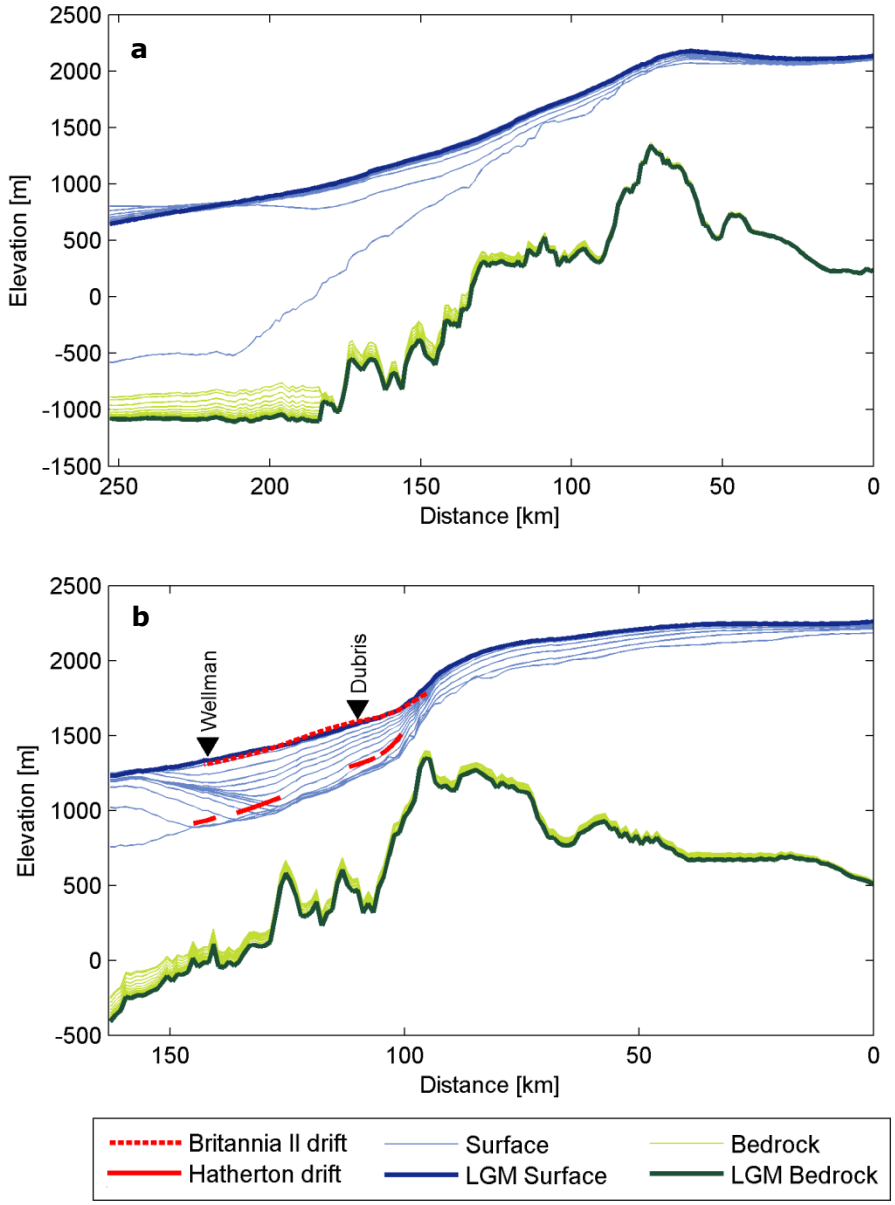

Figure 5.15. 1000 yr glacier surfaces (thin blue lines) and inferred LGM surface (thick blue line) along the (a) Darwin and (b) Hatherton transects (Figure 5.8). The associated glacier beds are show with green lines. Along the Hatherton transect, the level of the Britannia II (dashed red) and Hatherton (full red) drift sheets are shown (Bockheim et al. 1989).

During the LGM, build-up of the Darwin Glacier appears to be controlled by changes in the Ross Embayment only (Figure 5.15a). These changes induced a 830 m surface elevation increase at the Darwin Glacier outlet (at 200 km distance), while the LGM surface elevation at the glacier head was similar to present-day levels. The surface elevation continues to decrease monotonically from the Darwin Glacier outlet towards the Ross Embayment nested grid boundary. The Hatherton Glacier appears to have responded to an elevation increase of both

the Darwin Glacier and the EAIS upstream of the Byrd Glacier. The ice thickness increase which occurs on the Darwin Glacier propagates relatively quickly into the lower part of the Hatherton Glacier, after which the upstream surface elevation begins to slowly increase (Figure 5.15b). In the nested simulation, the rate of the upper Hatherton Glacier surface elevation increase is controlled predominantly by the surface elevation of the EAIS, but is sensitive to ice flux from local mountain glaciers. The LGM simulation shows that at the LGM, the Hatherton Glacier surface was elevated ~500 m above present-day levels at the confluence with the Darwin Glacier, whereas only a ~150 m increase occurred at the head of the glacier. Ice thickness at the threshold to the Hatherton Glacier is presently less than 200 m thick (Figure 3.18), and as the model illustrates, an increase of 150 m would have made a considerable impact on the flow behaviour.

One of the advantages of using the 3-D ice sheet-shelf model is that the model output can be readily compared to glacial drift sheet limits. These limits were delineated from aerial photographs and the maps produced by Bockheim et al. (1989) and compared to the advance of the Hatherton Glacier into the Lake Wellman and Dubris Valleys (Figure 5.8) during the LGM simulation (Figure 5.16). The Lake Wellman transect (Figure 5.16a) illustrates that although the Hatherton Glacier responds relatively quickly (~3000 yr) to an increased Darwin Glacier surface, it takes an additional 3000 yr before the glacier margin stabilises temporarily at a position below to the Hatherton drift sheet limit. Additional surface elevation increase and advance occurs as the changes caused by the elevated EAIS propagate to the lower part of the glacier. In comparison, the ice advance into the Dubris Valley (Figure 5.16b) occurs at a steadier pace in response to a continuous increase in surface elevation of the upper Hatherton Glacier controlled by the EAIS. At Lake Wellman and Dubris Valleys, the modelled LGM Hatherton Glacier terminates near the Britannia I limit, at between 600 and 800 m distance from, and less than 100 m below the Britannia II end-moraine. Given the 1 km resolution of the nested model, these results provide further support to the modelled LGM ice configuration of the DHGS.

Overall, the inferred LGM ice configuration compares well with the Britannia II surface elevation and extent, and consequently represents a significant improvement to the previous modelling study which failed to reproduce the former ice surface outlined by the drift limit (Figure 2.4). The modelled 830 m difference between LGM and present-day surface elevation at the Darwin Glacier outlet is significantly less than the 1100 m change estimated from extrapolation of the Britannia II drift sheet limit (Bockheim et al. 1989), but compares well with the 800 m difference indicated by the earlier modelling study (Anderson et al. 2004, Figure 2.4). In addition, the model results suggest that a simple extrapolation of drift sheet limits from the glacier outlet leads to a ~250 m overestimation of the Ross Ice Sheet surface elevation.

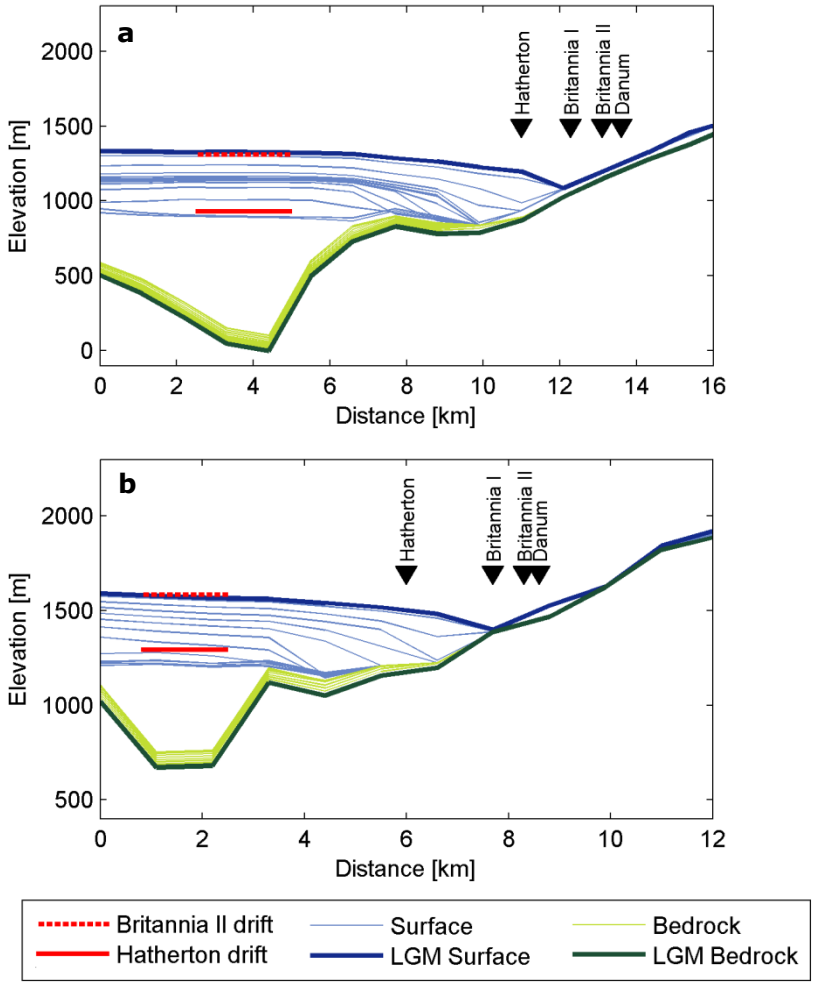

Figure 5.16. 1000 yr glacier surfaces (thin blue lines) and LGM equilibrium surface (thick blue line, +12,500 yr) along (a) the Wellman and (b) Dubris transects (Figure 5.8). The associated glacier beds are show with green lines. The limits of the glacial drift sheets are indicated with black arrows.

The general characteristics of the DHGS at the LGM are illustrated in Figure 5.17, which when compared to the present-day values (Figure 5.11) illustrates the considerable change which has occurred within the glacial system since then. Ice thickness change has been most dramatic at the mouth of the Darwin Glacier, where a thinning of more than 1500 m has occurred steepening the glacier profile (Figure 5.17a). The LGM ice thickness of both the Darwin and Hatherton Glacier generally exceed 1000 m and the surface of the glacial system is elevated more than 1000 m above the present-day sea level (Figure 5.17b). Present-day and LGM driving stresses are similar for the Hatherton Glacier where a gradual decrease downstream is observed during the LGM. In contrast, driving stresses are considerably lower

during the LGM for the Darwin Glacier because of a more gently sloping ice surface (Figure 5.17c). Cold EAIS ice propagated into the glacial system at the LGM and, although the ice thickness of the DHGS was significantly increased, the glacial system was warm-based only in the lowermost regions of the Darwin Glacier (Figure 5.17d). LGM and present-day surface and basal velocities (Figure 5.17e and Figure 5.17f) are generally similar for the Hatherton Glacier and lower during the LGM for the Darwin Glacier (maximum surface velocity <200 m yr^{-1}). The catchment basin of the DHGS and the proportion of inland ice captured by the Darwin and Hatherton Glaciers appear to remain constant over time (Figure 5.17e).

Continuous cold-based conditions since the LGM of the Hatherton Glacier raises questions about the source of glacial erratics showing evidence of active transport (Figure 2.6). Although significant erosion has been documented beneath cold-based Antarctic glaciers (Atkins et al. 2002; Davies et al. 2009), the abundance of abraded boulders surrounding the Hatherton Glacier indicates past warm-based states. This suggests that the boulders were abraded during previous warm-based conditions, possibly when the Hatherton Glacier surface was elevated to the Isca drift limit (Figure 2.8). However, additional modelling experiments are required in order to establish the source of these sediments.

The LGM simulation of the DHGS has provided interesting new insights into the response mechanisms of the glacial system as well as the magnitude of recent change, despite remaining uncertainties. Present-day simulation with the ice sheet-shelf model shows that during long simulations, the Hatherton Glacier surface elevation is sensitive to the model setup and input gridded datasets (section 5.5). Uncertainties in these quantities are likely to translate into uncertainties in the LGM simulation, and may affect the magnitude and rate at which the upper part of the Hatherton Glacier responds to changes in the Darwin Glacier and EAIS. However, the inflow from mountain glaciers is significantly reduced due to the SMB dependency on air temperature (section 5.2.3) and the modelled glacier surfaces appear to be controlled primarily by the ice thickness of the Darwin Glacier and EAIS. The inferred LGM ice configuration proposed by the nested model is therefore thought to accurately reflect the conditions in the Darwin-Hatherton region during this time. While the current nested model illustrates the way in which the DHGS responds to change and the magnitude of recent change, additional transient runs with the nested model would likely clarify the timing of these events.

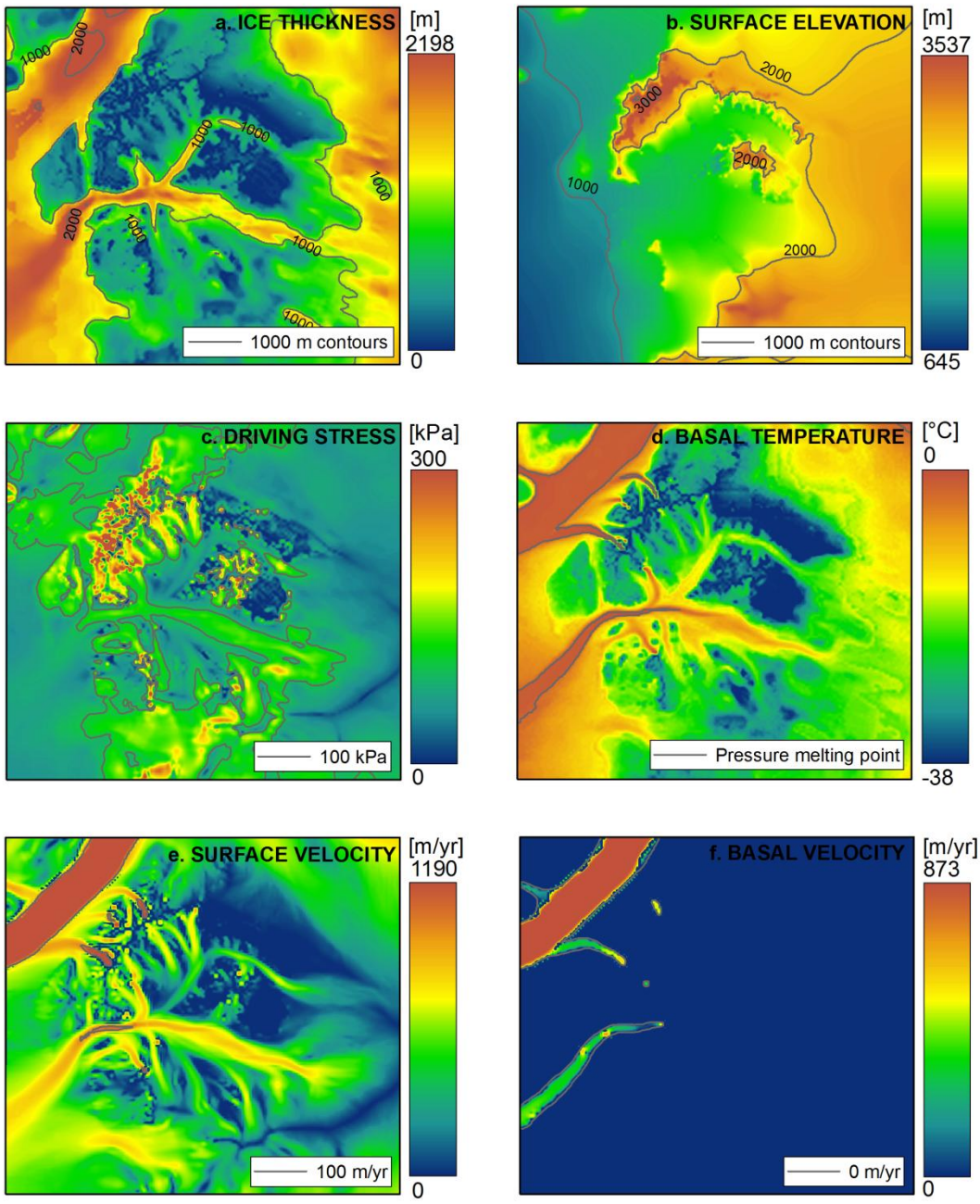

Figure 5.17. LGM (a) ice thickness, (b) surface elevation, (c) driving stress, (d) basal temperature, (e) surface ice velocity, and (f) basal velocity of the DHGS.

5.8 Present-day mass balance of the DHGS

Section 4.5.6 described the discrepancy which exists between grounding line discharge predicted by the SMB model that produces the best present-day model simulation (0.44 km^3 yr^{-1}, section 5.5.5), and a calculation of grounding line discharge from measurements of ice thickness and velocity (~0.52 km^3 yr^{-1}, section 3.9). Although the uncertainties of the SMB

map probably exceed the observed difference (section 4.5.6), it may at least partly reflect a negative mass balance of the DHGS.

The static simulation of LGM ice conditions within the DHGS presented above illustrate that the Darwin Glacier responds relatively quickly (~3000 yr) to changes in ice elevations of the EAIS and WAIS, whereas the dynamic response of the Hatherton Glacier is slow (>10,000 yr, section 5.7). Modelling experiments on the slow-moving Ferrar Glacier (Figure 1.5) have found that the glacier response time during retreat exceeds that of advance, the former of which is in the order of 10,000 yr (Golledge and Levy 2011). Previous studies suggest that the DHGS would have had between 7900 yr (Anderson et al. 2004) and 6800 yr (Conway et al. 1999, section 2.9.3) to adjust to the retreat of the WAIS grounding line south of the Darwin Glacier outlet. Although transient modelling experiments are required in order to accurately establish the response time of the Darwin and Hatherton Glaciers during a retreat, it seems likely that the Darwin Glacier is in equilibrium with the present-day climate, while the Hatherton Glacier is probably still thinning. However, as the Hatherton Glacier currently contributes very little to the grounding line discharge (section 2.4), uncertainties in SMB are likely to also be of importance in explaining the difference between ice discharge estimates (section 4.5.6). The inference of a continued thinning of the Hatherton Glacier compares well with results from the slow-moving Reedy Glacier (Figure 1.5, Todd et al. 2010), which show that the glacier has thinned 20 m during the last 1000 yr. Ultimately, additional measurements of SMB and grounding line ice thickness and velocity, or further modelling experiments are required in order to establish the cause of the difference between measured grounding line discharge and predicted catchment-wide SMB.

5.9 Conclusion

The results presented in this chapter illustrate a new approach to simulating the behaviour of TAM outlet glaciers, and of testing the dynamic response of these glaciers to past changes of the WAIS and EAIS. Previous modelling studies of TAM outlet glaciers have applied flow-line (Anderson et al. 2004; Golledge and Levy 2011) or flow-band models (Johnson and Staiger 2007), and the modelling study presented above represents the first attempt at applying a high-resolution 3-D model to simulate past and present flow behaviour of this particular glacier type. The 3-D nature of the model allows for a more accurate simulation of the coupling between the Darwin and Hatherton Glaciers as well as other important tributaries, and enables a good comparison of past ice extent to geological limits. In order to accurately account for the influence (ice thickness and temperature) of the EAIS and WAIS on the DHGS flow behaviour, the high-resolution 3-D model was nested within a lower resolution all-Antarctic model. Although nested experiments have been conducted with the ice sheet-shelf model before (Pollard and DeConto 2009b), the model setup applied to simulate the DHGS

represents the first attempt at running a small (220 x 220 km) nested ice sheet-shelf model at 1 km resolution. Because of the sudden and large change in scale upstream and downstream of the TAM outlet glaciers, the applied nesting approach is particularly suited to this region. The ice sheet-shelf model required considerable tuning in the sheet enhancement factor and basal slipperiness in order to produce a realistic present-day simulation of the DHGS. Following these adjustments, the nested ice shelf-shelf model simulates flow behaviour within the DHGS well, and ice thickness and extent fit glacial drift sheet boundaries during a LGM simulation. Therefore, despite the challenges involved, this study has successfully described the processes which control the current dynamics of the DHGS (objective A.1) and examined response mechanisms of the glacial system during the LGM (objective B.1).

The present-day nested simulation clearly demonstrates the differences which currently exist in glacier dynamics between the Darwin and Hatherton Glaciers. The Darwin Glacier is predominantly warm-based in the thickest regions and has high driving stresses (~150 kPa). This leads to relatively high ice velocities which reach maximum modelled levels of ~330 m yr^{-1} in the narrowest and steepest regions upstream of the glacier grounding line. The thickness of the ice shelf and applied oceanic melt rates are sensitive to the boundary ice flux, and with the adjusted nested setting, an oceanic melt rate of 2 m yr^{-1} maintains the grounding line close to the measured location. The Hatherton Glacier is entirely cold-based and has low driving stresses (<85 kPa) which peak over and just downstream of bedrock bumps where the surface slope is highest. Ice discharge is low, and modelled ice velocities generally do not exceed 2 m yr^{-1}. With its low discharge, the Hatherton Glacier is particularly sensitive to input SMB and modelled inflow from local mountain glaciers and the EAIS. Due to uncertainties in the SMB and modelled present-day experiment, it is unclear whether the Hatherton Glacier is in equilibrium with the current climate.

A model simulation of the LGM characteristics of the DHGS accurately reproduce former glacier surfaces indicated by glacial drift sheets and confirms that change in the WAIS grounding line is consistent with changes of the DHGS. The model results show that during the LGM the surface elevation at the Darwin Glacier outlet increased 830 m in response to a 600-750 m ice surface increase in the Ross Embayment (50 km from the Darwin Glacier outlet) caused by the advance of the WAIS. The induced change in Darwin Glacier surface elevation decreased inland and was close to zero at 100 km from the glacier grounding line. The Darwin Glacier responded quickly (~2000 yr) to changes in the Ross Embayment and was most likely in a LGM steady state. During the LGM, the Hatherton Glacier appears to have responded both to a 500 m increase in the Darwin Glacier surface elevation at the confluence and a ~150 m increase in the EAIS at the glacier head caused by a 80 m surface increase of the EAIS ~80 km further inland. The thickening of the Darwin Glacier led to a relatively rapid (~3000 yr) ice thickness increase in the lower part of the glacier, while an elevated EAIS resulted in a very

slow build-up of the ice surface further upstream. The time it takes for the Hatherton Glacier to reach equilibrium (15,000 yr) when run with static LGM boundary conditions, and the good correlation between a lower glacier surface (12,500 yr, inferred LGM surface) and the Britannia II drift sheet, both suggest that the Hatherton Glacier is unlikely to have reached a LGM steady state. The results illustrate that even minor changes in the EAIS may have had a significant influence on flow behaviour of glaciers such as the Hatherton Glacier, where inflow of ice from the ice sheet is restricted by high subglacial mountains. As other glacial drifts except the Hatherton drift sheet are deposited parallel to the Britannia II drift, it is inferred that the Hatherton and Darwin Glaciers have responded similarly to past variations in the WAIS and EAIS.

The shape of the various Hatherton Glacier surfaces produced by the nested model during the LGM steady state simulation illustrate that the Hatherton drift limit is unlikely to represent the LGM boundary as has been suggested based on recent surface exposure dates (Storey et al. 2010). The drift sheet may instead represent a much later adjustment of the Hatherton Glacier to a change in ice flow from the EAIS. In contrast, the modelled ice surface compares well with the Britannia II surface, which was inferred to outline the LGM extent of the Hatherton Glacier as suggested by Bockheim et al. (1989). The good comparison between the Britannia II drift limits and modelled glacier configuration provide confidence in the modelled glacier geometry and response mechanisms. It consequently seems likely that the LGM ice configuration suggested by the all-Antarctic model (EAIS and WAIS elevated 0-80 m and 600-750 m respectively above present-day surfaces) represents a realistic estimate of ice conditions at the nested boundaries at this time. The surface elevation increase this induced at the Darwin Glacier outlet (830 m) compares well with the 800 ±100 m found in a previous modelling study by Anderson et al. (2004). However, it is considerably lower than the 1100 m LGM surface elevation increase found by Bockheim et al. (1989) from a simple extrapolation of the Britannia II limit. The modelled LGM ice configuration within the nested domain suggests a monotonically decreasing surface elevation towards the Ross Embayment grid boundary. Prescribing WAIS LGM elevations directly from drift sheet limits at glacier outlets therefore leads to a large overestimation (~250 m) of surface elevation. The all-Antarctic surface elevation decrease predicted for the WAIS (600-750 m) and EAIS (0-80 m) since the LGM are thought to be representative for this region as a whole, as the south-eastern and north-western nested boundaries are located away from the immediate influence of the TAM. The estimate of Holocene change in ice surface elevation downstream of the DHGS is significantly lower than the 1100 m change proposed in the LGM reconstruction by Denton and Hughes (2000), which is constrained by extrapolated drift sheet limits in this region. Compared to this reconstruction, the work presented in this chapter supports the presence of a relatively thin Ross Ice Sheet in the Ross Embayment during the LGM.

The all-Antarctic LGM configuration produces realistic results within the DHGS, which confirms the modelled configuration of the EAIS and WAIS in this region despite the uncertainties of the model output (section 5.4.3). Further south, the LGM all-Antarctic model output suggests that ice surface elevations 50 km downstream of the Beardmore and Reedy Glaciers were elevated ~950 m (975 m a.s.l.) and ~620 m (1100 m a.s.l.) respectively above the modelled present-day surface (uncertainty of the present-day simulation <50 m). From geological evidence it has previously been inferred that the WAIS downstream of the Beardmore and Reedy Glaciers (Figure 1.5) was elevated 1100 m (Denton et al. 1989a) and 450-800 m (Todd et al. 2010) above present-day levels respectively. At Siple Dome (Figure 1.5) the all-Antarctic model suggests a LGM surface elevation of 940 m a.s.l. which indicates a 300 m surface increase compared to present-day elevations. This result compares well with previous modelling results, which found that a 200-400 m thinning has occurred at the Siple Dome since the LGM (Waddington et al. 2005). While the all-Antarctic LGM ice surface elevation in the Ross Embayment is lower than suggested at the Beardmore Glacier (Denton et al. 1989b) and by the LGM reconstruction of the Ross Embayment proposed by Denton and Hughes (2000), it compares well with evidence from the Siple Dome (Waddington et al. 2005) and the Reedy Glacier (Bromley et al. 2010; Todd et al. 2010). Despite the uncertainties of the all-Antarctic model output further north it appears that the simulated LGM ice configuration compares well with other evidence south of the DHGS.

In order to meet objective B.2, the present-day mass balance of the DHGS was discussed based on evidence of grounding line ice discharge (section 3.9), catchment-wide SMB (section 4.5.6 and 5.5.5) and modelled response time of the Darwin and Hatherton Glaciers (section 5.7). Although considerable uncertainties remain, evidence from the DHGS suggest that the Darwin Glacier is probably in equilibrium with the present-day climate, while the Hatherton Glacier is likely to still be adjusting slowly to the termination of the LGM.

6 Conclusion

Recent rapid dynamic changes in Antarctic outlet glaciers are largely responsible for the loss of mass observed in certain regions of the Antarctic ice sheet (Pritchard et al. 2009). The unexpected speed at which these changes have occurred have highlighted the need for a better understanding of the mechanisms responsible for, and the implications of, change of the Antarctic Ice Sheet. Glacial sediment deposits along margins of East Antarctic outlet glaciers in the TAM constitute the best preserved terrestrial evidence of past changes of the WAIS, and the magnitude and rate of changes have been determined largely from this record. Evidence from the LGM and subsequent retreat and thinning is well preserved. However, reconstructions of the LGM ice configuration of the Ross Ice Sheet rely on extrapolations of glacial drift sheet limits (Bromley et al. 2010; Denton and Hughes 2000), and do not account for the dynamic behaviour of TAM outlet glaciers, which are of importance (Anderson et al. 2004).

The research presented in this thesis has aimed to investigate the current and past behaviour of the DHGS, which belongs to a group of poorly understood, slow-moving TAM outlet glaciers. Evidence of past changes in both the EAIS and WAIS are preserved as glacial drift sheets in surrounding ice-free valleys, making the glacial system ideally located for studying temporal variations in Antarctic ice volume and extent. In order to address the proposed aims, data collected from glaciological, glaciomorphological and meteorological surveys were combined with a numerical ice-flow model to establish current flow dynamics of the DHGS as well as the response of the glacial system to past changes in the EAIS and WAIS.

6.1 Summary

The modelling experiments and the direct measurements of ice thickness, grounding line position, internal features and ice flow velocity enable a detailed description of dynamic behaviour of the DHGS and the main influencing processes (objectives A.1 – A.4).

One of the main findings to emerge from this study is the large difference in flow behaviour between the Hatherton and Darwin Glaciers. The Darwin Glacier is up to 1500 m thick, has relatively high driving stresses (~150 kPa) and is partially warm-based. Ice velocities of up to

180 m yr^{-1} were measured in the narrowest and steepest regions just upstream of the glacier grounding line, where modelled velocities also peak at ~330 m yr^{-1}. Ice drains into the Darwin Glacier from the EAIS through a 1000 m deep and narrow subglacial valley and constitutes the most important mass input. The upper Darwin Glacier is wide and relatively shallow and ice flows slowly (<30 m yr^{-1}) over large bedrock troughs and ridges causing variations in longitudinal stresses and indirectly affecting the SMB through changes in surface slope. Further downstream, basal temperatures reach the pressure melting point, ice velocities increase and a change in glacier valley shape suggests enhanced basal sediment erosion. The Darwin Glacier is grounded well below sea level for more than 40 km upstream of the grounding line which is located ~925 m below s.l. The grounding line is currently situated on a downward sloping bed and is therefore likely to be in a stable position; however, the undulating nature of the bed upstream of the grounding line indicate the potential for rapid grounding line changes. The grounding line ice discharge was inferred to be close to 0.52 km^3 yr^{-1} measured through a cross section 5 km further upstream. From calculations of ice flux upstream and downstream of the Darwin Glacier grounding line, an average oceanic melt rate of ~0.9 m yr^{-1} was determined for the first 7 km of the Ross Ice Shelf.

The relatively narrow Hatherton Glacier is surrounded by steep mountains and ice thickness does not exceed 900 m. Driving stresses are low (~85 kPa) compared to the Darwin Glacier and decrease slightly downstream. The glacier is entirely cold-based and modelled ice velocities do not exceed 5 m yr^{-1} although previous measurements suggest velocities of ~40 m yr^{-1} near the Darwin Glacier (Hughes and Fastook 1981). Ice velocity measurements presented here suggest that flow velocities are <10 m yr^{-1} in the middle regions of the glacier and are consequently in better keeping with the modelling results. Ice drainage from the EAIS is restricted by a high subglacial ridge at the head of the Hatherton Glacier, above which the ice thins to less than 200 m. The present-day model simulation of the Hatherton Glacier suggests that because of a very low ice discharge, the glacier is particularly sensitive to variations in the EAIS thickness, inflow from local mountain glaciers, and SMB. The Darwin and Hatherton Glaciers both have low flow indices, which appears to be a common characteristic for slow-moving TAM outlet glacier (Kavanaugh and Cuffey 2009). However, with its partially warm-based conditions and relatively high ice velocities, the Darwin Glacier has several characteristics in common with the fast-moving TAM outlet glaciers.

Both the Darwin and Hatherton Glaciers display a surface patchwork of blue ice and snow which is controlled primarily by the development of katabatic winds and kilometre-scale changes in glacier surface slope related to ice flow over large bed undulations. Measurements of surface ablation on the Hatherton Glacier blue ice surface suggests a relatively high average ablation rate of ~0.1 cm day^{-1} during the summer period, and annual sublimation rates may be as high as ~13 cm w.e. The catchment-wide SMB was calculated for a range of scenarios

and compared to measured ice discharge close to the grounding line, as well as model performance. Results show that the 0.46 km^3 yr^{-1} catchment-wide SMB suggested by scenario MB-3A best reflects the conditions within the DHGS. This is slightly less than the ~0.52 km^3 yr^{-1} inferred grounding line discharge. Although the discrepancy could be related to an underestimation of SMB by the MB-3A scenario it was inferred that it, at least partly, reflects a negative current mass balance of the DHGS caused by a continued thinning of the Hatherton Glacier.

Based on the research presented in this thesis it is inferred that the slow ice flow velocity which distinguishes the DHGS from the fast moving TAM glaciers is controlled by restricted inflow from the EAIS, partly (Darwin Glacier) or fully (Hatherton Glacier) cold-based conditions, low SMB, and a rough bedrock topography. However, the distribution of glacial drift sheets adjacent to the Hatherton Glacier and the LGM simulation presented in this chapter illustrate that large changes within the DHGS appear to be controlled by changes in the WAIS and to some extent the EAIS.

In order to investigate the magnitude of change within the DHGS to changes in the WAIS and EAIS, a high-resolution (1 km) 3-D numerical ice-flow model was nested within a low-resolution (20 km) all-Antarctic model. The all-Antarctic model simulation of past change in the Antarctic Ice Sheet suggests that a 600-750 m surface elevation increase occurred downstream of the DHGS outlet as the WAIS grounding line advanced north into the Ross Embayment during the last glaciation. This resulted in a damming of the TAM outlet glaciers, leading to a minor surface elevation increase in the EAIS (0-80 m) close to the TAM inland of the DHGS. This low resolution model output was used to drive a static LGM (at 14,000 yr BP) nested simulation in order to determine the LGM ice configuration within the DHGS (objective B.1). The high resolution model output confirms the ice configuration proposed by the all-Antarctic model at the boundary of the nested domain.

The high-resolution nested simulation of LGM ice configuration in the DHGS indicate that the Darwin Glacier responded rapidly (~2000 yr) to the increased surface elevations in the Ross Embayment and consequently is likely to have reached steady state during the LGM. In contrast, the build-up to a steady state of the Hatherton glacier was slow (15,000 yr) and the final surface profile too high in the middle regions, and it was inferred that the glacier did not reach equilibrium during the LGM. This result compares well with geological evidence from the Reedy Glacier (Figure 1.5) which shows that this glacier was not in equilibrium during the LGM despite its location further south and therefore would have had longer time to respond to increased ice thickness in the Ross Embayment. Modelled centre line glacier profiles of the Hatherton Glacier far exceed the levels proposed by the preferred minimum age model suggested by Storey et al. (2010) and instead compare well with the interpretation of drift

sheet ages presented by Bockheim et al. (1989). As a result, the modelled Hatherton Glacier surface which compared best with the Britannia II drift sheet limit (12,500 yr) was inferred to represent the LGM ice configuration within the DHGS.

The nested model suggests that at the LGM the Darwin Glacier was elevated 830 m above the present-day ice surface near the glacier outlet, while little change occurred at the glacier head ~100 km further inland. The Hatherton Glacier probably responded both to an upstream ~150 m increase in the EAIS ice surface near the glacier head and a downstream 500 m increase in the Darwin Glacier surface compared to present-day levels. The nested model output suggests that cold-based conditions persisted throughout the LGM at the Hatherton Glacier, and the exposed glacial sediments that show signs of active transport must have been abraded during earlier warm-based conditions. Since the LGM, the Darwin Glacier profile has steepened significantly, while the present-day Hatherton Glacier surface gradient was similar at the LGM, except near the EAIS where a steepening has occurred.

The LGM ice configuration suggested by the all-Antarctic and nested model confirms that change of the DHGS and other TAM outlet glaciers entering the Ross Embayment can be explained by changes in the WAIS grounding line. In addition the model results illustrate that for glaciers such as the Hatherton Glacier, where inflow of ice from the EAIS is restricted by subglacial mountains, even a minor increase in the EAIS may have had a significant influence on the LGM ice discharge. The 3-D nested model simulates present-day and LGM surface elevation and extent of the DHGS well, which provides confidence in the former ice configuration proposed by the model in regions where glacial sediments are absent. The model results illustrate that a 600-750 m surface elevation increase in the Ross Embayment downstream of the DHGS outlet would have been sufficient for the Hatherton Glacier to thicken to the Britannia II drift sheet limit. This suggests that the surface elevation of the Ross Ice Sheet was significantly lower than suggested by downstream extrapolation of the Britannia II drift sheet limit (Bockheim et al. 1989) or the surface elevation at the Darwin Glacier outlet (Anderson et al. 2004). If the all-Antarctic LGM ice configuration is accurate further south also, the Ross Ice Sheet was elevated ~950 m above the present-day surface 50 km downstream of the Beardmore Glacier. This is significantly less than the 1100 m elevation difference suggested by extrapolation of glacial drift sheets (Denton et al. 1989a). In contrast, the all-Antarctic model output compares well with estimates of LGM surface elevations at the Reedy Glacier (Bromley et al. 2010; Todd et al. 2010) and Siple Dome (Waddington et al. 2005), where evidence similarly suggest the presence of somewhat thinner grounded ice in the Ross Embayment than the reconstruction in Denton and Hughes (2000).

The examinations of ice discharge, SMB and model setup and output presented in chapter 3 to 5 allows for a discussion of the present-day mass balance of the DHGS (objective B.2). From

these results it was inferred that the Darwin Glacier is in equilibrium with the current climate, while the Hatherton Glacier is probably still adjusting to the termination of the LGM. Overall, the DHGS may consequently be experiencing a slightly negative mass balance at present.

The summarised research has combined newly acquired field measurements with a numerical ice-flow model in an effort to describe the present and past behaviour of the DHGS. The direct measurements of key parameters have provided valuable information about the geometry, dynamics and SMB of the DHGS and enabled the fitting of a high-resolution nested 3-D ice sheet-shelf model to a complex glacial system. In combination, the high quality field measurements and the modelling experiments have established the main processes which currently control the behaviour of the two glaciers as well as the forcing which has instigated change in the past. The modelling study presents new evidence to the significance of glacial deposits adjacent to the Hatherton Glacier and has provided further constraint on the LGM surface elevation of the EAIS and WAIS in the region surrounding the DHGS. These results may serve as guidelines in future studies of slow-moving TAM outlet glaciers. In addition, the all-Antarctic LGM ice surface elevations of the WAIS and EAIS in the vicinity of the DHGS can be used to test the performance of other ice sheet models in this region.

6.2 Future work

One of the key findings of this study is the sensitivity of the Hatherton Glacier in particular to uncertainties in SMB and ice discharge from local Mountain glaciers. Due to the lack of observations, the SMB of the glacier was inferred from one point measurement and ice thickness was linearly extrapolated into ice filled valleys from centre line measurements. In addition, the tuning process was further complicated by the uncertainty and scarcity of ice velocity measurements. As a result, some uncertainties exist in the model treatment of the Hatherton Glacier. These uncertainties could be reduced by additional measurements of SMB and/or the application of a regional climate model, additional GPR or airborne radar measurements, and longer in situ velocity surveys and/or a remote sensing study of flow field. Future modelling work should involve applying the 3-D nested model in transient simulations of the last glaciations and subsequent thinning and retreat. These experiments will provide additional information about the timing of past changes in the Ross Embayment and establish more accurately whether change is ongoing at the DHGS.

Finally, this work has highlighted the need to re-examine the way in which glacial drift sheet limits have been applied as indicators of former surface elevations of the WAIS. This will ultimately lead to more accurate estimates of LGM thickness and extent of grounded ice in the Ross Embayment, which will contribute towards quantifying past and present contributions of the Antarctic Ice Sheet to global sea level changes.

References

Ackert, RP, Barclay, DJ, Borns, HW, Calkin, PE, Kurz, MD, Fastook, JL and Steig, EJ 1999, 'Measurements of past ice sheet elevations in interior West Antarctica', *Science,* vol. 286, no. 5438, pp. 276-80.

ADD-Consortium 2000, *Antarctic Digital Database, Version 3.0, Database, manual and bibliography*, Cambridge.

Alley, RB, Spencer, MK and Anandakrishnan, S 2007, 'Ice-sheet mass balance: assessment, attribution and prognosis', *Annals of Glaciology,* vol. 46, pp. 1-7.

Anderson, BM, Hindmarsh, RCA and Lawson, WJ 2004, 'A modelling study of the response of Hatherton Glacier to Ross Ice Sheet grounding line retreat', *Global and Planetary Change,* vol. 42, no. 1-4, pp. 143-53. Article.

Anderson, JB, Shipp, SS, Lowe, AL, Wellner, JS and Mosola, AB 2002, 'The Antarctic Ice Sheet during the Last Glacial Maximum and its subsequent retreat history: A review', *Quaternary Science Reviews,* vol. 21, no. 1-3, pp. 49-70.

Annan, AP 2001, *Ground penetrating radar - Workshop notes*, Sensors and Software Inc., Mississauga, Ontario, Canada.

Annan, AP 2009, 'Chapter 1 - Electromagnetic Principles of Ground Penetrating Radar', in HM Jol (ed.), *Ground penetrating radar: theory and applications*, Elsevier, p. 524.

Arcone, SA 2002, 'Airborne-radar stratigraphy and electrical structure of temperate firn: Bagley Ice Field, Alaska, U.S.A', *Journal of Glaciology,* vol. 48, pp. 317-34.

Arcone, SA 2009, 'Chapter 12 - Glaciers and ice sheets', in HM Jol (ed.), *Ground penetrating radar: theory and applications*, Elsevier, p. 524.

Arthern, RJ, Winebrenner, DP and Vaughan, DG 2006, 'Antarctic snow accumulation mapped using polarization of 4.3-cm wavelength microwave emission', *Journal of Geophysical Research,* vol. 111, no. D6, p. D06107.

Atkins, CB, Barrett, PJ and Hicock, SR 2002, 'Cold glaciers erode and deposit: Evidence from Allan Hills, Antarctica', *Geology,* vol. 30, no. 7, pp. 659-62.

Augustin, L, Barbante, C, Barnes, PRF, Barnola, JM, Bigler, M, Castellano, E, Cattani, O, Chappellaz, J, DahlJensen, D, Delmonte, B and et al. 2004, 'Eight glacial cycles from an Antarctic ice core', *Nature,* vol. 429, no. 6992, pp. 623-8. Article.

Bamber, JL, Gomez-Dans, JL and Griggs, JA 2009a, 'Antarctic 1 km Digital Elevation Model (DEM) from Combined ERS-1 Radar and ICESat Laser Satellite Altimetry'. National Snow and Ice Data Centre (NSIDC), Colorado, USA.

Bamber, JL, Gomez-Dans, JL and Griggs, JA 2009b, 'A new 1km digital elevation model of the Antarctic derived from combined satellite radar and laser data – Part 1: Data and methods', *The Cryosphere,* vol. 3, no. 1, pp. 101-11.

Bamber, JL, Vaughan, DG and Joughin, I 2000, 'Widespread Complex Flow in the Interior of the Antarctic Ice Sheet', *Science,* vol. 287, no. 5456, pp. 1248-50.

Benjumea, B, Macheret, YY, Navarro, FJ, Teixid and Teresa 2003, 'Estimation of water content in a temperate glacier from radar and seismic sounding data', *Annals of Glaciology,* vol. 37, pp. 317-24.

Benn, DI and Evans, DJA 1998, 'Glaciers and glaciation', in.

Bindschadler, R 2006, 'The environment and evolution of the West Antarctic ice sheet: setting the stage', *Philosophical Transactions of the Royal Society a-Mathematical Physical and Engineering Sciences,* vol. 364, no. 1844, pp. 1583-605.

Bindschadler, R 2007, 'ICE CORES | Dynamics of the West Antarctic Ice Sheet', in *Encyclopedia of Quaternary Science*, Elsevier, pp. 1296-305.

Bintanja, R 1999, 'On the glaciological, meteorological, and climatological significance of Antarctic blue ice areas', *Reviews of Geophysics,* vol. 37, no. 3, pp. 337-59.

Bintanja, R 2000, 'Surface heat budget of Antarctic snow and blue ice: Interpretation of spatial and temporal variability', *Journal of Geophysical Research-Atmospheres,* vol. 105, no. D19, pp. 24387-407. Article.

Bintanja, R 2001, 'Characteristics of snowdrift over a bare ice surface in Antarctica', *J. Geophys. Res.,* vol. 106, no. D9, pp. 9653-9.

Bintanja, R, Lilienthal, H and g, H 2001, 'Observations of snowdrift over Antarctic snow and blue-ice surfaces', *Annals of Glaciology,* vol. 32, pp. 168-74.

Bintanja, R and Reijmer, CH 2001, 'Meteorological conditions over Antarctic blue-ice areas and their influence on the local surface mass balance', *Journal of Glaciology,* vol. 47, pp. 37-50.

Bintanja, R and van den Broeke, MR 1995, 'The climate sensitivity of Antarctic blue-ice areas', in DA Rothrock (ed.), *Annals of Glaciology, Vol 21, 1995 - Proceedings of the International Symposium on the Role of the Cryosphere in Global Change*, pp. 157-61.

Bockheim, JG, Wilson, SC, Denton, GH, Andersen, BG and Stuiver, M 1989, 'Late Quaternary Ice-Surface Fluctuations of Hatherton Glacier, Transantarctic Mountains', *Quaternary Research,* vol. 31, no. 2, pp. 229-54.

Bogorodsky, VV, Bentley, CR and Gudmandsen, PE 1985, *Radioglaciology*, D. Reidel Publishing Company, Dordrecht.

Brandt, RE and Warren, SG 1993, 'Solar-heating rates and temperature profiles in Antarctic snow and ice', *Journal of Glaciology,* vol. 39, no. 131, pp. 99-110.

Brecher, H 1982, 'Photogrammetric determination of surface and elevations on Byrd Glacier', *Antarctic Journal of U.S.,* vol. 17, no. 5, pp. 79-81.

Bromley, GRM, Hall, BL, Stone, JO, Conway, H and Todd, CE 2010, 'Late Cenozoic deposits at Reedy Glacier, Transantarctic Mountains: implications for former thickness of the West Antarctic Ice Sheet', *Quaternary Science Reviews,* vol. 29, no. 3-4, pp. 384-98.

Brown, IC and Scambos, TA 2004, 'Satellite monitoring of blue-ice extent near Byrd Glacier, Antarctica', *Annals of Glaciology,* vol. 39, pp. 223-30.

Budd, WF, Jenssen, D and Radok, U 1971, *Derived physical characteristics of the Antarctic ice sheet*, The Antarctic Division, Department of Supply, Melbourne, Australia.

Budd, WF and Warner, RC 1996, 'A computer scheme for rapid calculations of balance-flux distribution', *Annals of Glaciology,* vol. 23, pp. 21-7.

Catania, GA, Conway, H, Raymond, CF and Scambos, TA 2005, 'Surface morphology and internal layer stratigraphy in the downstream end of Kamb Ice Stream, West Antarctica', *Journal of Glaciology,* vol. 51, no. 174, pp. 423-31. Article.

Catania, GA, Hulbe, CL and Conway, H 2010, 'Grounding line basal melt rates determined using radar-derived internal stratigraphy', *Journal of Glaciology,* vol. 56, no. 197, pp. 545-54.

Chapman, WL and Walsh, JE 2007, 'A synthesis of Antarctic temperatures', *Journal of Climate,* vol. 20, no. 16, pp. 4096-117. Article.

Chinn, TJ 1998, 'Recent fluctuations of the Dry Valleys glaciers, McMurdo Sound, Antarctica', *Annals of Glaciology,* vol. 27, pp. 119-24.

Clark, PU and Mix, AC 2002, 'Ice sheets and sea level of the Last Glacial Maximum', *Quaternary Science Reviews,* vol. 21, no. 1-3, pp. 1-7.

Clarke, TS and Bentley, CR 1994, 'High-Resolution Radar on Ice Stream B2, Antarctica - Measurements of Electromagnetic Wave Speed in Firn and Strain History from Buried Crevasses', *Annals of Glaciology,* vol. 20, pp. 153-9. 5th International Symposium on Antarctic Glasiology (VISAG).

Comiso, JC 2000, 'Variability and trends in Antarctic surface temperatures from in situ and satellite infrared measurements', *Journal of Climate,* vol. 13, no. 10, pp. 1674-96.

Conway, H, Hall, BL, Denton, GH, Gades, AM and Waddington, ED 1999, 'Past and future grounding-line retreat of the West Antarctic Ice Sheet', *Science,* vol. 286, no. 5438, p. 280.

Cuffey, KM, Conway, H, Gades, AM, Hallet, B, Lorrain, R, Severinghaus, JP, Steig, EJ, Vaughn, B and White, JWC 2000, 'Entrainment at cold glacier beds', *Geology,* vol. 28, no. 4, pp. 351-4. Article.

Davies, MTL, Atkins, CB, van der Meer, JJM, Barrett, PJ and Hicock, SR 2009, 'Evidence for cold-based glacial activity in the Allan Hills, Antarctica', *Quaternary Science Reviews,* vol. 28, no. 27-28, pp. 3124-37. Article.

Davis, CH, Li, YH, McConnell, JR, Frey, MM and Hanna, E 2005, 'Snowfall-driven growth in East Antarctic ice sheet mitigates recent sea-level rise', *Science,* vol. 308, no. 5730, pp. 1898-901.

Denton, GH 1979, 'Glacial history of the Byrd-Darwin Glacier area, Transantarctic Mountains', *Antarctic Journal of U.S.,* vol. 14, no. 5, pp. 57-8.

Denton, GH, Bockheim, JG, Wilson, SC and Leide, JE 1989a, 'Late Quaternary Ice-Surface Fluctuations of Beardmore Glacier, Transantarctic Mountains', *Quaternary Research,* vol. 31, no. 2, pp. 183-209.

Denton, GH, Bockheim, JG, Wilson, SC and Stuiver, M 1989b, 'Late Wisconsin and Early Holocene Glacial History, Inner Ross Embayment, Antarctica', *Quaternary Research,* vol. 31, no. 2, pp. 151-82.

Denton, GH and Hughes, TJ 2000, 'Reconstruction of the Ross ice drainage system, Antarctica, at the last glacial maximum', *Geografiska Annaler Series a-Physical Geography,* vol. 82A, no. 2-3, pp. 143-66.

Denton, GH and Hughes, TJ 2002, 'Reconstructing the Antarctic Ice Sheet at the Last Glacial Maximum', *Quaternary Science Reviews,* vol. 21, no. 1-3, pp. 193-202.

Dowdeswell, JA and Evans, S 2004, 'Investigations of the form and flow of ice sheets and glaciers using radio-echo sounding', *Reports on Progress in Physics,* vol. 67, no. 10, pp. 1821-61.

Eisen, O, Frezzotti, M, Genthon, C, Isaksson, E, Magand, O, van den Broeke, MR, Dixon, DA, Ekaykin, A, Holmlund, P, Kameda, T, Karlof, L, Kaspari, S, Lipenkov, VY, Oerter, H, Takahashi, S and Vaughan, DG 2008, 'Ground-based measurements of spatial and temporal variability of snow accumulation in east Antarctica', *Reviews of Geophysics,* vol. 46, no. 1, p. 39. Review.

Eisen, O, Nixdorf, U, Wilhelms, F and Miller, H 2002, 'Electromagnetic wave speed in polar ice: validation of the common-midpoint technique with high-resolution dielectric-profiling and gamma-density measurements', in *Annals of Glaciology, Vol 34, 2002*, vol. 34, pp. 150-6.

Eisen, O, Wilhelms, F, Nixdorf, U and Miller, H 2003, 'Revealing the nature of radar reflections in ice: DEP-based FDTD forward modeling', *Geophysical Research Letters,* vol. 30, no. 5.

Fahnestock, M, Abdalati, W, Joughin, I, Brozena, J and Gogineni, P 2001, 'High Geothermal Heat Flow, Basal Melt, and the Origin of Rapid Ice Flow in Central Greenland', *Science,* vol. 294, no. 5550, pp. 2338-42.

Fahnestock, MA, Scambos, TA, Bindschadler, RA and Kvaran, G 2000, 'A millennium of variable ice flow recorded by the Ross Ice Shelf, Antarctica', *Journal of Glaciology,* vol. 46, no. 155, pp. 652-64.

Fountain, AG, Nylen, TH, MacClune, KL and Dana, GL 2006, 'Glacier mass balances (1993-2001), Taylor Valley, McMurdo Dry Valleys, Antarctica', *Journal of Glaciology,* vol. 52, no. 178, pp. 451-62.

Frezzotti, M, Capra, A and Vittuari, L 1998, 'Comparison between glacier ice velocities inferred from GPS and sequential satellite images', *Annals of Glaciology,* vol. 27, pp. 54-60.

Frezzotti, M, Tabacco, IE and Zirizzotti, A 2000, 'Ice discharge of eastern Dome C drainage area, Antarctica, determined from airborne radar survey and satellite image analysis', *Journal of Glaciology,* vol. 46, no. 153, pp. 253-64. Article.

Fricker, HA, Coleman, R, Padman, L, Scambos, TA, Bohlander, J and Brunt, KM 2009, 'Mapping the grounding zone of the Amery Ice Shelf, East Antarctica using InSAR, MODIS and ICESat', *Antarctic Science,* vol. 21, no. 5, pp. 515-32.

Fricker, HA, Warner, RC and Allison, I 2000, 'Mass balance of the Lambert GlacierAmery Ice Shelf system, East Antarctica: a comparison of computed balance fluxes and measured fluxes', *Journal of Glaciology,* vol. 46, pp. 561-70.

Fyke, JG, Weaver, AJ, Pollard, D, Eby, M, Carter, L and Mackintosh, A 2011, 'A new coupled ice sheet-climate model: description and sensitivity to model physics under Eemian, Last Glacial Maximum, late Holocene and modern climate conditions', *Geoscientific model development discussions,* vol. 4, pp. 117-36.

Giovinetto, M, Robinson, ES and Swithinbank, CW 1964, 'The regime of the western part of the Ross Ice Shelf drainage system', *Journal of Glaciology,* vol. 6, pp. 55-68.

Goldberg, D, Holland, DM and Schoof, C 2009, 'Grounding line movement and ice shelf buttressing in marine ice sheets', *J. Geophys. Res.,* vol. 114, no. F4, p. F04026.

Golledge, NR and Levy, RH 2011, 'Geometry and dynamics of an East Antarctic Ice Sheet outlet glacier under past and present climates', *Accepted by the Journal of Geophysical Research*.

Graf, WL 1970, 'The Geomorphology of the Glacial Valley Cross Section', *Arctic and Alpine Research,* vol. 2, no. 4, pp. 303-12.

Greuell, W 1992, 'Hintereisferner, Austria: mass-balance reconstruction and numerical modelling of the historical length variations', *Journal of Glaciology,* vol. 38, no. 129, pp. 233-44.

Greve, R and Blatter, H 2009, *Dynamics of Ice Sheets and Glaciers*, Springer, Dordrecht Heidelberg London New York.

Griggs, JA and Bamber, JL 2009, 'A new 1km digital elevation model of Antarctica derived from combined radar and laser data – Part 2: Validation and error estimates', *The Cryosphere,* vol. 3, no. 1, pp. 113-23.

Grinsted, A, Moore, J, Spikes, VB and Sinisalo, A 2003, 'Dating Antarctic blue ice areas using a novel ice flow model', *Geophysical Research Letters,* vol. 30, no. 19, p. 2005.

Hall, BL 2009, 'Holocene glacial history of Antarctica and the sub-Antarctic islands', *Quaternary Science Reviews,* vol. 28, no. 21-22, pp. 2213-30.

Hall, BL, Denton, GH and Hendy, CH 2000, 'Evidence from Taylor Valley for a grounded ice sheet in the Ross Sea, Antarctica', *Geografiska Annaler Series a-Physical Geography,* vol. 82A, no. 2-3, pp. 275-303.

Haskell, TR, Kennett, JP and M., PW 1965, 'Geology of the Brown Hills and Darwin Mountains, southern Victoria Land, Antarctica', *Transactions of the Royal Society of New Zealand (Geology),* vol. 2, pp. 231-48.

Hempel, L, Thyssen, F, Gundestrup, N, Clausen, HB and Miller, H 2000, 'A comparison of radio-echo sounding data and electrical conductivity of the GRIP ice core', *Journal of Glaciology,* vol. 46, no. 154, pp. 369-74. Article.

Herron, MM and Langway, CC 1980, 'Firn densification: an emperical model', *Journal of Glaciology,* vol. 25, no. 93, pp. 373-85.

Higgins, SM, Denton, GH and Hendy, CH 2000a, 'Glacial geomorphology of Bonney drift, Taylor Valley, Antarctica', *Geografiska Annaler Series a-Physical Geography,* vol. 82A, no. 2-3, pp. 365-89.

Higgins, SM, Hendy, CH and Denton, GH 2000b, 'Geochronology of Bonney drift, Taylor Valley, Antarctica: Evidence for interglacial expansions of Taylor Glacier', *Geografiska Annaler Series a-Physical Geography,* vol. 82A, no. 2-3, pp. 391-409.

Hindmarsh, RCA 1999, 'On the numerical computation of temperature in an ice sheet', *Journal of Glaciology,* vol. 45, no. 151, pp. 568-74.

Hindmarsh, RCA, Vieli, G, Raymond, MJ and Gudmundsson, GH 2006, 'Draping or overriding: The effect of horizontal stress gradients on internal layer architecture in ice sheets', *Journal of Geophysical Research-Earth Surface,* vol. 111, no. F2.

Hoffman, MJ, Fountain, AG and Liston, GE 2008, 'Surface energy balance and melt thresholds over 11 years at Taylor Glacier, Antarctica', *Journal of Geophysical Research-Earth Surface,* vol. 113, no. F4.

Hooke, R 2005, *Principles of Glacier Mechanics,* 2nd edn, Cambridge University Press, Cambridge.

Horwath, M, Dietrich, R, Baessler, M, Nixdorf, U, Steinhage, D, Fritzsche, D, Damm, V and Reitmayr, G 2006, 'Nivlisen, an Antarctic ice shelf in Dronning Maud Land: geodeticglaciological results from a combined analysis of ice thickness, ice surface height and ice-flow observations', *Journal of Glaciology,* vol. 52, pp. 17-30.

Hubbard, A 2000, 'The Verification and Significance of Three Approaches to Longitudinal Stresses in High-Resolution Models of Glacier Flow', *Geografiska Annaler. Series A, Physical Geography,* vol. 82, no. 4, pp. 471-87.

Hubbard, A, Lawson, W, Anderson, B, Hubbard, B and Blatter, H 2004, 'Evidence for subglacial ponding across Taylor Glacier, Dry Valleys, Antarctica', in *Annals of Glaciology, Vol 39, 2005*, vol. 39, pp. 79-84.

Hughes, T 1977, 'West Antarctic Ice Streams', *Reviews of geophysics and space physics,* vol. 15, no. 1, pp. 1-46.

Hughes, T and Fastook, JL 1981, 'Byrd Glacier: 1978-1979 field results', *Antarctic Journal of U.S.,* vol. 16, no. 5, pp. 86-9.

Humbert, A, Greve, R and Hutter, K 2005, 'Parameter sensitivity studies for the ice flow of the Ross Ice Shelf, Antarctica', *Journal of Geophysical Research-Earth Surface,* vol. 110, no. F4.

Huybrechts, P 1990, 'A 3-D model for the Antarctic ice sheet: a sensitivity study on the glacial-interglacial contrast', *Climate Dynamics,* vol. 5, no. 2, pp. 79-92.

Huybrechts, P 2009, 'GLOBAL CHANGE West-side story of Antarctic ice', *Nature,* vol. 458, no. 7236, pp. 295-6.

Huybrechts, P and Oerlemans, J 1988, 'Evolution of the East Antarctic Ice Sheet: a numerical study of thermo-mechanical response patterns with changing climate', *Annals of Glaciology,* vol. 11, pp. 52-9.

Ingolfsson, O 2007, 'Late Quaternary of Antarctica', in *Glaciations*, Elsevier, pp. 1076-84.

IPCC 2007, 'Summary for Policymakers', in S Solomon, D Qin, M M., Z Chen, M Marquis, KB Averyt, T M. and HL Miller (eds), *Climate Change 2007: The Physical Science Basis*, Cambridge University Press, Cambridge, United Kingdom and New York, USA, p. 18.

Irvine-Fynn, TDL, Moorman, BJ, Williams, JLM and Walter, FSA 2006, 'Seasonal changes in ground-penetrating radar signature observed at a polythermal glacier, Bylot Island, Canada', *Earth Surface Processes and Landforms,* vol. 31, no. 7, pp. 892-909.

Jenkins, A, Corr, HFJ, Nicholls, KW, Stewart, CL and Doake, CSM 2006, 'Interactions between ice and ocean observed with phase-sensitive radar near an Antarctic ice-shelf grounding line', *Journal of Glaciology,* vol. 52, pp. 325-46.

Jenkins, A and Doake, CSM 1991, 'Ice-Ocean Interaction on Ronne Ice Shelf, Antarctica', *Journal of Geophysical Research,* vol. 96, no. C1, pp. 791-813.

Jenkins, A, Dutrieux, P, Jacobs, SS, McPhail, SD, Perrett, JR, Webb, AT and White, D 2010, 'Observations beneath Pine Island Glacier in West Antarctica and implications for its retreat', *Nature Geosci,* vol. 3, no. 7, pp. 468-72.

Jezek, KC and Bentley, CR 1983, 'Field studies of bottom crevasses in the Ross Ice Shelf, Antarctica', *Journal of Glaciology,* vol. 29, no. 101, pp. 118-26.

Jezek, KC, Bentley, CR and Clough, JW 1979, 'Electromagnetic sounding of bottom crevasses on the Ross Ice Shelf, Antarctica', *Journal of Glaciology,* vol. 24, no. 90, pp. 321-30.

Jin, M, Dickinson, RE and Vogelmann, AM 1997, 'A Comparison of CCM2–BATS Skin Temperature and Surface-Air Temperature with Satellite and Surface Observations', *Journal of Climate,* vol. 10, no. 7, pp. 1505-24.

Johnson, JV and Staiger, JW 2007, 'Modeling long-term stability of the Ferrar Glacier, East Antarctica: Implications for interpreting cosmogenic nuclide inheritance', *Journal of Geophysical Research-Earth Surface,* vol. 112, no. F3.

Jol, HM 2009, *Ground penetrating radar: theory and applications*, Elsevier.

Joughin, I, Tulaczyk, S, Bamber, JL, Blankenship, D, Holt, JW, Scambos, T and Vaughan, DG 2009, 'Basal conditions for Pine Island and Thwaites Glaciers, West Antarctica, determined using satellite and airborne data', *Journal of Glaciology,* vol. 55, pp. 245-57.

Joyce, A, Adamson, J, Huntley, B, Parr, T and Baxter, R 2001, 'Standardisation of temperature observed by automatic weather stations', *Environmental Monitoring and Assessment,* vol. 68, no. 2, pp. 127-36.

Karlsson, NB, Rippin, DM, Vaughan, DG and Corr, HFJ 2009, 'The internal layering of Pine Island Glacier, West Antarctica, from airborne radar-sounding data', *Annals of Glaciology,* vol. 50, pp. 141-6.

Katz, RF and Worster, MG 2010, 'Stability of ice-sheet grounding lines', *Proceedings of the Royal Society. A, Mathematical, physical, and engineering sciences,* vol. 466, no. 2118, pp. 1597-620.

Kavanaugh, JL and Cuffey, KM 2009, 'Dynamics and mass balance of Taylor Glacier, Antarctica: 2. Force balance and longitudinal coupling', *J. Geophys. Res.,* vol. 114, no. F4, p. F04011.

Kavanaugh, JL, Cuffey, KM, Morse, DL, Bliss, AK and Aciego, SM 2009a, 'Dynamics and mass balance of Taylor Glacier, Antarctica: 3. State of mass balance', *J. Geophys. Res.,* vol. 114, no. F4, p. F04012.

Kavanaugh, JL, Cuffey, KM, Morse, DL, Conway, H and Rignot, E 2009b, 'Dynamics and mass balance of Taylor Glacier, Antarctica: 1. Geometry and surface velocities', *J. Geophys. Res.,* vol. 114, no. F4, p. F04010.

Kenneally, JR and Hughes, TJ 2004, 'Basal melting along the floating part of Byrd Glacier', *Antarctic Science,* vol. 16, no. 3, pp. 355-8.

Kerr, A and Huybrechts, P 1999, 'The response of the East Antarctic ice-sheet to the evolving tectonic configuration of the Transantarctic Mountains', *Global and Planetary Change,* vol. 23, no. 1-4, pp. 213-29.

King, EC 2009, 'Flow dynamics of the Rutford Ice Stream ice-drainage basin, West Antarctica, from radar stratigraphy', *Annals of Glaciology,* vol. 50, pp. 42-8.

Korona, J, Berthier, E, Bernard, M, Rémy, F and Thouvenot, E 2009, 'SPIRIT. SPOT 5 stereoscopic survey of Polar Ice: Reference Images and Topographies during the fourth International Polar Year (2007–2009)', *ISPRS journal of photogrammetry and remote sensing,* vol. 64, no. 2, pp. 204-12.

Laskar, J, Robutel, P, Joutel, F, Gastineau, M, Correia, ACM and Levrard, B 2004, 'A long-term numerical solution for the insolation quantities of the Earth', *Astronomy & Astrophysics,* vol. 428, no. 1, pp. 261-85.

Le Brocq, AM, Payne, AJ and Vieli, A 2010a, 'Antarctic dataset in NetCDF format'. doi:10.1594/PANGAEA.734145.

Le Brocq, AM, Payne, AJ and Vieli, A 2010b, 'An improved Antarctic dataset for high resolution numerical ice sheet models (ALBMAP v1)', *Earth Syst. Sci. Data Discuss.,* vol. 3, no. 1, pp. 195-230.

Leysinger Vieli, GJMC, Hindmarsh, RCA and Siegert, MJ 2007, 'Three-dimensional flow influences on radar layer stratigraphy', *Annals of Glaciology,* vol. 46, pp. 22-8.

LGP 2004, *Summary of 3 years of meteorological data from the Brown Hills AWS: 2005-2007*, Antarctica New Zealand, Christchurch. Retrieved 15 November, from http://www.lgp.aq/downloads/3YearsBrownHillsAWS.pdf

Lin, LI 1989, 'A Concordance Correlation-Coefficient to Evaluate Reproducibility', *Biometrics,* vol. 45, no. 1, pp. 255-68.

LINZ 2010, *Darwin Glacier Digital Elevation Model data*, Land Information New Zealand, May 2010, from http://www.linz.govt.nz/topography/topographic-data/antarctic-topo-data/index.aspx

Liu, H, Jezek, KC, Li, B and Zhao, Z 2001, *Radarsat Antarctic Mapping Project digital elevation model version 2.* , Boulder, CO: National Snow and Ice Data Center, 12 October 2009, from http://nsidc.org/data/nsidc-0082.html

Liu, HX, Jezek, KC and Li, BY 1999, 'Development of an Antarctic digital elevation model by integrating cartographic and remotely sensed data: A geographic information system based approach', *Journal of Geophysical Research-Solid Earth,* vol. 104, no. B10, pp. 23199-213. Article.

Lorius, C, Jouzel, J, Ritz, C, Merlivat, L, Barkov, NI, Korotkevich, YS and Kotlyakov, VM 1985, 'A 150,000-YEAR CLIMATIC RECORD FROM ANTARCTIC ICE', *Nature,* vol. 316, no. 6029, pp. 591-6.

Lucchitta, BK and Ferguson, HM 1986, 'Antarctica: Measuring Glacier Velocity from Satellite Images', *Science,* vol. 234, no. 4780, pp. 1105-8.

Lythe, MB and Vaughan, DG 2001, 'BEDMAP: A new ice thickness and subglacial topographic model of Antarctica', *Journal of Geophysical Research-Solid Earth,* vol. 106, no. B6, pp. 11335-51.

Lythe, MB, Vaughan, DG and BEDMAP-Consortium 2000a, 'BEDMAP - bed topography of the Antarctic. 1:10,000,000 scale map', ed. BAS 9. British Antarctic Survey, Cambridge, UK.

Lythe, MB, Vaughan, DG and BEDMAP-Consortium 2000b, *BEDMAP ice thickness data summary*, British Antarctic Survey, Cambridge. Retrieved 16 September, from http://www.antarctica.ac.uk/bas_research/data/access/bedmap/database/metadata.html

Ma, Y, Gagliardini, O, Ritz, C, Gillet-Chaulet, F, Durand, G and Montagnat, M 2010, 'Enhancement factors for grounded ice and ice shelves inferred from an anisotropic ice-flow model', *Journal of Glaciology,* vol. 56, no. 199, pp. 805-12.

MacAyeal, DR and Thomas, RH 1986, 'The effect of basal melting on the present flow of the Ross Ice Shelf, Antarctica', *Journal of Glaciology,* vol. 32, no. 110, pp. 72-86.

MacDonald, TR, Ferrigno, JG and Richard S. Williams, J 1989, 'Velocities of antarctic outlet glaciers determined from sequential Landsat images', *Antarctic Journal of U.S.,* vol. 24, no. 5, pp. 105-6.

Maule, CF, Purucker, ME, Olsen, N and Mosegaard, K 2005, 'Heat Flux Anomalies in Antarctica Revealed by Satellite Magnetic Data', *Science,* vol. 309, no. 5733, pp. 464-7.

McCormac, FG, Hogg, AG, Blackwell, PG, Buck, CE, Higham, TFG and Reimer, PJ 2004, 'SHCal04 Southern Hemisphere calibration, 0-11.0 cal kyr BP', *Radiocarbon,* vol. 46, no. 3, pp. 1087-92. Article.

Mercer, JH 1968, 'Glacial Geology of the Reedy Glacier Area, Antarctica', *Geological Society of America bulletin,* vol. 79, no. 4, p. 471.

Monaghan, AJ and Bromwich, DH 2008, 'Advances describing recent Antarctic climate variability', *Bulletin of the American Meteorological Society,* vol. 89, no. 9, pp. 1295-306. Article.

Naish, T, Powell, R, Levy, R, Wilson, G, Scherer, R, Talarico, F, Krissek, L, Niessen, F, Pompilio, M, Wilson, T, Carter, L, DeConto, R, Huybers, P, McKay, R, Pollard, D, Ross, J, Winter, D, Barrett, P, Browne, G, Cody, R, Cowan, E, Crampton, J, Dunbar, G, Dunbar, N, Florindo, F, Gebhardt, C, Graham, I, Hannah, M, Hansaraj, D, Harwood, D, Helling, D, Henrys, S, Hinnov, L, Kuhn, G, Kyle, P, Laufer, A, Maffioli, P, Magens, D, Mandernack, K, McIntosh, W, Millan, C, Morin, R, Ohneiser, C, Paulsen, T, Persico, D, Raine, I, Reed, J, Riesselman, C, Sagnotti, L, Schmitt, D, Sjunneskog, C, Strong, P, Taviani, M, Vogel, S, Wilch, T and Williams, T 2009, 'Obliquity-paced Pliocene West Antarctic ice sheet oscillations', *Nature,* vol. 458, no. 7236, pp. 322-U84.

Navarro, FJ, Macheret, YY and Benjumea, B 2005, 'Application of radar and seismic methods for the investigation of temperate glaciers', *Journal of Applied Geophysics,* vol. 57, no. 3, pp. 193-211.

Nobes, DC 1999, 'The directional dependence of the Ground Penetrating Radar response on the accumulation zones of temperate Alpine glaciers', *First Break,* vol. 17, no. 7, pp. 249-59.

Nye, JF 1952, 'The mechanics of glacier flow', *Journal of Glaciology,* vol. 2, no. 12, pp. 82-93.

Nye, JF 1963, 'Correction factor for accumulation measured by the thickness of the annual layers in an ice sheet', *Journal of Glaciology,* vol. 4, pp. 785-8.

Nye, JF 1965, 'The flow of a glacier in a channel of rectangular, elliptic or parabolic cross-section', *Journal of Glaciology,* vol. 5, no. 41, pp. 661-90.

Pattyn, F 2002, 'Ice-flow characteristics over a rough bedrock: implications for ice-core interpretation', *Polar Meteorology and Glaciology,* vol. 16, pp. 42-52.

Pattyn, F 2003, 'A new three-dimensional higher-order thermomechanical ice sheet model: Basic sensitivity, ice stream development, and ice flow across subglacial lakes', *Journal of Geophysical Research B: Solid Earth,* vol. 108, no. 8.

Pattyn, F, Huyghe, A, De Brabander, S and De Smedt, B 2006, 'Role of transition zones in marine ice sheet dynamics', *Journal of Geophysical Research F: Earth Surface,* vol. 111, no. 2.

Pattyn, F and Naruse, R 2003, 'The nature of complex ice flow in Shirase Glacier catchment, East Antarctica', *Journal of Glaciology,* vol. 49, no. 166, pp. 429-36.

Peters, ME, Blankenship, DD and Morse, DL 2005, 'Analysis techniques for coherent airborne radar sounding: Application to West Antarctic ice streams', *Journal of Geophysical Research-Solid Earth,* vol. 110, no. B6.

Plewes, LA and Hubbard, B 2001, 'A review of the use of radio-echo sounding in glaciology', *Progress in Physical Geography,* vol. 25, no. 2, pp. 203-36.

Pollard, D and Deconto, RM 2009a, *A Coupled Ice-Sheet/Ice-Shelf/Sediment Model Applied to a Marine-Margin Flowline: Forced and Unforced Variations*, Blackwell Publishing Ltd.

Pollard, D and DeConto, RM 2009b, 'Modelling West Antarctic ice sheet growth and collapse through the past five million years', *Nature,* vol. 458, no. 7236, pp. 329-33.

Pollard, D and DeConto, RM 2009c, 'Modelling West Antarctic ice sheet growth and collapse through the past five million years - SUPPLEMENTARY INFORMATION', *Nature,* vol. 458, no. 7236, pp. 1-19.

Pritchard, HD, Arthern, RJ, Vaughan, DG and Edwards, LA 2009, 'Extensive dynamic thinning on the margins of the Greenland and Antarctic ice sheets', *Nature,* vol. 461, no. 7266, pp. 971-5.

Rasmus, K 2009, 'A thermo-hydrodynamic modelling study of an idealized low-elevation blue-ice area in Antarctica', *Journal of Glaciology,* vol. 55, no. 194, pp. 1083-91.

Reddy, TE, Holland, DM and Arrigo, KR 2010, 'Ross ice shelf cavity circulation, residence time,and melting: Results from a model of oceanic chlorofluorocarbons', *Continental Shelf Research,* vol. 30, pp. 733-42.

Reijmer, CH and van den Broeke, MR 2003, 'Temporal and spatial variability of the surface mass balance in Dronning Maud Land, Antarctica, as derived from automatic weather stations', *Journal of Glaciology,* vol. 49, no. 167, pp. 512-20.

Reimer, PJ, Baillie, MG, Bard, E, Bayliss, A, Beck, JW, Bertrand, CJ, Blackwell, PG, Buck, CE, Burr, G, Cutler, KB, Damon, PE, Edwards, LR, Fairbanks, RG, Friedrich, M, Guilderson, TP, Hogg, AG, Hughen, KA, Kromer, B, McCormac, FG, Manning, S, Ramsey, CB, Reimer, RW, Remmele, S, Southon, JR, Stuiver, M, Talamo, S, Taylor, FW, Van der Plicht, J and Weyhenmeyer, CE 2004, 'IntCal04 Terrestrial radiocarbon age calibration, 0-26 cal kyr BP', *Radiocarbon,* vol. 46, no. 3, pp. 1029-58. Article.

Rémy, F and Frezzotti, M 2006, 'Antarctica ice sheet mass balance', *C. R. Geoscience,* vol. 338, pp. 1084-97.

Reusch, D and Hughes, T 2003, 'Surface "waves" on Byrd Glacier, Antarctica', *Antarctic Science,* vol. 15, no. 4, pp. 547-55.

Richardson, C and Holmlund, P 1999, 'Spatial variability at shallow snow-layer depths in central Dronning Maud Land, East Antarctica', in TH Jacka (ed.), *Annals of Glaciology, Vol 29, 1999*, vol. 29, pp. 10-6.

Rignot, E, Bamber, JL, Van Den Broeke, MR, Davis, C, Li, YH, Van De Berg, WJ and Van Meijgaard, E 2008, 'Recent Antarctic ice mass loss from radar interferometry and regional climate modelling', *Nature Geoscience,* vol. 1, no. 2, pp. 106-10. Article.

Rignot, E, Casassa, G, Gogineni, P, Krabill, W, Rivera, A and Thomas, R 2004, 'Accelerated ice discharge from the Antarctic Peninsula following the collapse of Larsen B ice shelf', *Geophysical Research Letters,* vol. 31, no. 18, p. 4. Article.

Rignot, E and Jacobs, SS 2002, 'Rapid bottom melting widespread near Antarctic ice sheet grounding lines', *Science,* vol. 296, no. 5575, pp. 2020-3.

Rignot, E and Thomas, RH 2002, 'Mass balance of polar ice sheets', *Science,* vol. 297, no. 5586, pp. 1502-6.

Rist, MA, Sammonds, PR, Oerter, H and Doake, CSM 2002, 'Fracture of Antarctic shelf ice', *Journal of geophysical research. JGR. Atmospheres,* vol. 107, no. b1.

Robin, GdQ 1955, 'Ice movement and temperature distribution in glaciers and ice sheets', *Journal of glaciology,* vol. 2, pp. 523-32.

Robinson, PH 1984, 'Ice Dynamics and Thermal Regime of Taylor Glacier, South Victoria Land, Antarctica', *Journal of Glaciology,* vol. 30, no. 105, pp. 153-60. Article.

Rotschky, G, Eisen, O, Wilhelms, F, Nixdorf, U and Oerter, H 2004, 'Spatial distribution of surface mass balance on Amundsenisen plateau, Antarctica, derived from ice-penetrating radar studies', *Annals of Glaciology,* vol. 39, pp. 265-70.

Scambos, T, Haran, T, Fahnestock, M, Painter, T and Bohlander, J 2007, 'MODIS-based Mosaic of Antarctica (MOA) data sets: Continent-wide surface morphology and snow grain size', *Remote Sensing of Environment,* vol. 111, no. 2-3, pp. 242-57.

Schenk, T, Csatho, B, van der Veen, CJ, Brecher, H, Ahn, Y and Yoon, T 2005, 'Registering imagery to ICESat data for measuring elevation changes on Byrd Glacier, Antarctica', *Geophysical Research Letters,* vol. 32, no. 23.

Schoof, C 2007, 'Ice sheet grounding line dynamics: Steady states, stability, and hysteresis', *Journal of Geophysical Research,* vol. 112, p. F03S28.

Schäfer, M, Gagliardini, O, Pattyn, F and Meur, EL 2008, 'Applicability of the Shallow Ice Approximation inferred from model inter-comparison using various glacier geometries', *Cryosphere Discussions,* vol. 2, no. 4, pp. 557-99.

Scofield, JP, Fastook, JL and Hughes, TJ 1991, 'Evidence for a frozen bed, Byrd Glacier, Antarctica', *Journal of Geophysical Research-Solid Earth and Planets,* vol. 96, no. B7, pp. 11649-55.

Scott, RF 1913, *Scott's Last Expedition Volume I - Being the journals of Captain R. F. Scott, R. N., C. V. O.*, Elder, London.

SeaRISE 2009, 'Antarctica_5km_withshelves_v0.7.nc', in *Interactive System for Ice sheet Simulation*. University of Montana-Missoula - http://websrv.cs.umt.edu/isis/, 4th November 2009.

Shapiro, NM and Ritzwoller, MH 2004, 'Inferring surface heat flux distributions guided by a global seismic model: particular application to Antarctica', *Earth and Planetary Science Letters,* vol. 223, no. 1-2, pp. 213-24.

Shepherd, A and Wingham, D 2007, 'Recent sea-level contributions of the Antarctic and Greenland ice sheets', *Science,* vol. 315, no. 5818, pp. 1529-32.

Shepherd, A, Wingham, D and Rignot, E 2004, 'Warm ocean is eroding West Antarctic Ice Sheet', *Geophysical Research Letters,* vol. 31, no. 23, p. 4. Article.

Siegert, MJ 1999, 'On the origin, nature and uses of Antarctic ice-sheet radio-echo layering', *Progress in Physical Geography,* vol. 23, no. 2, pp. 159-79. Article.

Siegert, MJ and Fujita, S 2001, 'Internal ice-sheet radar layer profiles and their relation to reflection mechanisms between Dome C and the Transantarctic Mountains', *Journal of Glaciology,* vol. 47, pp. 205-12.

Siegert, MJ, Hindmarsh, RCA, Corr, H, Smith, A, Woodward, J, King, EC, Payne, AJ and Joughin, I 2004a, 'Subglacial Lake Ellsworth: A candidate for in situ exploration in West Antarctica', *Geophysical Research Letters,* vol. 31, no. 23, p. L23403.

Siegert, MJ, Hindmarsh, RCA and Hamilton, GS 2003, 'Evidence for a large surface ablation zone in central East Antarctica during the last Ice Age', *Quaternary Research,* vol. 59, no. 1, pp. 114-21.

Siegert, MJ, Hodgkins, R and Dowdeswell, JA 1998, 'A chronology for the Dome C deep ice-core site through radio-echo layer correlation with the Vostok ice core, Antarctica', *Geophysical Research Letters,* vol. 25, no. 7, pp. 1019-22.

Siegert, MJ, Pokar, M, Dowdeswell, JA and Benham, T 2005, 'Radio-echo layering in West Antarctica: a spreadsheet dataset', *Earth Surface Processes and Landforms,* vol. 30, no. 12, pp. 1583-91.

Siegert, MJ, Welch, B, Morse, D, Vieli, A, Blankenship, DD, Joughin, I, King, EC, Vieli, GJMCL, Payne, AJ and Jacobel, R 2004b, 'Ice Flow Direction Change in Interior West Antarctica', *Science,* vol. 305, no. 5692, pp. 1948-51.

Sinisalo, A, Grinsted, A and Moore, J 2004, 'Scharffenbergbotnen (Dronning Maud Land, Antarctica) blue-ice area dynamics', *Annals of Glaciology,* vol. 39, pp. 417-22.

Sinisalo, A, Grinsted, A, Moore, JC, Karkas, E and Pettersson, R 2003, 'Snow-accumulation studies in Antarctica with ground-penetrating radar using 50, 100 and 800 MHz antenna frequencies', in *Annals of Glaciology, Vol 37*, vol. 37, pp. 194-8.

Sinisalo, A and Moore, JC 2010, 'Antarctic blue ice areas - towards extracting palaeoclimate information', *Antarctic Science,* vol. 22, no. 02, pp. 99-115.

Spencer, MK, Alley, RB and Creyts, TT 2001, 'Preliminary firn-densification model with 38-site dataset', *Journal of Glaciology,* vol. 47, no. 159, pp. 671-6.

Staiger, JW, Marchant, DR, Schaefer, JM, Oberholzer, P, Johnson, JV, Lewis, AR and Swanger, KM 2006, 'Plio-Pleistocene history of Ferrar Glacier, Antarctica: Implications for climate and ice sheet stability', *Earth and Planetary Science Letters,* vol. 243, no. 3-4, pp. 489-503.

Stearns, L 2007, *Outlet glacier dynamics in East Greenland and East Antarctica*, The University of Maine.

Stearns, L and Hamilton, G 2005, 'A new velocity map for Byrd Glacier, East Antarctica, from sequential ASTER satellite imagery', in *Annals of Glaciology, Vol 41, 2005*, vol. 41, Int Glaciological Soc, Cambridge, pp. 71-6.

Stearns, LA, Smith, BE and Hamilton, GS 2008, 'Increased flow speed on a large East Antarctic outlet glacier caused by subglacial floods', *Nature Geoscience,* vol. 1, no. 12, pp. 827-31. Article.

Steig, EJ, Morse, DL, Waddington, ED, Stuiver, M, Grootes, PM, Mayewski, PA, Twickler, MS and Whitlow, SI 2000, 'Wisconsinan and Holocene climate history from an ice core at Taylor Dome, western Ross Embayment, Antarctica', *Geografiska Annaler Series a-Physical Geography,* vol. 82A, no. 2-3, pp. 213-35.

Stone, JO, Balco, GA, Sugden, DE, Caffee, MW, Iii, LCS, Cowdery, SG and Siddoway, C 2003, 'Holocene Deglaciation of Marie Byrd Land, West Antarctica', *Science,* vol. 299, no. 5603, pp. 99-102.

Storey, BC, Fink, D, Hood, D, Joy, K, Shulmeister, J, Riger-Kusk, M and Stevens, MI 2010, 'Cosmogenic nuclide exposure age constraints on the glacial history of the Lake Wellman area, Darwin Mountains, Antarctica', *Antarctic Science,* vol. 22, no. 6, pp. 603-18.

Sugden, DE, Balco, G, Cowdery, SG, Stone, JO and Sass Iii, LC 2005, 'Selective glacial erosion and weathering zones in the coastal mountains of Marie Byrd Land, Antarctica', *Geomorphology,* vol. 67, no. 3-4, pp. 317-34.

Swithinbank, CW 1963, 'Ice Movement of Valley Glaciers Flowing into the Ross Ice Shelf, Antarctica', *Science,* vol. 141, no. 3580, pp. 523-4.

Sykes, HJ, Murray, T and Luckman, A 2009, 'The location of the grounding zone of Evans Ice Stream, Antarctica, investigated using SAR interferometry and modelling', *Annals of Glaciology,* vol. 50, no. 52, pp. 35-40.

Takahashi, A and Kameda, T 2007, 'Instruments and Methods Snow density for measuring surface mass balance using the stake method', *Journal of Glaciology,* vol. 53, pp. 677-80.

Takahashi, S, Endoh, T, Azuma, N and Meshida, S 1992, 'Bare ice fields developed in the inland part of Antarctica', *Proceedings NIPR Symposium on Polar Meteorology and Glaciology*, pp. 128-39.

Thomas, R, Rignot, E, Casassa, G, Kanagaratnam, P, Acuna, C, Akins, T, Brecher, H, Frederick, E, Gogineni, P, Krabill, W, Manizade, S, Ramamoorthy, H, Rivera, A, Russell, R, Sonntag, J, Swift, R, Yungel, J and Zwally, J 2004, 'Accelerated sea-level rise from West Antarctica', *Science,* vol. 306, no. 5694, pp. 255-8. Article.

Todd, C, Stone, J, Conway, H, Hall, B and Bromley, G 2010, 'Late Quaternary evolution of Reedy Glacier, Antarctica', *Quaternary Science Reviews,* vol. 29, no. 11-12, pp. 1328-41.

Truffer, M and Fahnestock, M 2007, 'Rethinking Ice Sheet Time Scales', *Science,* vol. 315, no. 5818, p. 1508.

Turner, J, Lachlan-Cope, T, Colwell, S and Marshall, GJ 2005, 'A positive trend in western Antarctic Peninsula precipitation over the last 50 years reflecting regional and Antarctic-wide atmospheric circulation changes', *Annals of Glaciology,* vol. 41, pp. 85-91.

Uratsuka, S, Nishio, F and Mae, SJ 1996, 'Internal and basal ice changes near the grounding line derived from radio-echo sounding', *Journal of Glaciology,* vol. 42, no. 140, pp. 103-9.

Vacco, DA, Alley, RB, Pollard, D and Reusch, DB 2009, 'Numerical modeling of valley glacier stagnation as a paleoclimatic indicator', *Quaternary Research,* vol. 73, no. 2, pp. 403-9.

van de Berg, WJ, van den Broeke, MR, Reijmer, CH and van Meijgaard, E 2006, 'Reassessment of the Antarctic surface mass balance using calibrated output of a regional atmospheric climate model', *J. Geophys. Res.,* vol. 111, no. D11, p. D11104.

van den Broeke, M, Konig-Langlo, G, Picard, G, Munneke, PK and Lenaerts, J 2009, 'Surface energy balance, melt and sublimation at Neumayer Station, East Antarctica', *Antarctic Science,* vol. 22, no. 1, pp. 87-96.

van den Broeke, M, van de Berg, WJ and van Meijgaard, E 2008, 'Firn depth correction along the Antarctic grounding line', *Antarctic Science,* vol. 20, no. 5, pp. 513-7. Article.

van den Broeke, M, van de Berg, WJ, van Meijgaard, E and Reijmer, C 2006, 'Identification of Antarctic ablation areas using a regional atmospheric climate model', *J. Geophys. Res.,* vol. 111, no. D18, p. D18110.

van der Veen, C 1998, 'Fracture mechanics approach to penetration of bottom crevasses on glaciers', *Cold Regions Science and Technology,* vol. 27, no. 3, pp. 213-23.

Vaughan, DG, Bamber, JL, Giovinetto, M, Russell, J and Cooper, APR 1999a, 'Reassessment of Net Surface Mass Balance in Antarctica', *Journal of Climate,* vol. 12, no. 4, pp. 933-46.

Vaughan, DG, Corr, HFJ, Doake, CSM and Waddington, ED 1999b, 'Distortion of isochronous layers in ice revealed by ground-penetrating radar', *Nature,* vol. 398, no. 6725, pp. 323-6.

Waddington, ED, Conway, H, Steig, EJ, Alley, RB, Brook, EJ, Taylor, KC and White, JWC 2005, 'Decoding the dipstick: Thickness of Siple Dome, West Antarctica, at the Last Glacial Maximum', *Geology,* vol. 33, no. 4, pp. 281-4.

Waddington, ED, Lingle, CS and Scott, AE 2007a, 'ICE CORES | Dynamics of the East Antarctic Ice Sheet', in *Encyclopedia of Quaternary Science*, Elsevier, Oxford, pp. 1305-11.

Waddington, ED, Neumann, TA, Koutnik, MR, Marshall, HP and Morse, DL 2007b, 'Inference of accumulation-rate patterns from deep layers in glaciers and ice sheets', *Journal of Glaciology,* vol. 53, no. 183, pp. 694-712.

Weertman, J 1974, 'Stability of the junction of an ice sheet and an ice shelf', *Journal of Glaciology,* vol. 13, no. 67, pp. 3-11.

Whillans, IM, Chen, YH, Van Der Veen, CJ and Hughes, TJ 1989, 'Force budget: III. Application to Three-dimensional flow of Byrd Glacier, Antarctica', *Journal of Glaciology,* vol. 35, pp. 68-80.

Wilson, CR and Crary, AP 1961, 'Ice movement on the Skelton Glacier', *Journal of Glaciology,* vol. 29, pp. 873-8.

Winther, J-G, Elverhøy, H, Bøggild, CE, Sand, K and Liston, G 1996, 'Melting, runoff and the formation of frozen lakes in a mixed snow and blue-ice field in Dronning Maud Land, Antarctica', *Journal of Glaciology,* vol. 42, no. 141, pp. 271-8.

Woodward, J and King, EC 2009, 'Radar surveys of the Rutford Ice Stream onset zone, West Antarctica: indications of flow (in)stability?', *Annals of Glaciology,* vol. 50, pp. 57-62.

Wuite, J, Jezek, KC, Wu, X, Farness, K and Carande, R 2009, 'The velocity field and flow regime of David Glacier and Drygalski Ice Tongue, Antarctica', *Polar Geography,* vol. 32, no. 3, pp. 111-27.

Zawar-Reza, P, George, S, Storey, B and Lawson, W 2010, 'Summertime boundary layer winds over the Darwin?Hatherton glacial system, Antarctica: observed features and numerical analysis', *Antarctic Science,* vol. 22, no. Special Issue 06, pp. 619-32.

A Appendix

A.1 Airborne radar data

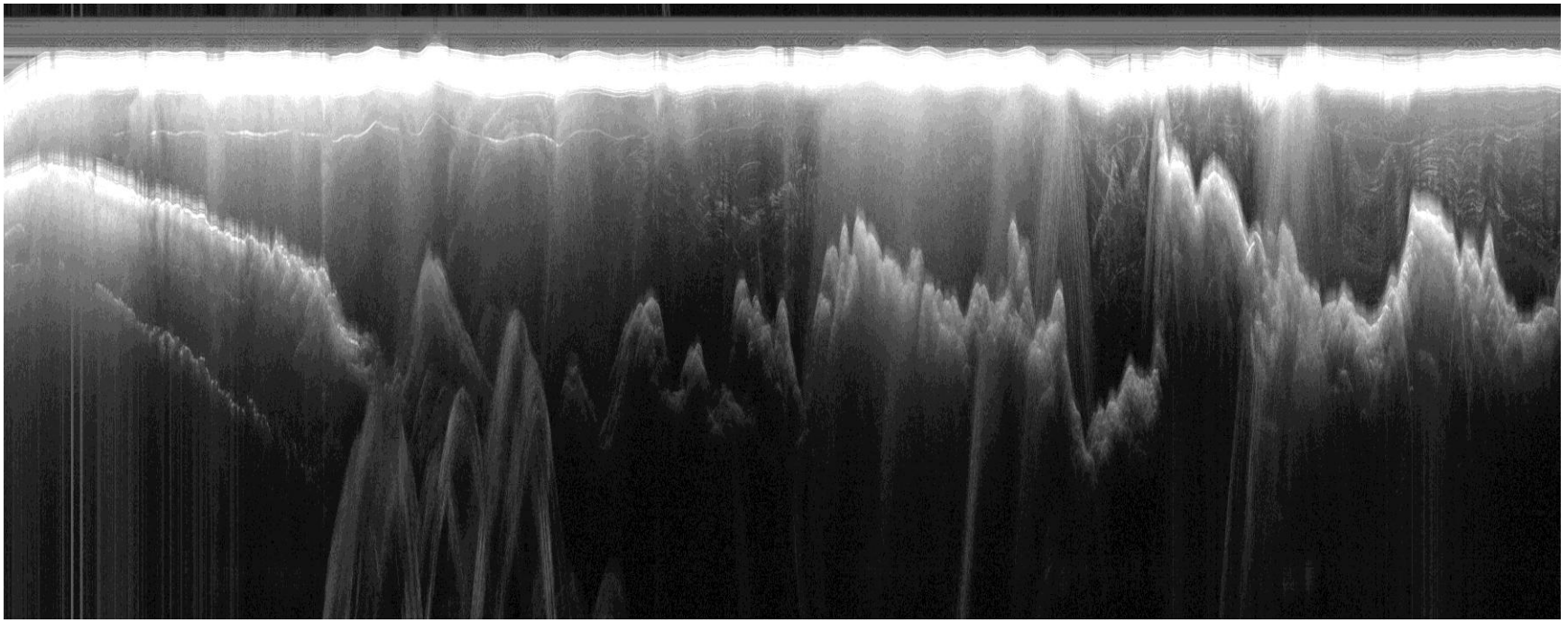

Figure A.1. Low gain airborne radar data collected along the Darwin Glacier from the Ross Ice Shelf to the polar plateau. The position of the flight path is shown on Figure 3.2 between B (start) and B’ (end).

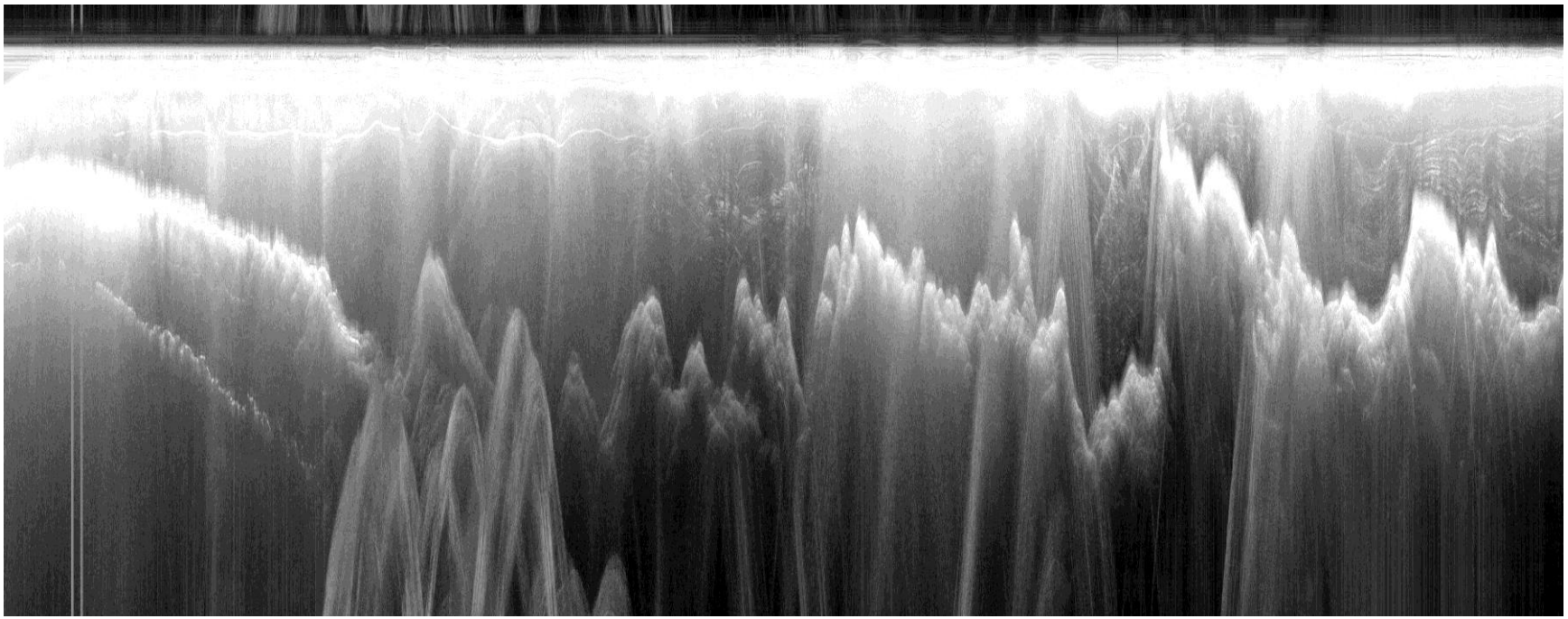

Figure A.2. High gain airborne radar data collected along the Darwin Glacier from the Ross Ice Shelf to the polar plateau. The position of the flight path is shown on Figure 3.2 between B (start) and B’ (end).

A.2 Interpolation routine for the ice thickness map

Developing an approach to accurately interpolate the ice thickness for DHGS is difficult, predominantly due to the irregular distribution of the data points and the varying orientation of the two major valley axes (Figure A.3a). Several different methods were tested in ArcMap and ultimately a completely regularized spline interpolation was chosen as the best option. This method is particularly good for gradually varying topographic surfaces as it fits a smooth surface with a minimum curvature through the exact data points. There are several reasons to prefer this interpolation method. First of all, the completely regularized spline interpolation is an exact interpolator and is therefore true to the input data (shown in section 3.3.2 to be of a very high quality). In addition, it enables the user to specify the size, angle and sector type of the area from which to include data points for the calculation of each interpolated value (the search area). Data points within individual sectors in the search area will have equal weights depending on the relative distance from the interpolated centre point. This is particularly useful when interpolating relatively simple topographic features such as valleys where variations in ice thicknesses are generally largest perpendicular to the valley axis. The ideal search area from which to include data points for the interpolated values depends on the orientation and width of the valley and the distribution of data points.

Because the Darwin and Hatherton glaciers, as well as the smaller tributaries have varying orientation and size, the DHGS was divided into nine different areas within which the valley characteristics are roughly similar (Figure A.3b). Elliptical search areas with an orientation parallel to the predominant valley axis were chosen for each of the nine areas. The shape and size of the ellipses were varied according to the width of the valleys and the distance between cross profiles in the data set (Figure A.4).

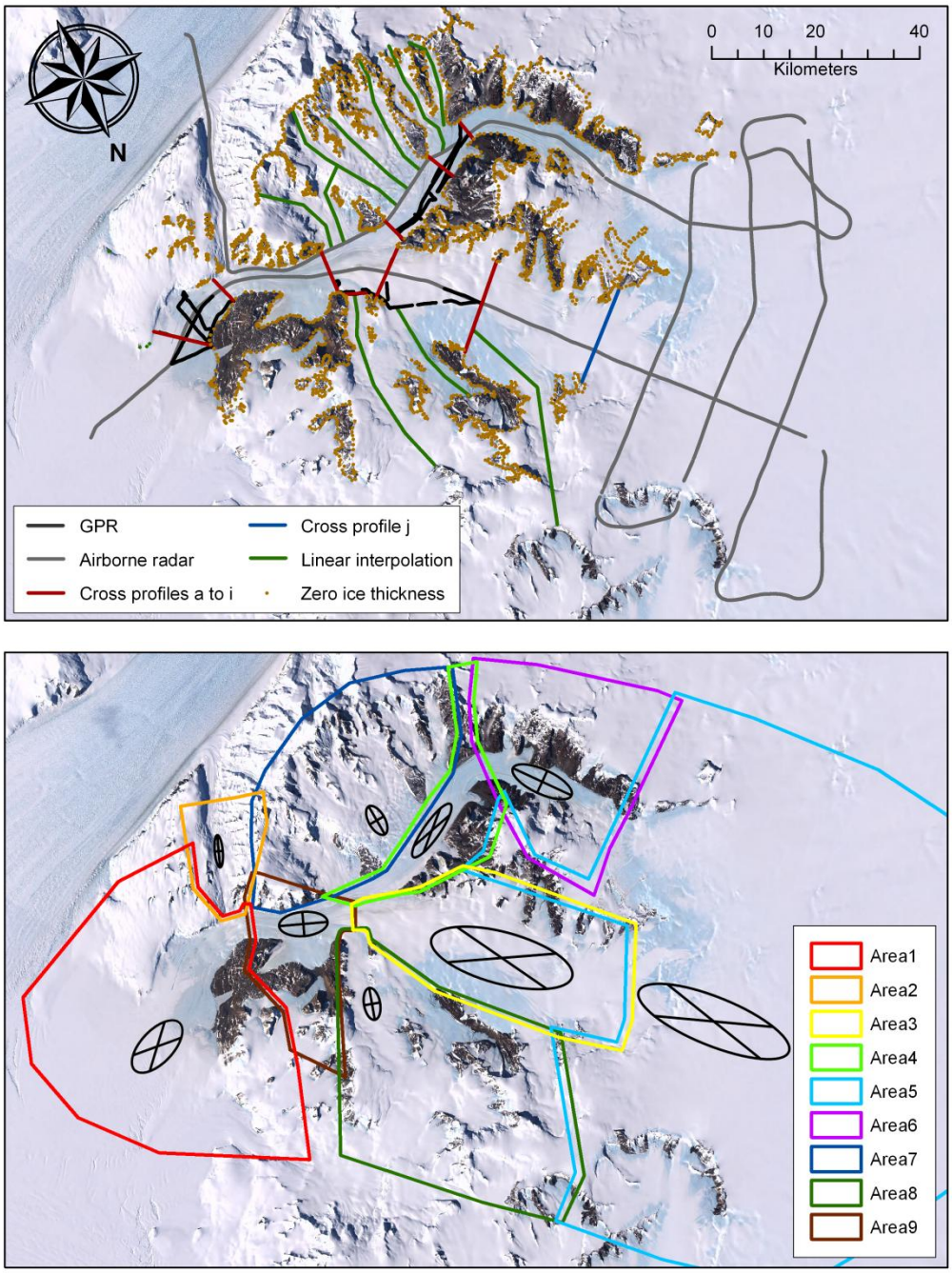

Figure A.3. (a) Overview of data included in the ice thickness interpolation and (b) location of the nine interpolation areas. Black oval shapes show the sector type (described below) as well as orientation and relative sizes of the interpolation search area.

Depending on the distribution of actual data points, the search area was divided into four separate sectors from which to include measurements. When cross profiles were present in the area, the search area was divided into four sectors and shifted 45° (left search area in Figure A.4). When no cross profiles existed within the area, the best results were found when the

search area was divided into four sectors but not shifted. Ice thickness maps were interpolated for each of the nine areas and subsequently merged by gradually blending the maps in the overlapping regions. Some artefacts related to the interpolation method were observed in regions where few data points were present to guide the interpolation. Therefore, several smoothing routines were tested, although a simple mean calculation within a radius of 500 m was found to be the best way to remove the artefact while preserving as much of the true variation in the interpolation map. The difference between the smoothed ice thickness map and the input data points were evaluated by comparing a 50 m resolution raster of the input data points (mean value for every cell) with the smoothed 50 m resolution map. Subtracting the interpolation from the input data gave a mean difference of 5.5 m and a standard deviation of only 46 m, showing that the smoothed map accurately represents the input dataset.

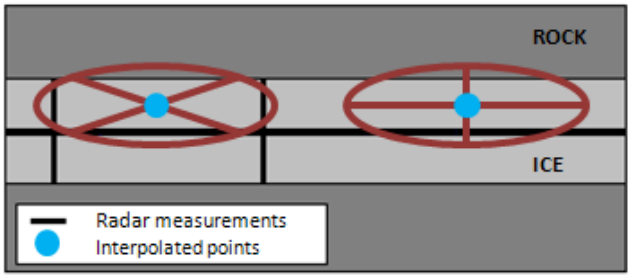

Figure A.4. Image of the two different sector types used for the interpolation and the difference settings for which they were applied.